Universitat Autònoma de Barcelona

Spatiotemporal analysis of brassinosteroid signaling in the vascular stem cells

Isabel Betegón Putze

Universitat Autònoma de Barcelona

Center for Research in Agricultural Genomics (CRAG)

Spatiotemporal analysis of brassinosteroid signaling in the vascular stem cells

Isabel Betegón Putze

November 27, 2020

Universitat Autònoma de Barcelona

Animal biology, Plant biology and Ecology department

Plant Biology and Biotechnology PhD program

Center for Research in Agricultural Genomics (CRAG)

Molecular Genetics department

Spatiotemporal analysis of brassinosteroid signaling in the vascular stem cells

Dissertation submitted in partial fulfillment of the requirements for obtaining the degree of Doctor (PhD) with International Doctorate Mention by Universitat Autònoma de Barcelona (Barcelona, Spain)

Author: Isabel Betegón Putze

Supervisor: Dr. Ana I. Caño Delgado

November 27, 2020

Abstract

This PhD thesis dissertation reports new insights for the Brassinosteroid signaling in the root stem cell niche of *Arabidopsis thaliana*.

Brassisnosteroids are the plant steroid hormones that play important roles in plant growth and development. In the Arabidopsis root, they are involved in the stem cell niche maintenance. Stem cells are the more undifferentiated cells that divide and differentiate to give rise to the distinct cell types of the root. Stem cells are located in the stem cell niche, a specific environment tightly controlled by internal and external factors. The low number each stem cell population makes it difficult to study them individually, therefore, recent advances in cell-type and single-cell specific approaches are starting to be used to understand this rare population. In this PhD thesis, we used an interdisciplinary approach, including genetics, transcriptomics analysis and mathematical modelling, to decipher the molecular signatures of the root stem cells and specifically in the role of Brassinosteroids in those cells.

Defects in growth and development processes is often reflected in abnormal primary root growth. In this PhD dissertation, we describe the development of MyROOT software for the accurate measurements of plant

primary root length, which is crucial for plant development studies. In addition, the results presented in this thesis uncover the role of BRs in the stem cell niche. A systems biology approach revealed a role of the BR-mediated BRAVO transcription factor together with WOX5 in overall root growth and development. Moreover, cell-type specific transcriptomic analysis uncover the transcriptional response mediated by BRAVO in the QC and adjacent vascular stem cells. Finally, single-cell RNAseq were used to generate a transcriptomic atlas of the stem cell niche that allowed to characterize the molecular signatures of the stem cells and to find novel stem cell populations within the BRAVO expression domain.

Overall, the present PhD thesis advances in the understanding of stem cells in plants and expose the necessity of multidisciplinary approaches to uncover fundamental biological questions in plant development.

Contents

Abbreviations

BES1 BRI1 EMS SUPRESSOR 1.

BL Brasinolide.

BR(s) Brassinosteroid(s).

BRAVO Brassinosteroid at vascular and organizing center.

CSC Columella stem cells.

DAG Days after germination.

FPPI False positives per image.

GFP Green fluorescent protein.

HOG Histogram of oriented gradient.

LR(s) Lateral root(s).

PCA Principal component analysis.

QC Quiescent center.

ROI Region of interest.

RSML RootSystemML.

SC Single cell.

SCN Stem cell niche.

TF(s) Transcription factor(s).

TPL TOPLESS.

VI Vascular initials.

WOX5 Wuschel-related homeobox 5.

WT Wild type.

Chapter 1

General Introduction

General Introduction

1.1 The Arabidopsis root as a model for plant development studies

Plants are sessile organisms that evolved unique mechanisms enabling them to grow, develop and react to changing environmental conditions. The plant root is an essential organ that provides the necessary structural and functional support for the incorporation of water and nutrients from the soil. Given its importance, the study of molecular processes involved in root growth and development is key to understand plant plasticity. Not only that, but the agricultural application of the gained academic knowledge could lead to the generation of more tolerant crops to the future climate change conditions (Gupta et al., 2020).

Most of our current understanding of plant growth and development was derived from studies on the model species Arabidopsis thaliana (Arabidopsis). Characteristics as its fast life cycle or the simple requirements for its growth in *in vitro* conditions, make it ideal for experimental research. Due to its thin radial morphology and transparency, the Arabidopsis primary root is highly amenable for microscopy studies. In the same manner, its

small and well characterized genome has accelerated the implementation of molecular genetics and computational approaches for the study of plant development.

1.2 The Arabidopsis root organization

The Arabidopsis root system consists in a primary root that emerges from the seed and that can develop several postembryonic lateral roots. The development of primary and lateral roots is hormonal and environmentally controlled and shapes the plant root system architecture. This branching is important for root functions in water uptake and soil anchoring as it increases the surface area of the root (Smith and De Smet, 2012; Motte et al., 2019).

The Arabidopsis primary root has a well-defined structure that serves as an excellent model to study root physiology. It is formed by several cell files arranged as concentric circles, with the stem cell niche (SCN) located at the inner site of the root apex (Figure 1.1 A, Dolan et al. (1993)). The four outer layers are the epidermis, cortex, endodermis and pericycle which surround the vascular tissues inside (Figure 1.1 A). The epidermis is organized in two different cell files starting from 16 initial cells. Upon maturation, the epidermis is formed by two types of cells, the hair cells (called trichoblasts) and the non-hair cells (called atrichoblasts; Dolan et al. (1993); Balcerowicz et al. (2015)). The cortex and the endodermis are formed by one cell type. The pericycle cells can initiate the formation of lateral roots, but only the cells overlying the xylem pole (Laskowski et al., 1995). In the inner cell layers, the vascular tissues have a bilateral symmetry in which a central xylem axis is flanked by two phloem poles

(Figure 1.1 B). Xylem and phloem transport water and solutes, respectively, through the plant. The stem cell niche is protected from the soil by several layers of cells at the root tip which form the root cap, including the central columella root cap and the peripheral lateral root cap. Columella cells are gravity-sensing cells that contain statoliths (starch filled plastids).

Along the longitudinal axis, three zones can be clearly identified in the root: meristematic (MZ), elongation (EZ) and differentiation (DZ). Stem cells originating from the MZ will differentiate into diverse cell lineages and divide in this region. In the EZ, cells elongate and gradually differentiate without further cell division. As they enter the DZ, cells are already mature and no longer elongate. They present secondary structures, such as root hairs and fully differentiated xylem. A fourth region known as the transition zone (TZ) could also be classified between the MZ and the EZ, where cells start increasing in length and width by endoreplication processes (Dolan et al., 1993; Ishikawa and Evans, 1995; Beemster et al., 2003; Verbelen et al., 2006; Takatsuka and Umeda, 2014).

Altogether, the Arabidopsis root provides a versatile model for the study of plant development in a spatiotemporal context, as root growth and development occur both in the radial and longitudinal axes throughout the life of the plant. Remarkably, spatiotemporal root development happens due to a tight regulation of stem cell division in the root stem cell niche.

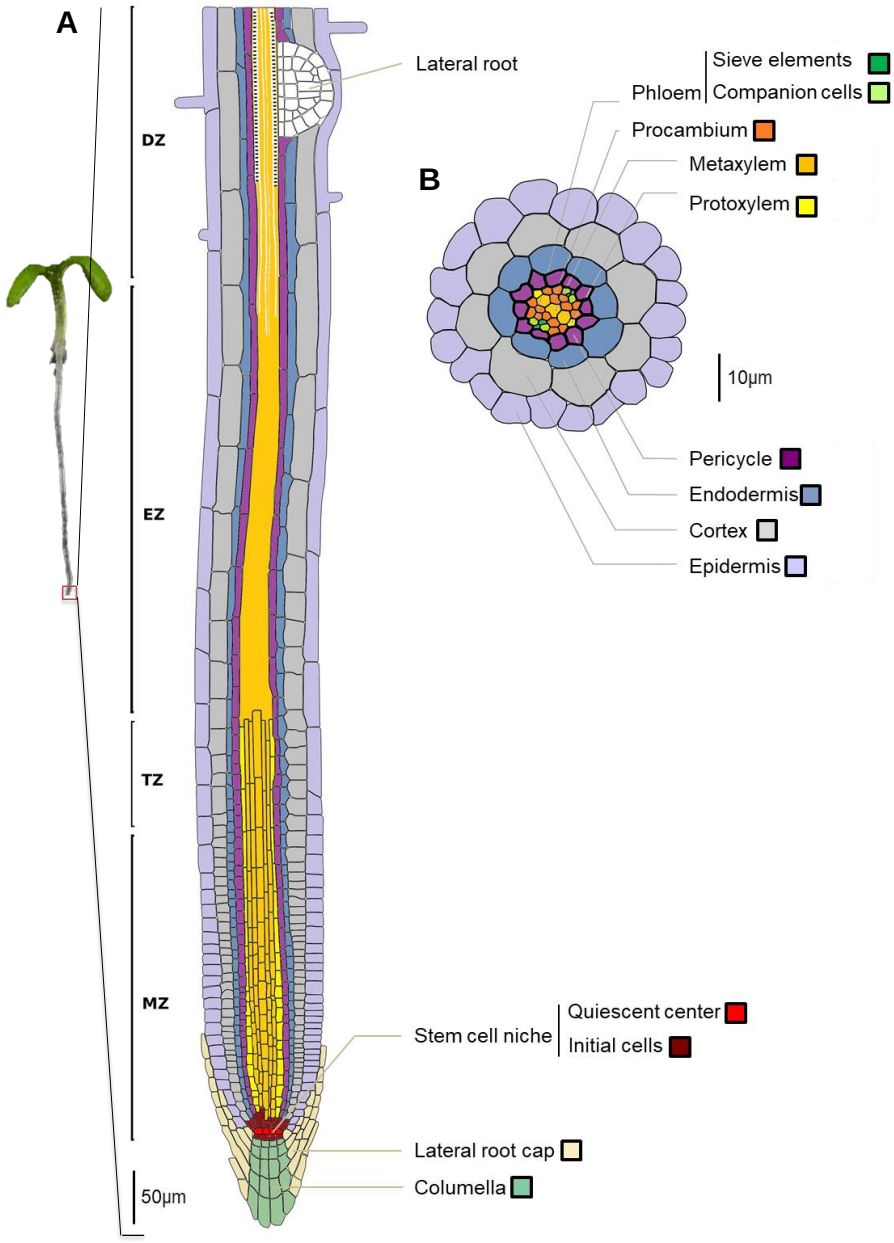

Figure 1.1: The Arabidopsis root.
Schematic representation of a 6-day-old *Arabidopsis thaliana* primary root. Cell types are highlighted in different colors. A) Longitudinal section indicating the meristematic (MZ), transition (TZ), elongation (EZ) and differentiation (DZ) zones. B) Transverse section.

1.3 The root stem cell niche

The primary root arises from the activity of a group of stem cells located in the root apical meristem (RAM), which is essential for root growth, development and regeneration. Stem cells are undifferentiated cells that have the capacity to produce differentiated daughter cells and to renew themselves to retain their stem cell identity (Cheung and Rando, 2013). Not only in the root, the development of all tissues and organs in plants occur after seed germination due to the function of both shoot and root meristems (Heidstra and Sabatini, 2014). Stem cells are maintained in special microenvironments called stem cell niches where local signals from an organizer act to maintain the adjacent stem cells.

The RAM is characterized by the presence of tissue-specific stem cells; different stem cell groups are committed to develop into different tissues of the root. These stem cells known as the root initials are located in the stem cell niche (SCN) of the root meristem where they are surrounding the quiescent center (QC, van den Berg et al. (1997); Figure 1.2). The QC is a group of few cells that show a lower mitotic activity and control the fate of the stem cells by the release of short-range signals that prevent their differentiation. Proximally to the QC, the vascular stem cells (also called vascular initials (VI)) give rise to functional procambial, xylem and phloem tissues (De Rybel et al., 2016). Distally to the QC, the columella stem cells (CSC) give rise to the columella cells (González-García et al. (2011); Stahl et al. (2009)). Adjacent to the QC, the cortex and endodermis initials (CEI) give rise to the cortex and endodermis cell layers (Figure 1.2).

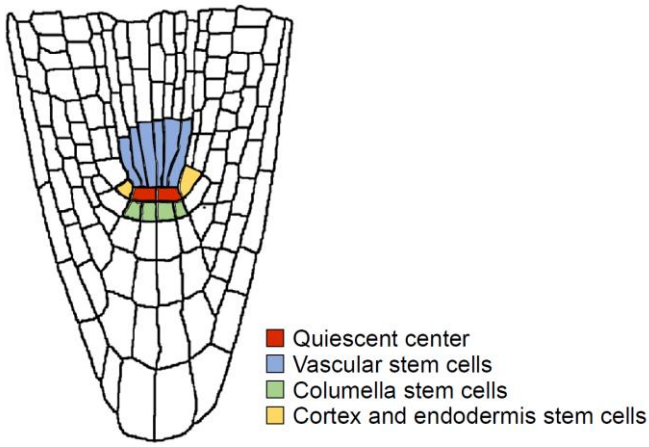

Figure 1.2: The Arabidopsis root stem cell niche.
Schematic representation of a medial longitudinal view of the 6-day-old *Arabidopsis thaliana* primary root apex. The stem cell niche is formed by the quiescent center and the surrounding stem cells, which are highlighted in different colors.

1.4 Factors regulating QC division and stem cell niche maintenance

The regulation of stem cell divisions and the balance between self-renewal and differentiation processes is crucial to the maintenance of tissue homeostasis during the lifetime of an organism. An asymmetric cell division regulates stem cell-fate decisions and it is essential for the conservation of the stem cell compartment as one daughter cell remains as a stem cell and the other enters the differentiation path. The proper balance among them is maintained by both intrinsic programs and environmental regulatory signals (Li and Xie, 2005).

Plants cannot escape environmental hazards such as drought or toxic compounds which can cause oxidative stress or DNA damage that could be fixed as mutations. The plant stem cells are the precursors of tissues

during the whole life of the plant, so the protection from DNA damage is especially important within the stem cell niche. It was also proposed that the QC in Arabidopsis acts as a reservoir to replace stem cells in the root in the presence of a cellular damage (van den Berg et al., 1997; Xu et al., 2006). The response to DNA damage in plants is mediated by ATAXIA-TELANGIECTASIA MUTATED (ATM) and ATM/RAD3-RELATED (ATR) protein kinases and mainly causes a cell cycle arrest, transcriptional activation of genes involved in DNA metabolism, repair and chromosome structure (Hu et al., 2016). When errors cannot be repaired, cell death is promoted exclude hazardous mutations. Mammalian cells trigger programmed cell death (PCD) mainly by the p53 effector, and although non-apoptotic PCD was already known to be present in plants, it has recently been shown in Arabidopsis that SOG1 might induce a similar effect (Fulcher and Sablowski, 2009; Yoshiyama et al., 2014). Treatment of Arabidopsis root tips with genotoxic factors, even with reduced levels of DNA damage, promotes PCD in a meristem cell-type dependent manner. This process is triggered both by ATM and ATR kinases, as the *atm-1* and *atr-2* mutants could not induce cell death (Fulcher and Sablowski, 2009). In particular, stem cells and vascular initial cells appear to be more susceptible to DNA damage than QC cells, since the latter remained alive after radiomimetic drug bleomycin treatment (Fulcher and Sablowski, 2009). The preponderance of PCD in this region over cell cycle arrest could be beneficial for plants, since fast-growing and diving regions cannot afford to spend too much time on cell-by-cell DNA damage repair.

Stem cells are maintained in an undifferentiated state due to the signals released by the QC. In Arabidopsis there are two genetic pathways that are involved in stem cell specification: the PLETHORA (PLT) pathway and

the SHORT ROOT (SHR)/SCARECROW (SCR) pathway (Aida et al., 2004; Helariutta et al., 2000).

PLT genes are induced by the auxin response regulators MONOPTEROS (MP) and BODENLOS (BDL) that are active at auxin peak levels and are proposed to function in establishing the QC in the root tip (Aida et al., 2004). The highest levels of PTL proteins are found in the stem cell area and the regulation of these levels determine the stem cell maintenance or differentiation (Galinha et al., 2007).

SHR and SCR are two members of the plant-specific GRAS transcription factor family (Benfey et al., 1993). SHR moves from the stele into the adjacent cell layers to activate SCR transcription. SCR is expressed in the QC where it maintains QC identity in a cell-autonomous way. SCR is enough to maintain the stem cell niche (Sabatini et al., 2003), since it specifically represses *ARABIDOPSIS RESPONSE REGULATOR 1 (ARR1)* auxin regulator specifically in the QC where cytokinin-dependent cell differentiation is repressed and therefore the stem cell niche activity is sustained (Moubayidin et al., 2013). The SCR protein is also important in maintaining RAM initial cells by regulating in a non-cell-autonomous way the RETINOBLASTOMA-RELATED PROTEIN (RBR) pathway. The RBR is a key point of entry into the G1 phase of the cell cycle, controlling the level of stem cells versus differentiated cell populations to maintain functional RAM (Wildwater et al., 2005). Likewise, SHR and SCR control periclinal division of the CEI through the regulation of CYCD6;1 and the BIRD family members MAGPIE (MGP) and NUTCRACKER (NUT; Levesque et al. (2006); Cui et al. (2007); Welch et al. (2007); Sozzani et al. (2010); Cruz-Ramírez et al. (2012)).

Another key transcription factor related with the QC identity is WUSCHEL-RELATED HOMEOBOX 5 (WOX5). Its expression depends on the induction in the root pole by MP-mediated auxin signalling and on SHR/SCR activity, and it is specific to the QC (Sarkar et al., 2007). WOX5 has been suggested as one of the short-range signals in the QC that prevent stem cell differentiation from the QC. WOX5 acts in restraining cell division in the QC cells by excluding CDKA/CYCLIN D complex (CYCD) activity from those cells and thus establishing the quiescence (Forzani et al., 2014; Pi et al., 2015). The specific expression of WOX5 in the QC is controlled by CLAVATA3/ESR-RELATED 40 (CLE40). This peptide acts through the receptor-like kinase ARABIDOPSIS CRINKLY4 (ACR4) to exclude WOX5 expression outside of the QC and promotes differentiation of columella cells, partly by restricting expression of WOX5 (Stahl et al., 2009). AUXIN RESPONSE FACTOR 10 (ARF10) is a transcription factor that is also involved in restricting the WOX5 domain and in promoting columella cell differentiation. Its expression is specific to the root cap and is dependent on auxin levels (Wang et al., 2005; Ding and Friml, 2010). The REPRESSOR OF WUS1 (ROW1) is a PHD-containing protein also required to maintain QC identity and stem cell niche development. It binds to the WOX5 promoter and represses its transcription. This allows normal proximal meristem cell differentiation and elongation in the maturation zone (Zhang et al., 2015).

An additional level of regulation of the stem cell niche is the movement of some of the aforementioned transcription factors from one cell to another. This movement occurs through the plasmodesmata, which are membrane-lined channels that allow symplastic movement of molecules between cells (Vatén et al., 2011). SHR moves from the stele into the neighboring endo-

dermis where it serves as an activator of endodermal cell fate (Nakajima et al., 2001; Vatén et al., 2011). The WOX5 protein also moves from the QC to the CSC, where it directly represses the transcription factor CYCLIN DOF FACTOR 4 (CDF4) that promotes differentiation (Pi et al., 2015).

1.5 Hormonal regulation in the stem cell niche: the case of brassinosteroids

Plant hormones are key elements involved in specification, development and maintenance of the RAM. They regulate the expression of core genes and their interplay is necessary for integrating external and internal signals into those processes.

Auxin gradients in the root peak at the QC. This gradient is formed by local biosynthesis and polar auxin transport along the root through complex regulations between PINFORMED (PIN) auxin efflux carriers and PLT proteins (Aida et al., 2004; Blilou et al., 2005; Petersson et al., 2009; Mähönen et al., 2014). Auxins also induce WOX5 expression which, in turn, allows maintenance of the auxin maximum (Gonzali et al., 2005). Cytokinins act antagonistically to auxins. They repress WOX5 expression by modulating the auxin flux in the root and promote cell divisions in the QC (Zhang et al., 2013a), and they also influence auxin accumulation in the QC through SCR suppression of cytokinin signaling (Moubayidin et al., 2013). Similarly, ethylene also induces QC divisions (Ortega-Martínez et al., 2007), and jasmonate reduces RAM activity, leading to defects in QC division and CSC differentiation through MYC2-

mediated repression of PLT expression (Chen et al., 2011). ABA promotes QC quiescence and suppresses the differentiation of stem cells and their daughters in root meristems (Zhang et al., 2010).

Brassinosteroids (BR(s)) are a group of polyhydroxylated compounds that control growth and development processes (Planas-Riverola et al., 2019; Nolan et al., 2020). BR are perceived in the plasma membrane by the extracellular domain of the Leucine-Rich-Repeat-Receptor-Like-Kinase (LRR-RLK) proteins (Kinoshita et al., 2005; Wang et al., 2001). The first BR receptor identified was BR-INSENSITIVE-1 (BRI1; Li and Chory (1997)) which is ubiquitously expressed and upon BR activation, it recruits BAK1 co-receptor kinase and initiates a signaling cascade that ends with the inactivation of the phosphatase BIN2 and the dephosphorylation of BES1 (BRI1 EMS SUPPRESOR 1) and BZR1 (BRASSINAZOLE RESISTANT 1) transcription factors (Li et al., 2002; Nam and Li, 2002; He et al., 2005; Li et al., 2001; Russinova et al., 2004). This active form of BES1 and BZR1 in the nucleus bind to the BR respond elements (BREEs) and E-boxes of their target genes and regulate their expression (Sun et al., 2010; Yu et al., 2011). In addition to BRI1, in Arabidopsis there are two other functional receptors called BRI1-LIKE 1 (BRL1) and BRI1-LIKE 3 (BRL3) with enriched expression in the vascular tissues (Caño-Delgado et al., 2004; Fàbregas et al., 2013; Salazar-Henao et al., 2016) where they are involved in vascular development and fine tune plant responses to stress (Lozano-Elena et al., 2018).

Brassinosteroids control primary root growth and promote cell division in the meristem (González-García et al., 2011). In the SCN, BRs play a key role in maintaining the identity and stemness of QC cells. BR signaling modulates BRAVO (BRASSINOSTEROIDS AT VASCULAR AND OR-

GANIZING CENTER) transcription factor, also called MYB56 that belongs to the R2R3-MYB family. BRs downregulate BRAVO expression in the QC and vascular initial cells, where it is specifically expressed. BRAVO inhibition occurs through its heterodimerization with BES1-D, the active dephosphorylated form of BES1 BR downstream effector. BRAVO and BES1 interact at the transcriptional and protein levels forming a signaling module that defines the BR-mediated regulation of stem cell quiescence. BRAVO represses QC division and upon BR signaling, it is sequestered by BES1, which inhibits its action and promotes the division of the QC cells (Vilarrasa-Blasi et al., 2014). Another transcription factor, TOPLESS (TPL) binds via BES1 to the promoter of BRAVO to suppress its expression. TPL directly interacts with BES1 via its ERF-associated amphiphilic repression (EAR) motif (Espinosa-Ruiz et al., 2017). Another BR-regulated transcription factor involved in QC division is ETHYLENE RESPONSE FACTOR 115 (ERF115). ERF115 regulates the expression of PHYTOSULFOKINES 5 (PSK5), a peptide hormone that enhances the frequency of QC divisions (Heyman et al., 2013, 2016), and it is induced by BRs. Altogether, BR signaling represses BRAVO activity and activates ERF115 to promote QC divisions when needed. A case in which BR signaling is activated and QC division is promoted is after a genotoxic stress, which causes cell death in the stele and induce the division of the QC to replenish the damaged ones (Vilarrasa-Blasi et al., 2014). In this response, a steroid paracrine signal is locally perceived by the BRI1 receptor and transduced downstream BES1 from the dead cells to the QC (Lozano-Elena et al., 2018).

In the SCN, BRs promote the expression of WOX5 (González-García et al., 2011), a transcription factor expressed specifically in the QC cells where it

inhibits their division and promote the differentiation of the CSCs (Sarkar et al., 2007). In addition, BRs also promote the differentiation of columella stem cells in a BR concentration-dependent and a signaling molecule-dependent manner (González-García et al., 2011; Lee et al., 2015).

Regarding the regulation of the vascular initial cells, BRs are known to repress periclinal cell division, as BL-treated plants show thinner stele width (González-García et al., 2011; Fàbregas et al., 2013). Interestingly, triple mutant *brl1brl3bak1-3* shows hypersensitivity to BRs in the stele when compared with *bak1* or *brl1 brl3* mutants, indicating a concerted action of BR receptors in the provascular cells (Fàbregas et al., 2013). However, little is known about the specific role of BRs in the stele and in the VI cells, neither about the role of BRI1 or BRL1/3 receptors that show different patterns of expression throughout the root (Fàbregas et al., 2013).

Altogether, BRs play important roles in stem cell division and maintenance which affect proper root growth and development. However, several fundamental questions regarding their mechanism of action or their role in certain stem cell populations remain unanswered. Technical issues such as the capacity to study molecular processes at a cell-type specific level might have hampered the molecular understanding with cell-specific resolution, and the advances made along this PhD thesis represent a breakthrough in this direction.

1.6 Cell-type specific transcriptomics in the Arabidopsis roots

Plant growth and development comprises complex processes that depend on the coordination between single cell, cell types and time. When studying those processes at the whole-organ level, most of the cell-type specific information is lost. Several disciplines have been developed to understand molecular processes with cell type resolution. Some examples are the local expression of signaling components (Marquès-Bueno et al., 2016) or the visualization of cell-specific protein-protein interactions (Long et al., 2017). Moreover, novel CRISPR-Cas9 based methods such as gene inducible systems (Siligato et al., 2016; Wang et al., 2020) and techniques for efficient mutagenesis in specific cell types are available (Decaestecker et al., 2019). CRISPR-Cas9 technology is a newly established gene editing tool that allows editing multiple loci simultaneously via single transformation events (Ma et al., 2015).

Genome-wide transcriptomics experiments enable to address the function of molecular components from specific signaling pathways through the analysis of the regulated genes in the desired experimental conditions. If they are performed with tissue specificity, genome-wide information can be obtained from a certain cell type. Some of the key points for cell-type-specific transcriptomics experiments are the isolation of the individual cells, which is usually done by enzymatic digestion of the cell walls, and the availability of cell-type-specific markers for fluorescent labelling of certain cell types.

Different methods were developed for the isolation of specific cells in

plants: (i) laser capture microdissection (LCM, Kerk et al. (2003)), (ii) protoplasting coupled to fluorescent activated cell sorting (FACS, Birnbaum et al. (2005)) and (iii) isolation of nuclei tagged in specific cell types (INTACT, Deal and Henikoff (2011)). The LCM consists in the isolation of the desired cells with a laser beam while observing them under the microscope. The FACS procedure consists in the generation of lines expressing green fluorescent protein (GFP) in the cell type of interest, the separation of individual cells by digesting their cell walls creating protoplasts, and the isolation of GFP-positive cells using FACS. The INTACT method requires the creation of transgenic plants expressing a biotinylated nuclear envelope protein in the cell type of interest, and it is based in the isolation and purification of those nuclei using streptavidin-coated magnetic beads. The last two methods require the generation of transgenic lines with specific promoters which are markers of the cell type of interest. Therefore, they are limited to the cell types in which markers have been identified.

To investigate cell-type specific responses in Arabidopsis, FACS has been the most used technology as this plant is easily transformed and grown on a large scale. Specifically, the Arabidopsis root, due to its well-characterized and defined tissue distribution, is a widely used model organ for this type of studies. The first transcriptomic-based expression map of the Arabidopsis root cell type was presented in Brady et al. (2007) where they started to elucidate the complex transcriptional network that underlies root spatiotemporal development. Since then, other studies have been done such as the one by Dinneny et al. (2008), describing that a combination of environmental stimuli enables the identification of a core of genes that stably determines cell identity. Regarding hormonal regulation, the role of aux-

ins or brassinosteroids was also evaluated at the cell-type level (Bargmann et al., 2013; Vragović et al., 2015).

The use of these technologies allows the generation of high-resolution transcriptional profiles of individual cell types and different developmental stages that are crucial for the understanding of cell-type specific processes involved in growth and development (Brady et al., 2007). FACS was successfully implemented in other plant tissues such as the shoot apical meristem stem cell niche (Yadav et al., 2009). It also allows the isolation of cell populations for metabolomic analysis (Moussaieff et al., 2013).

1.7 Single-cell transcriptomic technologies in plants

Most of the processes involved in plant organ growth and development are a result of the interplay between specific functions of the different cell types forming it (Brady et al., 2007). The advent of novel techniques that enable a higher resolution for understanding the molecular processes at tissue specific or single cell (SC) level opens new possibilities to investigate these fundamental questions. A recent approach in this direction is the development of single-cell RNAseq (scRNAseq) technologies that allow the identification of the transcriptional profile of individual cells. scRNAseq has already been used in animal systems for the discovery of new cell types and new molecular processes (Consortium, 2020; Cao et al., 2017; Karaiskos et al., 2017).

Single-cell technology in plants is emerging very fast, and it has been widely studied in recent years (Efroni and Birnbaum, 2016; Rodriguez-Villalon and Brady, 2019; Rich-Griffin et al., 2020; Iqbal et al., 2020;

Birnbaum, 2018). The main aspects of single cell technology in plants are reviewed in the following sections, focusing in the Arabidopsis root and in relevant aspects of the methodology, data analysis and recent findings regarding plant development.

Single-cell transcriptomic data generation

A comparison between the single-cell and the common bulk RNAseq methodologies is shown in Figure 1.3. The first step for both bulk and single-cell experiments is the breaking up of the root cells and the selection of the GFP marked cells through FACS. Remarkably, the use of single cell does not require the use of a reporter line and FACS, but they can be used depending on the objective of the research for the enrichment of a certain stem cell population. For bulk RNAseq, the sorted cells are collected together as a unique cell population, whereas in the SC, each cell is collected individually and treated as a single sample. In SC, the transcriptional profile of individual cells is obtained and, due to the unknown identity of each of them, the analysis is done in a unsupervised manner, so the identification of the different cell populations is based only in the similarities between their gene expression profiles. This aspect makes SC RNAseq suitable for the discovery of rare cell populations. On the other hand, in bulk RNAseqs, cell populations are well defined by the marker used for the experiment, and the comparisons or findings that can be done are always supervised by the user and previously defined. As an example, the use of a hormone treatment or a mutant background with the same GFP marker would allow the identification of the genes regulated in that specific experiment in the marked cells (Figure 1.3).

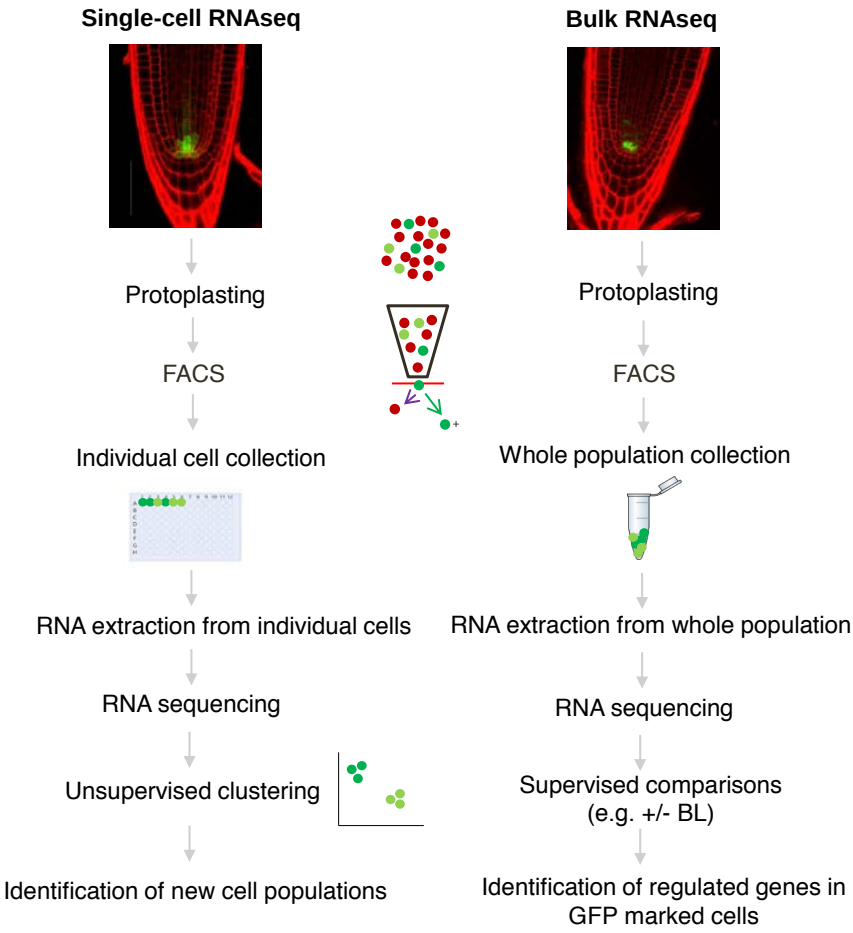

Figure 1.3: Comparison between single-cell and bulk RNAseq methodologies.
Scheme indicating the different steps of a single-cell (left) and bulk (right) RNAseq experiment starting from the isolation of a specific cell population in the SCN. The main differences are the collection of individual cells for the identification of novel cell population using the single-cell methodology (left), and the collection of a whole population for the analysis of differential expression analysis in the bulk methodology (rigth).

A number of different methods are currently available for the obtention of individual cells: plate-based and droplet-based methods. In plate-based methods, cells are sorted individually into microwell plates where the next steps of lysis and reverse transcription are performed. Droplet-based methods are more automatized and employ microfluidics that encapsulate individual cells in droplets containing the reagents for reverse transcription inside each droplet. These two methods have been successfully implemented, and the choice of one or the other is decided based on the aim of the experiment. Plate-based methods resulted in higher sensitivity in terms of number of detectable mRNAs per cell, but lower throughput in terms of number of cells. Plate-based methods are usually coupled with a previous step of FACS that allows the enrichment of a fluorescent-tagged cell population. Droplet-based methods, on the other hand, have lower cell capture rates, making them less appropriate for the discovery of rare cell populations; whereas a much larger number of cells can be processed. A novel method called single-cell combinatorial indexing RNA sequencing allows the molecular reactions to occur inside each cell (Cao et al., 2017). Once the individual cells are isolated, a crucial step is the amplification and labeling of the mRNA from each cell. This happens due to the addition of unique barcodes for the cDNA synthesis and library preparation.

Single-cell transcriptomic data analysis

There are different methods and tools designed for single cell data analysis, which could be consulted in a scRNA-tools database (Zappia et al., 2018). Luecken and Theis (2019) review discussed the existing methods for the single cell data analysis, including Seurat, one of the most used R software packages for single-cell data analysis (Butler et al., 2018).

The basic workflow for the transcriptomic data analysis is the same for bulk and SC in the initial steps. First, the reads are mapped to the genome of reference, the sequences of the adapters are removed, and the gene quantification is performed. Next, a matrix with the gene counts per cell is obtained, that will be the base for the subsequent analysis, revealing the answer for a specific biological question (Figure 1.4).

Preprocessing steps of the data include the removal of lowly-expressed transcripts or empty droplets, which are quite common in droplet-based methods. The presence of many unmapped genes is also common mainly due to the low gene expression levels or low method sensitivity. Nevertheless, single-cell data analysis tools can process them or even replace them with estimations (Peng et al., 2019).

Once high-quality cells have been selected, data is normalized and scaled so the variability between different cells is corrected. Then, the highly variable genes among the dataset are identified. These genes are used for the subsequent analysis as they include most of the variability of the data. Next step is dimensionality reduction for proper visualization and data summarization (Figure 1.4).

Linear dimensional reduction of the data is done with Principal component analysis (PCA) and non-linear dimensional reduction with t-distributed Stochastic Neighbourhood Embedding (tSNE) or Uniform Manifold Approximation and Projection (UMAP). These analyses are done to visualize the data in two dimension plots and have been specifically developed to visualize such complex high-dimensional data as scRNAseq counts (van der Maaten and Hinton, 2008; McInnes et al., 2020).

Clustering analysis consists of grouping the cells based on gene expression

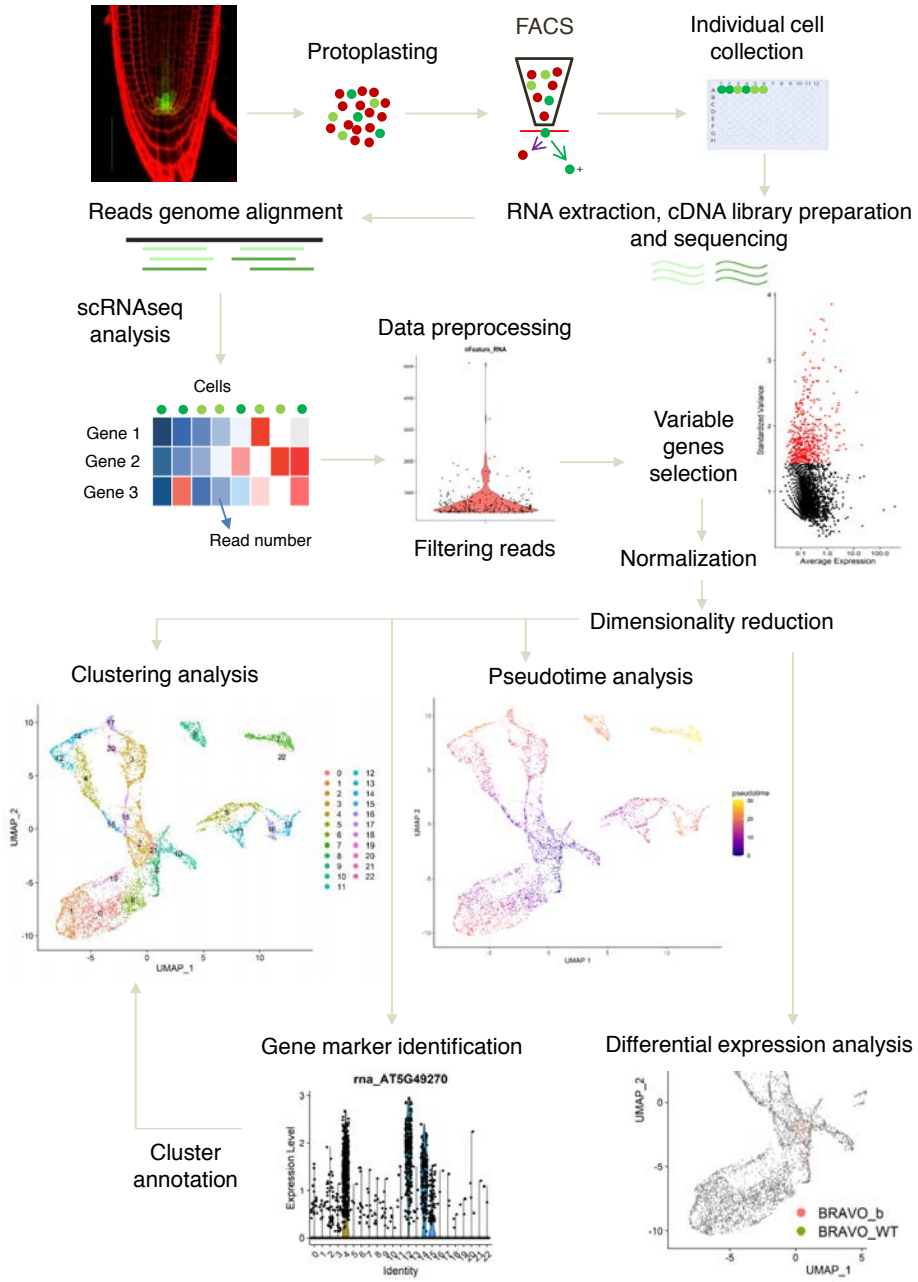

Figure 1.4: Single-cell RNAseq methodology and data analysis. Scheme indicating the different steps of a single-cell RNAseq experiment from the isolation of individual cells to the data analysis.

profiles similarity. Therefore, it allows the identification of biologically significant cell groups that correspond to different cell populations that might be cell types. There are different clustering algorithms such as k-means or graph-based approaches (extensively described in Jain et al. (1999); Rodriguez et al. (2019)). Clustering analysis is usually represented over the tSNE or UMAP graph and the position of the different populations can be an indicator of similarities between them, as groups that are closer might be more similar.

To give identity to the identified clusters, supervised and unsupervised approaches have been stablished. Supervised approaches require knowledge of cell type specific genes previously reported (Brady et al., 2007; Birnbaum et al., 2003) and the evaluation of their expression levels in the dataset. One of these methods allows the use of informative markers sets, which are required to be uniquely expressed in a single cell type and for assigning cell type identity based on the levels of several marker genes (Efroni et al., 2015). The unsupervised approaches consist of the identification of putative marker genes which are the ones defining each cluster. This analysis can be performed with the Seurat software (Butler et al., 2018) and further functional analysis of those marker genes might give information about the nature of the clustered cells. These unsupervised approaches would allow, not only to annotate one cluster identity, but also the discovery of new cell-type markers (Denyer et al., 2019).

One of the main objectives of genome-wide transcriptional experiments is the comparison between two experimental conditions (such as a hormone treatment or a mutant background) in differential expression (DE) analysis. This can also be applied to single-cell RNAseq data. Interestingly, this type of data allows the comparison within a specific cell population as

it can be done in each cluster separately. This allows the characterization of the response of individual cell identities to the experimental condition (Figure 1.4). On the other hand, in bulk RNAseq data, DE can only be evaluated as a whole population.

Comprehensive studies conclude that DE analysis methods developed for bulk RNAseq are equally suitable as those developed specifically for SC data (Soneson and Robinson, 2018). The special characteristics that SC DE methods take into account are the low library sizes, high noise levels and 'dropout' phenomena, in which a gene is observed at a low or moderate expression level in one cell but is not detected in another cell of the same cell type (Soneson and Robinson, 2018; Qiu, 2020). One of the key parameters for DE analysis and for the relevant application of these methods is the sample size, as results are more reliable when the sample is bigger (Soneson and Robinson, 2018).

As root development is a dynamic process, computational models can be applied to organize root cells based on gene expression patterns similarity along a trajectory. The modeling of these trajectory inference methods is also called pseudotime analysis (Figure 1.4). The pseudotime variable is related to transcriptional distances from a root cell and it is often interpreted as developmental time (Trapnell, 2015; Cannoodt et al., 2016; Moon et al., 2018). Pseudotime method was first introduced by the R software package Monocle (Trapnell et al., 2014). Currently, more than 70 tools are available which differ mainly in their underlying algorithm, required input information and produced outputs. Two important parameters are the capacity of the tools to fix the topology of the trajectory and the type of graph topologies they can detect (Saelens et al., 2019). Potential benefits of these methods are the identification of the transcriptional changes that

accompany developmental processes; the construction of gene regulatory networks (Moignard et al., 2015); the identification of the cell types at the beginning, intermediate and end states of the trajectory; and the identification of branching points in the trajectory which may be indicators of cellular decision points (Haghverdi et al., 2016). Comprehensive studies of the comparison between different trajectory inference methods conclude that the use of different tools can be complementary, and the method choice should be based on the dataset characteristics and purpose of the experiment. Generally, any inferred trajectory should be confirmed with an alternative method. Saelens et al. (2019) reviews this topic extensively.

Another important aspect of single-cell RNAseq analysis is visualization of the results. Some of the most important outputs are the expression levels of specific genes in certain cluster. Software is available for the visualization in SC datasets in a fast and user-friendly manner, such as EFP browser (http://bar.utoronto.ca/), PscB (Ma et al., 2020), Arabidopsis Root Cell Atlas (http://wanglab.sippe.ac.cn/rootatlas/, Zhang et al. (2019)) or Plant SC atlas (https://bioit3.irc.ugent.be/plant-sc-atlas/, Wendrich et al. (2020)). Recent versions of Monocle also allow the visualization of clustering or trajectory analysis in 3D graphs and even Stein et al. (2020) developed software for visualization in virtual reality.

Importantly, for single cell data analysis there is not a standardized method, and these analyses are usually done several times changing different parameters such as the number of highly variable genes, principal components and cell type markers. The selection of one or other tool or parameter should be based on the results and their agreement with the biology that is known at that time.

Application of single-cell technology in plant development

Recent studies successfully applied single cell technologies to plant systems. Most of them were performed in the Arabidopsis root using the droplet-based platforms and correspond to the first transcriptomic landscape of a plant organ with single cell resolution (Ryu et al., 2019; Shulse et al., 2019; Denyer et al., 2019; Zhang et al., 2019; Jean-Baptiste et al., 2019; Shahan et al., 2020; Wendrich et al., 2020). These studies have similar objectives and methodology, as they sequence cells from whole roots for the characterization of novel cell types identities, cell specific marker genes and developmental trajectories.

The basic pipeline incorporates the use of Seurat package (Butler et al., 2018; Stuart et al., 2019) or similar single-cell specific software packages for the analysis of the scRNA-seq datasets. By using the most variable genes, clustering analysis is performed to combine root cells in groups based on their gene expression similarity. Then, previously described marker genes for specific cell types are used to assign the identity of the different clusters (Ryu et al., 2019; Shulse et al., 2019; Denyer et al., 2019; Zhang et al., 2019; Jean-Baptiste et al., 2019; Shahan et al., 2020; Wendrich et al., 2020). Some of the studies use unsupervised approaches for the identification of new marker genes (Denyer et al., 2019; Jean-Baptiste et al., 2019; Wendrich et al., 2020) which can be experimentally validated (Denyer et al., 2019) or perform subclustering analysis to assign molecular features inside the same cell type (Denyer et al., 2019; Wendrich et al., 2020).

The root atlas datasets contain between 3000 and 15000 individual cells, except one of the most recent studies that includes more than 110000,

making it a powerful resource for further SC studies (Shahan et al., 2020). This dataset combines data from Ryu et al. (2019) and Denyer et al. (2019) to include experimental variability.

In the Arabidopsis primary root there are low differentiated cells (the stem cells) and fully differentiated cells (in the mature tissues). Single cell data allows the organization of those cells following a trajectory based on their developmental stage and the corresponding transcriptional changes analysis along it. The Pseudotime analysis has been used for the study of specific cell type development, such as endodermis (Shulse et al., 2019), hair cells, cortex cells (Jean-Baptiste et al., 2019), epidermal cells (Ryu et al., 2019), root cap and proximal meristem cells (Zhang et al., 2019). Denyer et al. (2019) organized all cells from meristematic cells to mature tissues and found that the meristematic cells cluster together according to their less differentiated state. In Wendrich2020 they obtained developmental trajectories for all the root tissues (xylem, phloem, procambium, pericycle, endodermis, cortex, epidermis, lateral root cap and columella).

The identification of transcriptional profiles with single cell resolution allows the study of molecular processes at individual cell levels. Few studies compare single-cell data throughout different conditions and treatments to advance in the understanding of certain processes. Ryu et al. (2019) analyzed two root epidermis mutants (*rhd6* and *gl2*), and found that these mutations prevent the transition from one epidermal cell type to another. Shahan et al. (2020) generated single cell resolution atlas of *shortroot* and *scarecrow* mutants and found an alternative pathway acting in mature cells to specify endodermal identity.

Jean-Baptiste et al. (2019) applied heat stress to Arabidopsis roots and

through scRNAseq they found subtle but significant gene expression differences among different cell types, advancing in the understanding of stress responses with single-cell resolution. Studies from Shulse et al. (2019) evaluated sucrose effects at single-cell level and found that plants grown with sucrose present altered proportions of mature cell populations.

Wendrich et al. (2020) used SC datasets to find the role of TMO5/LHW vascular complex in the regulation of root hair development. They found that cytokinin signaling linked root hair responses in the epidermis to perception of phosphate depletion in the vascular cells.

SC analysis were also used for the identification of the transcriptome of regenerating cells that mimic those of the of embryonic roots (Efroni et al., 2016) and for the characterization of VND7-mediated xylem differentiation in the root (Turco et al., 2019). Using previously published datasets, Torii et al. (2020) reanalyzed Ryu et al. (2019) SC data to construct trajectories based on the cell cycle progression to identify genes expressed in specific phases of the cell cycle.

It is noteworthy that, in previous studies, information obtained from apical meristem stem cells is scarce. Regarding the identification of rare cell types such as the QC, only Ryu et al. (2019), Denyer et al. (2019) and Wendrich et al. (2020) were able to identify 2, 36 and 37 QC cells respectively. In most recent studies, more QC cells have been detected and used as the starting stage for developmental trajectory analysis (Shahan et al., 2020; Wendrich et al., 2020), although little specific information about their molecular features in the surrounding initial cells was revealed. Previous studies lack information about the surrounding stem cells such as VI, CSC or CEI and they often refer to the SCN a unique cell type. These facts

support the use of single cell technologies for the identification of very small populations such as the QC, but also highlights the importance of combining it with other methodologies, such as FACS, for the enrichment in rare cell populations before scRNAseq. In this regard, Efroni et al. (2015) used FACS with pWOX5:GFP expressing roots for the isolation of QC cells.

Regarding other Arabidopsis tissues, leaves have been used in SC analysis for Kim et al. (2020) and Lopez-Anido et al. (2020). Kim et al. (2020) generated a SC transcriptome atlas of the leaf vasculature, revealing distinct features of the different vascular cell types. Lopez-Anido et al. (2020) generated a SC population enriched in epidermal cells to evaluate the dynamic developmental states of the stomatal lineage.

This technology has potential application in other plant species with agricultural value, such as Sorghum (Martignago et al., 2019), maize (Nelms and Walbot, 2019) and soybean (Hossain et al., 2017). In this direction, the transcriptional landscape of the maize shoot stem-cell niche and its differentiating cellular descendants (Satterlee et al., 2020) and a high-resolution atlas of the tomato shoot apical meristem (Tian et al., 2020) have been characterized. Cell wall digestion and the lack of genomic resources for the description of cell type specific genes are challenges yet to overcome. Future implementation of single cell analysis of crops certainly opens yet unexplored opportunities for modern breeding.

1.8 Multidisciplinary approaches support experimental analysis in plant development studies

The increasing in knowledge of biological networks, the growing capacity of data processing and modeling, combined with the interplay between biology, physics, mathematics and computation, are redirecting the aim of research to plant development as a whole. Together with computational analysis, several disciplines can complement biological studies such as mathematical modeling or software engineering.

Root growth and development is a complex process orchestrated by the interplay between different signaling networks. The development of mathematical modeling can help to address fundamental questions cannot be easily approached experimentally. Developed models can be used to explain empirical data and to make predictions that can be tested experimentally, which can result in a more robust theory (Shou et al., 2015). Examples of the combination of mathematical modeling and experimental biology are found in studies regarding the root stem cell niche due to its unique properties for studying cell identity, division and differentiation in an isolated environment. Vilarrasa-Blasi et al. (2014) used experimental data to understand the BR-mediated regulation of BRAVO through the construction of a mathematical model that predicts the creation of a molecular switch between BRAVO and BES1 to regulate QC divisions. More recently, the combination of cell-type-specific transcriptomics and mathematical modeling allowed to predict a stem cell regulatory network for the identification of the stem-cell-ubiquitous TCX2 gene that regulates stem cell division (Clark et al., 2019). The role of SHR and SCR in the CEI and QC cells was also approached theoretically and experimentally in

Clark et al. (2020) where they predicted how SHR-SCR complex expression levels and complex stoichiometries regulate the timing of the division of both cell types. García-Gómez et al. (2020) predicted how SHR is key for cell fate transition from QC to columella.

The need for combining biology with other technologies is not exclusive for genetic studies, it is also present in the field of phenotyping. The development of gene editing techniques (such as CRISPR-Cas9) and the need of agriculture to evaluate roots, demanded automatic and high-throughput methods that allow to process large amounts of plant material and the evaluation of a wide range of root traits. Softwares such as BRAT (Slovak et al., 2014) and EZ-Rhizo (Armengaud et al., 2009) permit the automatization of the phenotyping process in Arabidopsis roots growing in agar plates. The implementation of complex systems that combine software and hardware has begun. Xiang et al. (2020) developed an automated robotic imaging system to accurately determine BR-mediated responses through the evaluation of morphological and growth-related traits in the shoot.

1.9 Conclusions and perspectives

The Arabidopsis primary root is an ideal model to study cell-type specific responses due to its physiological and genetic characteristics, and the constant development of technology, resources and knowledge for the understanding of growth and development molecular processes. The root stem cell niche is crucial for those processes, but its unique characteristics difficult its study compared to other cell types.

Previous studies in the laboratory of Dr. Caño-Delgado enlighten the molecular understanding of hormone signaling in stem cell development in the Arabidopsis primary root through system biology approaches. The discovery of novel components of the BR pathway at stem cells such as the BRAVO defined a novel mechanism for maintaining stem cell quiescence (Vilarrasa-Blasi et al., 2014). Additionally, studies of BR receptors highlighted the importance of cell type specific responses for growth, development and stress responses (Fàbregas et al., 2013; Salazar-Henao et al., 2016; Lozano-Elena et al., 2018; Fàbregas et al., 2018). However, specific signatures of the stem cells and the response mediated by BRs and BRAVO in those cells remains unknown. Together, these findings provide fundamental understanding of plant growth and development that may have potential applications for agriculture improvement in the future.

Objectives

The general objective of this PhD thesis was to investigate the roles of brassinosteroids in the stem cell niche, focusing in the vascular stem cells, in the plant model *Arabidopsis thaliana*.

In particular, the following specific objectives have been accomplished:

1. Develop a software tool for the automatic measurement of plant primary root length.
2. Characterize the role of BRAVO and WOX5 in the stem cell niche.
3. Investigate the transcriptional roles of BRAVO in the root quiescent center and vascular stem cells.
4. Identify the molecular signatures of the stem cell niche with single-cell resolution.

Chapter 2

MyROOT software for plant root length analysis

Part of this chapter was published as:

MyROOT: a method and software for the semiautomatic measurement of primary root length in Arabidopsis seedlings. Betegón-Putze, I.*, González, A.*, Sevillano, X., Blasco-Escámez, D. and Caño-Delgado, A.I. (2019) *The Plant Journal*, 98, 1145-1156.

MyROOT 2.0: An automatic tool for high throughput and accurate primary root length measurement. González, A., Sevillano, X., Betegón-Putze, I., Blasco-Escámez, D., Ferrer, M. and Caño-Delgado, A.I. (2020) *Computers and Electronics in Agriculture*, 168, 105125.

MyROOT software for plant root length analysis

2.1 Introduction

The root is an essential organ for overall plant growth and development. The characterization of different root traits is therefore important not only for understanding organ growth, but also for evaluating the impact of roots in agriculture (Kuijken et al., 2015). As such, generating tools for precise, high-throughput phenotyping and imaging of the root is essential for plant research and agriculture. Even phenotyping facilities such as the ones available in the European Plant Phenotypic Network (http://www.plant-phenotyping-network.eu/) have started to implement tools for the massive screening of roots.

Roots provide the necessary structural and functional support for the incorporation of nutrients and water from the soil. In Arabidopsis, the primary root has a very simplified anatomy that makes it very amenable for genetic and microscopic analyses (Dolan et al., 1993; Ishikawa and Evans, 1995; Iyer-Pascuzzi et al., 2009). Different root cell lineages are derived from the activity of the stem cells that occasionally divide asymmetrically

to renew themselves and to form daughter stem cells. From the root apex, these cells actively divide in the meristematic zone, and before exiting the cell cycle in the transition zone, continue to elongate and differentiate in spatially separated regions of the root. In this way, primary root growth is determined by the balance between cell division and cell elongation within the different zones of the root (van den Berg et al., 1997; Beemster and Baskin, 1998; Verbelen et al., 2006; Takatsuka and Umeda, 2014).

The most straightforward symptom of abnormal root growth or development can be identified by examining the length of the primary root in seedlings. Abnormalities in length can usually be observed and measured just five to six days after germination (DAG), where still reflect their embryonic origin (Jürgens et al., 1995). Growth defects in the primary root of seedlings are not only consistent with overall growth defects, but also persistent along the entire plant life cycle (Benfey et al., 1993; González-García et al., 2011; Potuschak et al., 2003). Indeed, Arabidopsis root analyses were the foundations for multiple genetic screens that ultimately led to the identification of several key regulators of plant growth and development (Benfey et al., 1993; Hauser et al., 1995; Caño-Delgado et al., 2000; Mouchel et al., 2004; Ubeda-Tomás et al., 2008).

Root analysis of young seedlings offers direct information regarding overall plant growth and viability. Despite important advances in plant imaging techniques such as microscopic visualization (Pfister et al., 2014; González-García et al., 2015; Lobet, 2017), the root length of seedlings growing in agar plates is generally measured by manually indicating the position of each seedling or manually tracking each root using the ImageJ software (`https://imagej.nih.gov/ij/`). For this reason, the development and use of methods that enable the automatic and accurate analysis of a large

number of roots represents a step forward for high-throughput root analysis. Automatic analysis of root system architecture is just beginning to be implemented, and novel methods based on acquiring, processing, and obtaining quantitative data from root images are now available.

There are several root analysis softwares available that are designed for different purposes. Some of them are applied to crops phenotyping and are more focus in traits related to root architecture such as branching or biomass (Le Bot et al., 2010; Lobet et al., 2011; Nagel et al., 2012; Pound et al., 2013; Pace et al., 2014; Kuijken et al., 2015; Wu et al., 2018). On the other hand, other root image analysis softwares are oriented for the analysis of plant model species as Arabidopsis (Armengaud et al., 2009; French et al., 2009; Yazdanbakhsh and Fisahn, 2012; Slovak et al., 2014). Most of them can reliably measure different root traits (primary root length, lateral roots, etc; Arsenault et al. (1995); Le Bot et al. (2010); Clark et al. (2013); Ristova et al. (2013); Slovak et al. (2014); Cai et al. (2015)). The analysis usually requires intensive user intervention to set the optimal parameters for the root detection and to identify the individual roots (Armengaud et al., 2009; French et al., 2009; Clark et al., 2013). Despite the time-consuming manual tracking of each single root, ImageJ is often used as a tool for primary root length quantification. A summary of the existing softwares for root analysis and their main features are summarized in Table 2.1.

Despite the numerous tools for root analysis, those lack the capability of precisely measure primary root length of seedlings, which is key for the genetic, physiological and developmental studies in the plant model Arabidopsis and it is often done manually. Here, we present MyROOT, a software capable of semi-automatically calculating primary root length in

a fast and user-friendly manner, able to adapt to different imaging and experimental conditions. By automatically identifying the scale and precisely detecting all individual roots and hypocotyls growing on an agar plate from a JPEG image, this software simplifies and minimizes user intervention during the calculation of root length. MyROOT merely requires the user to define the region in which the seedlings are placed on the plate, and then subsequently operates in a semi-automatic fashion. We show that MyROOT can be used both in low scale and high throughput experiments due to the incorporation of a batch processing option for the automatic processing of several images without losing its accuracy.

2.2 MyROOT is a software for high-throughput analysis of root length

MyROOT method is based on pictures of whole agar plates on which young seedlings are growing vertically on the surface and implements novel algorithms capable of separately detecting the root and the hypocotyl of each individual seedling. MyROOT detects and measures root length by following a series of steps that can be easily performed in the software graphical interface (Figure 2.1 A). First, a digital image of the plate containing the growing seedlings is taken and used for the analysis. The image has to include a ruler (at least 1 cm long) placed on top of the plate (Figure 2.1 B). From the JPEG image, the software: (i) detects 1 cm of the ruler to automatically compute the scale and calculate the equivalence between pixels and millimeters (Figure 2.1 C); (ii) generates a binary mask from the manually selected area that allows for root segmentation (this separates those pixels that belong to a root from those of the background (Figure 2.1

Table 2.1: Comparison of available semi-automatic softwares for quantification of root traits.

Software	Plant material	Developmental stage	Root traits	Scale detection		Automatic detection of hypocotyls	Automatic detection of root tips	Degree of automation	Export formats	Batch processing option	Reference
MyROOT	Arabidopsis	Seedlings	Root length	Automatic	Yes	Yes	Semi automatic	txt, xlsx, rsml	Yes	This work	
RootDetection	Arabidopsis	Seedlings	Root length	Manually indicated	No	Yes	Automatic	csv, xlsx, SQLite	Yes	http://www.labutils.de/rd.html	
PlaRQM	Arabidopsis	Seedlings	Root length and curvature	Not mentioned	No	Yes	Semi automatic	xml	Yes	Yazdanbakh et al., 2012	
BRAT	Arabidopsis	Seedlings	Root length, curvature and width traits	Not mentioned	Yes	Yes	Semi automatic	txt	Yes	Slovak et al., 2014	
RootReader2D	Arabidopsis and crops	Seedlings and mature plants	Number and length of indicated roots	Manually indicated	No	No	Semi automatic ¶	csv	No	Clark et al., 2012	
RootTrace	Arabidopsis	Seedlings	Root length and curvature	Manually indicated	No	Yes	Semi automatic ¶	csv	Yes	French et al., 2009	
EZ-Rhizo	Arabidopsis	Seedlings	Root system architecture †	Manually indicated	Yes	Yes	Semi automatic ¶	txt	No	Armengaud et al., 2009	
PlantRoot	Crops	Seedlings and mature plants	Root system architecture ‡	Not mentioned	No	Yes	Semi automatic	txt, csv, sql	Yes	Wu et al., 2018	
RootGraph	Crops	Seedlings and mature plants	Root system architecture †	Not mentioned	No	No	Automatic	csv	No	Cai et al., 2015	
RootScape	Arabidopsis	Seedlings	Root system architecture	Not mentioned	No	No	Semi automatic	csv	No	Ristova et al., 2013	
DART	Arabidopsis and crops	Seedlings and mature plants	Root system architecture	Manually indicated	No	No	Manual	txt	No	Le Bot et al., 2010	
WinRhizo	Arabidopsis and crops	Seedlings and mature plants	Root system architecture §	Not mentioned	No	Yes	Automatic	txt	No	Arsenault et al., 1995	
GROWSCREEN-Root	Arabidopsis and crops	Mature plants	Root system architecture †	Not mentioned	No	No	Automatic	Not mentioned	Yes	Nagel et al., 2012	
RootNav	Arabidopsis and crops	Seedlings and mature plants	Root system architecture	Manually indicated	No	Yes	Semi automatic	sql, csv	No	Pound et al., 2013	
SmartRoot	Arabidopsis and crops	Seedlings and mature plants	Root system architecture	Manually indicated	No	No	Semi automatic	sql, csv	No	Lobet et al., 2011	
ARIA	Arabidopsis and crops	Seedlings	Root system architecture	Not mentioned	No	Yes	Automatic	xlsx	Yes	Pace et al., 2014	

† Primary root and lateral root traits
‡ Root geometry and spatio-temporal growth patterns
§ Color, diameter, length, topology, volume and surface
¶ Requires manual indication of each individual root to analyze

D)); (iii) measures the length of the roots through a root-tracking process (Figure 2.1 E); (iv) computes a regression curve based on the detection of the hypocotyls to identify the starting point of each root (Figure 2.1 F); (v) measures the root length again from the root tip to the end of the hypocotyl (Figure 2.1 G); and (vi) exports the measurements and the generated masks to a new folder. Finally, the results are saved in: (i) a Microsoft Excel spreadsheet or a .txt file in which each root is identified by an ID tag, length value and a descriptive text label introduced by the user; (ii) an image showing the detected and measured roots; (iii) MATLAB variables including the intermediate data such as hypocotyl position and the detection curve that was generated while quantifying root length and (iv) a RSML file so the images can be analyzed with other compatible softwares (Lobet et al., 2015).

One of the advantages of MyROOT is that it allows the user to supervise the different steps of the process as the results of each step are displayed before executing the following one. This feature enables the user to modify the different parameters (e.g., segmentation thresholds for ruler and root detection, and model for hypocotyl detection, etc.) at any point in the process to take into account different image conditions. Nonetheless, default parameter values have been set for satisfactory operation on a wide range of images for pre-defined acquisition conditions (see Material and Methods). Furthermore, the position of any hypocotyl that is not automatically detected can be manually indicated, and undesired roots can be manually removed from the results before saving. These manual features help the user to finely select the seedlings for the analysis, thus increasing the accuracy of the final results.

In addition, to reduce the time required for root measurement, MyROOT

incorporates a batch processing option for an automatic high-throughput analysis of several images. In this case, the different parameters are set for the first image from a specific folder and they are automatically applied to the rest of them.

In summary, by determining the pixel-millimeter equivalence and detecting seedling morphology (roots and hypocotyls) from an image of a seedling-containing agar plate, MyROOT offers a valuable analytical tool for precisely measuring root growth in a semi-automatic and non-invasive manner. As such, this software clearly provides a solution to the timely task of manually quantifying root length. As a proof of concept, MyROOT software was used for root length measurement of Arabidopsis wild type and BR-signaling mutants grown in control, exogenous BR hormones treatment and plants grown un under osmotic stress conditions (Fàbregas et al., 2018). MyROOT software is available at https://www.cragenomica.es/research-groups/brassinosteroid-signaling-in-plant-development/software.

2.3 MyROOT workflow and implementation

MyROOT has been developed for the high-throughput, accurate, and non-invasive measurement of root length from seedlings growing in agar plates. In this respect, the three most crucial steps are to precisely determine the scale, identify the roots, and measure their length. The scale information is obtained from a piece of measuring tape that is placed on the surface of the Petri dish. This allows the measurements to be completely independent from the specific characteristics of the image capture system. For this study, the images of the plates were taken with a standard camera situated

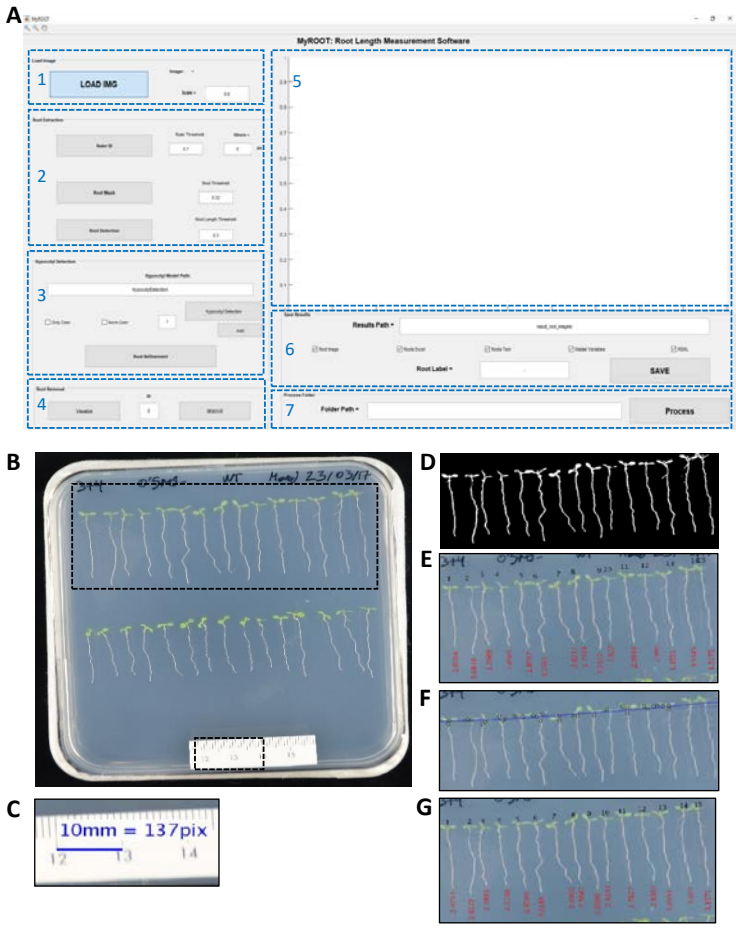

Figure 2.1: The graphical interface and steps of MyROOT.
A) The graphical user interface of MyROOT is organized into seven sections: 1. Input image information, 2. Root extraction parameters, 3. Hypocotyl detection parameters, 4. Manual removal of roots, 5. Visualization of the image and the different detection steps, 6. Saving parameters, and 7. Batch processing. B) The input image required for analysis is a picture of the square plate in which the aligned seedlings are growing. By using information from this image, MyROOT performs the following steps: C) Identification of the ruler to determine the scale (i.e., the equivalence between pixels and millimeters), D) Root segmentation to identify the seedlings, E) Root tracking to measure the roots, F) Hypocotyl detection to identify the hypocotyls and separate them from the roots, and G) Root measurement to quantify the length of individual seedlings (i.e., the distance from the root tip to the end of the hypocotyl).

Figure 2.2: Laboratory setup for taking the pictures of the plates.
The image shows the position of the lights, the camera and the plate to be analyzed, all positioned over a black surface.

over the plate (Figure 2.2). The first step for detecting the ruler is based on its color contrast with the background. By computing the vertical and horizontal profiles of the image, the algorithm is designed to explore the entire image in search of a white patch (Figure 2.3). As the border of the plate has a similar color contrast with the background, a median filter is applied to reduce the border effect. The maximum values in the filtered profiles define the image area where the white patch is present. Next, the resulting area is further cropped and processed. By applying a threshold based on Otsu's algorithm (Otsu, 1979), the black lines representing cm and mm marks are not filtered out. Finally, a horizontal profile of this binary image is generated in which the pixel-mm equivalence is defined as the difference between consecutive local maxima. In case that there is not ruler tape in the image to analyze, MyROOT includes the option of manually indicating the correspondence between pixels and millimeters.

The automatic detection of the scale was validated by compating the correspondence between pixels and millimeters measured by MyROOT and by Image J (measured by three different plants scientists). It was measured over twenty different plate images that have different image characteristics such as different scales, illumination conditions or placement, size and orientation of the measuring tape to test the robustness of the method. The correlation between the correspondence with both methods was positive ($R^2 = 0.998$, Pearson's r = 0.9990), therefore confirming that the algorithm implemented in MyROOT can accurately determine the scale from a plate image (Figure 2.3).

The core of the whole method is the root extraction and measurement process. In order to extract roots, the user must first manually define the area in which roots are present (only one row of seedlings should be included when defining the area). Then, with just a few mouse clicks from the user, a binary mask is generated that allows root segmentation. This later leads to the identification of individual roots through a root tracking process, and finally allows the individually identified roots to be measured (Figure 2.4). The root segmentation process can be divided into four main steps: i) color normalization, ii) ridge detection, iii) root tracking, and iv) root identification. During the color normalization step, the image is processed and a global working framework is set (i.e., all images going through this process become color-balanced and have the same lower and higher white values). This allows the user to manage different initial conditions (illumination, color, and saturation, etc.) while continuing with the same subsequent steps of the pipeline (Figure 2.4 A). In the next step, a ridge (i.e., white contrasted area) detector identifies roots based on their contrast with the background (for this, the level of

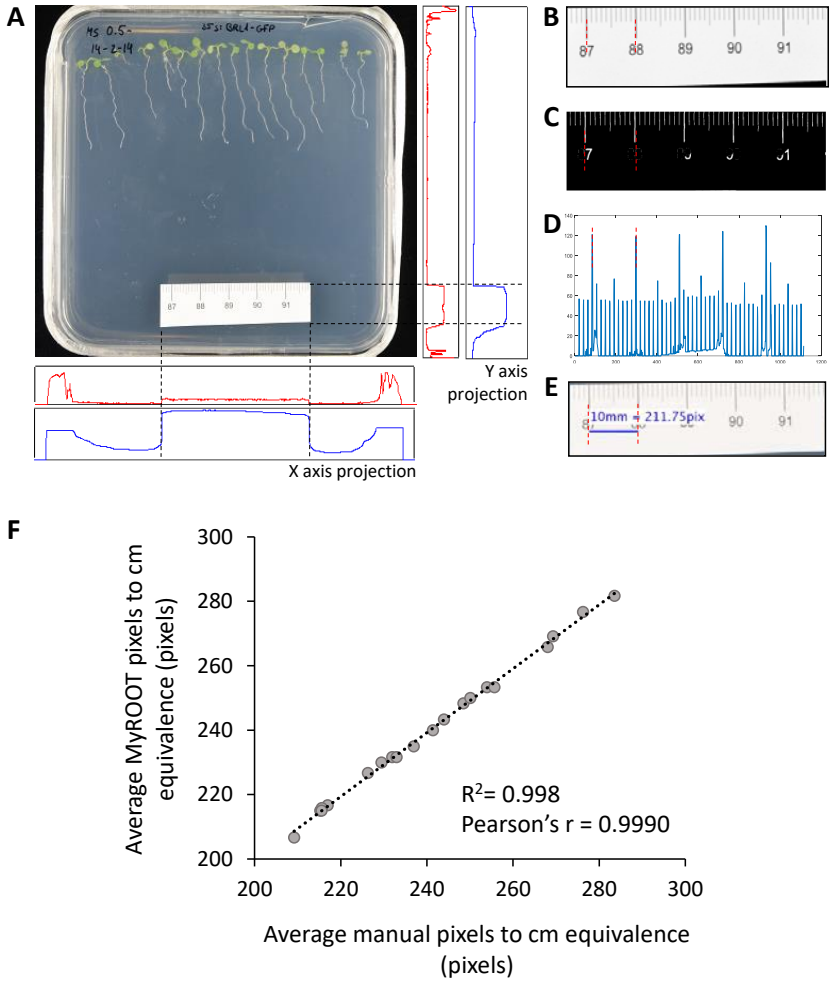

Figure 2.3: The ruler identification process.
A) MyROOT computes the vertical and horizontal profiles of the image to look for a white patch. B) The ruler is identified. C) The area corresponding to the ruler is then segmented into light and dark areas (binarization), for which black lines (dark areas) are identified with high values and white areas with lower values. D) A profile is generated in which black lines are identified as peaks. E) By using the distance between peaks, the equivalence between pixels and millimeters is calculated. F) Correlation of pixels-millimeter correspondence measurements using MyROOT (y-axis) and ImageJ (x-axis). The value in ImageJ is the average of three different measurements done by three different plant scientist. Each point corresponds to a different plate (n=20).

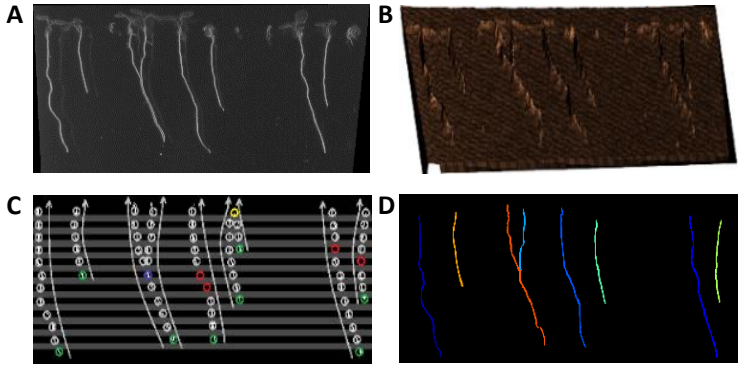

Figure 2.4: Root extraction method.
A) Colors are normalized in the area where roots are present, and white roots are detected. B) Segmentation is performed by applying a ridge detector. C) Starting at the root tip, the roots are tracked using a bottom-up approach. D) Each root is measured using its historical recorded tracking, and root length is calculated by taking into account the pixel-millimeter equivalence.

whiteness is irrelevant) (Figure 2.4 B). After the detection step, a final mask is generated for tracking the roots. Due to the linear disposition of the roots in the plate, we employed a bottom-up tracking approach. As such, tracking starts at the end point of each root and continues upward, row by row, until the hypocotyl detection curve is found (Figure 2.4 C). Finally, the tracking of each root makes it possible to identify which pixels correspond to which root (Figure 2.4 D).

Once the root tracking process has been completed, each individual root is measured based on previous positions saved in the historical record. Specifically, root length is calculated in pixels by adding the distances between previous consecutive points and then applying the previously calculated pixel-mm equivalence. Next, a refinement process is applied in which very short roots, which are often associated with noise, are discarded. By default, MyROOT discards any root measurement shorter than 30% of

the longest one. However, this percentage can be manually chosen by the user if need be. A second filter is then applied in order to keep those roots that terminate close to the previously calculated hypocotyl curve. If a root surpasses the hypocotyl curve, it is cut at this level. Finally, a unique numeric identifier (ID) is assigned to all roots that are not filtered out during processing.

As two roots can be located so close to one another that they cannot be detected as individual roots, MyROOT was trained with the following characteristics: (i) when a split occurs and a current root matches more than one detection (blue circle in Figure 2.4), a new root sharing the same historical record is created, and (ii) when a fusion occurs and two roots match a single detection (yellow circle in Figure 2.4), the shortest root is eliminated from the root set and added as a sub-root of the longest one; therefore indicating the root length of the primary root which is longer than the lateral roots.

2.4 Validation of root length measurements

To validate MyROOT software, we compared root length measurements obtained using MyROOT with manual measurements performed using ImageJ. We compared the root length values of different experiments. First, 6-days-old seedlings of wild type and BR-related mutants grown in control and in osmotic stress conditions (data published in Fàbregas et al. (2018), n > 600, Figure 2.5), and second, the same seedlings over 6 consecutive days (from three to eight DAG; n > 116). We obtained a positive correlation between the measurements with both methods (R^2 = 0.997, Pearson's r = 0.9985). These results indicated that measurements

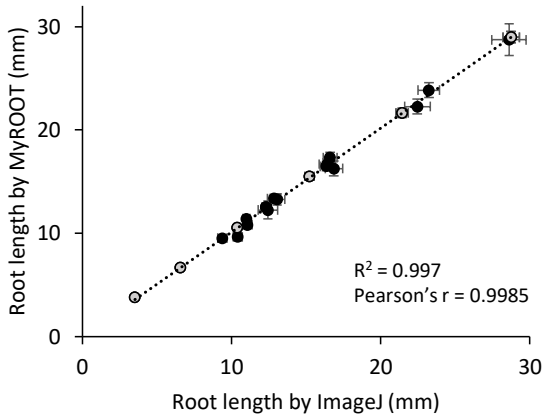

Figure 2.5: Validation of root length measurements.
Correlation of root length measurements using MyROOT (y-axis) and ImageJ (x-axis). Each point corresponds to a different experiment (n>20 in each one): time course data from 3 DAG to 8 DAG seedlings (grey) and BR-related mutants in control and osmotic stress conditions (black, Fàbregas et al. (2018)). Errors bars indicate the standard error. For the time course experiment, seedlings that were not measured by MyROOT in at least 4 time points were discarded.

made using our software coincided with manual measurements, thereby supporting the use of MyROOT for root length analysis in seedlings in different growth stages and experimental conditions.

We also evaluated the time required by MyROOT to determine root lengths, and compared it with the time needed for manual measurements using ImageJ, as it is widely used for the analysis of a low number of plates as a routine task in many plant biology laboratories. Importantly, we found that MyROOT reduces the time required to measure one plate by approximately half (Figure 2.6).

When using MyROOT for high-throughput experiments, the analysis of a batch of images can be done automatically after setting the optimal

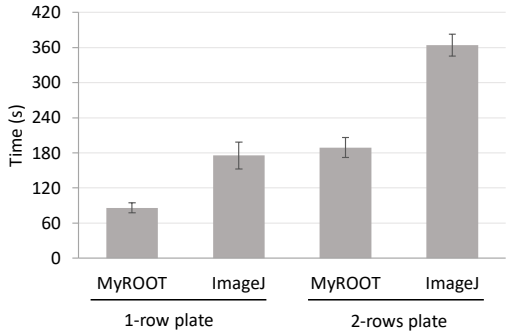

Figure 2.6: Evaluation of the time required to measure root length.
Time (in seconds) required for three different scientists to measure the root length of two different plates containing one and two rows of seedlings respectively. The measurements were done with MyROOT and ImageJ. Error bars indicate the standard error.

parameters for adapting to the imaging conditions of the experiment. The time required for the analysis of one row of seedlings of different plates was evaluated. MyROOT spends approximately 1 min per image when the hypocotyl detection is not performed and 1 min more if it is performed. Importantly, this process is completely automatic and does not require the user intervention. The accuracy of the batch processing was evaluated by comparing the results of the analysis of 10 different plates using MyROOT by single upload followed by individual setting of the optimal parameters and using MyROOT for a batch analysis of all of them automatically (Figure 2.7). The correlation obtained between both methods was positive ($R^2 = 0.996$, Pearson's r = 0.9981), therefore confirming that the batch processing option can be performed without losing accuracy in the final measurements.

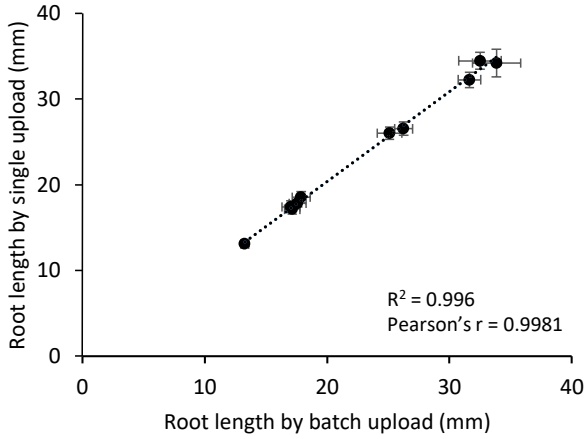

Figure 2.7: Validation of MyROOT batch analysis processing.
Correlation of root length measurements using MyROOT by single upload (y-axis) and MyROOT by batch upload of the images (x-axis). Each point corresponds to a different experiment (n>12 in each one). Error bars indicate the standard error.

2.5 Hypocotyl detection method

One of the main advantages of MyROOT is its ability to identify hypocotyls of growing seedlings. This characteristic is important for accurately determining the start point of each root. The hypocotyl detection process is based on visual features (appearance and color) extracted from the image. These features were used to generate a hypocotyl model by introducing 1259 hypocotyls of seedlings of different ages and characteristics and 7915 samples with background information (see Experimental procedures). The learned model is able to determine whether a given sample is a hypocotyl or not. To extract visual features, we implemented the histogram of oriented gradient (HOG, Dalal and Triggs (2005)) method. The HOG method is based on the orientation of the contours in the image, and generates a histogram that represents the appearance/shape of the sample. For extracting color features, color distribution histograms representing the amount of color in a given sample area are used (Figure 2.8 A). To train the model, we implemented a linear support vector machine classifier that uses appearance and color features from the hypocotyl images. This classifier generates the best hyperplane that classifies samples as positive (hypocotyls) and negative (no hypocotyls) examples. During the hypocotyl detection stage, the sliding window approach (Glumov et al., 1995) is used to perform an exhaustive search for hypocotyls. Finally, by keeping the highest scored windows as true positives, polynomial regression is used to define a curve that passes through all the detected hypocotyls. Although the user can manually insert the location of the hypocotyls, this curve enables the position of undetected hypocotyls to be estimated, and therefore corrects the curve tracing. The intersection between the hypocotyl detection curve and each root is used to define the

root start point.

We first evaluated our hypocotyl detection process in terms of different hypocotyl detection models. Both the precision-recall curve (Figure 2.8 B) and the number of false positives per image (FPPI; Figure 2.8 C) were calculated for three different models that differ in the type of feature they use for describing hypocotyls: only color information, only appearance information (via HOG features), or both types of information (HOG + color).

Upon analyzing the precision-recall curve of each model, we found the HOG + color model to be the most robust (Figure 2.8 B). In the case of FPPI, the lowest miss rate was also found when using the HOG + color model (Figure 2.8 C). These results indicated that when considering both color and appearance (i.e., the HOG + color model), a higher number of hypocotyls were identified than when using only one of the features. Therefore, this validates our MyROOT method because it incorporates both HOG and color information.

Next, we evaluated the influence of different regression curve models on the root measurement refinement used to set up the limits of individual roots (Figure 2.8 D). To create these curves, a regression upon the detected hypocotyls was performed. To define which regression model gives the better fit, we tested different polynomial models that were evaluated in terms of the average distance (in pixels) between the real hypocotyl position and the point of intersection between the root and the regression curve (Figure 2.8 D). The results indicated that when using a hypocotyl regression curve of order 4, a good balance between accuracy and flexibility that is able to account for small changes in hypocotyl position is reached.

Therefore, we chose to employ this regression curve in our software.

The use of the hypocotyl detection method permits the fine identification of the starting point of the root (Figure 2.9). However, depending on the user judgement, this option can be skipped, therefore reducing the time of the measurement process but losing accuracy in the final root length results (Figure 2.9). We compared the root length measurements of two plates, one containing seedlings with standard hypocotyls (Col-0 wild type plants) and other with shorter hypocotyls and roots (Col-0 wild type in osmotic stress conditions), using and skipping the hypocotyl detection step (Figure 2.9). In both plates, when using the method, only the primary root is measured (Figure 2.9 A and C), whereas when it is not used, some parts of the hypocotyl are measured too (Figure 2.9 B and D). When not using the hypocotyl detection method, we only found statistically significant differences in the root length of the shorter seedlings, as the proportion of hypocotyl length measured significantly increased the overall root length measurement (Figure 2.9 E, $n > 30$). These results highlighted the importance of the hypocotyl detection process for accurately measuring the root length, but also point to just using it when the experiment requires high precision.

2.6 Comparison with similar tools

The choice of software is usually based in a balance between the appropriateness of the characteristics of the software to the experimental design, the accuracy of the measurements obtained and the time required for the analysis (Table 2.1). We compared the accuracy and the time spent by MyROOT with BRAT and EZ-Rhizo, the two most similar software tools,

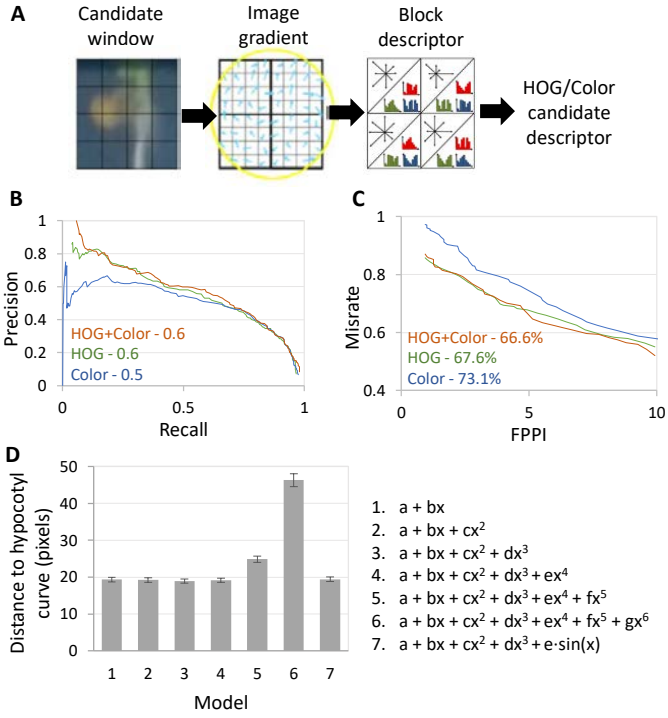

Figure 2.8: Hypocotyl detection method and validation.
A) Scheme of the hypocotyl detection method. A candidate window is defined as a square area inside the image. In order to describe a candidate, appearance/shape (HOG) and color information are extracted. Appearance information is extracted to calculate the gradient of the image (i.e., the direction of the contours within the image at each pixel). Histograms of Oriented Gradient (HOG) and the histograms of color are calculated over regular spaced, non-overlapping cells inside the candidate window (forming the block descriptor). Finally, all color/HOG cell histograms are concatenated to obtain the candidate window description. B) Precision-Recall curve for three different models of hypocotyl detection (HOG, Color and HOG+Color). The curve is obtained by changing the threshold that defines the frontier between positive and negative samples. For each threshold, the precision (well classified ratio) and the recall (poor classified ratio) were calculated. The area under the curve represents the robustness of the classifier, with a higher value indicating greater robustness (a higher well classified ratio to poor classified ratio over the entire range of the classifier). C) False Positives Per Image (FPPI) curve for three different models of hypocotyl detection (HOG, Color and HOG+Color). The curve plots the miss rate against the FPPI. In this way, the average miss rate over a specific FPPI range (1 to 10) represents the sensitivity of the classifier to not miss good samples and keep the false positive ratio low. D) The average distance in pixels between the real hypocotyl position and the point of intersection between the root and the polynomial regression curves, for polynomial regression curves of orders 1 to 6 and an extra model including a sine component. Error bars indicate the standard error.

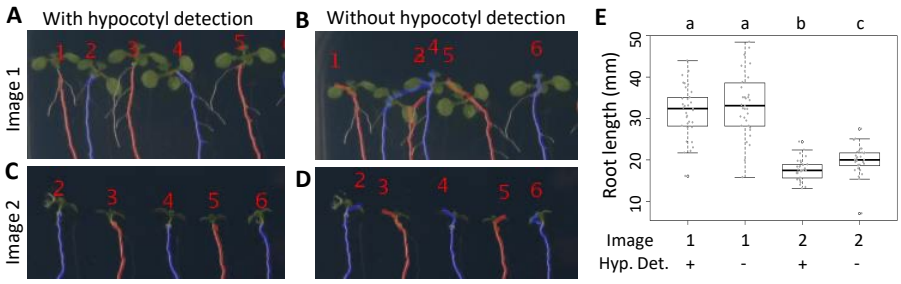

Figure 2.9: Evaluation of hypocotyl detection method for the root length measurements using MyROOT.
A-D) Qualitative analysis of the hypocotyl detection method in two different images. E) Root length measurement of seedling grown in two different plates (shown in (A-D)) using and not using the hypocotyl detection method. Different letters indicate statistically significant differences (*p<0.05; Student's t-test, n>30).

in the quantification of primary root length of two independent plates containing Arabidopsis seedlings (Figure 2.10 and Table 2.2).

We first compared the root length obtained with the three softwares with the ImageJ results. The absolute difference of mean root length between the measurements obtained with the softwares and with ImageJ show that MyROOT differs 1.39 mm and 0.22 mm for plates 1 and 2 respectively. With regard to this parameter, our results indicated the better performance of MyROOT in comparison with BRAT (15.08 mm and 1.77 mm) and to EZ-Rhizo (2.67 mm and 2.42 mm) (Table 2.2).

Root detection on the plate was similar between MyROOT (> 90%) and EZ-Rhizo (> 96%), yet MyROOT provided more accurate measurements (Figure 2.10 and Table 2.2). In addition, due to the incorporation of the hypocotyl detection method, MyROOT requires less user intervention to clearly indicate the roots, this is reflected in a reduction in the time spent

for the analysis. We spent around 3 min to analyze each plate when using MyROOT, 0.5 min with BRAT and 15 min with EZ-Rhizo (Table 2.2). Some seedlings on the plates analyzed had overlapping hypocotyls. We found that MyROOT was able to identify these and correctly indicate the shoot-root junction in cases with higher precision than EZ-Rhizo and BRAT, which presented a more basic algorithm for the hypocotyl detection based only on color and shoot border curvature information, respectively. These observations highlight the utility and importance of the hypocotyl detection method incorporated in MyROOT and its capacity to identify the individual seedlings and the precise starting point of each root.

Overall, MyROOT fills a specific gap in root phenotyping by allowing a precise, fast and semi-automatic quantification of primary root length of seedlings on a plate and a batch of plates.

Table 2.2: Comparison of MyROOT, BRAT and EZ-Rhizo softwares.
Results of the measurements done by the three softwares over the two plates shown in Figure 2.10 indicating the time required for each plate.

Plate	**Software**	**Number of detected roots**	**Percentage of detected roots**	**Mean root length (mm)***	**Root length difference (mm)****	**Time (min)**
1	MyROOT	54	90	16.81 ± 0.50	1.39	3
1	BRAT	1	1.7	3.44	15.08	0.5
1	EZ-Rhizo	57	95	18.09 ± 0.64	2.67	15
2	MyROOT	55	96.5	10.61 ± 0.43	0.22	3
2	BRAT	14	24.6	8.62 ± 1.18	1.77	0.5
2	EZ-Rhizo	57	100	12.82 ± 0.49	2.42	15

*The mean length is indicated with the standard error.

**Absolute difference of mean root length between the softwares and with measurement obtained with the softwares and with the manual measurements done with ImageJ.

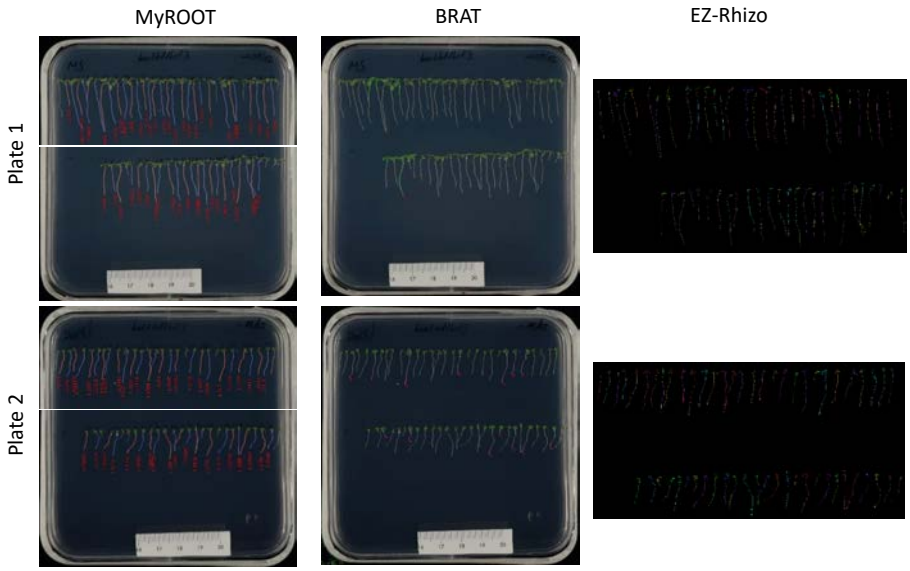

Figure 2.10: Comparison of MyROOT, BRAT and EZ-Rhizo softwares.
Results displayed by MyROOT, BRAT and EZ-Rhizo softwares for the analysis of two different agar plates containing Arabidopsis seedlings. Colored roots are the ones detected and measured. Plate 1 contains 60 seedlings and plate 2 contains 57 seedlings.

2.7 MyROOT 2.0 version includes an increase in automation

MyROOT is an ongoing project. The original version of the softwre that is described in the previous sections succesfully substitutes the most common tools used until now for the analysis of plant root length. Whereas, in our aim to completely automatize this task, we have developed a new version (named MyROOT 2.0) that incorporates important improvements that allow less user intervention throughout the process. The aspects that were improved in MyROOT 2.0 include the automation of the detection of the area containing the seedlings and the simplification of the scale information introduction. Importantly, the incorporation of these two features does not make the use of the tool more complex neither reduce the accuracy of the final measurements, as the core of the algorithms is not changed from the original version (Figure 2.11, González et al. (2020)).

In MyROOT software, the area containing the seedlings was indicated by manually pointing the region. In this way, we assured a precise selection of the roots to analyze, but requiring the user intervention. In the batch processing mode, it demanded that the seedlings were growing in the same position in the different plates, so the area indicated in the first image was the same in the following ones. To solve this limitation, in MyROOT 2.0, this process can be done completely automatically due to the incorporation of algorithms that detect the rows of seedlings present in the plate.

In MyROOT 2.0 the root segmentation process starts by detecting the seedling rows in the plate. The roots of each seedling row are considered to belong to a root region of interest (ROI). Thus, the detection of root

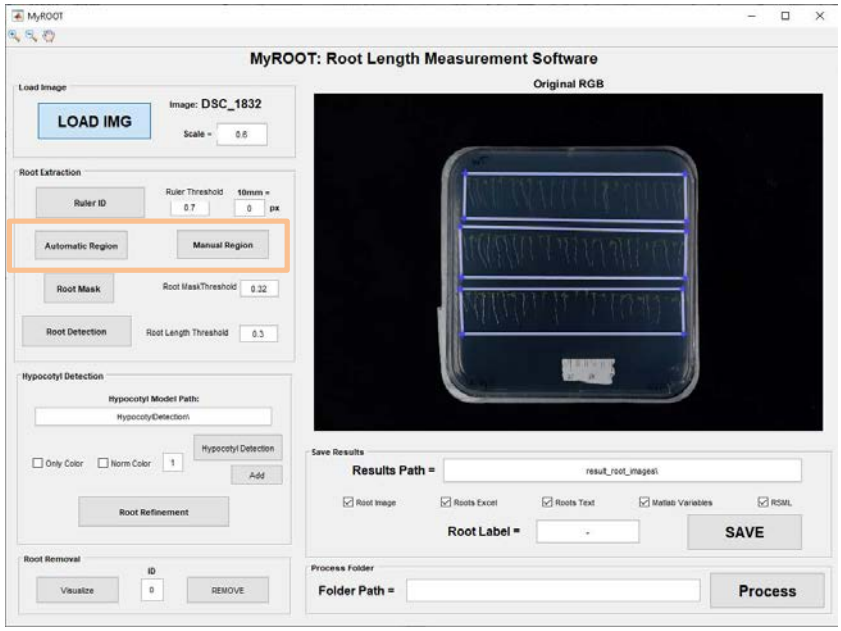

Figure 2.11: The graphical interface of MyROOT 2.0.
The graphical interface of MyROOT 2.0 has the same structure as MyROOT but incorporating the option of automatic or manual detection of the region containing the seeds (highlited in orange).

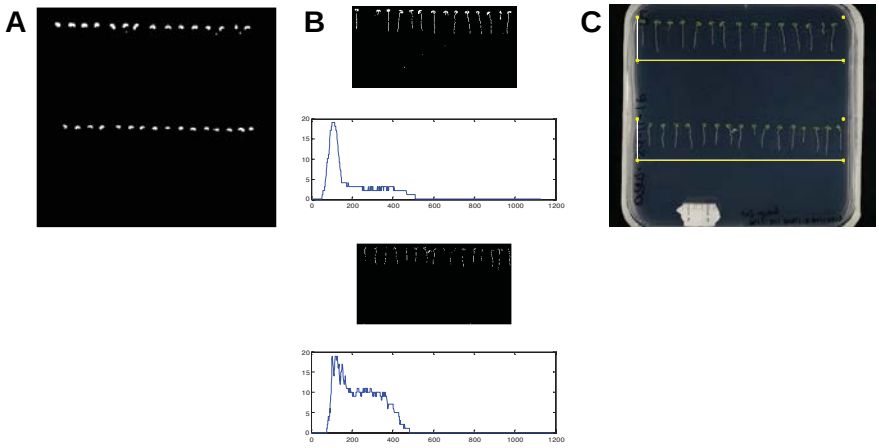

Figure 2.12: Root ROI detection
In MyROOT 2.0 the detection of the area containing the seedling is automatic. The steps for this process are: hypocotyl detection (A), longest root detection (B) and root ROI generation (C).

ROI consists of two main steps: the detection of seedling rows, and the determination of each root ROI bounding box (Figure 2.12). To detect seedling rows, the inner plate region is first automatically cropped by detecting plate borders. Then, the resulting image is segmented in the RGB space to detect the green leaves of the seedlings, considering as leaf pixels all those in which the green channel takes the highest value (Figure 2.12 A). This information is used to determine the number of seedling rows and to define the upper and lateral edges of the bounding box enclosing the seedlings. Lastly, those edges are used to obtain subimages corresponding to each root ROI. In those subimages, Otsu's method is applied to perform a preliminary detection of the roots; which allows to find the longest one (Figure 2.12 B) to define the bottom edge of the bounding box (Figure 2.12 C). As a result, MyROOT 2.0 presents the input image with the detected bounding boxes superimposed.

In this version 2.0, there is the possibility of processing several rows of seedlings at the same time, thus reducing the user intervention time during the process. Importantly, the vertices of the bounding boxes are draggable, so the user can modify the detected root ROI. Moreover, it is also possible to add a new root ROI in an entirely manual manner if necessary.

The second aspect improved in MyROOT 2.0 is the removal of the need to place a piece of measuring tape on the plate lid in all the images to analyze. Many image capture systems (e.g. fixed camera setups or flatbed scanners) used by plant scientist allow plant scientists to know the exact equivalence between pixels and centimeters. For this reason, we facilitated the introduction of this data manually through MyROOT 2.0 graphical user interface. In addition, when using the batch processing mode, the scale information has to be included (manually or automatically identified) only in the first image and it will be used for the rest of the analysis.

2.8 Future Perspectives

In this chapter we demonstrated that MyROOT software is accurate and fast for determining primary root length in Arabidopsis seedlings. However, we have detected some aspects that can be improved in coming versions to be used for a wider plant scientist community:

- Plant root phenotyping is usually performed by quantifying several root architecture parameters such us branching, curvature, biomass or shape (Grabov et al., 2005). The incorporation of methods for the measurement of these parameters would allow to do a more complete analysis of the root plant system.

- Several plant development studies include the phenotypic analysis of hypocotyls through the quantification of its length, area or color. We would like to incorporate these features in our software, as there is not any capable of automatically quantified both shoot and root parameters from young seedlings.

- Current versions of MyROOT are only compatible to Windows and Linux computers. We aim to make it compatible with other operative systems or even with smartphones.

- The automatic detection of hypocotyls was only developed for Arabidopsis. The development of algorithms for the identification of hypocotyls from other plant species would increase the applicability of our tool with other plant species such as tomato or sorghum.

- Currently, the main limitation in the use of plant phenotyping softwares is their capacity to adapt to different imaging and plant growing conditions, which complicates the proper identification of the root over the plates. To overcome this, MyROOT incorporates machine learning for the automatic detection of hypocotyls based on its training with pre-acquired images. Recent softwares allow the user to train it with their images so it is able to perfectly adapt to their conditions. This is already incorporated in software for the analysis of hypocotyls (Dobos et al., 2019) whereas in roots has not been incorporated yet.

Chapter 3

BRAVO and WOX5 control quiescence in the Arabidopsis root stem cell niche

Part of this chapter was published as:

Precise transcriptional control of cellular quiescence by BRAVO/WOX5 complex in Arabidopsis roots. Betegón-Putze, I.*, Mercadal, J.*, Bosch, N.*, Planas-Riverola, A., Marquès-Bueno, M., Vilarrasa-Blasi, J., Frigola, D., Burkart, R.C., Martínez, C., Stahl, Y., Prat, S., Ibañes, M. † and Caño-Delgado, A.I.† (2020) *BioRxiv*.

BRAVO and WOX5 control quiescence in the Arabidopsis root stem cell niche

3.1 Introduction

Roots are indispensable organs to preserve plant life and terrestrial ecosystems under normal and adverse environmental conditions. In Arabidopsis, the primary root derives from the activity of the stem cells located at the base of the meristem in the root apex (Dolan et al., 1993; van den Berg et al., 1995). The root stem cell niche (SCN) is composed of a set of proliferative stem cells that surround the mitotically less active cells, named the quiescent centre (QC; Scheres (2007)). Proximally to the QC, the vascular stem cells (VSC, also called vascular initial cells) give rise to functional procambial, xylem and phloem conductive vessels in the plant (De Rybel et al., 2016). Distally to the QC, the columella stem cells (CSC) give rise to the columella cells (Figure 1.2, González-García et al. (2011); Stahl et al. (2009)). The QC prevents differentiation of the surrounding stem cells (van den Berg et al., 1997), and its low proliferation rate provides a way to preserve the genome from replication errors. It also acts as a root

stem cells reservoir, having the ability of promoting its own division rate to replenish the stem cells when they are damaged (Fulcher and Sablowski, 2009; Lozano-Elena et al., 2018).

BRASSINOSTEROIDS AT VASCULAR AND ORGANIZING CENTER (BRAVO) and WUSCHEL RELATED HOMEOBOX 5 (WOX5) are two transcription factors (TF(s)) that are expressed in the QC and control its quiescence, as mutation of either BRAVO or WOX5 promotes QC cell division (Forzani et al., 2014; Pi et al., 2015; Vilarrasa-Blasi et al., 2014). BRAVO is an R2R3-MYB transcription factor and besides being expressed at the QC, it is also present at the vascular initials (Vilarrasa-Blasi et al., 2014). It was identified as a target of Brassinosteroid (BR) signaling, being directly repressed by BRI1-EMS-SUPPRESSOR 1 (BES1), one of the main effectors of the BR signaling pathway, altogether with its co-repressor TOPLESS (TPL) (Espinosa-Ruiz et al., 2017; Vilarrasa-Blasi et al., 2014). WOX5 is a member of the WUSCHEL homeodomain transcription factor family which is localized mainly at the QC and to a lesser extent at the surrounding CSC and vascular initials (Pi et al., 2015; Sarkar et al., 2007). WOX5 can repress QC divisions by repressing CYCLIN D3;3 (Forzani et al., 2014), and in contrast with BRAVO, is also involved in CSC differentiation, as in the *wox5* mutant CSC differentiate prematurely (Sarkar et al., 2007).

Although BRAVO and WOX5 are well-studied plant cell-specific repressors of QC division, their molecular connection and the biological relevance in SCN proper functioning has not yet been established. In this study, we set the regulatory and molecular interactions between BRAVO and WOX5 at the SCN and disclose a common role as regulators of primary and lateral root growth and development. Our results show that BRAVO and

WOX5 promote each other expressions and can directly bind to form a protein regulatory complex. BRAVO/WOX5 protein interaction underlies its functions as QC repressors to maintain stem cell development, which is essential for root growth and adaptation to the environment.

3.2 BRAVO and WOX5 control QC division

In order to understand the role of BRAVO and WOX5 in the QC, where both transcription factors are expressed, we evaluated the QC phenotypes of *bravo* and *wox5* mutants. It has been previously shown that *bravo* mutants have a phenotype of increased divisions at the QC compared to the wild-type (WT, Vilarrasa-Blasi et al. (2014), Figure 3.1 A, B), which resembles the one described for *wox5* mutants (Bennett et al. (2014); Forzani et al. (2014); Sarkar et al. (2007), Figure 3.1 C). To address BRAVO and WOX5 interplay at repressing QC divisions, we generated the double *bravo wox5* mutant and analysed the frequency of QC division. We found that *bravo wox5* mutants also exhibited increased cell division compared to the WT (89% of QC division in *bravo wox5* vs 39% in the WT; Figure 3.1 A, D) and that the frequency of divided QC was similar to that of *bravo* and *wox5* single mutants (87% in *bravo* and 81% in *wox5*; Figure 3.1 E). The mutual epistatic effect of these mutations suggests that BRAVO and WOX5 function interdependently at the WT primary root apex to supress QC divisions.

Previous studies proposed that WOX5 represses CSC differentiation in a non-cell autonomous manner (Bennett et al., 2014; Sarkar et al., 2007), whereas no link was reported between this process and BRAVO, since the *bravo* mutants are not defective in CSC differentiation (Figure 3.1 A, B, F).

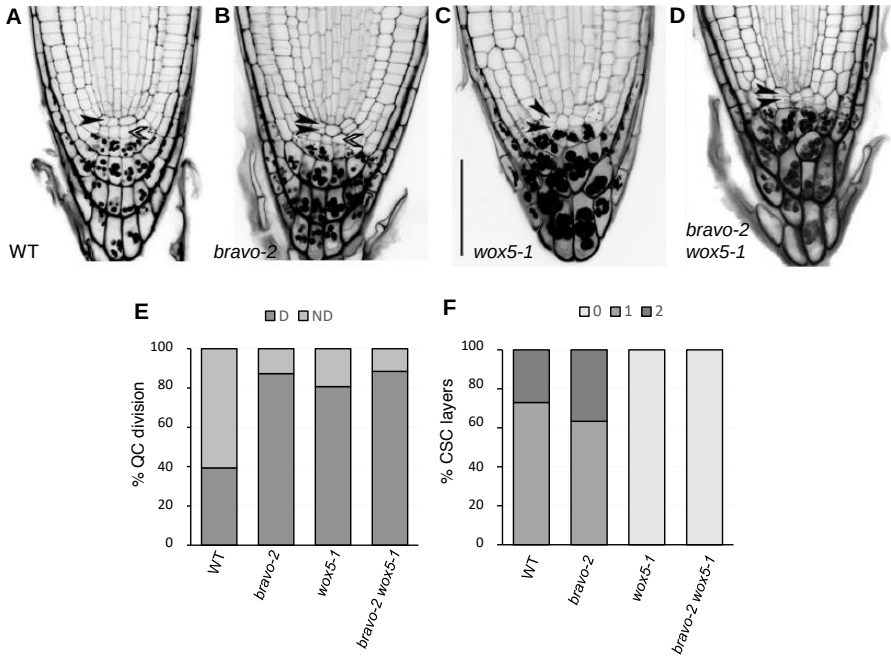

Figure 3.1: BRAVO and WOX5 are required for QC identity and stem cells maintenance.
A-D) Confocal images of mPS-PI stained 6-day-old seedlings of WT (A), *bravo-2* (B), *wox5-1* (C) and *bravo-2 wox5-1* (D) mutants. Left black arrows indicate QC cells and right white arrows indicate CSC. Scale bar: 50 μm. E) Quantification of the QC divisions in 6–day-old roots expressed in percentage (n>50, 3 replicates). D: QC divided; ND: QC non divided. F) Quantification of CSC layers in 6-day-old roots expressed in percentage (n>50, 3 replicates).

Genetic analysis showed that *bravo wox5* mutants display the same CSC differentiation as *wox5* single mutant (Figure 3.1 C, D, F), corroborating that BRAVO does not control CSC differentiation (Vilarrasa-Blasi et al., 2014).

3.3 BRAVO and WOX5 control overall root growth

To address whether these stem cell-specific defects account for overall alterations in root growth and development, we analyzed root architecture in *bravo* and *wox5* mutants (Figure 3.2). We first analyzed root length in 6-day-old seedings. The *bravo wox5* double mutant shows slightly but significantly shorter roots than the WT (Figure 3.2). This difference was also observed and more exaggerated after a Brasinolide (BL) treatment that negatively affects root growth (González-García et al., 2011). These results suggest that BRAVO and WOX5 interplay have a role in root growth.

As stem cells are also found in lateral roots (LRs), we evaluated the lateral root (LR) density in the different mutants at 7 and 10 days after germination (Figure 3.3). 7-day-old *bravo*, *wox5* and *bravo wox5* seedlings have fewer lateral root density than the WT. They show the same phenotype between them (Figure 3.3), in agreement with previous reports for *wox5* (Tian et al., 2014). We found that lateral root density defects become more exaggerated in the *bravo wox5* double mutant in 10-day-old seedlings (Figure 3.3) where the LR density is lower than the WT and the single mutants. These findings support the joint contributions of these two transcription factors to overall root growth and architecture.

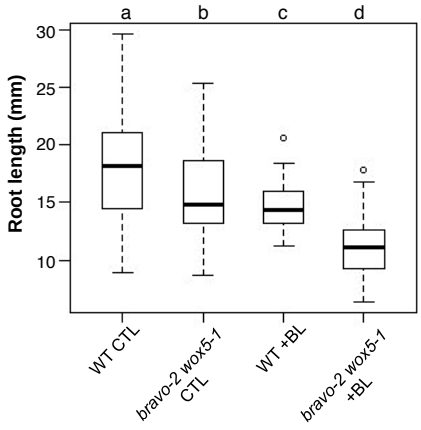

Figure 3.2: BRAVO and WOX5 promote primary root growth.
Root length of 6-day-old WT and *bravo-2 wox5-1* mutants in control and after BL

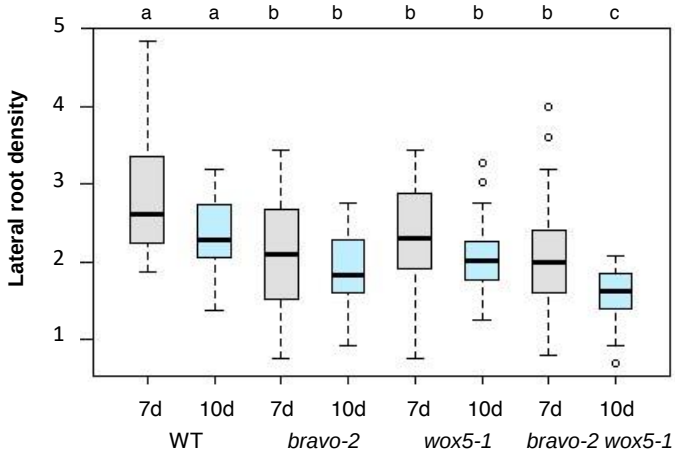

Figure 3.3: BRAVO and WOX5 promote lateral root development.
Lateral root density (number of lateral roots per mm of root length) of 7-day-old (7d) and 10-day-old (10d) WT, *bravo-2*, *wox5-1* and *bravo-2 wox5-1* mutants (n>40, 2 replicates 7d and 3 replicates 10d). Different letters indicate statistically significant differences vs WT in the same conditions. (p-value < 0.05 Student's t-test).

3.4 BRAVO and WOX5 reinforce each other at the root stem cell niche

The QC division phenotype of the double *bravo wox5* mutant suggests an interplay between BRAVO and WOX5 at regulating QC divisions. Such interplay may take place through cross-regulation of their expressions. Indeed, it was previously shown that *WOX5* expression is reduced in the *bravo* mutant (Vilarrasa-Blasi et al., 2014), indicating that BRAVO regulates *WOX5* expression. To gain insight on the mutual regulatory activity of these two transcription factors, we thoroughly investigated *BRAVO* and *WOX5* expressions at the SCN in the single mutant and in the double *bravo wox5* mutant backgrounds. For that aim we generated *pBRAVO:GFP* and *pWOX5:GFP* lines in WT, *bravo*, *wox5* and *bravo wox5* backgrounds and evaluated the promoters expression in the confocal microscope. We quantified the GFP intensity in the SCN area with a manually selected ROI for *pBRAVO:GFP* and *pWOX5:GFP* lines separately (Figure 3.4). We also analysed their expression in inducible lines 35S:BRAVO-Ei and 35S:WOX5-GR through confocal microscopy and RT-qPCR.

In the WT primary root, *BRAVO* expression, reported by the *pBRAVO:GFP* line, is specifically located in the QC and the vascular initials (Figure 3.5 A, Vilarrasa-Blasi et al. (2014)). The *pBRAVO* signal was increased in the *bravo* mutant (Figure 3.5 B, D), suggesting that BRAVO negatively regulates its own expression. In contrast, in the *wox5* mutant, *pBRAVO* expression was strongly reduced, suggesting that WOX5 promotes *BRAVO* expression (Figure 3.5 C, D).

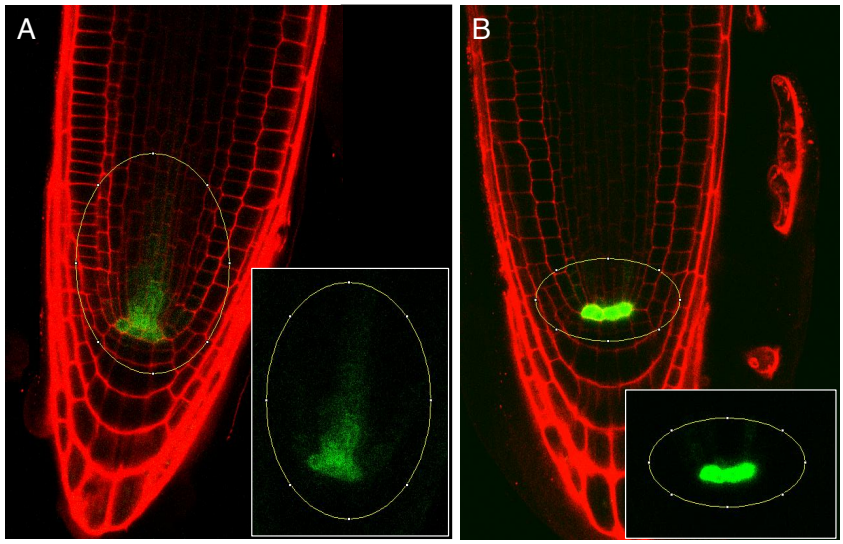

Figure 3.4: ROIs used for GFP quantification.
Confocal images of *pBRAVO:GFP* (A) and *pWOX5:GFP* (B) PI-stained 6-day-old roots. GFP-tagged expression is shown in green. Insets show the GFP channels that were used for the quantification. Only the area inside the yellow circle was used for GFP quantification.

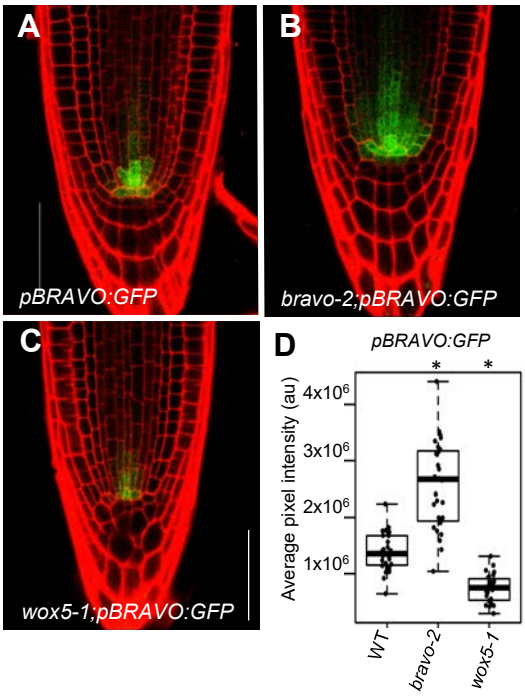

Figure 3.5: *BRAVO* expression in the root stem cell niche.
A-C) Confocal images of PI-stained 6-day-old roots. GFP-tagged expression is shown in green. A-C) *pBRAVO:GFP* in WT (A), *bravo-2* (B) and *wox5-1* (C) knockout backgrounds. Scale bar: 50 μm. D) Quantification of the GFP fluorescent signal of the roots in A-C. Boxplot indicating the average pixel intensity of the GFP in the stem cell niche. (n>25, 3 biological replicates, *p-value < 0.05 Student's t-test for each genotype versus the WT in the same condition).

Figure 6: BRAVO expression in the root stem cell niche.
A-C) Confocal images of PI-stained 6-day-old roots. GFP-tagged expression is shown in green. A-C) *pBRAVO:GFP* in WT (A), *bravo-2* (B) and *wox5-1* (C) knockout backgrounds. Scale bar: 50 µm.
D) Quantification of the GFP fluorescent signal of the roots in A-C. Boxplot indicating the average pixel intensity of the GFP in the stem cell niche. (n>25, 3 biological replicates, *p-value < 0.05 Student´s *t*-test for each genotype versus the WT in the same condition).

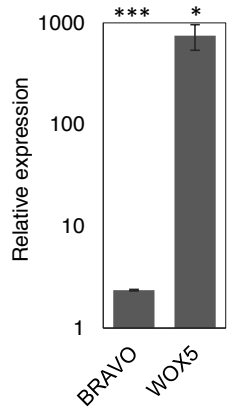

Figure 3.6: *BRAVO* expression is increased in the WOX5 inducible line.
Bars show the relative expression of *BRAVO* and *WOX5* in 35S:WOX5-GR lines when induced with 1 μM Dexamethasone for 24 hours. Values in control conditions are not represented as are 1. Asterisks indicate significant differences versus values in control conditions (* p-value < 0.05, *** p-value < 0.001 Student's t-test, 2 biological replicates).

The expression of *BRAVO* was also evaluated by RT-qPCR of root tips in the inducible line 35S:WOX5-GR (Figure 3.6). *BRAVO* expression was increased in this overexpressor plants, supporting that WOX5 activates *BRAVO* expression. The fact that the increase is not as strong as the fold-induction of *WOX5*, suggests that WOX5 induces *BRAVO* only within the BRAVO native domain.

Moreover, *pBRAVO* expression was equally reduced in the double *bravo wox5* mutant (Figure 3.7), as in the *wox5* mutant (Figure 3.5), suggesting that BRAVO regulates its own expression aside the induction by WOX5.

In the primary root, *WOX5* expression reported by the *pWOX5:GFP* line, is known to be mainly restricted to the QC, yet some expression is detected in the vascular initials (Figure 3.8 A, Pi et al. (2015)). We found

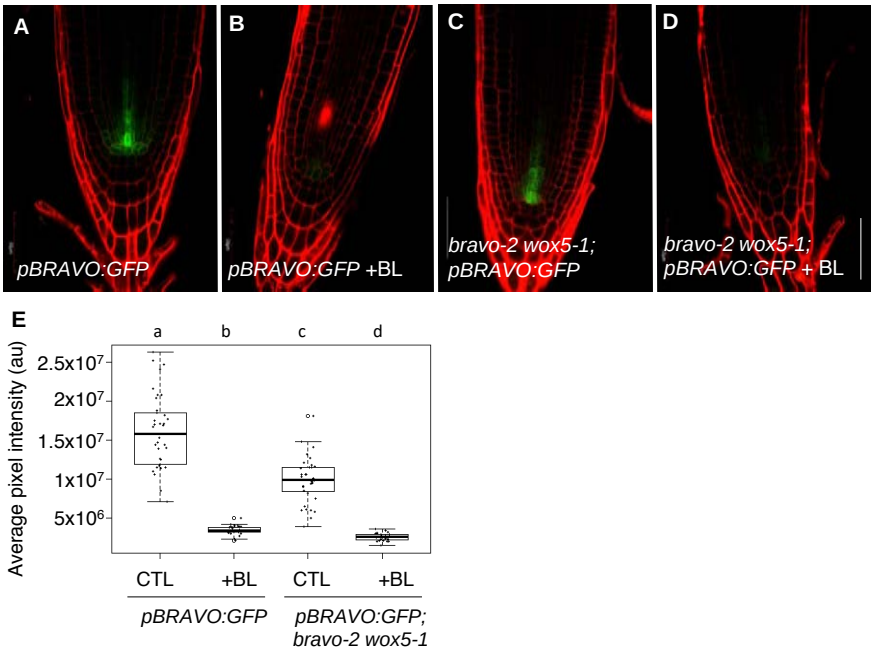

Figure 3.7: *BRAVO* expression in the *bravo wox5* mutant background.
A-D) Confocal images of PI-stained 6-day-old roots. GFP-tagged expression is shown in green. *pBRAVO:GFP* in WT and *bravo-2 wox5-1* background in control (A, C) and after BL treatment (B, D). Scale bar: 50 μm. E) Quantification of the GFP fluorescent signal of the roots in A-D in the stem cell niche. Different letters indicate statistically significant differences (p-value < 0.05 Student's t-test, n>25, 3 biological replicates).

that *bravo* mutant displayed a significant reduction of *WOX5* expression (Figure 3.8) B), supporting that BRAVO in turn induces expression of the *WOX5* gene.

Further analysis of *WOX5* expression upon overexpressing BRAVO under an inducible 35S promoter (35S:BRAVO-Ei) showed that when BRAVO levels were induced, *pWOX5* levels remained similar to the WT, indicating that BRAVO is not able in its own to induce *WOX5* (Figure 3.9). Together, these results support that BRAVO is necessary to maintain proper *WOX5* levels in the QC but does not induce them.

Subsequently, an increased *pWOX5:GFP* expression towards the provascular cells was observed in the *bravo wox5* double mutant (Figure 3.8 D, E), similar to *wox5* mutant (Figure 3.8 C, E). These findings suggest that WOX5 restricts its own expression to the QC, while BRAVO-dependent activation of *WOX5* acts upstream such *WOX5* autoregulation.

Brassinolide (BL) is the most active BR hormone compound. BL treatment is known to modify *BRAVO* and *WOX5* expression, by reducing the first and increasing the second of these genes (Figures 3.7, 3.10, 3.11; González-García et al. (2011); Vilarrasa-Blasi et al. (2014)). When seedlings were grown in BL, *pBRAVO* expression was extremely low. However, we still observed a small increase in the GFP expression in *bravo* background, similar trend to that observed in untreated conditions (Figure 3.10 A, B, D, E, G). In the case BL-treated *pBRAVO:GFP* plants in *wox5* and *bravo wox5* mutants, GFP expression is hardly detected (Figures 3.7 D and 3.10 F). Quantification in the SCN reveals we reduction in the GFP expression, being only significant in the case of the double mutant background (Figures 3.7 and 3.10).

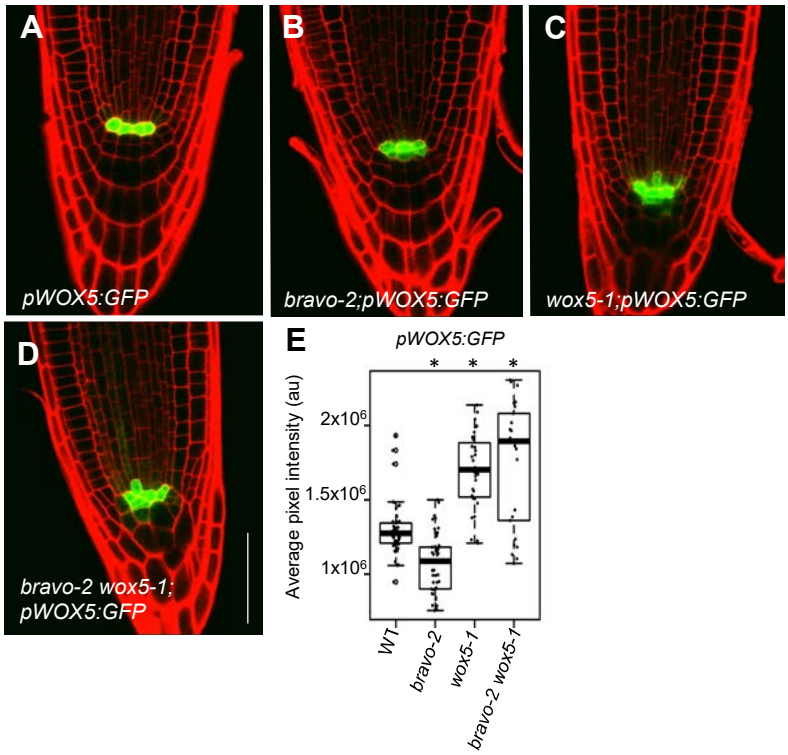

Figure 3.8: *WOX5* expression in the root stem cell niche.
A-D) Confocal images of PI-stained 6-day-old roots. GFP-tagged expression is shown in *WOX5:GFP* in the WT (A), *bravo-2* (B), *wox5-1* (C) and *bravo-2 wox5-1* (D) knockout backgrounds. Scale bar: 50 μm. E) Quantification of the GFP fluorescent signal of the roots in A-D. Boxplot indicating the average pixel intensity of the GFP in the stem cell niche (n>25, 3 biological replicates, *p-value < 0.05 Student's *t*-test for each genotype versus the WT in the same condition).

Figure 3.8: *WOX5* expression in the root stem cell niche.
A-D) *pWOX5:GFP* in the WT (A), *bravo-2* (B), *wox5-1* (C) and *bravo-2 wox5-1* (D) knockout backgrounds. Scale bar: 50 µm.
E) Quantification of the GFP fluorescent signal of the roots in A-D. Boxplot indicating the average pixel intensity of the GFP in the stem cell niche. (n>25, 3 biological replicates, *p-value < 0.05 Student´s *t*-test for each genotype versus the WT in the same condition).

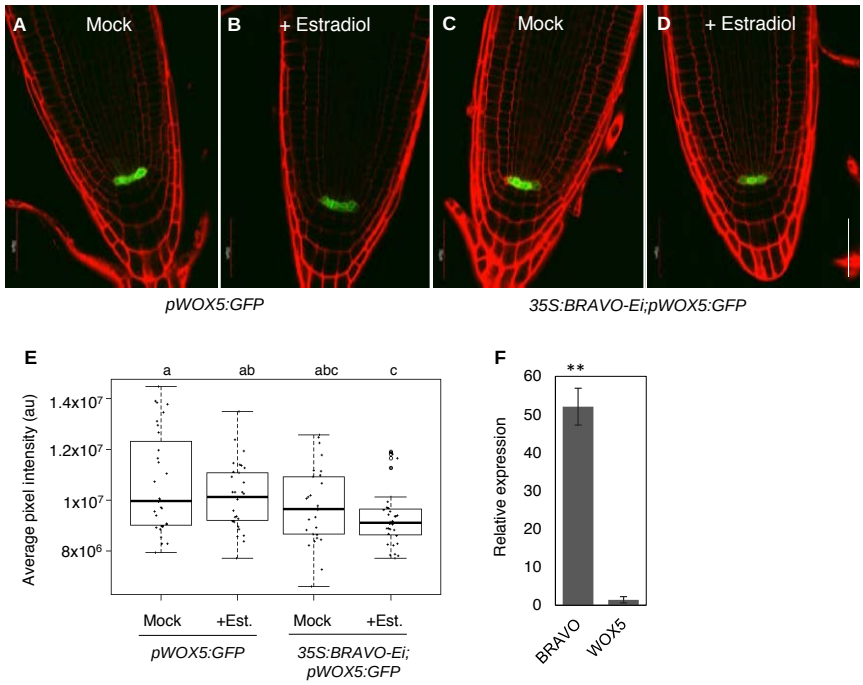

Figure 3.9: *WOX5* expression is not altered in BRAVO inducible line.

A-D) Confocal images of PI-stained 6-day-old roots. GFP-tagged expression is shown in green. *pWOX5:GFP* in WT and 35S:BRAVO-Ei background in control (A, C) and after 6 days 30 μM β-estradiol induction (B, D). Scale bar: 50 μm. E) Quantification of the GFP fluorescent signal of the roots in A-D. Boxplot indicating the average pixel intensity of the GFP in the stem cell niche. Different letters indicate statistical significant differences (p-value < 0.05 Student's t-test, n>29, 3 biological replicates). F) Bars show the relative expression of *BRAVO* and *WOX5* in 35S:BRAVO-Ei lines when induced with 30 μM β-estradiol for 24 hours. Values in control conditions are not represented as are 1. Asterisks indicate significant differences versus values in control conditions (** p-value<0.01 Student's t-test, 3 biological replicates).

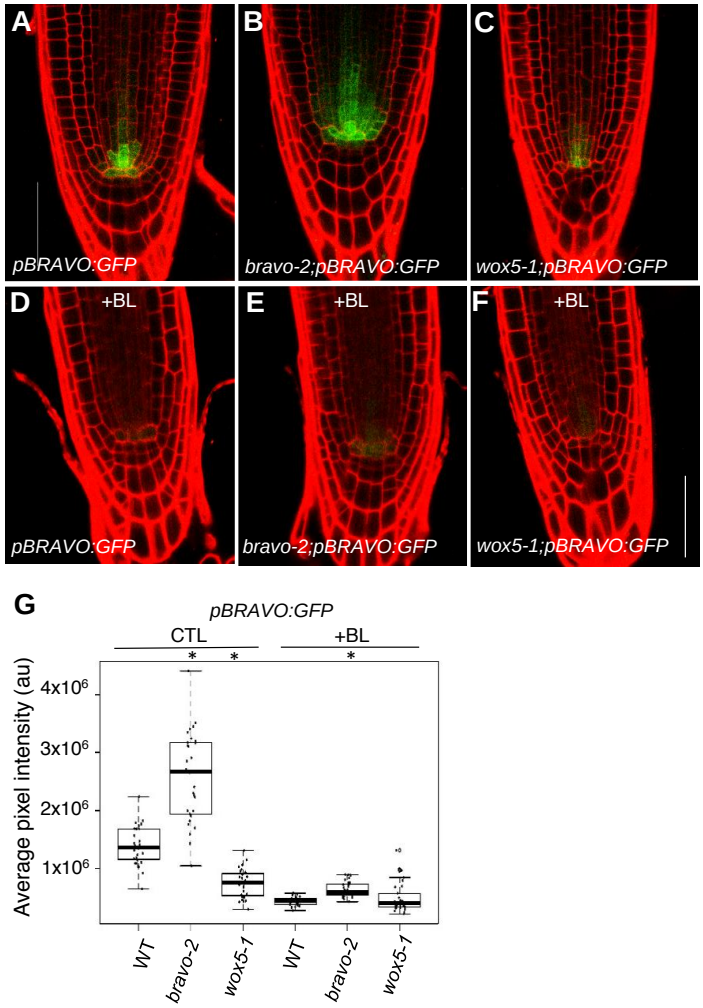

Figure 3.10: *BRAVO* expression is BL regulated.
A-F) Confocal images of PI-stained 6-day-old roots. GFP-tagged expression is shown in green. *pBRAVO:GFP* in WT, *bravo-2* and *wox5-1* knockout backgrounds in CTL (A-C) and after 48h 4nM BL treatment (D-F). Images in control conditions are the same that are shown in Figure 3.5. Scale bar: 50 μm. G) Quantification of the GFP fluorescent signal of the roots in A-F. Boxplot indicating the average pixel intensity of the GFP in the stem cell niche (n>25, 3 biological replicates, *p-value < 0.05 Student's t-test for each genotype versus the WT in the same conditions). Quantification of lines in control conditions are the same that are shown in Figure 3.5.

In the case of *pWOX5* expression after BL treatment, we observed an increase in its expression and a shift towards the stele cells (Figure 3.11). Quantification of the GFP intensity indicates an increase in *wox5* and *bravo wox5* mutant (Figure 3.11 C, D, G, H, I), and similar levels in *bravo* mutant background compared to the WT (Figure 3.11 B, F, I).

Altogether, we found that when roots were grown on BL, the changes in *BRAVO* and WOX5 expressions in *bravo*, *wox5* and *bravo wox5* double mutant respect to the WT exhibited very similar trends as when plants were grown in control media without BL (Figures 3.7, 3.10, 3.11). These results suggest that the mutual regulation of *BRAVO* and *WOX5*, as well as their autoregulation, is not significantly altered by BL treatment.

3.5 *WOX5* induces *BRAVO*, which alleviates *WOX5* self-inhibition

To provide a comprehensive scheme of *BRAVO* and *WOX5* cross-regulation in the SCN able to account for the changes in expression levels observed in the various mutant backgrounds, we turned into mathematical modeling. Because *BRAVO* is induced in the WOX5 overexpression line (Figure 3.6) and *BRAVO* expression decreases in the *wox5* mutant (Figure 3.5), the model considered that WOX5 induces (either directly and/or through intermediate molecules) the expression of *BRAVO* (Figure 3.12 A). To account for the increase in *pBRAVO* expression in the *bravo* background (Figure 3.5), the model assumed that BRAVO drives an effective inhibition on its own expression (Figure 3.12 A), probably in an indirect manner. The model indicates that these two regulations can drive a decrease

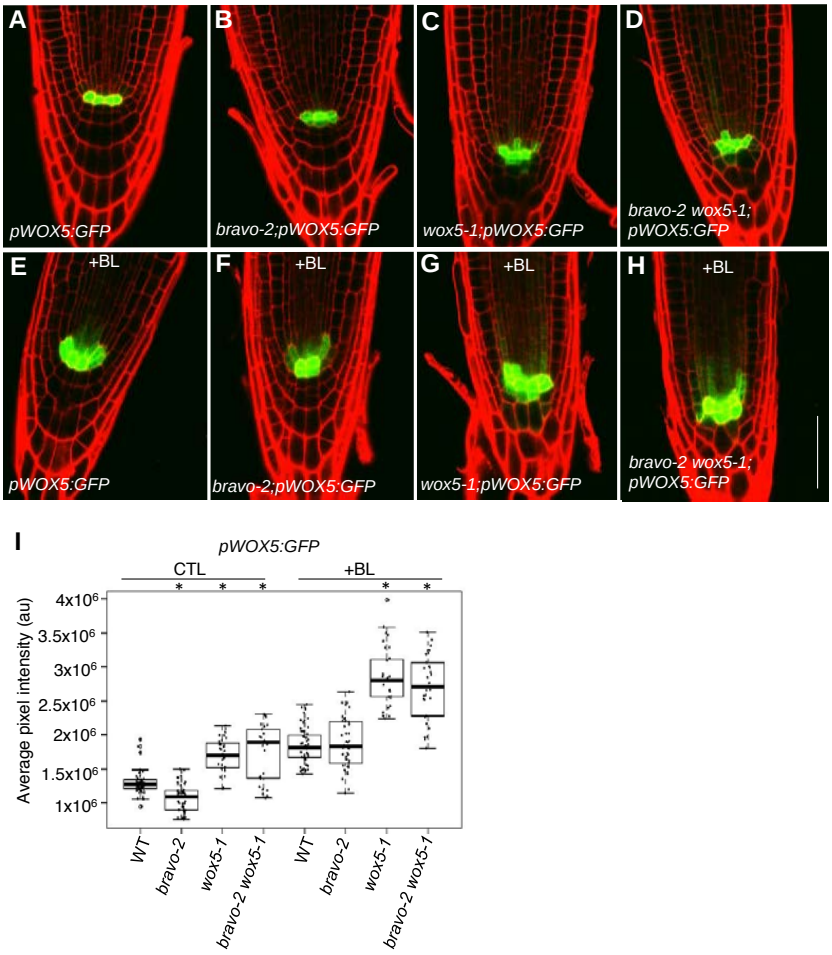

Figure 3.11: *WOX5* expression is BL regulated.
A-H) Confocal images of PI-stained 6-day-old roots. GFP-tagged expression is shown in green. *pWOX5:GFP* in WT, *bravo-2*, *wox5-1* and *bravo-2 wox5-1* knockout backgrounds in CTL (A-D) and after 48h 4 nM BL treatment (E-H). Images in control conditions are the same that are shown in Figure 3.8. Scale bar: 50 μm. I) Quantification of the GFP fluorescent signal of the roots in A-H. Boxplot indicating the average pixel intensity of the GFP in the stem cell niche (n>25, 3 biological replicates, *p-value $<$ 0.05 Student's t-test for each genotype versus the WT in the same conditions). Quantification of lines in control conditions are the same that are shown in Figure 3.8.

in *BRAVO* expression in the *bravo wox5* double mutant (Figure 3.12 B), as found by the GFP expression data (Figure 3.7). Therefore, the model indicates that these two regulations on *BRAVO* are sufficient to account for its levels of expression in the single and double mutants (Figure 3.12 B).

Because *pWOX5* expression in the SCN increases in the *wox5* mutant (Figure 3.8), the model considered that WOX5 represses (directly or indirectly) its own promoter activity (Figure 3.12 A). In addition, the model assumed that BRAVO inhibits partially this repression (Figure 3.12 A). With these regulations, the model accounts for the increase of *WOX5* expression in the *bravo* mutant, as well as for the *WOX5* decreased expression in the *wox5* and *bravo wox5* mutants (Figure 3.12 B), as we found in the GFP expression studies (Figure 3.8). Therefore, the model proposes that BRAVO promotes *WOX5* expression by alleviating *WOX5* self-inhibition.

With these interactions, the model precisely captures all changes in *BRAVO* and *WOX5* expression in the *bravo*, *wox5* and *bravo wox5* mutants (Figure 3.12 B, C). In the model, parameter values were adjusted such that the fold-changes between promoter activities in the single mutants compared to the WT matched the fold-changes in GFP expressions of our empirical data (Figure 3.12 C). In addition, these values were restricted so that under control conditions *pBRAVO* expression is lower than *pWOX5* expression in the WT (Figure 3.12 B), as suggested by GFP expression and RNAseq of the root tip (Clark et al., 2019).

The model indicates that the trends in the changes of expression levels between each mutant and the WT are maintained when the rate of BRAVO

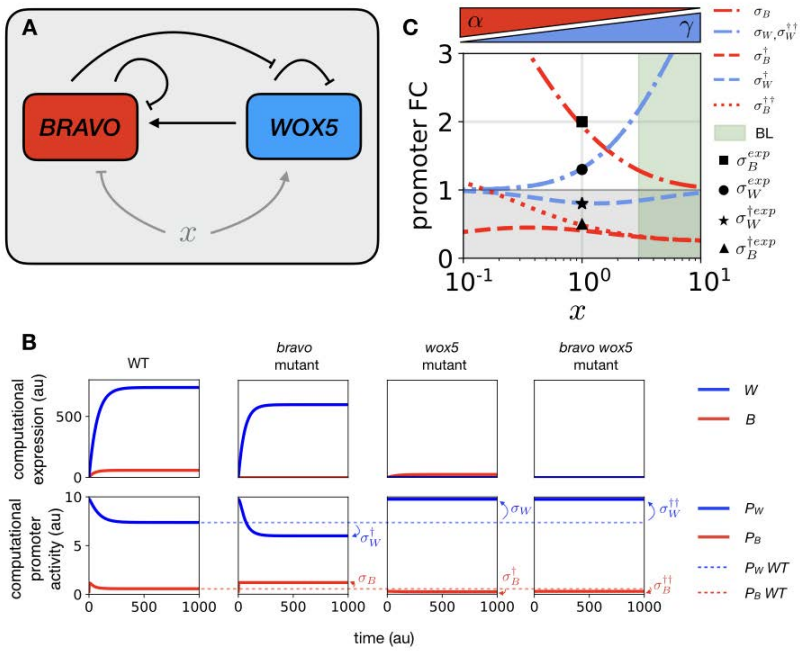

Figure 3.12: *WOX5* activates *BRAVO* which in turn alleviates *WOX5* self-inhibition in the stem cell niche.
A) Schematic representation of the effective regulations in the SCN between *BRAVO* and *WOX5*: BRAVO feeds back on its own activity by reducing it and is activated by WOX5. WOX5 also feeds back on its own activity by reducing it, a regulation that becomes partially impaired by BRAVO. Additional factors x can be regulating both *BRAVO* and *WOX5* or either one. We exemplify one such a factor that regulates both, by downregulating *BRAVO* and upregulating *WOX5*. x can be understood as BR signaling. Arrows denote activation and bar-ended lines denote inhibition. B) Model solutions for the temporal evolution of expression and promoter activities for the WT and mutants using as initial condition all activities set to zero ($B(t=0)=0, W(t=0)=0$) and parameter values as in Table 6.5). This time-evolution does not intend to mimic any data but is only shown to depict the changes in the stationary levels between WT and each mutant. Manifest in the panels are the fold-changes in stationary promoter activities in the mutant compared to the WT (σ). C) Fold-changes in promoter activity (σ) in the mutant compared to the WT predicted by the mathematical model as a function of the control parameter x. This control parameter increases *WOX5* and reduces *BRAVO* promoter activities (blue and red triangles; according to α=0.3/x, γ=250x/(x+9)). x=1 corresponds to the CTL condition, while x > 1 can mimic BL condition (green shaded area). The experimentally observed values in CTL conditions (computed as ratios of the median GFP) are drawn as black markers (see legend). The experimental fold-changes corresponding to the double mutants are not shown, as are assumed to be equal to the single mutants within the confidence interval of the experiments ($\sigma_B^{\dagger\dagger exp} = \sigma_B^{\dagger exp} and \sigma_W^{\dagger\dagger exp} = \sigma_W^{\dagger exp}$). Error bars of these data (which can span ranges $\pm\,\sigma$) are not depicted for clarity. The experimentally measured fold-change values for the *bravo wox5* double mutants are similar to those measured in the *wox5* mutant. In the plot, the region of fold change FC < 1 (i.e. the promoter activity is reduced in the mutant) is shaded in gray to visually distinguish it from the region where FC > 1 (i.e. the promoter activity is increased in the mutant).

promoter activity decreases and/or the rate of WOX5 promoter activity is increased (Figure 3.12 C). This is in agreement with the results obtained upon BL treatment (Figures 3.7, 3.5 and 3.8), which reduces *BRAVO* expression whereas it increases *WOX5* expression.

3.6 BRAVO and WOX5 directly interact into a transcriptional complex

Our results so far support that BRAVO and WOX5 reinforce each other at the SCN. To further decipher BRAVO and WOX5 interplay, we next evaluated the possible physical interaction between the BRAVO and WOX5 proteins. Using Förster resonance energy transfer measured by fluorescence lifetime microscopy (FRET-FLIM, Figure 3.13 A-K) and yeast two-hybrid assays (Figure 3.13 L) we observed that BRAVO can directly interact with WOX5 (Figure 3.13 B, G, K, L), which indicates that BRAVO and WOX5 form a transcriptional complex.

It was previously demonstrated that the BR-regulated BES1/TPL complex acts as a transcriptional repressor of BRAVO transcription (Espinosa-Ruiz et al., 2017; Vilarrasa-Blasi et al., 2014), that BES1 directly interacts with BRAVO (Vilarrasa-Blasi et al., 2014), and that TPL interacts with WOX5 (Pi et al., 2015). We further investigated the binding of BRAVO and WOX5 to these transcriptional regulators. We found that both BRAVO and WOX5 physically interact with BES1, and this interaction was stronger for the active BES1-D protein (Figure 3.13 C, D, H, I, K; (Yin et al., 2002)), consistent with previous findings which showed that the BES1 EAR domain is necessary for BES1/BRAVO interaction (Vilarrasa-

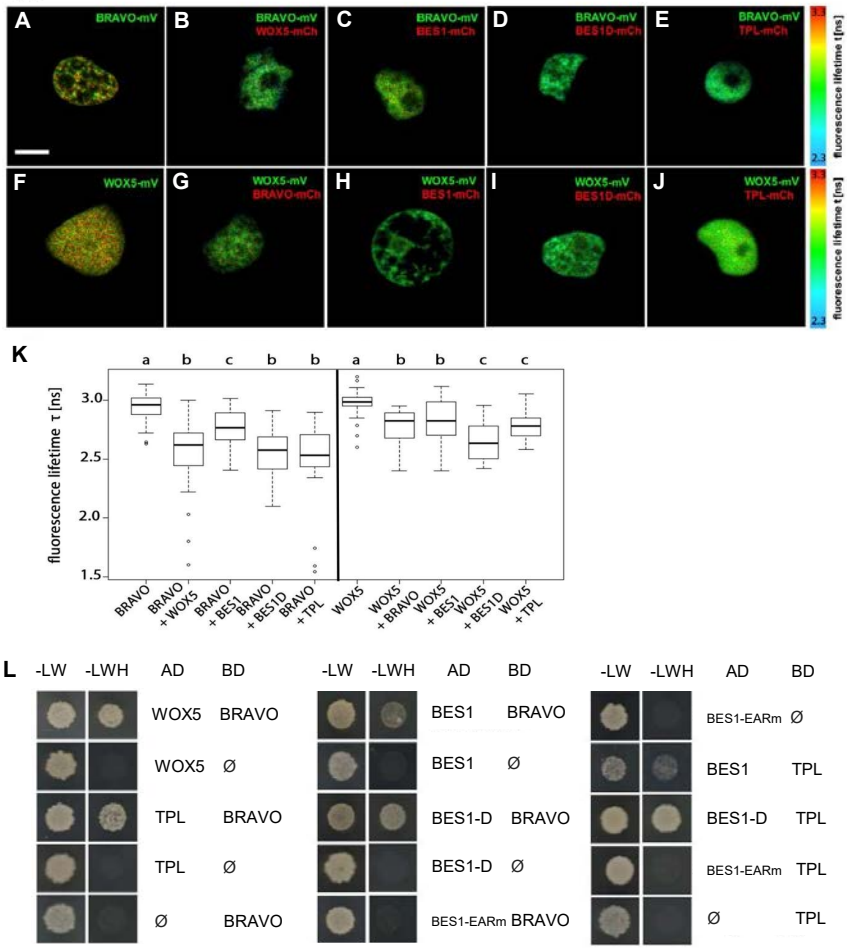

Figure 3.13: BRAVO interacts with WOX5.
A-J) Interaction of BRAVO with WOX5 (B), BES1 (C), BES1D (D) and TPL (E); and interaction of WOX5 with BRAVO (G), BES1 (H), BES1D (I) and TPL (J) measured by FRET-FLIM. GFP fluorescence lifetime τ [ns] was measured in transiently expressing Nicotiana benthamiana leaf epidermal cells. GFP fluorescence lifetime fitted pixel-wise with a mono-exponential model of BRAVO and WOX5 interactions. mV, mVenus; mCh, mCherry. Scale bar: 5 μm. K) Fluorescence-weighted average lifetimes of BRAVO and WOX5 interactions fitted with a double-exponential model of the indicated samples are summarized in box plots. Statistical significance was tested by one-way ANOVA with a Sidakholm post-hoc test. Different letters indicate statistically significant differences (p-value < 0.01; n>20). L) Yeast two-hybrid assay showing BRAVO interacting with WOX5, BES1 and TPL in vitro. In the left column yeast cells were grown on control media, and in the right column yeast cells were grown on control media lacking Leu, Trp and His, indicating interaction between the proteins.

Blasi et al., 2014). Our analysis shows that BES1 binds to WOX5 (Figure 3.13 H, I, K, L) with an equivalent affinity as to BRAVO (Figure 3.13 K, L), and that this interaction is stronger with BES1-D (Figure 3.13 K). Moreover, both BRAVO and WOX5 were also observed to interact with the co-repressor TPL (Figure 3.13 E, J, K, L). Collectively, these data show that BRAVO and WOX5 directly interact to form a transcriptional complex, and that each can bind active BES1 and TPL, suggesting these proteins are able to compete for their mutual binding.

3.7 BRAVO-WOX5 complex is relevant for the control of QC divisions

The equal divided QCs in the double *bravo wox5* mutant compared to the single mutants (Figure 3.1) suggests that BRAVO and WOX5 interplay at repressing QC divisions. We found two ways for this interplay to take place: through mutual regulation of their expressions (Figure 3.5, 3.6, 3.7, 3.8, 3.9, 3.12) and through the formation of a protein BRAVO-WOX5 complex (Figure 3.13). We turned into mathematical modeling to assess the contribution of each of these regulations to the phenotype of divided QCs. We set a regulatory function for the frequency of divided QCs that explicitly incorporates the individual contributions mediated by BRAVO (T_B) and by WOX5 (T_W) and the jointly mediated contribution by both BRAVO and WOX5 together (hereafter named "joint contribution", T_{BW}). In this regulatory function, the joint contribution (T_{BW}) is the one that takes into consideration the existence of the BRAVO-WOX5 complex. In contrast, the mutual regulations of *BRAVO* and *WOX5* expressions act independently from the joint contribution and are only in-

cluded in the individual contributions (i.e. T_B and T_W). Specifically, since *WOX5* expression decreases in the *bravo* mutant (Figure 3.8), we reasoned that individual WOX5 repression of QC divisions is attenuated by a factor $q_W^{Bm} < 1$ in the *bravo* mutant compared to the WT). Similarly, to take into account the regulation that WOX5 makes on *BRAVO* expression, we considered that the individual contribution by BRAVO was attenuated by a factor q_B^{Wm} in the *wox5* mutant compared to that in the WT ($q_B^{Wm} < 1$). Because the extent of these attenuations and hence the values of q_W^{Bm} and q_B^{Wm} (which range from 0 to 1) cannot be measured, we estimated them through the fold-changes in expression in the mutants as follows. We used $q_W^{Bm} = 0.8$, which is similar to the fold-change of *WOX5* expression in the *bravo* mutant compared to the WT (Figure 3.8, 3.12). The fact that *wox5* exhibits phenotypes that are absent in the *bravo* mutant, such as CSC differentiation, also suggests that q_W^{Bm} is not too small. The estimate for q_B^{Wm} based on the fold-change of BRAVO expression in the *wox5* mutant is $q_B^{Wm} = 0.5$ (Figure 3.5, 3.12). Yet, from the root phenotypes of the mutants we cannot exclude other, e.g. smaller, values. Therefore we evaluated the model results for different values of q_B^{Wm}.

We used the experimental data on the frequency of divided QCs in the WT, the single mutants and the double mutant (Figure 3.1), with an estimation of their confidence intervals, to extract which are the individual contributions (i.e. the BRAVO-mediated and the WOX5-mediated) as well as the joint BRAVO-WOX5 contributions in the WT. For intermediate q_B^{Wm} values ($q_B^{Wm} > 0.4$ upwards, being $q_B^{Wm} = 0.5$ the estimate from fold-change BRAVO expression in the *wox5* mutant), the model results show that in the WT the joint contribution of BRAVO-WOX5 is the only one relevant (Figure 3.14 A). Therefore, the analysis indicates that the

joint BRAVO-WOX5 contribution is essential to describe the QC division data if BRAVO and WOX5 control each other action on QC division only partially. Individual BRAVO contribution becomes relevant only for small q_B^{Wm} values, i.e. only if BRAVO's role on QC division is mostly controlled by WOX5. Yet in this scenario, which would correspond to BRAVO acting downstream of WOX5 to repress QC divisions, the model indicates that the joint contribution of BRAVO and WOX5 is also relevant to the regulation of QC divisions in the WT, regardless of its specific activatory/inhibitory role (Figure 3.14 A). Taken together, our analyses highlight the significant contribution of the BRAVO/WOX5 heterodimeric complex in the control of QC divisions in the stem cell niche (Figure 3.14 B), to the preservation of the normal growth and development of primary and lateral root organs in the plant.

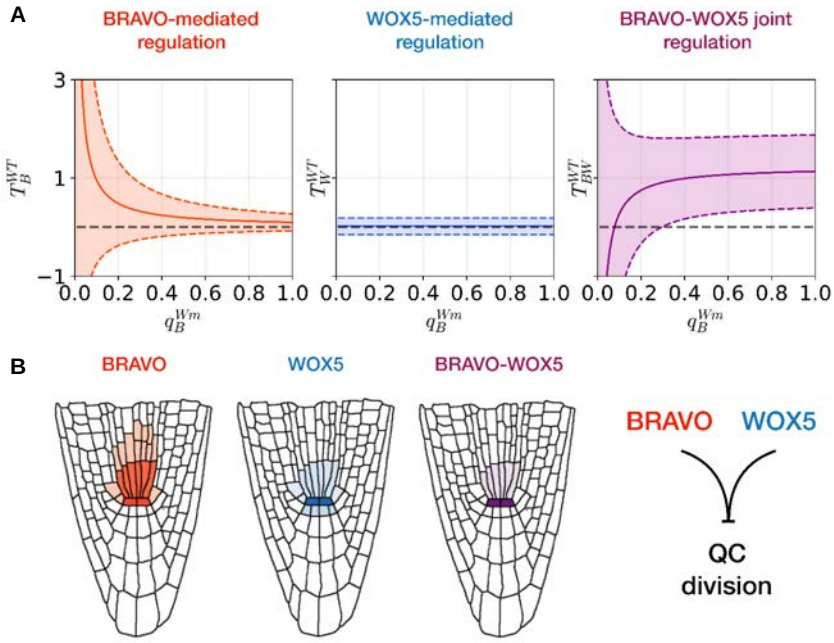

Figure 3.14: BRAVO and WOX5 have a joint role in repressing QC divisions.
A) Computational estimation of the contributions of BRAVO-mediated (T_B^{WT}), WOX5-mediated (T_W^{WT}) and BRAVO-WOX5 joint (T_{BW}^{WT}) regulations of QC divisions in the WT, as a function of the attenuating factor of BRAVO contribution in the *wox5* mutant, q_B^{Wm}. Continuous lines represent the best estimated values, while dashed lines are the enveloping confidence intervals (e.g. $T_B^{WT} \pm \delta T_B^{WT}$). The horizontal grey dashed lines mark the zero lines. For a wide range of q_B^{Wm} values, the joint contribution of BRAVO and WOX5 is important, while the individual contribution of BRAVO only increases for small values of q_B^{Wm}. In all three panels, we set $q_B^{Bm} = 0.8$. Positive contributions correspond to repression of QC divisions, while negative contributions correspond to activation of QC divisions. B) Sketch representing the spatial distribution of BRAVO, WOX5 and their product BRAVO x WOX5, which can be interpreted as the protein complex. Their joint interaction peaks at the QC, where repression of cell division occurs.

Chapter 4

A cell-type specific transcriptomics approach uncovers the role of BRAVO in root development

A cell-type specific transcriptomics approach uncovers the role of BRAVO in root development

4.1 Introduction

The vascular tissues are key for plant growth and development as they provide mechanical support and the capacity to transport water, nutrients, and other molecules throughout the plant. Plant vascular development has been mostly studied in Arabidopsis and it is tightly regulated by hormones (Caño-Delgado et al., 2010; De Rybel et al., 2016). In the Arabidopsis roots, the vascular tissues are specified during early stages of the embryogenesis. Auxin transport and signaling are essential for vascular patterning and differentiation, as provascular inital cells receive more auxin than the surrounding ones (Friml et al., 2003; Reinhardt et al., 2003; Schlereth et al., 2010; De Rybel et al., 2014). During embryo development auxin-regulated genes such as MONOPTEROS (MP) or TARGET OF MONOPTEROS (TMO5) play an essential role in the division of provascular initial cells (De Rybel et al., 2013; Hardtke and Berleth, 1998). Cy-

tokinins control the provascular cell division and xylem development in the primary root. The cytokinin receptor WOODEN LEG (WOL) promotes periclinal cell divisions and cytokinin signaling inhibits protoxylem formation through the ARABIDOPSIS HISTIDINE PHOSPHOTRANSFER PROTEIN 6 (AHP6) cytokinin signaling inhibitor. Hence, an inhibitory feedback between auxin and cytokinins specifies the vascular patterning in roots (Scheres et al., 1995; Mähönen et al., 2000, 2006a,b; Bishopp et al., 2011). The patterning of the xylem axis is also controlled by the SHORTROOT (SHR)–miR165/166–class III HOMEODOMAIN LEUZIPPER (HD-ZIPIII) pathway (De Rybel et al., 2014; Helariutta et al., 2000; Mähönen et al., 2006a; Carlsbecker et al., 2010; Ohashi-Ito and Bergmann, 2007; Ohashi-Ito et al., 2014; Muraro et al., 2014). Other cytokinin regulated factors involved in positioning vascular boundaries are AT-HOOK MOTIF NUCLEAR LOCALIZED 3 and 4 (AHL3 and AHL4). They are expressed in the procambium and move towards the xylem to regulate the boundary between both tissues (Zhou et al., 2013). Downstream vascular cell differentiation events are regulated through a complex molecular process that ends in the formation of secondary cell walls. VASCULAR-RELATED NAC-DOMAIN 6 (VND6) and VND7 control metaxylem and protoxylem differentiation respectively (Kubo et al., 2005) through regulating genes involved in programmed cell death (PCD) and cell wall thickening (Ohashi-Ito et al., 2010; Yamaguchi et al., 2011). Other hormones such as Strigolactones has been recently described in controlling PIN auxin transporter proteins, which resulted in impaired vascular development (Zhang et al., 2020a).

Brassinosteroid hormones control several aspects of vascular development. Initially identified to promote the differentiation of tracheary elements in

Zinnia cell cultures (Fukuda, 1997; Yamamoto et al., 1997), later studies in Arabidopsis mutants of the BRI1-like family demonstrate their role in xylem differentiation and vascular development (Caño-Delgado et al., 2004; Ibañes et al., 2009). Other aspects in which BRs control vascular development is through cell wall differentiation. It has been shown that increased BRs promotes the transcription of xylem differentiation components, such as the VND7 (Yamaguchi et al., 2010). In addition, mutants in the BR synthesis genes DWARF4 and DIM1 show defects in their secondary cell wall (Choe et al., 1998; Hossain et al., 2012; Takahashi et al., 1995). Primary cell wall deposition is also controlled by BRs also through CELLULOSE SYNTHASE A (CESA) genes that are direct targets of BES1 (Xie et al., 2011). Recently, the specific overexpression of BRL3 in the vasculature was described to affect sugars and osmoprotectants transport in those tissues, which generates drought resistance (Fàbregas et al., 2018). In the root provascular tissue, little is known about the function of BRs in controlling their meristematic activity. BRs regulate periclinal cell division, as BL treated plants show thinner stele than untreated ones (González-García et al., 2011; Fàbregas et al., 2013), whereas any specific role has been further characterized. Overall, different roles of BR in the vascular development and differentiation has been widely reported; however, any comprehensive study regarding BRs in xylem and phloem specification, differentiation and function has been yet performed.

The vasculature of the Arabidopsis primary root provides an amenable model for studying plant gene regulatory networks with cell specific resolution due to its stereotyped pattern of division and differentiation as well as the great number of molecular genetic resources available (Birnbaum et al., 2003; Brady et al., 2007; Lee et al., 2006; Levesque et al., 2006;

Nawy et al., 2005). The use of cell-type specific transcriptomics has become essential to decipher the spatiotemporal control of plant hormones in developmental process (Bargmann et al., 2013; Vragović et al., 2015; Vilarrasa-Blasi et al., 2014). Previous studies have led to the identification of mutants with vascular defect caused by BRs (Yamaguchi et al., 2010; Kang et al., 2017), yet little is known about the transcriptional control of BR responses in the vascular tissues.

In the root apical meristem, BRs play important roles in stem cell maintenance by controlling QC cell division through repressing the transcription of BRAVO. BRAVO is a member of the R2R3-MYB transcription factor family (Vilarrasa-Blasi et al., 2014). MYB proteins are characterized for containing the MYB highly conserved DNA-binding domain. It is formed by up to four amino acid sequence repeats of around 52 amino acids. Depending on the number of adjacent repeats, MYB transcription factors are divided in different classes. Among them is the R2R3-MYB family containing more than 100 transcription factors that have a structure with a N terminal MYB DNA-binding domain and an activation or repression domain usually located at the C terminus (Ogata et al., 1996; Stracke et al., 2001). This family of transcription factors has been related to important aspects of plant development such as primary and secondary metabolism, response to stresses or cell identity (Dubos et al., 2010). BRAVO has two closest homologues that are MYB52 and MYB54 which are involved in secondary cell wall biosynthesis (Zhong et al., 2008).

BRAVO is expressed in the QC and in the surrounding initial cells. In the provascular cells, its expression is considerably higher and specially in the vascular initial cells that are just proximally located to the QC (Figure 4.1 A). Multidisciplinary approaches revealed that BRAVO, together with

WOX5, controls QC division and overall root growth and development (Vilarrasa-Blasi et al., 2014; Betegón-Putze et al., 2020). However, any role in the vascular tissues has been reported yet (Vilarrasa-Blasi et al., 2014).

In this study, we aimed to characterize BRAVO transcriptional roles in the QC and vascular initial cells using cell-type specific transcriptomics. Fluorescent activated cell sorting (FACS) was used to isolate QC and VI cells from plants expressing pWOX5:GFP and pARF7:GFP respectively. The transcriptome of those cells was sequenced, and comparison between wild-type, *bravo-2* and BL-treated conditions revealed distinct roles of BRs and BRAVO in both cell populations.

4.2 A cell-type specific approach to decipher the transcriptome of BRAVO in the QC and VI cells

Previous work in our laboratory led to the identification of BRAVO transcription factor specifically localized in the QC and the VI cells of the Arabidopsis root apex (Figure 4.1 A). Based on mutant phenotypic analysis, a role of BRAVO as repressor of the QC division was reported (Vilarrasa-Blasi et al., 2014; Betegón-Putze et al., 2020). In contrast, detailed microscopic analysis on *bravo* mutants failed to unveil any phenotype in the vascular cells (Vilarrasa-Blasi et al., 2014). As BRAVO has a precise localization in the VI cells (Figure 4.1 A), we further investigated if BRAVO plays a functional role in the vascular tissues.

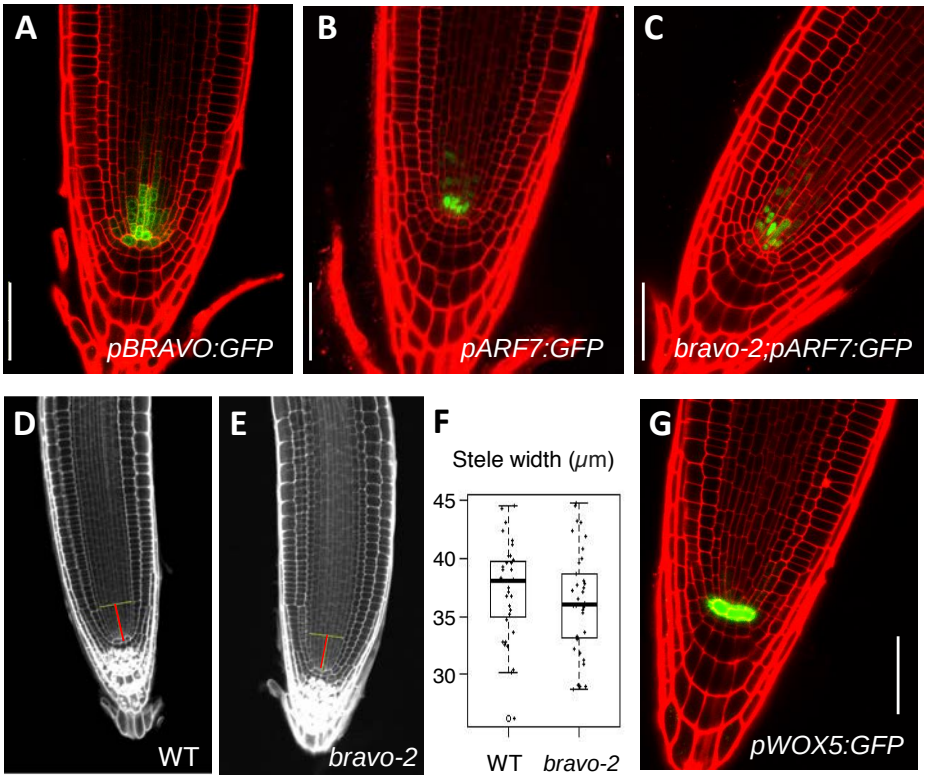

Figure 4.1: Cell-type specific role of BRAVO in the stem cell niche.

A) Confocal image of PI-stained 6-day-old pBRAVO:GFP root. B, C) Confocal images of pARF7:GFP in WT (B) and bravo-2 background (C) PI-stained 5-day-old roots. D, E) Confocal images of mPS-PI stained 6-day-old roots of WT (D) and bravo-2 (E). Red line correspond to 50 μm above the QC where stele width was measured (indicated as a yellow line). F) Quantification of stele width in roots in D and E (n>35, 3 biological replicates). No statistically significant differences in Student's t-test

G) Confocal image of PI-stained 5-day-old pWOX5:GFP root. GFP-tagged expression is shown in green in A, B, C and G. Scale bar: 50um.

Figure 1: Cell-type specific role of BRAVO in the stem cell niche.
A) Confocal image of PI-stained 6-day-old pBRAVO:GFP root. B, C) Confocal images of pARF7:GFP in WT (B) and *bravo-2* background (C) PI-stained 5-day-old roots. D, E) Confocal images of mPS-PI stained 6-day-old roots of WT (D) and *bravo-2* (E). Red line correspond to 50 um above the QC where stele width was measured (indicated as a yellow line).
F) Quantification of stele width in roots in D and E (n>35, 3 biological replicates). No statistically significant differences in Student's t-test
G) Confocal image of PI-stained 5-day-old pWOX5:GFP root. GFP-tagged expression is shown in green in A, B, C and G. Scale bar: 50 μm.

The expression pARF7:GFP as a marker of the vascular initial cells and the phenotype of stele width were used as an indicator of vascular initial cell division in WT and *bravo* mutants (Figure 4.1 B, D, E, F; Rademacher et al. (2011)). The expression of pARF7:GFP is restricted to the vascular initial cells, showing higher intensity in the first layer just above the QC and lower expression in the following vascular stem cells (Rademacher et al., 2011). Five-day-old seedlings revealed similar expression of pARF7:GFP marker levels and patterns when comparing the expression in WT and *bravo* mutant plants (Figure 4.1 B, C). The comparison between the stele width 50 μm above the QC of WT and *bravo* mutant seedlings did not show any differences (Figure 4.1 D, E, F), similar to what was reported previously (Vilarrasa-Blasi et al., 2014). In despite of the absence of phenotypes, we used these genetic crosses to investigate whether BRAVO modulates differential responses in the QC and VI cells at the transcriptional level using cell-type transcriptomics by combining FACS with bulk RNAseq analysis (Figure 1.3). Thus, the primary roots of 5-day-old seedlings expressing pWOX5:GFP and pARF7:GFP (as markers of QC and VI respectively) were used to sort cells from the QC and VI domains (Figure 4.1 G, B; Sarkar et al. (2007); Rademacher et al. (2011)). The RNAseq experiment was done in roots of WT and *bravo-2* backgrounds, as well as in WT treated with 10 nM BL for 2 hours.

4.3 Differential transcriptional responses are modulated by BRs and BRAVO in the quiescent center and vascular initial cells of the root apex

RNAseq of the sorted cells lead to identify QC and VI cell transcriptomes in WT and *bravo* seedlings, as well to physiological BL treated ones. To evaluate the main sources of variation between the QC and VI transcriptomes, a principal component analysis (PCA) with all the RNAseq samples was done (Figure 4.2). The three replicates of each condition were found to group together, thus validating our experiment. A clear separation between QC and VI samples was also observed, which indicates different transcriptional profiles between both cell types. In addition, the separation between BL-treated and bravo mutant samples in both cell type populations indicates that BRs and BRAVO regulate the QC and VI transcriptomes in different ways, suggesting that the set of genes that are regulated by BRs and BRAVO are different in the QC and VI cells, pointing to different roles in the distinct cell populations.

Next, the number of deregulated genes (q-value < 0.05, Fold change (FC) > 1) in each cell type, genotype and treatment was evaluated, separating between up and downregulated genes (Figure 4.3). The comparisons including BL-treated samples were done by calculating the ratio between BL treated samples over the untreated ones (named “BL reg”). BRAVO regulated genes were calculated with the ratio between WT samples over *bravo* mutant ones (named ”BRAVO reg”). Thus, upregulated genes are more expressed in the WT than in the *bravo* mutant and therefore they

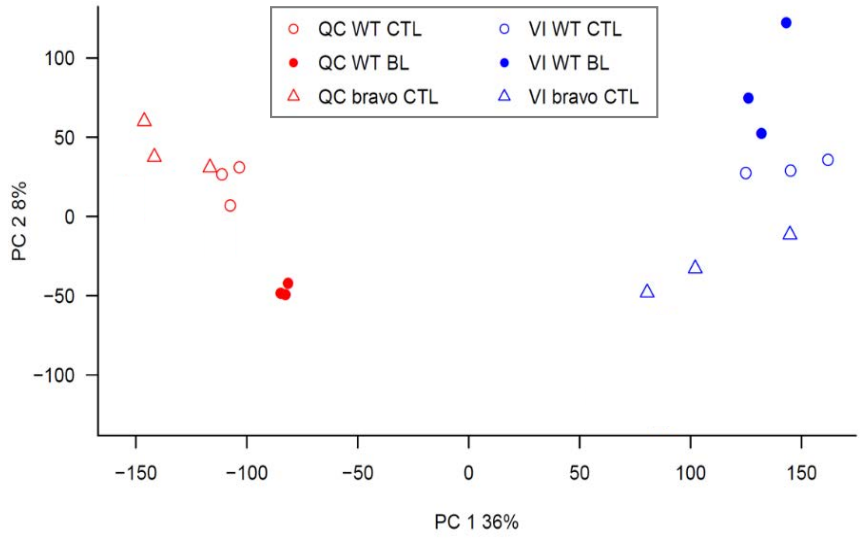

Figure 4.2: PCA analysis of QV and VI cell-type specific RNAseqs.
PCA analysis of all RNAseqs reveals a clear separation between QC (red) and VI (blue) transcriptomes.

Figure 2: PCA analysis of QV and VI cell-type specific RNAseqs.

PCA analysis of all RNAseqs reveals a clear separation between QC (red) and VI (blue) transcriptomes.

will be positively regulated by BRAVO in WT conditions. On the contrary, if genes are described as downregulated, it indicates that these genes will be repressed by BRAVO in WT conditions, as they show increased level of expression in the *bravo* mutant than in the wild type.

In the QC cells, the number of BL-upregulated and downregulated genes was similar (2273 and 2694 respectively). In contrast, in the VI cells the number of BL-downregulated genes was significantly higher than the upregulated ones (2009 and 609 respectively; Figure 4.3 A) pointing diverse transcriptional control of BRs in these two adjacent cell types. Regarding BRAVO-regulated genes, in the QC there are more genes that are positively regulated by BRAVO (1841 up and 11 downregulated; Figure 4.3 A) and in the VI there are more that are negatively regulated by BRAVO (821 up and 3074 downregulated; Figure 4.3 A). In addition, the same trend of up and downregulation was found when evaluating the number of transcription factors in each BL and BRAVO comparisons (Figure 4.3 B), also pointing to separate roles for BRs and BRAVO transcriptional control of QC and VI transcriptomes.

In general terms, that data shows: (i) BRs control the transcription of 4967 genes in the QC, approximately the double of the number in the VI (2618; Figure 4.3 C, D). (ii) BRAVO transcriptional regulation in the VI affects 3895 genes, the double of BRAVO in the QC where it affects the transcription of 1852 genes (Figure 4.3 C, D). Altogether, BRs appear to exert a wider transcriptional response in the QC, whereas BRAVO seems to be acting more in the transcriptional response in the VI cells.

The RNAseq data points to preferential roles for BRAVO in transcriptional activation in the QC and in transcriptional repression in the VI. In

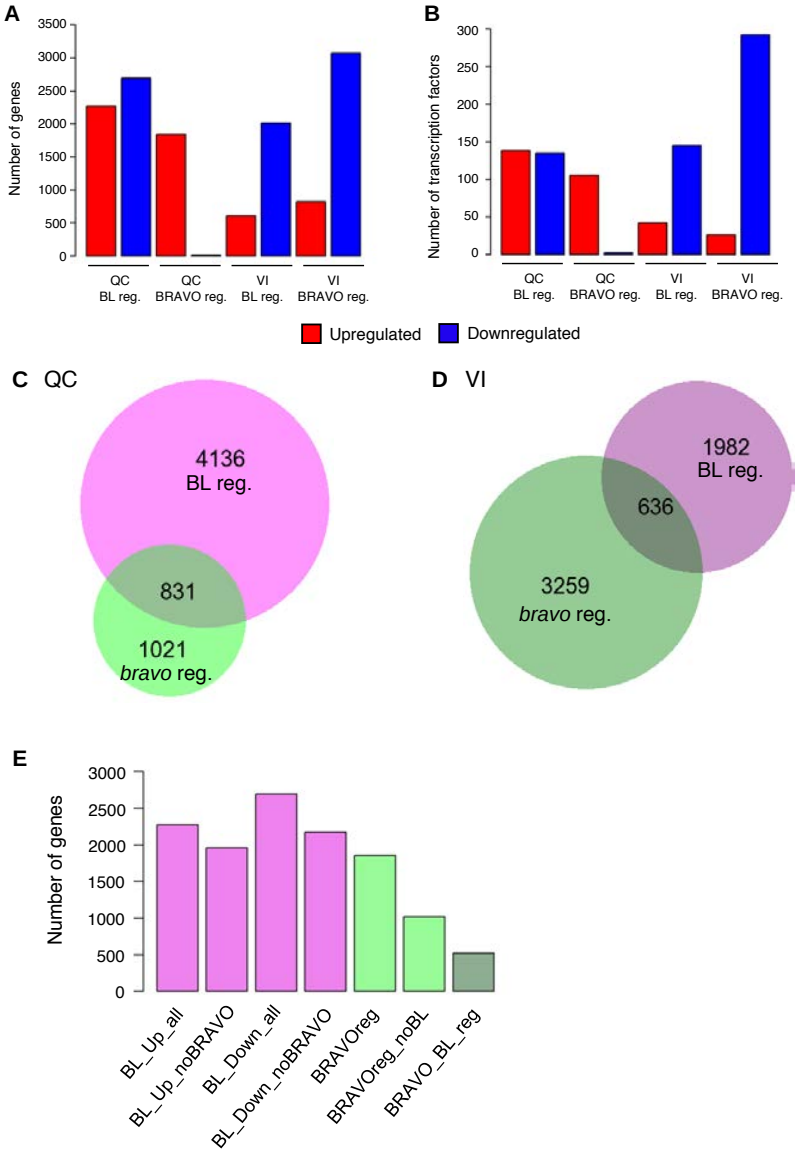

Figure 4.8: Number and overlap of BL and BRAVO regulated genes in the QC and VI cells. A, B) Number of genes (A) and transcription factors (B) regulated by BL and BRAVO in the QC and VI (q-value < 0.05 and fold change > 1). Upregulated (red) and downregulated (blue) are shown separately. The comparisons done are: BL vs CTL and WT vs *bravo*. C, D) Area-proportional Venn diagram showing the overlap between BL and bravo regulated genes in the QC (C) and VI (D). E) Number of BL and BRAVO regulated genes in the QC in different scenarios: BL upregulated, BL upregulated BRAVO independent, BL downregulated, BL downregulated BRAVO independent, BRAVO regulated, BRAVO regulated BL independent and BRAVO and BL regulated.

this line, PCA shows different transcriptomic profiles between the QC and VI cells in BL-treated and *bravo* root cells (Figure 4.2).

4.4 Transcriptional profiling of QC cells in *bravo* mutant and upon BL treatment

The transcriptomic datasets of BL and BRAVO regulated genes in the QC was analyzed first. We distinguished different scenarios in terms of BL and BRAVO regulation: (i) genes that are regulated by BRs, (ii) genes that are regulated by BRAVO, and (iii) genes co-regulated both by BRs and BRAVO, i.e. the fraction of BRAVO regulated genes that acts downstream of BR signaling (Figure 4.3 E).

The different scenarios were defined to evaluate which fraction of BRAVO response depends on BRs. To this aim, the number of regulated genes in the different BL and BRAVO datasets was analyzed (Figure 4.3 E and 4.4). For BR-regulated genes, distinction between up and downregulation was done; whereas for BRAVO regulated genes, as there is a clear predominance of BRAVO upregulated genes (Figure 4.3 A), no distinction between up and downregulation was done (Figure 4.3 E). To better understand the processes in which BRs and BRAVO are involved, Gene Ontology (GO) enrichment analysis of the different BL and BRAVO regulated set of genes was also performed (Figure 4.4). The set of genes that were analyzed are described in Table 4.1.

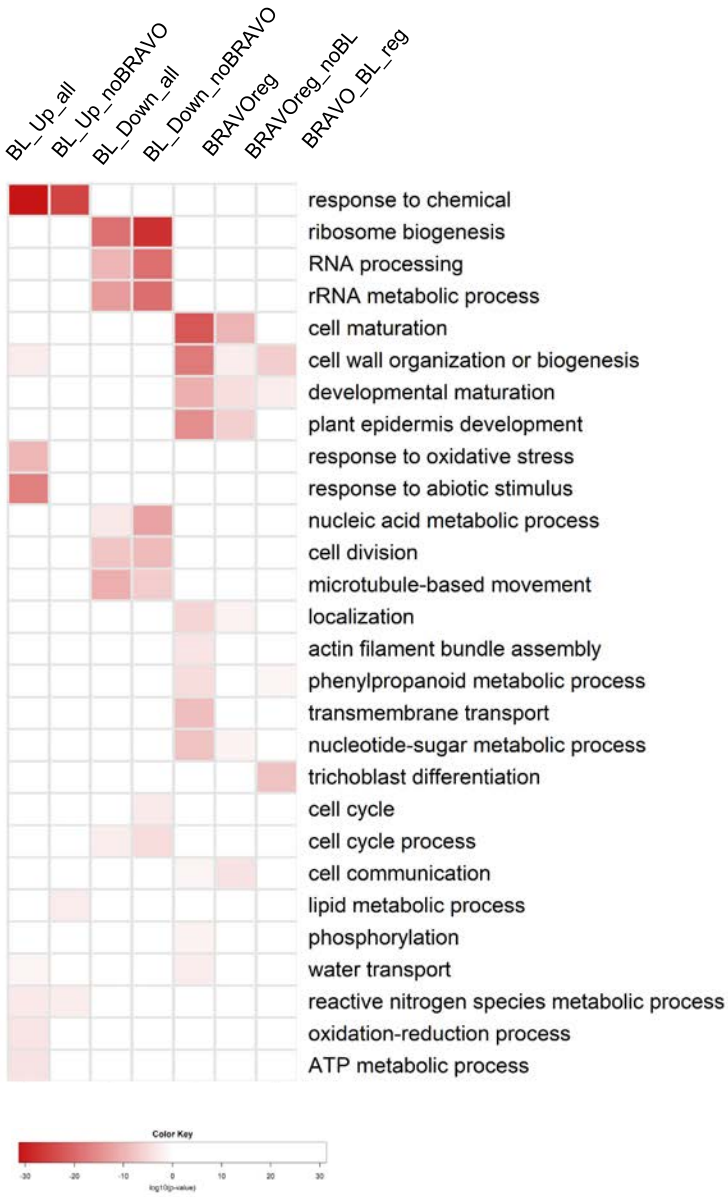

Figure 5: GO enrichment analysis of BL and BRAVO regulated genes in the QC.
A) GO enrichment analysis of BL and BRAVO regulated genes in the QC. Same separation in groups as shown in Fig 8B. GO enrichment performed in Araport thalemine, selected categories with pvalue < 0.05 in HolmBonferroni test. Category reduncancy was reduced with REVIGO and selected categories were manually curated. Darker red correspond to lower pvalue in GO enrichment analysis.

Figure 4.4: GO enrichment analysis of BL and BRAVO regulated genes in the QC.

GO enrichment analysis of BL and BRAVO regulated genes in the QC. Same separation in groups as shown in Figure 4.3 E. GO enrichment performed in Araport thalemine, selected categories with pvalue < 0.05 in HolmBonferroni test. Category reduncancy was reduced with REVIGO and selected categories were manually curated. Darker red correspond to lower pvalue in GO enrichment analysis.

Table 4.1: Groups of genes based on their regulation by BRs and BRAVO in the QC. The group of genes considered for each scenario are indicated with the symbols: + if the condition was happening in all the genes in the group, ? if the condition was not taking into account to create the group, and - if the condition was not happening in any gene in the group. As an example, in the first category, all genes are BR upregulated and no distinction was done if they are BRAVO regulated or not.

Scenario	BR up-regulated	BR down-regulated	BRAVO regulated	Number of genes
BL_Up_all	+	-	?	2273
BL_Up_ no-BRAVO	+	-	-	1960
BL_Down_ all	-	+	?	2694
BL_Down_ noBRAVO	-	+	-	2176
BRAVOreg	?	?	+	1852
BRAVOreg_ noBL	-	-	+	1021
BRAVO_BL_ reg	+	+	+	519

4.4.1 BR regulated genes in the QC

From the total 4967 BR- regulated genes in the QC, there are 2273 upregulated and 2694 downregulated genes. Of those, more that 80% (1960 up and 2176 downregulated genes) appeared not to be deregulated in *bravo* mutants (Figure 4.3 E). The GO enrichment analysis of these gene list is shown in Figure 4.4. For the 2273 BR-upregulated genes, a significant GO enrichment in "response to chemical" GO category was found, with 458 genes. Additional GO categories such as "response to abiotic stimulus" and "response to oxidative stress" are also significantly enriched. BRs has been involved in controlling the balance between growth and resistance against stresses which includes the regulation of stress-responsive pathways, the activation of antioxidant components or the promotion of

osmoprotectants (Ye et al., 2017; Lima and Lobato, 2017; Tunc-Ozdemir and Jones, 2017; Xia et al., 2009; Zou et al., 2018; Fàbregas et al., 2018; Planas-Riverola et al., 2019). These findings point to a role of BRs in maintaining the homeostasis of the QC as it is a specialized environment tightly controlled in terms of cell division and stress responses. Focusing in GO category "response to oxidative stress", a number of 93 genes of the 2273 (4%) was found in this category, from which 40 genes have a FC higher than 2. These 40 genes are shown in Figure 4.5 A.

Reactive oxygen species (ROS) are products of normal metabolism of the plant, but several stresses can contribute to an overproduction of these products, which can cause oxidative stress (Huang et al., 2019). Apart from their toxicity, they can also act as signaling molecules or in defense against pathogens. In this category, some of the most BL upregulated genes are SULFURTRANSFERASE 15 (STR15), KUNITZ TRYPSIN INHIBITOR 1 (KTI1), PEROXIDASE 38 (PER38), GLUTATHIONE S-TRANSFERASE 6 (GSTF6), WRKY DNA-BINDING PROTEIN 8 (WRKY8), PEROXIDASE 46 (PER46) and ALKENAL REDUCTASE (AER). STR15 (SEN1) has been linked to plant defense and senescence responses (Schenk et al., 2005). KTI1 encodes a serine protease inhibitor involved in plant cell death (Li et al., 2008). GSTF6 is an uncharacterized glutation transferase. WRKY8 transcription factor involved in basal defense in Arabidopsis (Chen et al., 2010). AER is involved in the detoxification of reactive oxygen species (Islam et al., 2016). Several peroxidases, that are proteins with no catalytic activity that are crucial to maintain redox homeostasis, also appear in the list. Interestingly, among the genes in this GO category, only PEROXIDASE 45 (PER45) and METHIONINE SULFOXIDE REDUCTASE B9 (MSRB9) appeared upregulated by

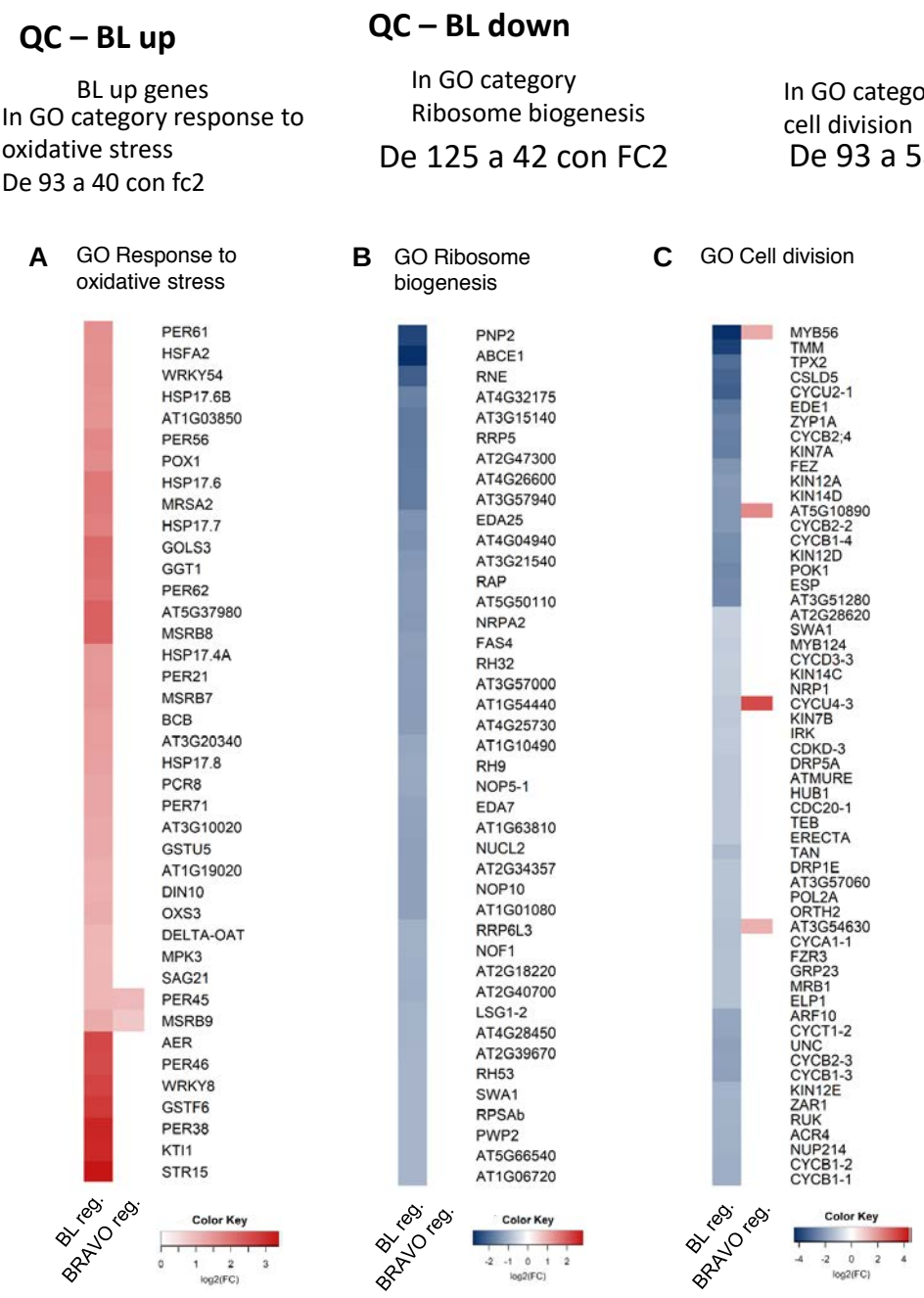

Figure 4.5: BL regulated genes in the QC from selected GO categories.

Figure 6. BL-regulated genes in the QC from selected GO categories.

Genes included in GO category "response to oxidative stress" (A), "ribosome biogenesis" (B) and "cell division" (C) from heatmap in Fig 8. Only genes with FC > 2 in BL regulated dataset are shown. Left column in the heatmap shows expression in BL-treated vs untreated comparisons. Right column in the heatmap shows expression in WT vs *bravo* comparisons. Color bar: log2 of the fold change. White color in the right column indicates no significant fold change for that gene in WT vs bravo comparison.

Genes included in GO category "response to oxidative stress" (A), "ribosome biogenesis" (B) and "cell division" (C) from heatmap in Figure 4.4. Only genes with FC > 2 in BL regulated dataset are shown. Left column in the heatmap shows expression in BL-treated vs untreated comparisons. Right column in the heatmap shows expression in WT vs *bravo* comparisons. Color bar: log2 of the fold change. White color in the right column indicates no significant fold change for that gene in WT vs *bravo* comparison.

BRAVO too. Together, our results support that BR signaling modulate ROS metabolism involved in stress responses at the QC cells.

Regarding the set of 2694 genes transcriptionally repressed by BRs in the QC, the highest significant enrichment was found in "ribosome biogenesis" and "cell division" GO categories (Figure 4.4). A total of 125 genes appeared in "ribosome biogenesis" GO category that are involved in different aspects such as rRNA maturation, processing and ribosome assembly. Of those, 42 genes BL-downregulated have FC higher than 2 (shown in figure 4.4 B). GO enrichment in this category was previously described in other BL-treated datasets of Arabidopsis root tips, therefore linking this GO process to BRs before (Chaiwanon and Wang, 2015).

The most BR-downregulated genes that were found in the GO category "ribosome biogenesis" are POLYRIBONUCLEOTIDE NUCLEOTIDYL-TRANSFERASE 2 (PNP2), ATP-BINDING CASSETTE E1 (ABCE1) and RIBONUCLEASE E/G-LIKE (RNE). PNP2 is a putative and not characterized polyribonucleotide nucleotidyltransferase. ABCE1 is a RNA silencing suppressor (Kärblane et al., 2015). RNE is a ribonuclease involved in the processing of plastid ribonucleic acids (Stoppel et al., 2012). Ribosomes are ribonucleoprotein complexes that are responsible for catalyzing the translation process. Ribosome biogenesis includes different steps of ribosome maturation such as pre-rRNA processing, modification, folding and the incorporation of ribosomal proteins (Palm et al., 2016).These ribosome-related categories are typical of cells with active transcriptional machinery, probably related to cell division processes, as defects in ribosomal biogenesis has been linked to defects in cell division (Shi et al., 2005; Griffith et al., 2007). BRs regulate QC division (González-García et al., 2011; Vilarrasa-Blasi et al., 2014), however if this

is due to the BR regulation of the ribosomal machinery in those cells remain unknown. Further experimental validation of genes in this category might help to understand whether ribosome biogenesis in the QC is key for the low rate of cell division.

The second enriched GO category in which BL downregulated genes are involved is "cell division" (Figure 4.4), in agreement with previous findings showing that exogenous BRs promote the division of QC cells (González-García et al., 2011; Hacham et al., 2011). In these cells, BRs promote cell division by repressing BRAVO (Vilarrasa-Blasi et al., 2014). We found 93 genes within "cell division" GO category, from which 58 have a fold change higher than 2 (shown in Figure 4.5 C). Supporting previous results (Vilarrasa-Blasi et al., 2014), one of the downregulated gene in response to BRs is BRAVO (MYB56) indicating that RNAseq experiment was successful. We found that BRs downregulate the expression of TOO MANY MOUTHS (TMM), TARGETING PROTEIN FOR XKLP2 (TPX2) and CELLULOSE SYNTHASE-LIKE D5 (CSLD5) genes. TMM is a LRR receptor-like protein that controls stomatal production and patterning (Bhave et al., 2009). It has been related to BR signaling before in hypocotyls (Wang et al., 2015). TPX2 is a protein important for microtubule nucleation and mitotic spindle assembly (Dvořák Tomaštíková et al., 2020). CSLD5 encodes cellulose synthase like 5 involved in cell plate formation (Gu et al., 2016). In the set of BR regulated genes in the QC we also found significant downregulation of cyclins and cyclin-dependent kinases that are key elements of cell-cycle progression (Gutierrez, 2009) (Figure 4.5 C). According to the results obtained with eFP browser (https://bar.utoronto.ca/efp/cgi-bin/efpWeb.cgi, these cyclins (CYCB2;4, CYCB2;2, CYCB1;4, CYCD3;3, CYCA1;1, CYCB2;3, CYCB1;3, CYCB1;2

and CYCB1;1) are expressed in several root cell types including the QC. Only one cyclin was regulated by BRAVO too. It is CYCU4.3 and any role in the QC has been described yet.

Taken together, the transcriptome of QC cells in response to BRs identify genes involved in different processes like cyclins and cyclin-dependent kinases and components of the last stages of spindle and cell plate formation. In addition, it can be that repression of cell division causes the repression of translational machinery such as ribosome biogenesis. For example, SLOW WALKER1 (SWA1) gene appears in both categories "ribosome biogenesis" and "cell division". SWA1 plays a role in rRNA biogenesis which is required for the progression of the mitotic division cycles during gametogenesis (Shi et al., 2005). Remarkably, the BL regulation of those response to stresses, ribosome biogenesis and cell division categories seems to be independent of BRAVO, as there is not enrichment when analyzing BRAVO regulated genes. In addition, very few genes involved in those categories were found to be BRAVO regulated (Figure 4.5). Regarding cell division, BRAVO is known to repress QC division downstream BL, so further analysis of BRAVO regulated genes will help to elucidate its mechanism of action.

4.4.2 BRAVO regulated genes in the QC

A total number of 1852 genes were found to be BRAVO regulated, i.e., genes that require BRAVO function to transcribe properly, and therefore appear deregulated in WT with respect to *bravo* mutant cells . Of those, 1021 are BRAVO specific and did not appear to modify their transcription in the BL-treated plants (Figure 4.5 B). This indicates that a 55% of

BRAVO transcriptional response is BRAVO specific and not necessarily downstream BRs. In order to decipher the role of BRAVO in the QC, GO enrichment analysis within the groups containing the BRAVO regulated genes was performed (Figure 4.4). Regarding all BRAVO regulated genes, there is higher enrichment in "cell maturation", "cell wall organization or biogenesis", "plant epidermis development" and "transmembrane transport" categories. When separating BRAVO-regulated genes in independent and downstream of BL, we observe enrichment in similar GO categories. Remarkably, in BRAVO regulated genes downstream BL, there is a high enrichment in "trichoblast differentiation". Trichoblasts are epidermal root hair cells. These results point to a role of BRAVO in controlling root hair development through the upregulation of genes involved in this process from the QC , both mediated by and independent of BRs. The role of BRAVO in trichoblast development can be due to the expression of those genes in the QC and not exclusively in the epidermal cells.

In the epidermis, only trichoblast cells form root hairs. Root hairs are single cell tubular extensions of root epidermal cells that support the functions of the primary root by increasing their absorptive surface (Vissenberg et al., 2020). Determination of trichoblast or atrichoblast identity depends on the signal from the cortex cells (Ishida et al., 2008; Grebe, 2012). Root hair development is controlled by different hormones and internal and external stimulus (Vissenberg et al., 2020). Regarding BRs in the root, they are essential for position-dependent epidermal cell fate specification (Wei and Li, 2016). Experimentally, it was found that BR signaling-enhanced plants have lower hair numbers compared to the WT (Cheng et al., 2014), yet this has been proposed to be modulated on a cell-autonomous bases.

To narrow down BRAVO-regulated genes involved in cell differentiation,

a total of 49 genes in this category genes present in "cell maturation" GO category were analyzed (Figure 4.6 A). Of those, the AT5G61350 (CAP1) and the yet uncharacterized AT3G01730 are the most deregulated ones. We found that BRAVO expression is required to maintain CAP1 levels, a gene that participate maintaining root hairs polar growth (Bai et al., 2014). Another gene in the list is COBRA-LIKE 9 (COBL9) involved in tip growth in root hairs (Parker et al., 2000). In agreement with the role of those genes in root hair development, analysis of the tissue-enriched expression of genes using TOTEM in that GO category indicates a higher enrichment in hair cell specific genes (Figure 4.6 B). These findings indicate a non-autonomous action of BRAVO at the QC cells as an activator of root-hair (trichoblast) cell differentiation, and encourage the phenotypic characterization of root hairs in *bravo* mutants.

A significantly enriched GO category in BRAVO-regulated genes is "transmembrane transport" (Figure 4.4), composed of 123 genes, from which 59 have FC $>$ 2 (Figure 4.7 A). The most deregulated genes are AT5G18840, DTX42 (AT1G51340, MATE), POTASSIUM TRANSPORTER 5 (POT5), PLASMA MEMBRANE INTRINSIC PROTEIN 2-8 (PIP2-8) and ABC TRANSPORTER B FAMILY MEMBER 5 (ABCB5). AT5G18840 is an uncharacterized sugar transporter. DTX42 (MATE) encodes a Citrate transporter involved in aluminum tolerance (Liu et al., 2009). POT5 (HAK5) is a potassium transporter (Lara et al., 2020). PIP2-8 is a probable aquaporin. ABCB5 is a glycoprotein that belongs to the ABC transporter family. There are also several TONOPLAST INTRINSIC PROTEIN (TIP) genes which are aquaporins, proteins that facilitate water movement along the plant (Quigley et al., 2002). Together, the majority of these genes encode for transporter proteins that are required for main-

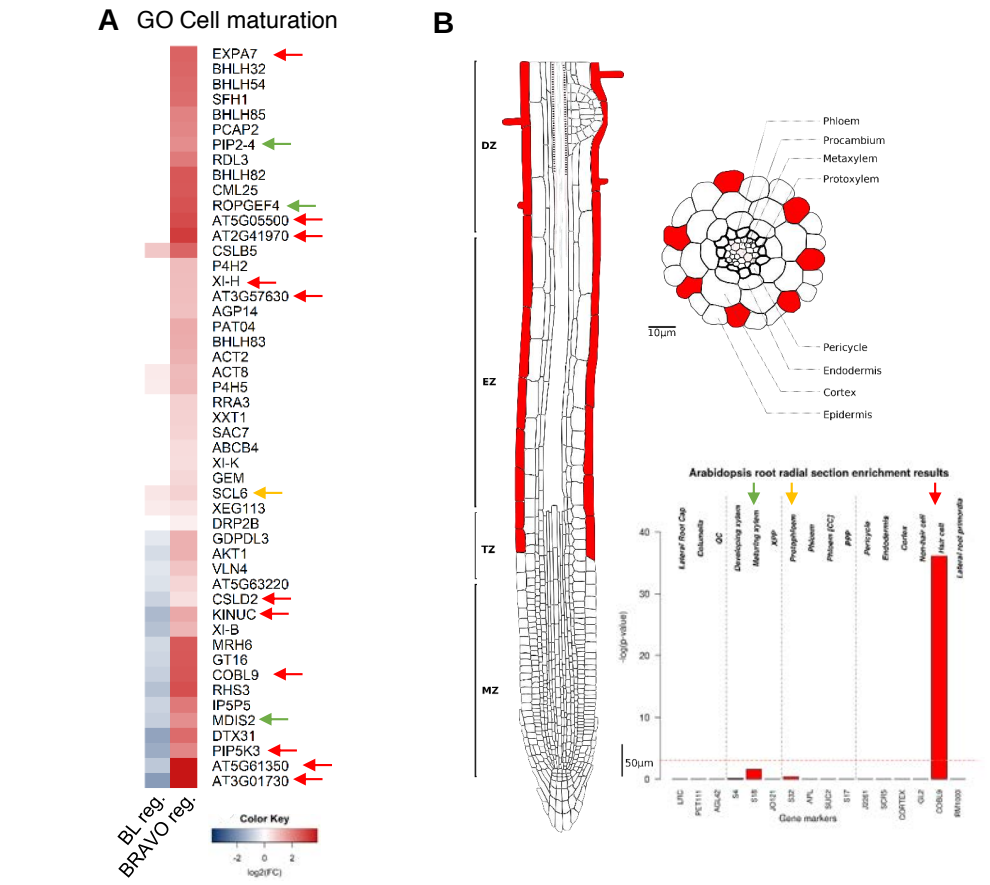

Figure 4.6: BRAVO regulated genes in the QC are involved in trichoblast differentiation.

A) Genes included in GO category "cell maturation" from heatmap in Figure 4.4. Left column in the heatmap shows expression in BL-treated vs untreated comparisons. Right column in the heatmap shows expression in WT vs *bravo* comparisons. Color bar: log2 of the fold change. White color in the left column indicates no significant fold change for that gene in BL vs CTL comparison. B) Arabidopsis root tissue enrichment for genes showed in A obtained with TOTEM software. Coloured arrows indicate genes specific from hair cells (red), maturing xylem (green) and protophloem (yellow) from Brady et al. (2007).

Figure 7: BRAVO regulated genes in the QC are involved in trichoblast differentiation.
A) Genes included in GO category "cell maturation" from heatmap in Fig 8. Left column in the heatmap shows expression in BL-treated vs untreated comparisons. Right column in the heatmap shows expression in WT vs bravo comparisons. Color bar: log2 of the fold change. White color in the left column indicates no significant fold change for that gene in BL vs CTL comparison. B) Arabidopsis root tissue enrichment for genes showed in A obtained with TOTEM software. Coloured arrows indicate genes specific from hair cells (red), maturing xylem (green) and protophloem (yellow) from Brady et al., 2007.

taining the tissues homeostasis by facilitating the movement of nutrients and water in the plant (Chrispeels et al., 1999).

4.4.3 BRAVO regulated genes acting downstream brassinosteroids in the QC

In this section we present the analysis of BRAVO-regulated genes acting downstream BRs in the QC cells of the root apex (Figure **??** A). We found a total of 519 genes to be both regulated by BL treatment and BRAVO. In this case, only genes in two scenarios were included: (i) genes downregulated by BRs and upregulated by BRAVO, and (ii) genes upregulated by BRs and downregulated by BRAVO. As BL treatment downregulates BRAVO levels, genes in those scenarios are the ones showing the same expression pattern in BL and BRAVO datasets.

A GO category significantly enriched in both BRAVO and BR-regulated genes is "cell wall organization", were we found 40 genes with FC $>$ 1 (Figure 4.7 B). The most deregulated gene is the transcription factor DOF3.4 (OBF BINDING PROTEIN 1, OBP1). DOF3.4 is described to affect growth by targeting the expression of genes encoding for cell wall loosening enzymes (Skirycz et al., 2008). DOF3.4 is also involved in cell division, and more precisely in cell cycle re-entry, operating as a transcriptional regulator of key cell cycle genes (Skirycz et al., 2008). There are also a number of XYLOGLUCAN ENDOTRANSGLYCOSYLASE/HYDROLASE (XTH) genes and two LRR-EXTENSINS LRX1 and LRX2 that are involved in cell wall formation during root hair development (Baumberger et al., 2003). CASPARIAN STRIP MEMBRANE DOMAIN PROTEIN 1, 2 and 3 (CASP1, CASP2 and CASP3) are involved

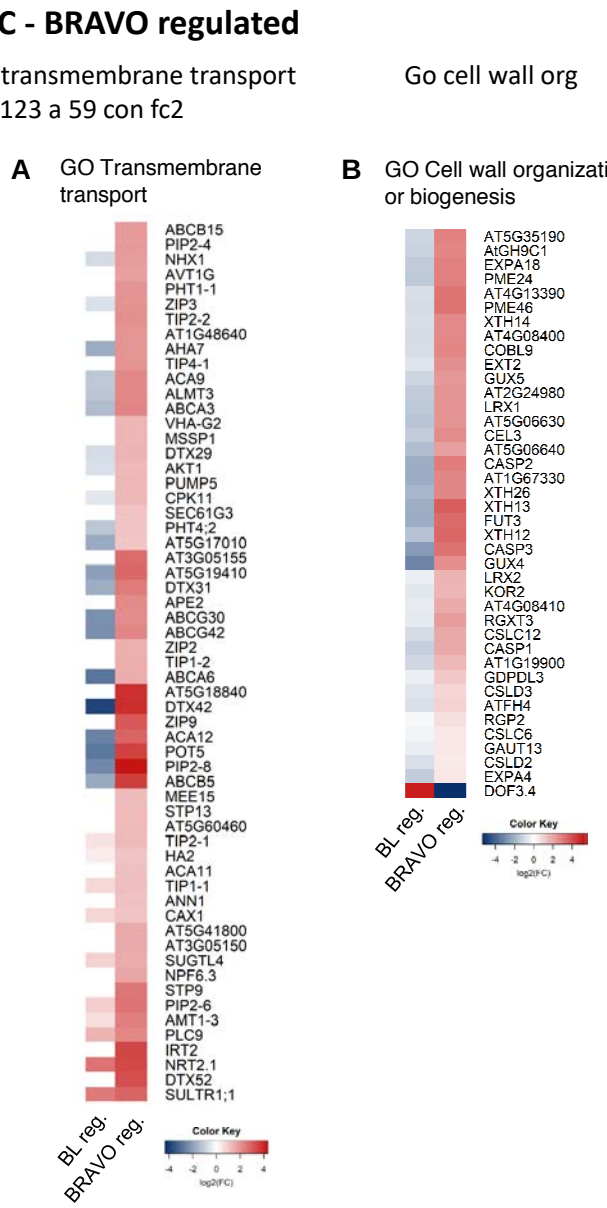

Figure 4.7: BRAVO regulated genes in the QC from selected GO categories. Genes included in GO category "transmembrane transport" (A) and "cell wall organization or biogenesis" (B) from detailed in Figure 4.4 category "transmembrane transport" (A) and "cell wall organization or biogenesis" (B), from heatmap in Figure 4.4. In A only genes with FC > 2 in BRAVO regulated dataset are shown. Left column in the heatmap shows expression in BL-treated vs untreated comparisons. Right column in the heatmap shows expression in WT vs *bravo* comparisons. Color bar: log2 of the fold change. White color in the left column indicates no significant fold change for that gene in BL vs CTL comparison.

Figure 8. BRAVO regulated genes in the QC from selected GO categories.
Genes included in GO category "transmembrane transport" (A) and "cell wall organization or biogenesis" (B) from detailed in Figure 4.4 category "transmembrane transport" (A) and "cell wall organization or biogenesis" (B), from heatmap in Figure 4.4. In A only genes with FC > 2 in BRAVO regulated dataset are shown. Left column in the heatmap shows expression in BL-treated vs untreated comparisons. Right column in the heatmap shows expression in WT vs *bravo* comparisons. Color bar: log2 of the fold change. White color in the left column indicates no significant fold change for that gene in BL vs CTL comparison.

in Casparian strip development (Roppolo et al., 2011). The lignin-based Casparian strip is in the endodermis and represents a selective filter for nutrient and water transport. There are several factors involved in the formation of that strip such as CASPs, peroxidases or TFs (Kamiya et al., 2015). Overall, BRAVO seems to be mostly regulating the expression of genes reported to play a role in outer layers outside the QC, such as in epidermis or endodermis cells, all suggesting that BRAVO acts mostly in a non-cell autonomous manner.

Next, we investigated BRAVO transcriptional network to better understand the role of BRAVO in the QC. The analysis was focused on the transcription factors functioning downstream BRAVO. As *BRAVO* is known to be a direct target of BES1 and BZR1 (Vilarrasa-Blasi et al., 2014), if this TFs are their targets was also evaluated, so they are more likely to be acting together (Figure 4.8). A total of 22 transcription factors appeared in the analysis with FC $>$ 1, being 21 positively regulated and only one (DOF3.4) downregulated by BRAVO. BRAVO levels itself appeared downregulated by BRs, thus validating our experiment. We found DOF3.4 the most deregulated TF, which could indicate that DOF3.4 is involved in the control of QC divisions downstream both BRs and BRAVO. Interestingly, DOF3.4 is a regulator of cell division genes (Skirycz et al., 2008) and a high fidelity direct target of BZR1 (Figure 4.8; He et al. (2005)).

The rest of TFs appear upregulated by BRAVO and have been related to different biological processes. Some of them are involved in response to different biotic and abiotic stresses such as RELATED TO AP2 11 (RAP2.11; Kim et al. (2012)), TGACG (TGA) MOTIF-BINDING PROTEIN 9 (TGA9; Wang et al. (2020)) and NAC DOMAIN CONTAINING PROTEIN 102 (NAC102; D'Alessandro et al. (2018)) to ROS, WRKY47

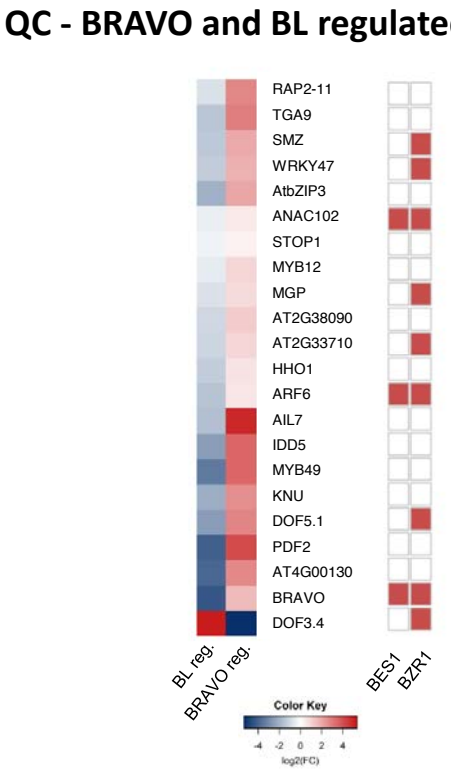

Figure 4.8: BRAVO downstream TFs in the QC.
Common BL and BRAVO regulated transcription factors in the QC. Left column in the heatmap shows expression in BL treated vs mock comparisons. Right column in the heatmap shows expression in WT vs *bravo* comparisons. Color bar: log2 of the fold change. Red squares indicate TFs as direct targets of BES1 and BZR1.

Figure 4.8: BRAVO downstream TFs in the QC.
Common BL and BRAVO regulated transcription factors in the QC. Left column in the heatmap shows expression in BL treated vs mock comparisons. Right column in the heatmap shows expression in WT vs bravo comparisons. Color bar: log2 of the fold change. Red squares indicate TFs as direct targets of BES1 and BZR1.

(Li et al., 2019) to aluminum, BASIC LEUCINE-ZIPPER 3 (bZIP3; Sanagi et al. (2018)) to sugars, SENSITIVE TO PROTON RHIZOTOXICITY 1 (STOP1) to acid soils (Balzergue et al., 2017), MYB49 (Zhang et al., 2020b) to salt and AT3G25790 (HHO1) to nitrogen starvation (Kiba et al., 2018). In the shoot, SCHLAFMUTZE (SMZ) represses flowering (Mathieu et al., 2009) and PREFOLDIN 2 (PDF2) cooperates for normal development of the floral organs (Kamata et al., 2013). INDETERMINATE(ID)-DOMAIN 5 (IDD5) is a positive regulator of starch granule formation in leaves (Ingkasuwan et al., 2012). AUXIN RESPONSE FACTOR 6 (ARF6) is positive regulator of adventitious root initiation (Lakehal et al., 2019) and MYB DOMAIN PROTEIN 12 (MYB12) mediates GA-regulated root growth via flavonols (Tan et al., 2019). This indicates that BRAVO action in the QC is required for both development and stress responses. This data support previous hypotheses considering the QC as a reservoir of cells to replenish the damaged ones after being damaged (van den Berg et al., 1997; Xu et al., 2006). Future characterization of these TFs could shed light on the role of BRAVO not only in root development, but also in root adaptation to stress.

Interestingly, some TFs have been related to stem cells and cell division before, whereas no relation with BRs has been proposed. For example, MAGPIE (MGP, IDD3) regulates tissue boundaries and asymmetric cell division and can control SHR and SCR activity (Welch et al., 2007). AIL7 (PLT7) is crucial for meristematic gene activation during lateral root formation (Du and Scheres, 2017). KNUCKLES (KNU) acts as a repressor of WUSCHEL which is essential for stem cell maintenance in the floral meristems (Sun et al., 2019). PEAR2 promote transcription of their inhibitory HD-ZIP III genes to demark the zone of cell division for radial

growth (Miyashima et al., 2019). Among them, MGP and PEAR2 are BZR1 direct targets. Other TFs have not been characterized (AT2G38090, AT2G33710 and AT4G00130) and are potential candidates to investigate their role in the BRAVO mediated pathway, specially AT2G33710 which is a high fidelity BZR1 direct target.

Altogether, our cell-type-specific transcriptomics approach developed in this PhD thesis led to the identification of putative genes regulated by BRAVO in the QC. The functional analysis of those genes indicates the biological functions in which they might be involved, so further experimental validation of those genes and functions will reveal novel components of BRAVO mediated pathway in the QC. Most of these TFs were not associated to QC function before, so this analysis advances in the redefinition of their function in root development.

We found that BR response mediated by BRAVO is mostly affecting genes outside the QC, especially in the root hair cells where it regulates their differentiation and cell wall properties. According to that, other TFs were found to regulate cell wall properties from other cell types, for example MYB36 regulates Casparian strip formation and it is also expressed in cell types different to the endodermis (Kamiya et al., 2015). Recently, it was shown that TMO5/LHW heterodimer from the vascular tissues mediates root hair responses in the epidermis (Wendrich et al., 2020).

4.5 Transcriptional profiling of VI cells in *bravo* mutant and upon BL treatment

The present section deals with the characterization of the transcriptional responses meditated by BRAVO in the VI cells (Figure 4.1 A). These specific cell population was also isolated and sequenced in WT, *bravo* mutant background and upon BL treatment. Analysis of their transcriptomes revealed BRAVO acting mostly as a repressor of transcription (Figure 4.3) and regulating a higher number of genes than in the QC. Nevertheless, these transcriptomic results might support a role of BRAVO in those cells, where pBRAVO:GFP also appear to show higher (brighter) expression than in the QC (Figure 4.3).

For the RNAseq analysis of VI sorted cells, similar to that of the QC cells, BL and BRAVO regulated genes were grouped based on their regulation in the different datasets (Figure 4.9). In light of the results, three different scenarios were defined: (i) genes that are regulated by BRs, (ii) genes that are regulated by BRAVO, and (iii) genes that are both regulated by BRs and BRAVO. In this case, up and downregulated genes in both BL and bravo datasets were separated, as the number of genes in all cases was remarkable (Figure 4.3 A). To further characterize the role of those regulated genes, GO enrichment analysis of the different set of genes was performed (Figure 4.10). The set of genes that were analyzed are described in Table 4.2.

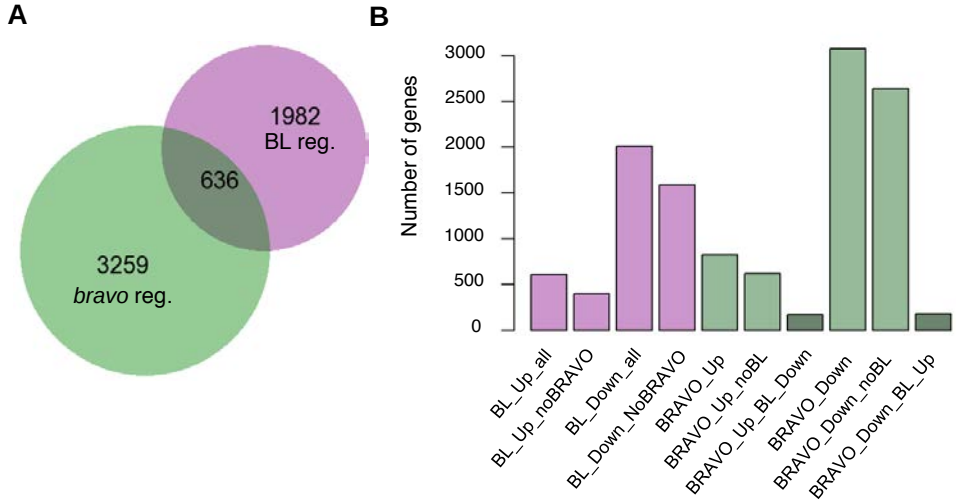

Figure 4.9: Number of BL and BRAVO regulated genes in the VI.

A) Area-proportional Venn diagram showing the overlap between BL and *bravo* regulated genes in the VI (same as in Figure 4.3 D). B) Number of BL and BRAVO regulated genes in the VI in different scenarios: BL upregulated, BL upregulated BRAVO independent, BL downregulated, BL downregulated BRAVO independent, BRAVO upregulated, BRAVO upregulated BL independent and BRAVO downregulated BL upregulated.

Figure 10: Number of BL and BRAVO regulated genes in the VI

A) Area-proportional Venn diagram showing the overlap between BL and *bravo* regulated genes in the VI (same as in Fig 8D).

B) Number of BL and BRAVO regulated genes in the VI in different scenarios: BL upregulated, BL upregulated BRAVO independent, BL downregulated, BL downregulated BRAVO independent, BRAVO upregulated, BRAVO upregulated BL independent, BRAVO upregulated BL downregulated, BRAVO downregulated, BRAVO downregulated BL independent and BRAVO downregulated BL upregulated.

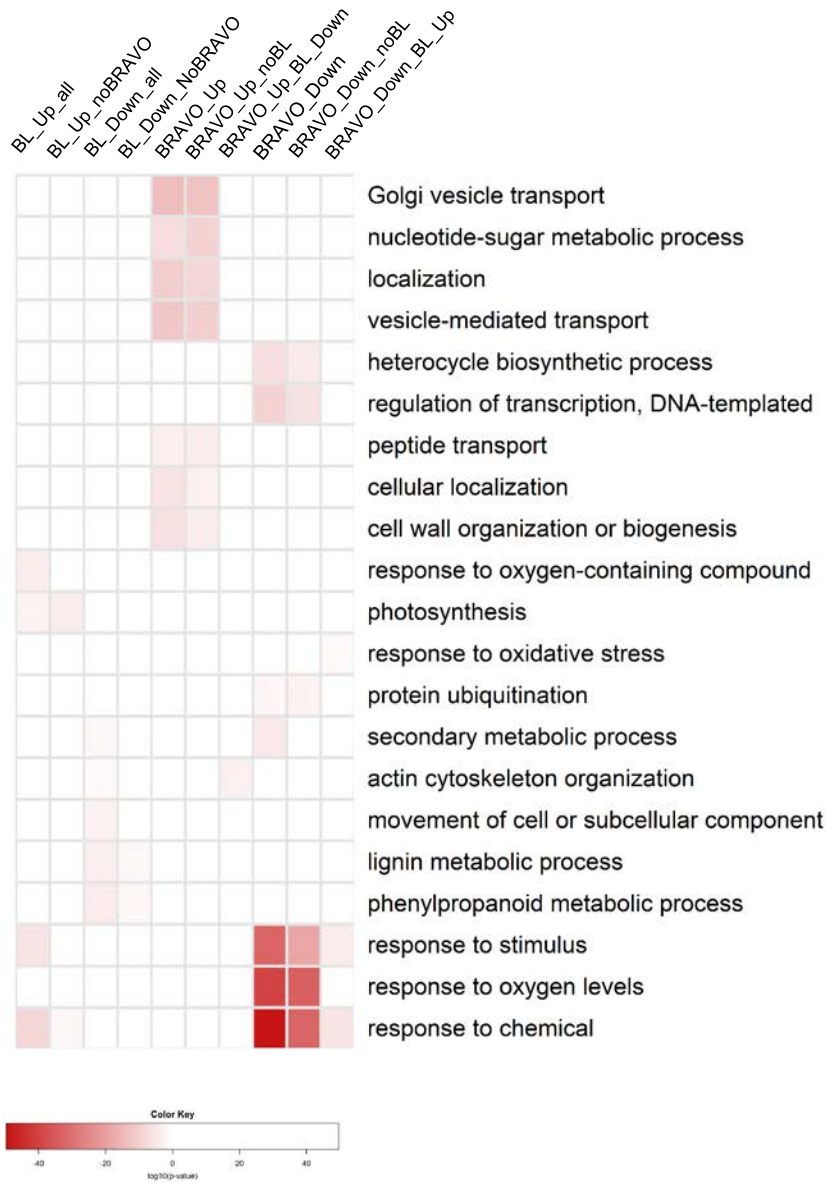

Figure 11: GO enrichment analysis of BL and BRAVO regulated genes in the VI.

A) GO enrichment analysis of BL and BRAVO regulated genes in the VI. Same separation in groups as shown in Fig 4.9 B. GO enrichment performed in Araport thalemine, selected categories with pvalue < 0.05 in HolmBonferroni test. Category reduncancy was reduced with REVIGO and selected categories were manually curated.

Figure 4.10: GO enrichment analysis of BL and BRAVO regulated genes in the QC.

GO enrichment analysis of BL and BRAVO regulated genes in the QC. Same separation in groups as shown in Figure 4.9 B. GO enrichment performed in Araport thalemine, selected categories with pvalue < 0.05 in HolmBonferroni test. Category reduncancy was reduced with REVIGO and selected categories were manually curated. Darker red correspond to lower pvalue in GO enrichment analysis.

4.5.1 BR regulated genes in the VI

The number of BR-regulated genes in the VI was first evaluated. A number of 609 were found to be upregulated and 2009 downregulated. Of those, more than 65% for up and 84% for downregulated genes (395 and 1687 respectively) appeared not to be deregulated in *bravo* mutants (Figure 4.9 B). GO enrichment of those genes was performed to analyze the molecular function in with they are involved (Figure 4.10).

First, the analysis of the BR-upregulated genes revealed higher enrichment in "response to chemical", "response to stimulus" and "photosynthesis" GO categories (Figure 4.10).

"Response to chemical" category was also found for BL upregulated genes in the QC. This category is very broad and include genes related to many stress responses both biotic and abiotic, in which BRs are involved. Therefore, this type of responses might not be unique for each cell type. So further analysis were focused in categories unique for the VI cells compared to the QC. Within "photosynthesis" category, which is unique for BL upregulated genes, there are 22 genes (Figure 4.11 A). Among the most upregulated genes there are several from the same family LHC that correspond to light harvesting complex proteins, which are regulated by multiple environmental and developmental cues (Xu et al., 2012); among them, BRs are known to regulate the thylakoid membrane architecture and the photosystem II function (Krumova et al., 2013). It was described that BR treatment can compensate a decreased photosynthetic rate under stresses through increasing carboxylation efficiency and enhanced antioxidant systems (Hasan et al., 2011). These findings indicate that BRs control genes involved in the photosynthesis. However, it is possible that

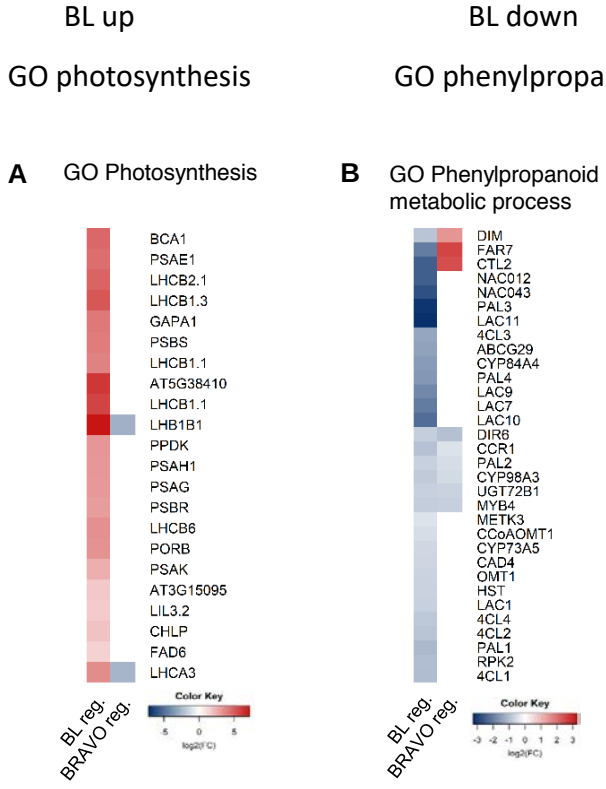

Figure 4.11: BL regulated genes in the VI from selected GO categories. Genes included in GO category "photosynthesis" (A) and "phenylpropanoid metabolic process" (B) from heatmap in Figure 4.10. Left column in the heatmap shows expression in BL-treated vs untreated comparisons. Right column in the heatmap shows expression in WT vs *bravo* comparisons. Color bar: log2 of the fold change. White color in the right column indicates no significant fold change for that gene in WT vs *bravo* comparison.

Figure 12: BL regulated genes in the VI.

Genes included in GO category "photosynthesis" (A) and "phenylpropanoid metabolic process" (B) from in Fig 4.10. Left column in the heatmap shows expression in BL-treated vs untreated comparisons. Right the heatmap shows expression in WT vs *bravo* comparisons. Color bar: log2 of the fold change. White c right column indicates no significant fold change for that gene in WT vs bravo comparison.

these genes have a different role in the VI cells that has not discovered yet, so experimental analysis regarding the role of these genes would be needed to address that.

BRs play important role in in cell expansion and differentiation by controlling the deposition of primary and secondary cell wall components ((Xie et al., 2011; Wolf et al., 2012, 2014; Sánchez-Rodríguez et al., 2017). Our analysis uncovers that in the case of BL downregulated genes, there is higher enrichment in "phenylpropanoid metabolic process" and "lignin metabolic process" GO categories (Figure 4.10). Phenylpropanoids are

plant secondary metabolites contribute to cell growth and differentiation as well as in the response to different stresses (Deng and Lu, 2017). Lignin is synthesized through phenylpropanoid metabolism, so both categories are related. There are 32 genes within "phenylpropanoid metabolic process" category (Figure 4.11 B). Among these genes, PHENYLALANINE AMMONIA-LYASE 1, 2 and 4 (PAL1, PAL2 and PAL4) are related with tissue-specific lignin synthesis, and PAL1 and PAL2 also have functional specialization in abiotic environmental-triggered flavonoid synthesis (Olsen et al., 2008). LAC genes are lacases involved in lignin biosynthesis. 4CL3 coumarate:CoA ligases involved general phenylpropanoid pathway. NAC012 (NST3) and NAC043 (NST1) redundantly regulate the secondary wall thickenings in interfascicular fiber of inflorescence stems and secondary xylem of hypocotyls in Arabidopsis. Mutants of these genes have defects in cellulose and lignin production (Mitsuda et al., 2007). DIM1 es DWARF1 involved in BR synthesis and in lignin metabolism for cell wall formation (Hossain et al., 2012).

Overall, these results support a role of BRs in cell wall differentiation by controlling the expression of genes that are involved in secondary cell wall composition and homeostasis processes already at the vascular initial cells.

4.5.2 BRAVO regulated genes in the VI

Here, BRAVO regulated genes in the VI cells were analyzed. A total of 821 genes were found to be upregulated and 3074 genes downregulated by BRAVO. From them, 618 and 2641 are not regulated by BRs respectively. This represents the 75% and 86% of the BRAVO-mediated response to be BR independent for BRAVO up and downregulated genes respectively

(Figure 4.9 B).

For the BRAVO upregulated genes, there was higher enrichment in "Golgi vesicle transport" GO category (Figure 4.10). The Golgi apparatus is an organelle functioning in polysaccharide and glycolipid synthesis, protein glycosylation and protein sorting towards various cellular compartments (Neumann et al., 2003). Among the most deregulates genes in this category are AT5G24350 (MAG2-INTERACTING PROTEIN 2, MIP2), AT5G16300 (CONSERVED OLIGOMERIC GOLGI COMPLEX SUBUNIT 1, COG1) and the uncharacterized SEC16B (AT5G47490) (Figure 4.12 A). This points a role for BRAVO on the feedback for protein trafficking from the Golgi to the plasma membrane. MIP2 knockout mutants have defects in ER-Golgi vesicle transport and in the response to the environment (Li et al., 2013; Zhao et al., 2018). ARF GUANINE-NUCLEOTIDE EXCHANGE FACTOR GNL1 (GNL1) is also upregulated. GNL1 has a role in endoplasmic reticulum (ER)–Golgi trafficking and GNL1/GNOM-mediated early secretory pathway selectively regulates PIN1 basal polarity establishment in a manner essential for normal plant development (Doyle et al., 2015). These genes are positively regulated by BRAVO in the VI cells but not regulated by BL (Figure 4.12 A).

Overall, this analysis revealed a role of BRAVO in regulating genes involved in Golgi vesicle transport. These processes have not yet been studied in the root stem cells and its impact in overall root development remain unknown. This lack of knowledge might be due to the complexity of experimentally observe the vesicles in these small and innermost located cells.

For BRAVO downregulated genes, GO enrichment analysis revealed cat-

Figure 4.12: BRAVO regulated genes in the VI from selected GO categories.

Genes included in GO category "Golgi vesicle transport" (A) and "response to oxygen levels" (B) from heatmap in Figure 4.10. In B only genes with FC > 2 in BRAVO regulated dataset are shown. Left column in the heatmap shows expression in BL-treated vs untreated comparisons. Right column in the heatmap shows expression in WT vs *bravo* comparisons. Color bar: log2 of the fold change. White color in the left column indicates no significant fold change for that gene in BL vs CTL comparison.

Figure 13. BRAVO regulated genes in the VI from selected GO categories.

Genes included in GO category "Golgi vesicle transport" (A) and "response to oxygen levels" (B) from heatmap in Figure 14.

In B only genes with FC > 2 in BRAVO regulated dataset are shown. Left column in the heatmap shows expression in BL-treated vs untreated comparisons. Right column in the heatmap shows expression in WT vs *bravo* comparisons. Color bar: log2 of the fold change. White color in the left column indicates no significant fold change for that gene in BL vs CTL comparison.

egories related to response to chemical and other stresses as the most enriched ones (Figure 4.10). Focusing on the genes in "response to oxygen levels" category, there are 120 genes in this category (with FC higher than 1). To narrow down the number of genes, we get the 58 ones with FC higher than 2 (Figure 4.12 B). The most deregulated ones are PER4, PER5 and AT2G32200 (CYSTM5). PER4 and PER5 are peroxidases. PER4 has a role in lignification (Fernández-Pérez et al., 2015). CYSTM5 has been reported as induced by environmental stresses, whereas no specific function was known (Xu et al., 2018).

Most of these genes does not appear as BL regulated (Figure 4.12 B), contrary to what was observed in the QC where BL regulates a big group of genes involved in ROS responses (Figure 4.8 A). This indicates that redox homeostasis in the QC and VI is differently regulated, and that BRAVO is more involved in this process in the VI cells. Further analysis dissecting ROS responses in the QC and VI separately would be required to better understand the differences between both cell types and their possible implications in development and stress responses.

4.5.3 BRAVO regulated genes acting downstream brassinosteroids in the VI

For BL and BRAVO downstream genes, we found 170 BRAVO upregulated and BL downregulated, and 181 BRAVO downregulated and BL upregulated (Figure 4.9 B).

To better understand the role of BRAVO in the VI, we focus our analysis in the transcription factors downstream BRAVO, as they might be form-

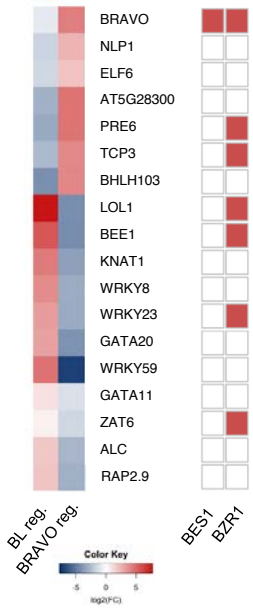

Figure 4.13: BRAVO downstream TFs in the VI.
Common BL and BRAVO regulated transcription factors in the VI. Left column in the heatmap shows expression in BL-treated vs untreated comparisons. Right column in the heatmap shows expression in WT vs *bravo* comparisons. Color bar: log2 of the fold change. Red square indicate TFs are direct targets of BES1 and BZR1.

Figure 14. BRAVO downstream TFs in the VI.
Common BL and BRAVO regulated transcription factors in the VI. Left column in the heatmap shows expression in BL-treated vs untreated comparisons. Right column in the heatmap shows expression in WT vs bravo comparisons. Color bar: log2 of the fold change. Red square indicate TFs are direct targets of BES1 and BZR1.

ing part of BRAVO transcriptional complex. We found 18 transcription factors (Figure 4.13), one of them is BRAVO, finding that validates our experiment.

Among the TFs, two of them are linked to BR signaling: EARLY FLOWERING 6 (ELF6) plays a role in BRs signaling affecting histone methylation in the promoters of BR-responsive genes (Yu et al., 2008) and BR ENHANCED EXPRESSION 1 (BEE1) acts downstream of BES1 and is a positive regulator of photoperiodic flowering (Wang et al., 2019a). Related to response to stresses, we found WRKY8 involved in basal defense in Arabidopsis (Chen2010), AT5G28300 (GT2L) in plant responses

to cold and salt stresses (Xi2012) and ZINC FINGER OF ARABIDOPSIS 6 (ZAT6) involved in salt, cadmium and phosphate stress responses (Liu et al., 2013; Chen et al., 2016; Devaiah et al., 2007). NITRILASE-LIKE PROTEIN 1 (NLP1) involved in the biosynthesis of polyamines (Piotrowski et al., 2003). ALC involved in fruit development (Groszmann et al., 2011). PRE6 (KIDARI, KDR) is involved in light signaling (Hyun and Lee, 2006). LSD ONE LIKE 1 (LOL1) acts as a positive regulator of cell death (Epple et al., 2003). KNAT1 (BP, BREVIPEDICELLUS) involved in growth and cell differentiation of the inflorescence stems (Venglat et al., 2002) and in secondary growth (Liebsch et al., 2014; Woerlen et al., 2017). WRKY23 involved in stem cell specification and in auxin distribution patterns through control of flavonol biosynthesis (Grunewald et al., 2012, 2013). TCP3 transcription factor is involved in flavonoid production, which further negatively modulates the auxin response (Li and Zachgo, 2013). The rest of them have not been characterized yet: BHLH103 (B70), GATA20 (HANL1), WRKY59, GATA11 and RAP2.9 (DEAR5).

Interestingly, two of the TFs, WRKY23 and TCP3, are related to flavonol biosynthesis influencing auxin signaling. Flavonoids are derived from phenylpropanoid metabolism are act as ROS-scavenging compounds which accumulate and affect root growth and development (Sanz et al., 2014). In this aspect, BRs were reported to regulated flavonoid biosynthesis to mediate growth and stress responses under changing UV-B conditions (Liang et al., 2020), and several R2R3-MYBs are involved in the regulation of flavonoid biosynthesis too (Dubos et al., 2010).

4.6 Transcriptional regulation by BRAVO and WOX5 in the QC

We showed in chapter 3 that there is a mutual regulation between BRAVO and the QC specific transcription factor WOX5 and that their interaction is relevant for overall root growth and development. To further understand this connection, WOX5 regulated genes in the QC were evaluated using a similar FACS based approach as used for BRAVO. pWOX5:GFP plants were used to isolate QC specific cells in WT and *wox5-1* mutants, and their transcriptome was compared (Clark et al., 2020).

In the QC, WOX5 regulates 1365 genes, from which 579 are up and 786 downregulated. Comparisons were done WT over wox5 mutant, so upregulated genes are more expressed in WT than in *wox5*, and the opposite for downregulated genes (Figure 4.14 A). The transcriptional response mediated by WOX5 was compared to the one mediated by BRAVO in the QC (Figure 4.14 B), to identify their action together in those cells, where they are controlling cell division. Overlap between WOX5 and BRAVO regulated genes indicates that 985 are WOX5 regulated and independent of BRAVO, and 380 are common between BRAVO and WOX5 (Figure 4.14 B).

Focusing in the 985 genes that are only WOX5 regulated, GO enrichment analysis indicates that they are mostly related to biological processes including response to stresses, chemical or hypoxia (Figure 4.14 C). Next, the common BRAVO and WOX5 regulated genes were evaluated. We found 380 BRAVO and WOX5 common deregulated genes (Figure 4.14 B). GO enrichment analysis of those genes indicates trichoblast differenti-

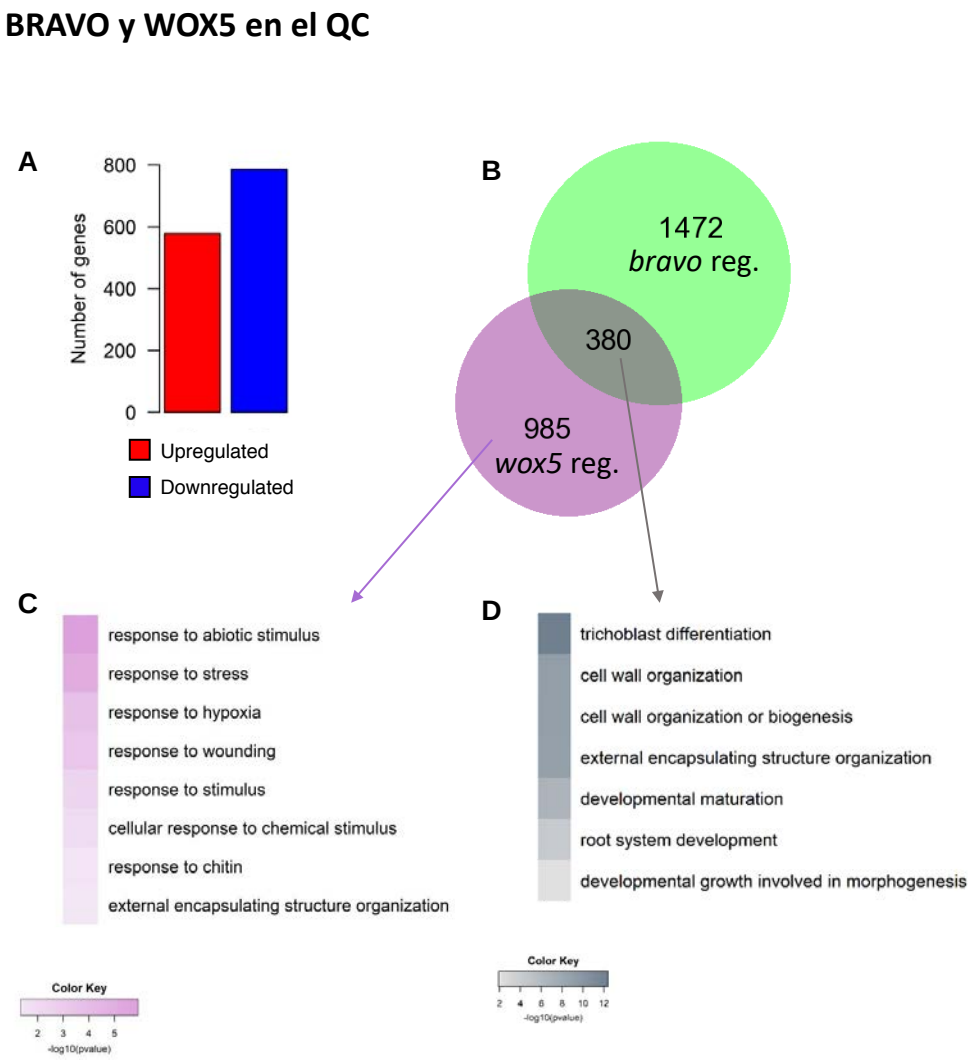

Figure 4.14: WOX5 regulated genes in the QC.

Figure 15: wox5 regulated genes in the QC.

A) Number of genes regulated by WOX5 in the QC (q-value < 0.05 and FC > 1). Upregulated (red) and downregulated (blue) are shown separately. The comparisons done are WT vs *wox5*. B) Area-proportional Venn diagram showing the overlap between BRAVO and WOX5 regulated genes in the QC. C) GO enrichment analysis of WOX5 regulated genes in the QC. D) GO enrichment analysis of common BRAVO and WOX5 regulated genes. GO enrichments in C and D were performed in Araport thalemine, selected categories with pvalue < 0.05 in HolmBonferroni test and category redundancy was reduced with REVIGO.

A) Number of genes regulated by WOX5 in the QC (q-value < 0.05 and FC > 1). Upregulated (red) and downregulated (blue) are shown separately. The comparisons done are WT vs *wox5*. B) Area-proportional Venn diagram showing the overlap between bravo and wox5 regulated genes in the QC.

ation and cell wall organization as the most enriched ones (Figure 4.14 D). This is in agreement with the significant number of BRAVO upregulated genes in the QC involved in root hair cell development (Figure 4.6).

This data was used to evaluate if the BRAVO WOX5 complex is having a role in transcription in the QC. For that we analyzed the genes that are similarly regulated by both TFs, as it can mean that are regulated by the complex. To deeper understand the behavior commonly deregulated genes in bravo and wox5 mutants, cluster analysis was done based on their expression fold change in both mutants (Figure 4.15 A). There is a set of 53 genes with a similar expression pattern of upregulation (orange square in Figure 4.15 A), which might be regulated by the complex, or at least, they are regulated by BRAVO and WOX5 in the same manner. These findings suggest a minor role of BRAVO and WOX5 joint function in the regulation of transcription in the QC, as the number of regulated genes is low. GO enrichment analysis does not gives any significant category.

Among those genes we found BRAVO. In agreement with our previous results (Figure 3.8), WT plants have a higher BRAVO expression compared to *wox5* mutants. Regarding the rest of genes, some of them has been previously characterized. Some examples are Cysteine endopeptidase 2 (CEP2), which is involved in PCD expressed in the root tip (Helm et al., 2008), AT4G30520 is SENESCENCE-ASSOCIATED RECEPTOR-LIKE KINASE (SARK) that regulates leaf senescence (Xu et al., 2011), and QUASIMODO2 LIKE 2 (QUL2) is involved in environmental-dependent stem and vascular development (Fuentes et al., 2010).

Among the common TFs regulated by BRAVO and WOX5, there are ERF055, BHLH83 which is ROOT HAIR DEFECTIVE 6 involved in root

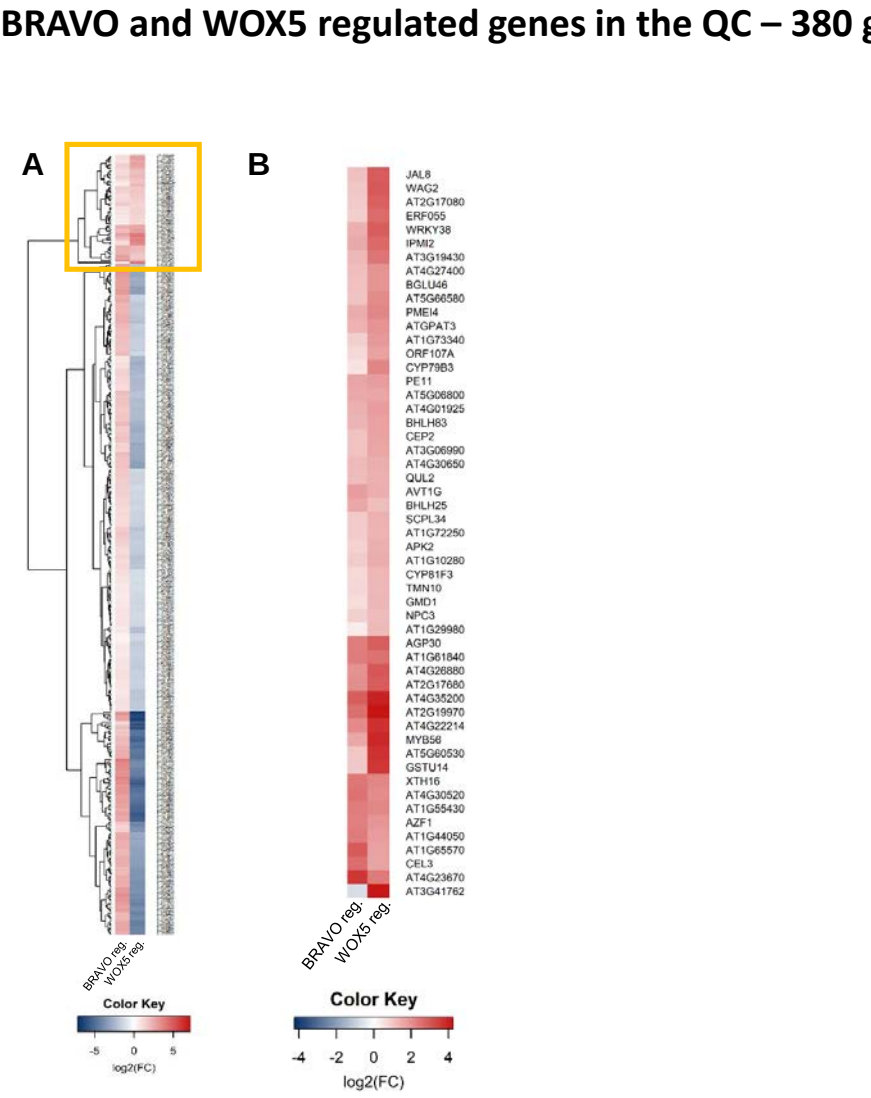

Figure 4.15: BRAVO and WOX5 regulated genes in the QC.
A) Expression of the 380 common BRAVO and WOX5 regulated genes from Figure 4.14 B. Yellow square delimits the genes with similar expression pattern in both conditions. B) Expression of the 53 genes from que yellow square in A. Left column in the heatmap shows expression WT vs *bravo* comparisons. Right column in the heatmap shows expression in WT vs *wox5* comparisons. Color bar: log2 of the fold change

Figure 16: BRAVO and WOX5 regulated genes in the QC.
A)
B)
C)

hair initiation (Mendoza and Alvarez-Buylla, 2000), WRKY38 related to basal defense (Kim et al., 2008) or ARABIDOPSIS ZINC-FINGER PROTEIN 1 (AZF1) acts as a transcriptional repressors involved in the inhibition of plant growth under abiotic stress conditions (Kodaira et al., 2011). These TFs are possible interactors of BRAVO and WOX5 participating in the same transcriptional complex. Many of the common deregulated genes are uncharacterized, such as AT4G35200, AT2G17680, AT4G35200, AT2G19970, AT4G22214 and AT4G23670.

Taking into account tissue specificity of those genes, only AT1G29980 and BRAVO show enriched expression in the QC. AT1G29980 has unknown function and belongs to the DUF642 family which is related to cell wall development (Cruz-Valderrama et al., 2019). Therefore, these genes is a candidate for further study in relation to the role of BRAVO and WOX5 together specifically in the QC cells.

Comparing WOX5 with BRAVO regulated genes (Figures 4.4 and 4.14 C), we observed that WOX5 is mostly involved in stem cell homeostasis and BRAVO in more differentiation processes, indicating that they play different roles and that their interaction is not essential for their function. As we showed in chapter 4, BRAVO and WOX5 form part of the same transcriptional complex. The comparison between BRAVO and WOX5 regulated genes revealed a group of 53 genes that are regulated by both TFs, pointing them to be acting downstream BRAVO/WOX5 complex. Remarkably, any of those genes has been related to QC identity or function before, so experimental characterization of them would permit to identify new roles in root stem cell development.

To conclude, the cell-type specific approach described in this PhD thesis

allowed the identification of BRs and BRAVO transcriptional responses in the QC and VI cells separately. We found that BRs and BRAVO regulate different transcriptomes in both cell types. Enrichment in genes annotated in stress responses appeared in the QC and VI datasets upon BL treatment, however, the genes were different, pointing to cell-type specific mechanisms regarding stem cell homeostasis. This approach also allowed to decipher a role of BRAVO in the QC acting non-cell autonomously in cell differentiation processes, and a role of BRAVO in the VI cells in flavonol metabolism. Finally, several candidate genes were described as targets of future research for uncovering BRAVO-mediated cell-type specific responses in the stem cells in root development and stress adaptation.

Table 4.2: Groups of genes based on their regulation by BRs and BRAVO in the VI. The group of genes considered for each scenario are indicated with the symbols: + if the condition was happening in all the genes in the group, ? if the condition was not taking into account to create the group, and - if the condition was not happening in any gene in the group. As an example, in the first category, all genes are BR upregulated and no distinction was done if they are BRAVO regulated or not.

Scenario	**BR upregulated**	**BR downregulated**	**BRAVO upregulated**	**BRAVO downregulated**	**Number of genes**
BL_Up_all	+	-	?	?	609
BL_Up_ noBRAVO	+	-	-	-	395
BL_Down_ all	-	+	?	?	2009
BL_Down_ noBRAVO	-	+	-	-	1587
BRAVO_ Up_all	?	?	+	-	821
BRAVO_ Up_noBL	-	-	+	-	618
BRAVO_ Up_BL_Down	-	+	+	-	170
BRAVO_ Down_all	?	?	-	+	3074
BRAVO_ Down_noBL	-	-	-	+	2641
BRAVO_ Down_BL_Up	+	-	-	+	181

Chapter 5

A single-cell transcriptomic map of the stem cell niche

A single-cell transcriptomic map of the stem cell niche

5.1 Introduction

The stem cell niche is formed by distinct cell types with different degree of stemness. The QC is in the most undifferentiated state and it divides to originate the rest of cell types (VI, CSC and CEI), which will differentiate to form the mature tissues. There are cell-type specific mechanisms that regulate the maintenance of the different cell populations (Kajala et al., 2020). Therefore, the use of cell-type specific approaches is key to understand certain processes affecting each individual cell type.

The study of the stem cells has been mostly approached with the use of FACS coupled to microarray or bulk RNAseqs, thus allowing the isolation of certain cell types for which reporter lines has been previously created. These approaches allowed to decipher fundamental molecular processes affecting stem cell development (Brady et al., 2007; Clark et al., 2019, 2020). However, the use of markers limits the analysis to populations that have already been described. In this aspect, single-cell technologies have demonstrated the potential to discriminate cell populations without the

need of reporter lines.

In the case of the Arabidopsis root, single-cell RNAseq was successfully applied for the isolation of root cells comprising all root tissues including stem cells. These studies generated a complete single-cell transcriptomic map of the root (Ryu et al., 2019; Shulse et al., 2019; Denyer et al., 2019; Zhang et al., 2019; Jean-Baptiste et al., 2019; Shahan et al., 2020; Wendrich et al., 2020). However, the information about the stem cells is still limited, probably due to the relative low number of stem cells compared to the rest of tissues. In addition, the expression signatures that are related to cell fate are known to be lower than the ones defining stem cell identity (Denyer et al., 2019), which might difficult the separation of distinct stem cell populations. In this aspect, we wanted to delve into the molecular signatures that define the stem cell niche with single cell resolution.

In this chapter we used single-cell RNAseq technology to explore the different stem cell populations in the root apex, and to further understand the role of BRAVO in these cells. We generated a single-cell RNA expression atlas of the Arabidopsis root specifically enriched in stem cell niche cells. We combined available datasets of cells from whole root tissues (Denyer et al., 2019; Jean-Baptiste et al., 2019) with those of cells from the SCN expressing pBRAVO:GFP. Those SCN cells were obtaining by FACS. All this data was used to define different stem cell populations based on gene expression profiles. We found that cells in the SCN can be separated in different populations, including subpopulations in the VI cells.

5.2 BRAVO and SUC2 markers allow the isolation of individual stem and phloem cells of the Arabidopsis root apex

In order to generate a single-cell RNA expression atlas of the stem cell niche, we first isolated individual root cells expressing pBRAVO:GFP in the root tip through FACS. Then, individual cells were sequenced. The whole experiment consisted in the use of plants expressing pBRAVO:GFP in WT and *bravo-2* mutant backgrounds (Figure 5.1A), and plants pSUC2:BRL3:GFP in WT and *brl3-2* backgrounds (Figure 5.1B). In this last case, the expression of BRL3 was driven to the phloem companion cells by using the pSUC2 promoter (Imlau et al., 1999). The line containing only pSUC2 promoter fused to GFP was not used because of its broader expression in the root tips where the GFP is unloaded from the phloem (Imlau et al., 1999). The expression of pSUC2:BRL3:GFP was confirmed to be expressed specifically in phloem cells (Figure 5.1 B). The comparison between WT and mutant backgrounds allowed us to further investigate the role of BRAVO in the SCN and the role of BRL3 in phloem cells. For the isolation of the individual cells, root tips of 5-day-old Arabidopsis plants were enzymatically digested to break up the cells and to generate individual protoplasts. The GFP positive cells were selected using FACS and were placed in 96-well-plates, placing only one cell per well. The RNA of those cells was extracted, cDNA was synthetized and single-cell RNAseq was performed (Figure 1.4).

A total number of 660 cells were sequenced including pBRAVO:GFP in WT and in *bravo-2* backgrounds, and pSUC2:BRL3:GFP in WT and *brl3-*

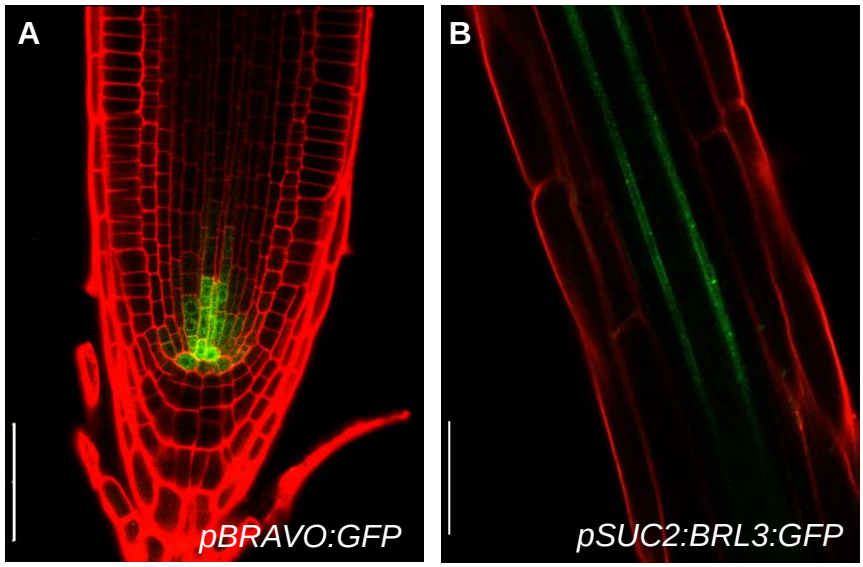

Figure 5.1: Markers used for the isolation of individual stem and phloem cells of the Arabidopsis root apex.
A-B) Stem cell niche (A) and phloem (B) marker lines used for the single-cell RNAseq experiment. Confocal images of PI-stained 6-day-old pBRAVO:GFP (A) and pSUC2:BRL3:GFP (B) roots. GFP-tagged expression is shown in green. Scale bar: 50 μm. Image A is the same showed in FigurepBRAVOchapterQCVI.

Figure 1. Isolation of individual stem and phloem cells of the Arabidopsis root apex.
A-B) Stem cell niche (A) and phloem (B) marker lines used for the single-cell RNAseq experiment. Confocal images of PI-stained 6-day-old pBRAVO:GFP (A) and pSUC2:BRL3:GFP (B) roots. GFP-tagged expression is shown in green. Scale bar: 50um. Image A is the same showed in Figure_pBRAVO_chapterQCVI

2 backgrounds. Subsequent bioinformatic analysis of the scRNAseqs was done using Seurat package available in R studio (Butler et al., 2018; Stuart et al., 2019). After filtering, 228 cells were selected for further analysis: 43 pBRAVO:GFP, 125 pBRAVO:GFP;*bravo-2*, 9 pSUC2:BRL3:GFP and 51 pSUC2:BRL3:GFP;*brl3-2* cells.

PCA analysis was used to explore primary sources of variation between the different cells (Figure 5.2 A). This analysis showed clear separation in two cell groups, corresponding mostly to the stem cell niche and the phloem. This result indicates that the difference between both cell populations is the highest source of heterogeneity in the data, pointing to higher transcriptional differences between both cell tissues than between WT and the different mutants (Figure 5.2 A).

Subsequently, a non-linear dimensional reduction (UMAP) and clustering analysis was performed to identify different cell populations within the sequenced cells (Figure 5.2 B). Similarly to the PCA, a clear separation between the stem and the phloem cells was observed with UMAP (Figure 5.2 B). The identity of these was evaluated with the expression of stem cell and phloem specific genes, BRAVO and SUC2 respectively (Figure 5.2 C, D). BRAVO was expressed in the largest group of cells (Figure 5.2 C) and SUC2 in the smallest one (Figure 5.2 D). Clustering analysis revealed the division of the stem cells in three different populations (Figure 5.2 B). However, when analyzing the number of cluster marker genes (the genes that differentiate one cluster from the others), we found that it was exceptionally low in some of them (94 for cluster 0, 16 for cluster 1, 299 for 2 and 352 for 3). This suggests a lack of differences between the four groups. This result might be consequence of the low number of cells and the high similarity between them. Therefore, we decided to integrate

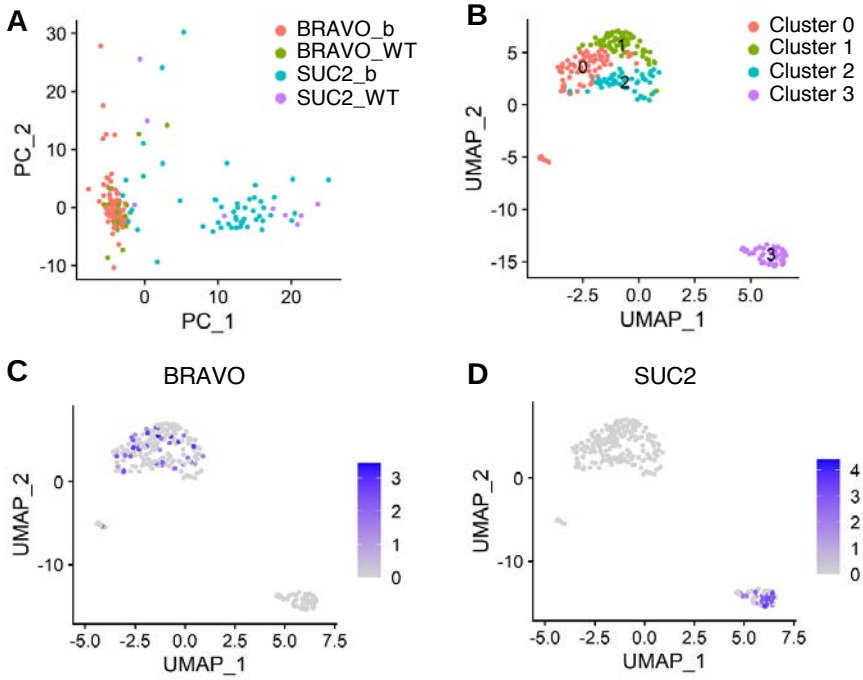

Figure 5.2: PCA and UMAP visualization of single stem and phloem cells.
A) PCA analysis of the 228 scRNAseqs used for the analysis. Different colors indicate cells from different marker lines. BRAVO_b: pBRAVO:GFP;bravo, BRAVO_WT: pBRAVO:GFP, SUC2_b: pSUC2:BRL3:GFP;brl3, SUC2_WT: pSUC2:BRL3:GFP. B) UMAP plot of the 228 stem and phloem cells. Different colors and numbers indicate different clusters. C, D) Expression of BRAVO (C) and SUC2 (D) across cells in the UMAP in B.

Figure 2. PCA and UMAP visualization of single stem and phloem cells.
A) PCA analysis of the 228 scRNAseqs used for the analysis. Different colors indicate cells from different marker lines. BRAVO_b: pBRAVO:GFP;bravo, BRAVO_WT: pBRAVO:GFP, SUC2_b: pSUC2:BRL3:GFP;brl3, SUC2_WT: pSUC2:BRL3:GFP
B) UMAP plot of the 228 stem and phloem cells. Different colors and numbers indicate different clusters.
C, D) Expression of BRAVO (C) and SUC2 (D) across cells in the UMAP in B.

our results with bigger single-cell datasets in order to find transcriptional differences inside the stem cell niche.

Our analysis did not show differences between cells from *bravo* mutant and WT plants; which suggests that the effect of BRAVO is negligible in the transcriptional profile of those cells, which is in agreement with our previous analysis of BRAVO bulk RNAseqs (Figure 4.2).

We were able to isolate and sequence individual cells of the SCN and phloem tissue in the root apex. Unfortunately, the number of cells obtained was too low to characterize the BRL3 mediated transcriptional response in those cells. However, we used these cells as a negative control for subsequent analysis of the stem cell niche, which we obtained by the same experimental and computational procedures.

5.3 Generation of a single-cell RNA expression atlas of the Arabidopsis root

To increase the resolution of existing single-cell atlas in the SCN, two complete published datasets containing cells from whole root tissues were integrated with our dataset. The first one is described in Denyer et al. (2019) containing 4727 single-cell transcriptomes and the second one described in Jean-Baptiste et al. (2019) containing 3121. In both cases they reported the presence of cells corresponding to all major root cell types.

The integration of the three datasets was done with the Seurat R package (Butler et al., 2018; Stuart et al., 2019), and resulted in data from 8076 cells. UMAP visualization of the integrated dataset showed homogeneous

distribution of cells corresponding to the different datasets (Figure 5.3 A). As expected, cells from our dataset are concentrated in specific positions of the UMAP plot, as they only represent specific cell types, i.e. the stem cell niche and phloem (Figure 5.3 A). In our original dataset, we observed the SCN and the phloem cells grouped in two different cell populations (Figure 5.3 B), which is in agreement with our previous analysis where we clearly observed transcriptional differences between both types of cells (Figure 5.2).

To identify the distinct cell populations, an unbiased clustering analysis based on the gene expression profiles of the 8076 cells was performed (Figure 5.4). A number of 23 different clusters were identified (Figure 5.4). The cells from the two published datasets were scattered among all 23 clusters (Table 5.1), suggesting that the experimental differences from their respective sources have no effect in their distribution. In contrast, our data from pBRAVO:GFP cells were grouped in clusters 2, 8, 10, 19, and 21; and pSUC2:BRL3:GFP cells in clusters 2, 5, 8, 11, and 21 (Figure 5.4; 5.1).

To assign cell identities to the different clusters, the expression of known cell-type specific genes in the 23 identified clusters was evaluated (Figure 5.5). Marker genes were obtained from several transcriptomic datasets and were used to define cell identities in the single-cell datasets used in this study (Denyer et al., 2019; Jean-Baptiste et al., 2019). These markers showed expression in specific clusters and allowed us to attribute identities to most of the clusters and to identify all principal root tissues (Figure 5.5). Altogether, we generated a single-cell RNA atlas of the Arabidopsis root with over 8000 individual cells in which we successfully integrated our high resolution single cell transcriptomic analysis of the root stem cell

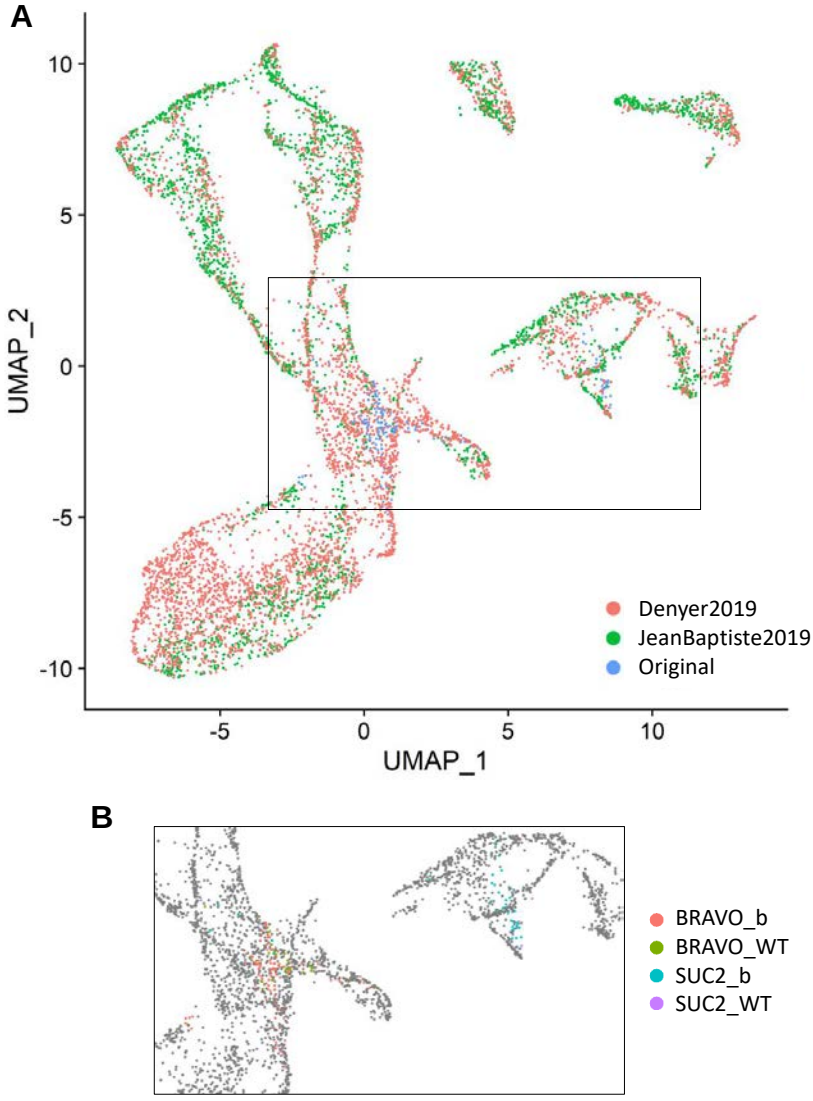

Figure 5.3: UMAP visualization of the integrated dataset.
A) UMAP plot of the 8076 cells in the integrated dataset. Different colors indicate different origin of the datasets: Denyer2019: Denyer et al. (2019), JeanBaptiste2019: Jean-Baptiste et al. (2019), Original: our experiment. B) Inset of the part of the UMAP including the cells from our experiment. Different colors indicate cells from different marker lines: BRAVO_b: pBRAVO:GFP;*brl3*, BRAVO_WT: pBRAVO:GFP, SUC2_b: pSUC2:BRL3:GFP;brl3, SUC2_WT: pSUC2:BRL3:GFP.

Figure 3. UMAP visualization of the integrated dataset.
A) UMAP plot of the 8076 cells in the integrated dataset. Different colors indicate different origin of the datasets: Denyer2019: \cite{Denyer2019}, JeanBaptiste2019: \cite{JeanBaptiste2019}, Original: our experiment. B) Inset of the part of the UMAP including the cells from our experiment. Different colors indicate cells from different marker lines: BRAVO_b: pBRAVO:GFP;*brl3*, BRAVO_WT: pBRAVO:GFP, SUC2_b: pSUC2:BRL3:GFP;brl3, SUC2_WT: pSUC2:BRL3:GFP.

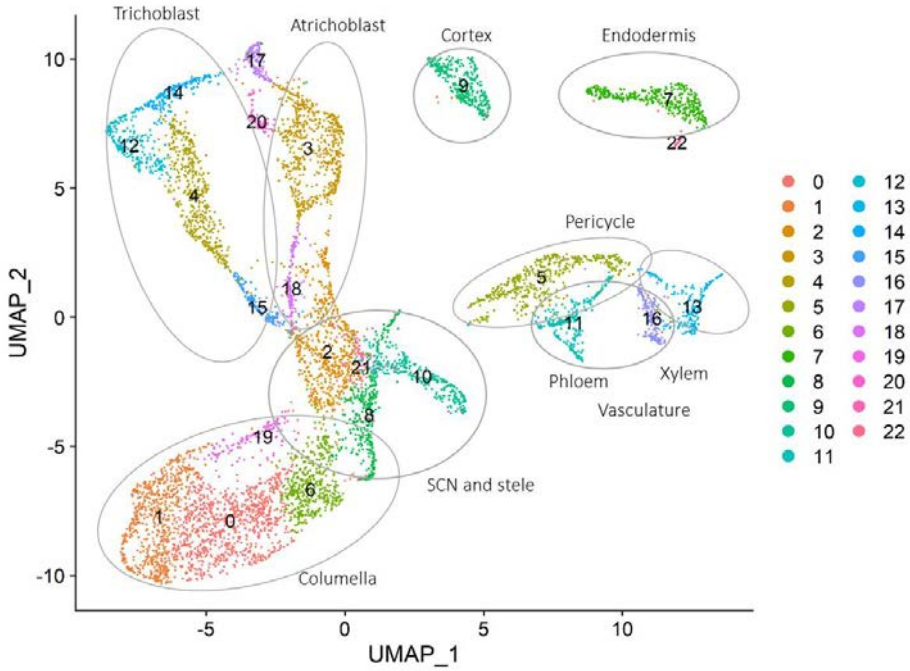

Figure 5.4: Single-cell RNA expression atlas of the Arabidopsis root.
UMAP plot of the integrated dataset. Different colors indicate different clusters. Clusters corresponding to the distinct root cell types are indicated.

Figure 4. Single-cell RNA expression atlas of the Arabidopsis root.
UMAP plot of the integrated dataset. Different colors indicate different clusters. Clusters corresponding to the distinct root cell types are indicated.

Table 5.1: Number of cells per cluster. Number of cells corresponding to different experiments in each cluster of the integrated dataset. Clusters containing the majority of stem and phloem cells from our experiment are highlighted in bold. pB: pBRAVO:GFP; pB;b: pBRAVO:GFP;*bravo*; pS: pSUC2:BRL3:GFP; pS;b: pSUC2:BRL3:GFP;*brl3*; Denyer: Denyer et al. (2019); JeanB.: Jean-Baptiste et al. (2019)

Cluster	pB	pB;b	pS	pS;b	Denyer	JeanB.
1	0	0	0	0	587	111
2	**4**	**34**	**1**	**6**	**422**	**142**
3	0	0	0	0	256	350
4	0	0	0	0	144	340
5	**0**	**0**	**0**	**11**	**221**	**214**
6	1	0	0	0	270	166
7	0	0	0	0	129	280
8	**0**	**23**	**0**	**1**	**313**	**12**
9	0	0	0	2	133	210
10	**9**	**23**	**0**	**0**	**219**	**65**
11	**0**	**0**	**6**	**28**	**93**	**140**
12	0	0	0	0	82	138
13	0	0	0	0	145	62
14	0	0	0	0	35	146
15	0	0	0	0	57	104
16	0	0	0	0	65	84
17	0	0	0	0	35	106
18	1	1	1	1	92	45
19	**4**	**3**	**0**	**0**	**73**	**53**
20	1	0	0	0	21	65
21	**24**	**42**	**1**	**1**	**7**	**6**
22	0	0	0	0	9	19

niche in already existing whole-root single-cell datasets (Figure 5.4).

In the integrated single-cell atlas, distinct particularities can be observed between the different clusters related to their tissue identity. (i) Some clusters showed a clear separation from the others, such as clusters 7 and 9, from endodermis and cortex respectively (Figure 5.4). This suggests high transcriptional differences of these cells compared to the rest. (ii) Other clusters share tissue identity, such as 16 that has both phloem and

pericycle, possibly corresponding to phloem pole pericycle cells (Figure 5.4). (iii) Some root tissues like trichoblasts and atrichoblasts are divided in several clusters. This can reflect the presence of different cell types or developmental stages from the meristem to the differentiation zone, thus allowing the identification of young and mature differentiations states of the same cell type. (iv) Finally, some clusters containing a small number of cells lack a clear identity, such as clusters 17, 20 and 22, as any evaluated marker gene showed specific expression in that cell group (Figure 5.4). Further analysis of these clusters could allow the discovery of new cell populations, as they have molecular signatured that differ from the rest of cells. These results support the use of single-cell technology for the discovery of small or rare cell populations.

Stem cell niche and stele tissue can be divided in several populations (clusters 2, 6, 8, 10, 19 and 21; Figure 5.5). We hypothesize that this is due to the presence of multiple stem cell populations (QC, CEI, VI, CSC). Clusters 6, 8 and 19 contain some columella cells, and clusters 2, 8, 10 and 21 contain mostly cells from the QC and surrounding stele cells (Figure 5.5).

One mayor advantage of the Arabidopsis root is its stereotypical organization comprising cells in all developmental stages, from stem cells to differentiated tissues from mature root cell types. This makes single-cell root isolation and analysis a powerful approach to study developmental trajectories through Pseudotime analysis. In order to understand the developmental progression of the identified clusters in the root atlas, pseudotime analysis was performed to all cells in our integrated dataset (Figure 5.6 A). The QC is formed by the less differentiated cells in the root, as they originate the rest of cells in the root (Heyman et al., 2014). Therefore,

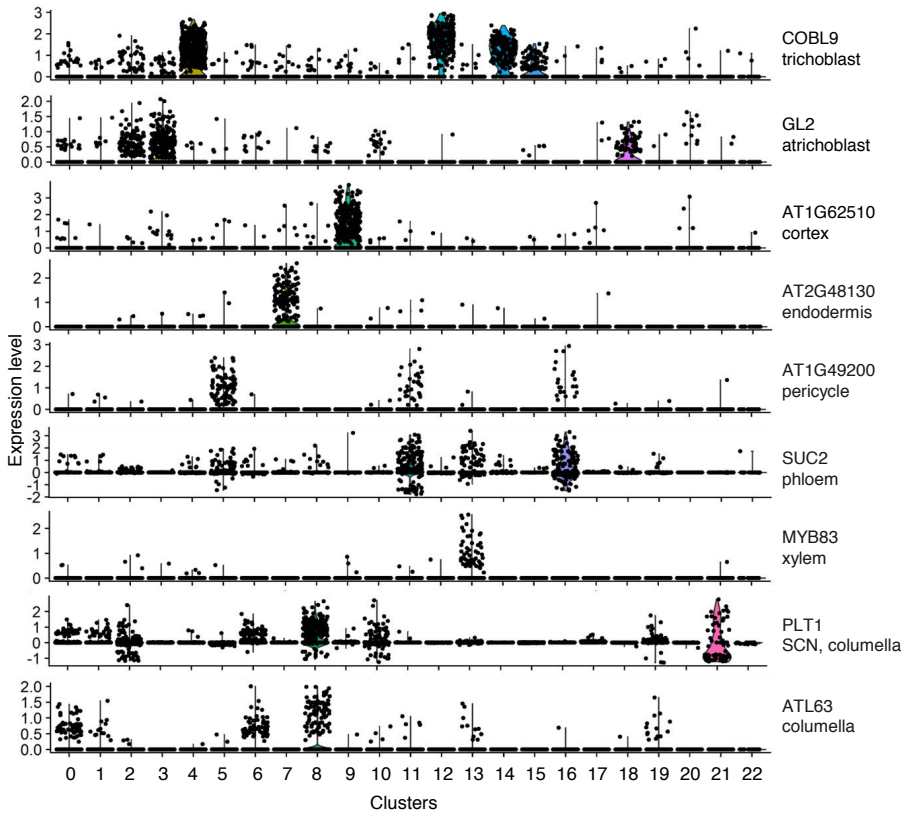

Figure 5.5: Expression of selected marker genes in the integrated dataset.

Expression of marker genes for cell type annotation of the single-cell RNA expression atlas of the Arabidopsis root shown in Figure 5.4. Representative selection of gene markers used for cell type annotation and their expression levels in the 23 clusters of the integrated dataset. Each dot corresponds to an individual cell. Right labels indicate the gene and the cell type in which it is expressed.

Figure 5. Expression of selected marker genes in the integrated dataset.
Expression of marker genes for cell type annotation of the single-cell RNA expression atlas of the Arabidopsis root shown in Figure 4. Representative selection of gene markers used for cell type annotation and their expression levels in the 23 clusters of the integrated dataset. Each dot corresponds to an individual cell. Right labels indicate the gene and the cell type in which it is expressed.

the QC cells were selected as Pseudotime 0 for the analysis. The selection of QC cells was done by identifying the cells expressing WOX5 and PAN, two QC-specific genes (Sarkar et al., 2007; de Luis Balaguer et al., 2017), which were enriched in cluster 8 (Figure 5.6 B, C). Pseudotime analysis revealed a group of less differentiated cells corresponding with the SCN and stele cell clusters mostly, supporting the annotation of this group. In agreement with Denyer et al. (2019), meristematic cells are grouped together independently of the cell type that they are going to originate.

In conclusion, the integration of published single-cell datasets with our scRNAseqs of the stem and phloem cells allowed us to generate a whole root dataset containing all root cell types with specific enrichment in stem cells.

5.4 The stem cell niche can be separated in four different stem cell populations

To study the transcriptional profile of the stem cells, we enriched the root atlas dataset with our data from cells expressing pBRAVO:GFP. BRAVO is expressed in the SCN, and specifically in the QC and the VI cells (Figure 5.7 A). In *bravo-2* mutant, the expression of pBRAVO:GFP increased and shifted to more stele cells and to the cortex and endodermis initials (Figure 5.7 B).

We first evaluated BRAVO expression in the integrated dataset, based on the assumption that clusters expressing BRAVO corresponded to the stem cell niche. Most of the cells expressing BRAVO were found in clusters 2, 8, 10 and 21 (Figure 5.7 C), which supports our previous result of these

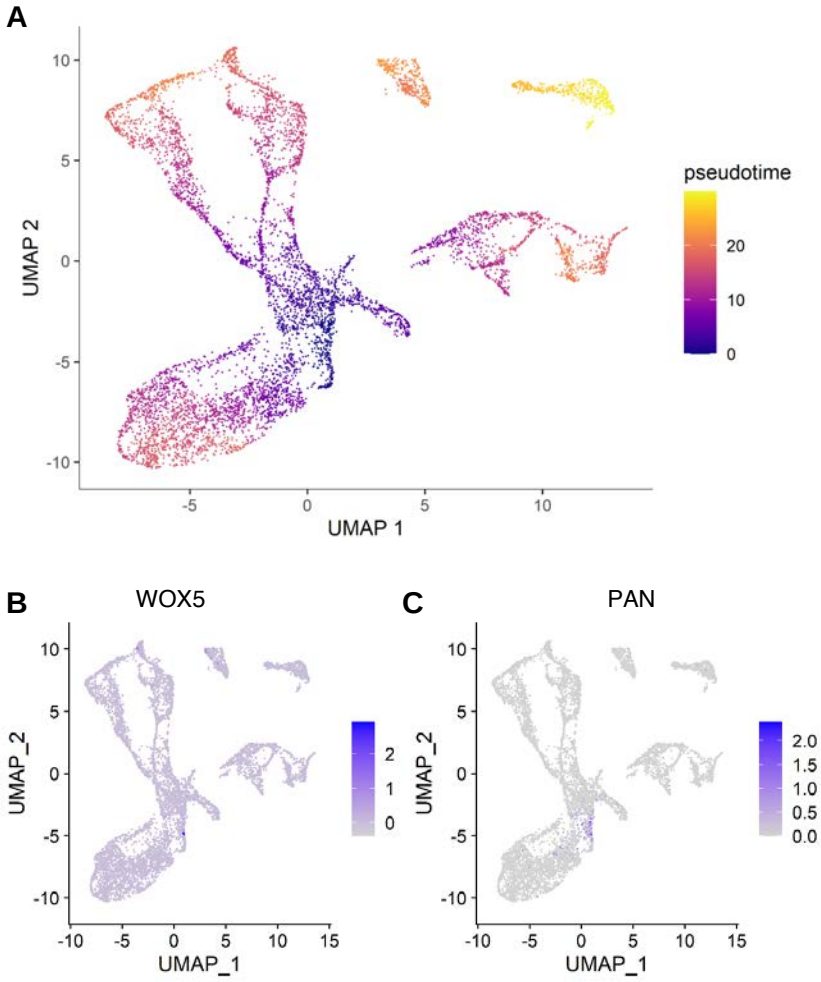

Figure 5.6: Pseudotime analysis of the integrated dataset.
A) Pseudotime analysis of the 8076 root cells. SCN and stele clusters correspond with cells positioned early in the pseudotime trajectory. B, C) WOX5 (B) and PAN (C) expression in the cells was used to specify stem cells as pseudotime 0.

Figure 6. Pseudotime analysis of the integrated dataset.
A) Pseudotime analysis of the 8076 root cells. SCN and stele clusters correspond with cells positioned early in the pseudotime trajectory.
B, C) WOX5 (B) and PAN (C) expression in the cells was used to specify stem cells as pseudotime 0.

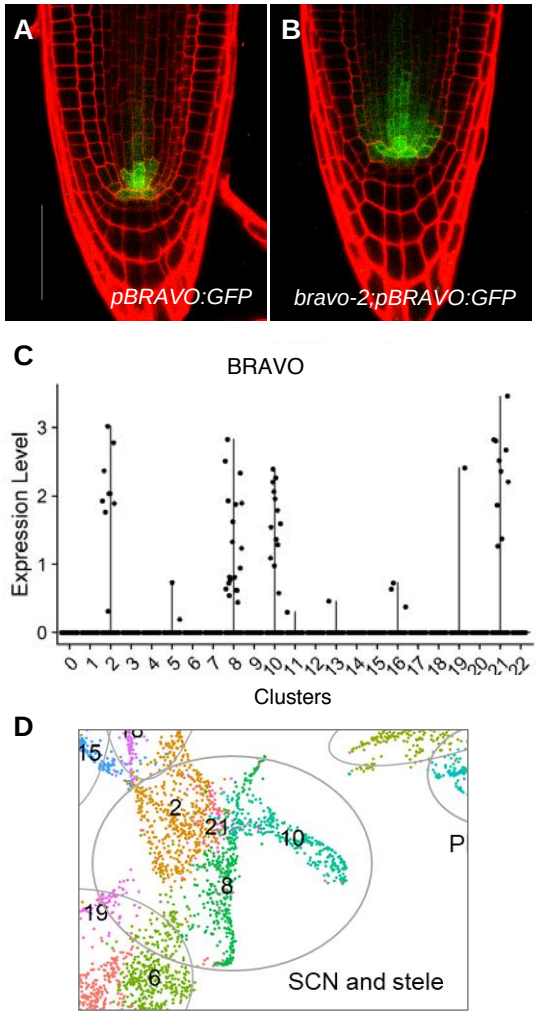

Figure 7: BRAVO is expressed in different stem cell populations. A, B) Confocal images of PI-stained 6-day-old pBRAVO:GFP (A) and pBRAVO:GFP;bravo (B) roots. GFP-tagged expression is shown in green. Scale bar: 50um. Images are the same showed in Figure pBRAVO chapterbravowox5. C) Expression of BRAVO in individual cells of the different clusters in the integrated dataset. D) Inset of Figure 4 indicating clusters 2, 8,10 and 21 where BRAVO is expressed that correspond to stem cell populations.

Figure 5.7: BRAVO is expressed in different stem cell populations. A, B) Confocal images of PI-stained 6-day-old pBRAVO:GFP (A) and pBRAVO:GFP;bravo (B) roots. GFP-tagged expression is shown in green. Scale bar: 50um. Images are the same showed in 3.5. C) Expression of BRAVO in individual cells of the different clusters in the integrated dataset. D) Inset of Figure 5.4 indicating clusters 2, 8,10 and 21 where BRAVO is expressed that correspond to stem cell populations.

clusters containing most of the cells expressing pBRAVO:GFP, annotated as SCN and stele in the root atlas (Table 5.1, Figure 5.3). Altogether, we concluded that pBRAVO domain can be separated in 4 different cell populations corresponding to clusters 2, 8, 10 and 21 (Figure 5.7 D).

To further characterize and assign identity to the 4 SCN populations identified, we evaluated the expression of QC and VI specific genes, the expression of cell division genes, and the defining genes of each cluster through GO enrichment analysis.

In order to identify QC and stele cells, the expression of known QC and stele genes was assessed (Denyer et al., 2019; Jean-Baptiste et al., 2019). For the QC, BRAVO, WOX5, AGL42, SCR, PAN, RGF8, TEL1, BBM and DUF9 gene expression was evaluated (Figure 5.8). For the stele, BRAVO, AHP6, ATHB15, SHR, WOL, ARF7, ROW1 and PHB gene expression was evaluated (Figure 5.9). QC genes were expressed mainly in clusters 8 and 10 (Figure 5.8), while stele genes were mostly observed in clusters 2 and 21 (Figure 5.9). Remarkably, in all clusters there was some expression of the other cell type marker genes, which indicated the presence of both cell types, whereas there is a clear predominant one. Although these results indicate differences between QC and stele cell populations, these differences are not sufficient to separate between clusters, thus suggesting that there might be some differences, as for example in developmental processes such as cell division.

The stem cell niche is characterized by the high mitotic rate of their cells, except the QC cells, which are the ones with the lowest rate that remain quiescent (Heyman et al., 2014). To further understand the cell division status of the 4 stem cell populations identified, we evaluated the expression

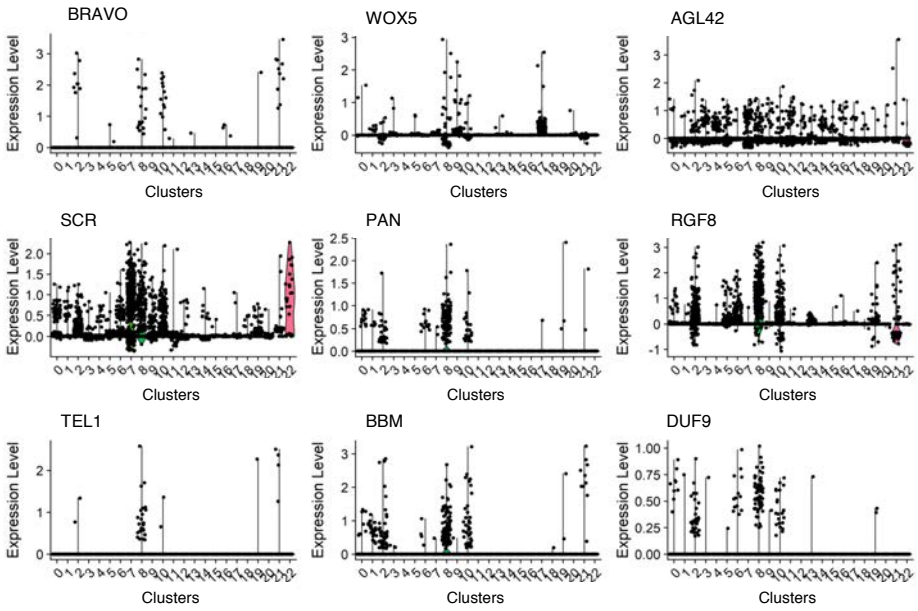

Figure 5.8: Clusters 8 and 10 have more QC identity.
Expression of genes expressed in the QC in individual cells of the different clusters in the integrated dataset.

Figure 8. Clusters 8 and 10 have more QC identity.
Expression of genes expressed in the QC in individual cells of the different clusters in the integrated dataset.

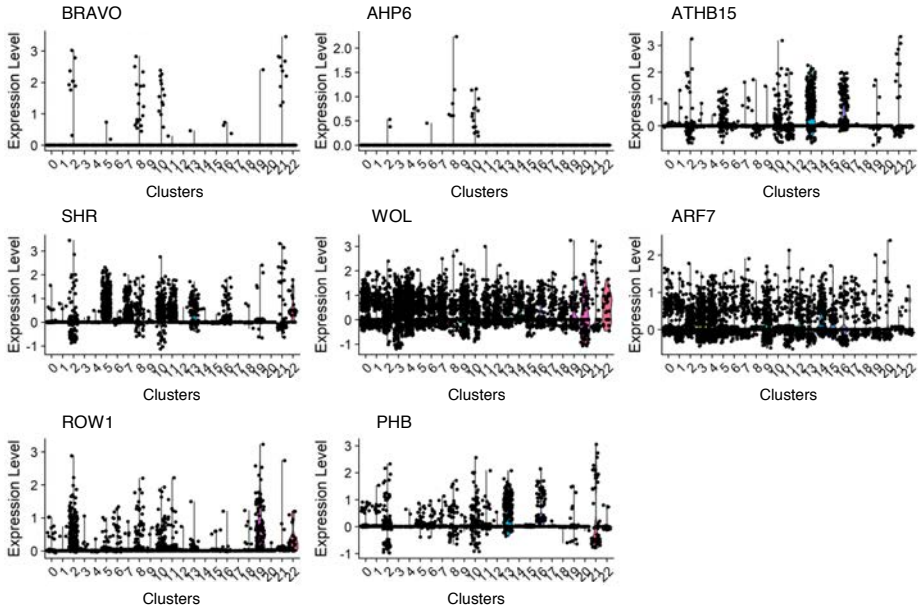

Figure 5.9: Clusters 9 and 21 have more stele identity.
Expression of genes expressed in the stele in individual cells of the different clusters in the integrated dataset.

Figure 9. Clusters 9 and 21 have more stele identity.
Expression of genes expressed in the stele in individual cells of the different clusters in the integrated dataset.

of cell cycle related genes (Torii et al. (2020), Figure 5.10). The cell cycle can be divided in different stages: G1 corresponding to the gap between mitosis and DNA replication, S to the DNA replication, G2 to the gap between DNA replication and mitosis, and M to the mitosis and cytokinesis (Gutierrez, 2009).

The analysis of stage-specific gene expression in the integrated dataset revealed a clear enrichment of genes related to G2 and M phases in cluster 10 cells (Figure 5.10 A). The higher levels of expression of S phase genes was found in cells from clusters 21, 2 and 10 (Figure 5.10 B). As for G1 phase, any cluster with higher expression of those genes was found (Figure 5.10 C). These results highlight the molecular signature of the stem cells in terms of cell division genes, as cell cycle genes are more express in stem cells than in the rest of root cells (Figure 5.10). Our analysis indicates that cluster 2 contains cells in S phase, cluster 10 in G2/M and S phases, and cluster 21 in S phase of the cell cycle. Clusters 2 and 21 showed mainly VI identity (Figure 5.8), although cluster 21 presented higher expression of G2/M and G1 phase genes than cluster 2 (Figure 5.10).

To finely differentiate the four stem cell populations, we analyzed the genes that distinguish one population from the others (called marker genes). We first compared each cluster to the whole root atlas and we found 878 genes marker genes for cluster 2, 1007 for cluster 8, 1061 for cluster 10 and 1708 for cluster 21 (Figure 5.11 A). To focus on the stem cell niche, we also compared each cluster against the other three and we found 163 marker genes for cluster 2, 441 for cluster 8, 171 for cluster 10 and 995 for cluster 21 (Figure 5.11 B). This indicated that clusters 8 and specially 21 presented a more unique transcriptional profile, as the number of marker genes was higher.

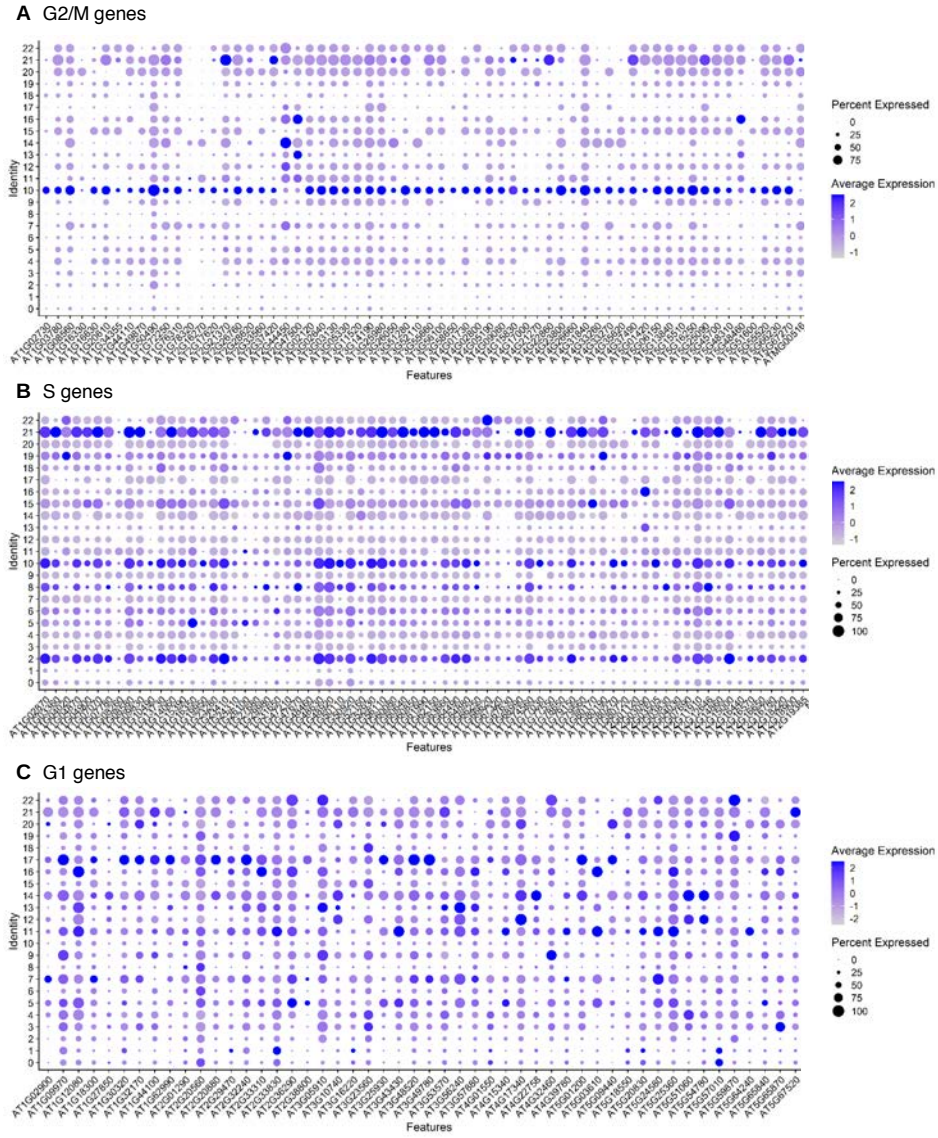

Figure 10. Expression of cell cycle-stage-specific genes in the integrated dataset.
Expression of cell cycle stage-specific genes from Torii2020 in the different clusters of the integrated dataset. Dot diameter indicates the proportion of cluster cells expressing a given gene, and color indicates the mean expression across cells in that cluster.

Figure 5.10: Expression of cell cycle stage-specific genes in the integrated dataset.
Expression of cell cycle stage-specific genes from Torii et al. (2020) in the different clusters of the integrated dataset. Dot diameter indicates the proportion of cluster cells expressing a given gene, and color indicates the mean expression across cells in that cluster.

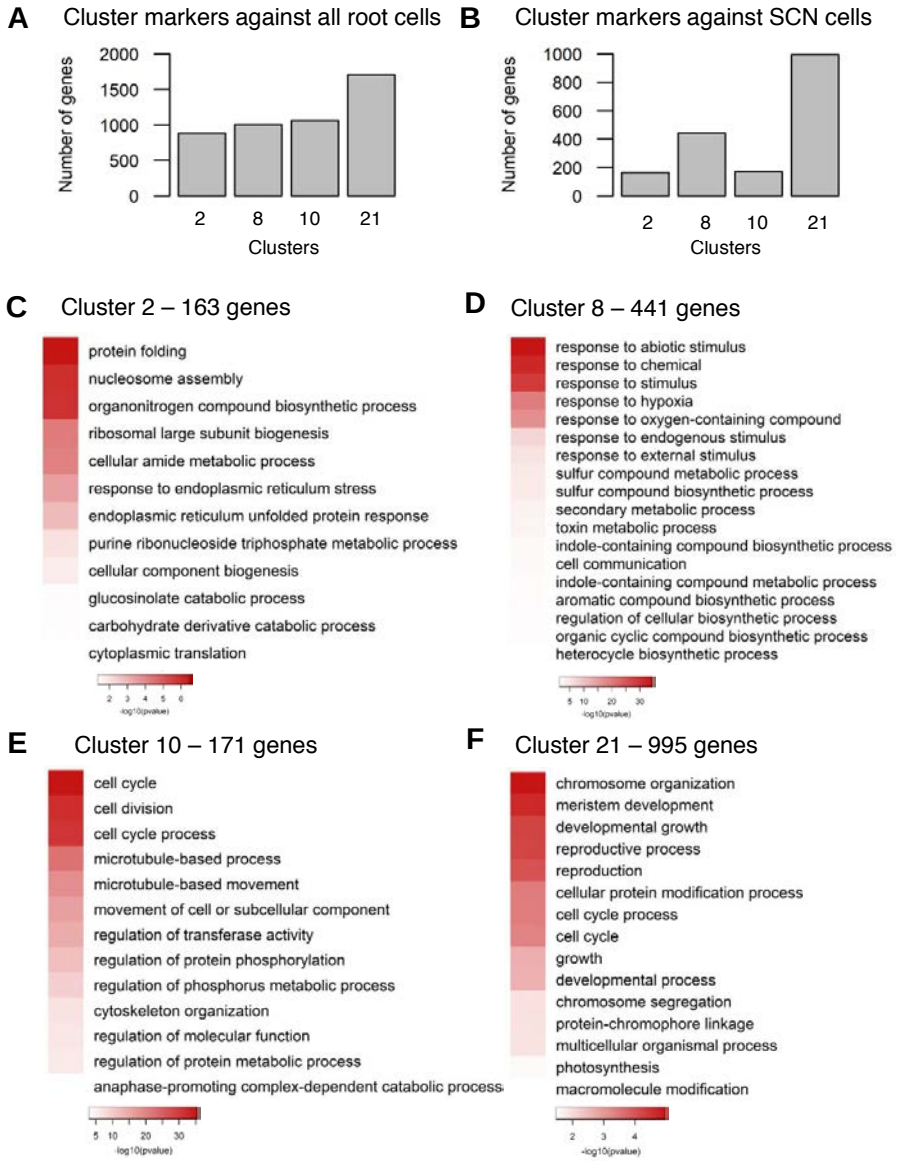

Figure 5.11: Cluster marker gene number and GO analysis of the different stem cell populations.

Figure 11. Cluster marker gene number and GO analysis of the stem cell populations.
A, B) Number of cluster marker genes for clusters 2, 8, 10 and 21 from the integrated dataset calculated against rest of cells of all tissues (A) and against rest of SCN cells (B). C – F) GO enrichment analysis of cluster marker genes for cluster 2 (C), 8 (D), 10 (E) and 21 (F) against rest of SCN clusters. GO enrichment performed in Araport thalemine, selected categories with pvalue < 0.05 in HolmBonferroni test. Category redundancy was reduced with REVIGO 0.5.

To find out the molecular process that characterize each population, GO enrichment analysis of the marker genes that distinguish each population in the stem cell niche was performed (Figure 5.11 C-F). Each cluster showed enrichment in categories related to different processes: cluster 2 related to protein processes such as protein folding and nucleosome assembly (Figure 5.11 C), cluster 8 related to different stresses response (Figure 5.11 D), cluster 10 related to cell cycle and cell division (Figure 5.11 E), and cluster 21 related to cell division and meristem development (Figure 5.11 F). These results highlight the differences between the 4 stem cell populations, as their cluster marker genes were involved in distinct molecular processes.

Overall, our computational approach permitted the identification of four different stem cell populations with unique molecular characteristics:

(i) Cluster 2 cells showed higher stele identity, expression of cell cycle genes from phase S and enrichment in protein synthesis GO categories. This suggested that they were mostly stele cells that activate the machinery required for division (in phase S of the cell cycle).

(ii) Cluster 8 corresponded mostly to QC cells and showed enrichment in genes involved in response to different stimulus. Cluster markers of this population failed to show enrichment in any cell cycle stage. These results suggest that cluster 8 cells were in a quiescent state ready to divide if some stimulus appears.

(iii) Cluster 10 cells have both QC and stele identity, and they show high expression of cell division genes mostly involved in G2/M phase of the cell cycle. This suggest that these cells are probably dividing and stating to differentiate from QC to vascular initial cells and from vascular initial

cells to vascular cells.

(iv) Cluster 21 contained mainly stele cells expressing cell cycle genes from S phase. Their distinctive genes were involved in several processes such as cell division, chromosome segregation and meristem development; and the number of those distinctive genes is the highest. These results pointed to a unique population of stele cells with well-defined molecular features different from the rest of stem cells.

Clustering analysis and functional annotation of the transcriptional profile of stem cells allowed us to identify different stem cell populations, mainly through their cell type and cell division status. We proposed that cluster 8 were undivided QC, cluster 10 were divided QC or newly formed VI cells, and cluster 21 and 2 were more differentiated VI cells. These populations might be representative of different stages of stem cell development, from more quiescent to more mature stem cells.

Overall, we were able to identify quiescent QC (cluster 8) cells, mitotic QC and stele cells (cluster 10) and phase-S stele cells with abundant protein synthesis processes (cluster 2). Interestingly, cluster 21 presented unique characteristics both in the cell cycle state and in the molecular processes in which their genes were involved, so we decided to further investigate this specific population.

5.5 Identification of a novel vascular stem cell population

To further investigate the molecular signatures of the identified stem cell populations, the tissue-specificity the cluster marker genes was evaluated. TOTEM tool was used to calculate if the markers identified as distinctive of the SCN populations are enriched in any tissue of the Arabidopsis root (Lozano-Elena et al., unpublished). This tool incorporates cell-type specific datasets from both radial and longitudinal sections (Brady et al., 2007) and allows the inference of enrichment in particular tissues and developmental stages of the root. The obtained results informed about specific tissues that are more abundant in each cluster (Figure 5.12).

Tissue-enrichment analysis revealed that marker genes from cluster 2 were enriched in the provascular and epidermis tissues (Figure 5.12 A), from cluster 8 in the QC and columella (Figure 5.12 B), and from cluster 10 in the vascular initials (Figure 5.12 C). These findings were in agreement with the previously assigned QC and stele identity of clusters 2, 8 and 10 cells, based on the expression of QC and stele markers (Figures 5.8 and 5.9). Interestingly, cluster 21 cells presented enrichment in the VI area, specifically in the central section, that is unique in comparison to clusters 2 and 10 (Figure 5.12 D). Also, the cluster 21 tissue-enrichment analysis did not show a clear enrichment in any specific cell type, even when several of them were represented, especially phloem and xylem related tissues (Figure 5.12 D). These results might indicate that cluster 21 cells were in an undifferentiated state, or that their marker genes have not been associated to a known cell type yet.

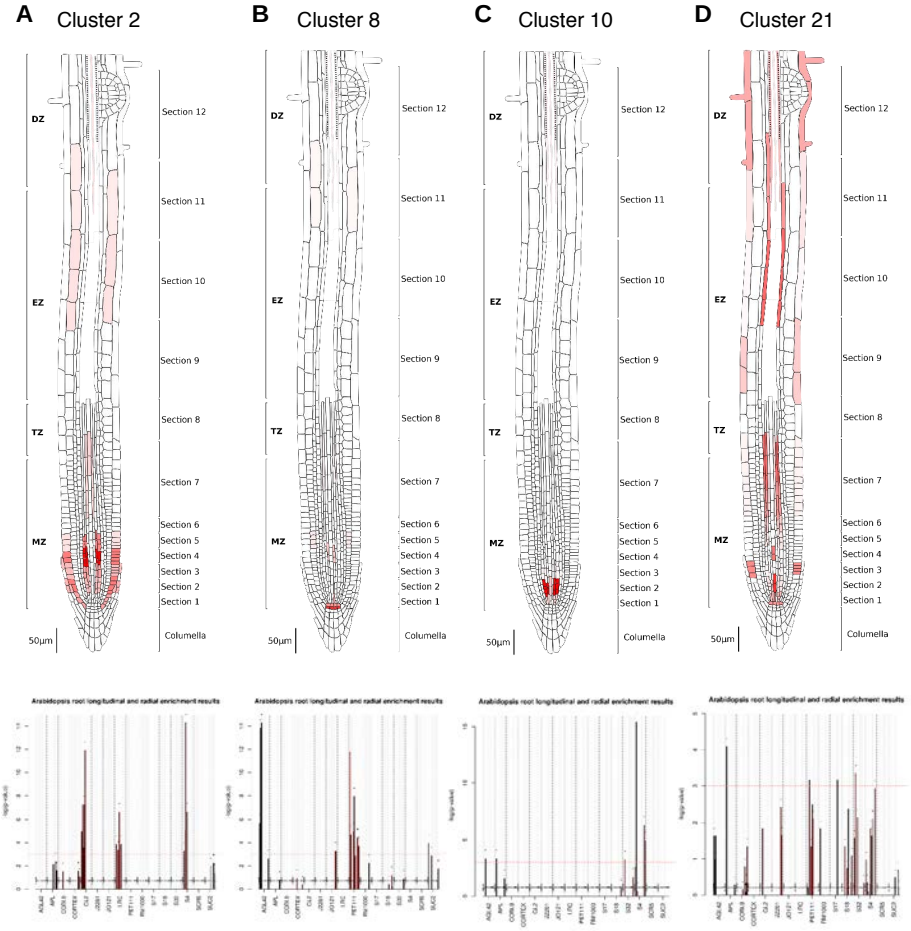

Figure 5.12: Tissue-specific enrichment of cluster marker genes. Results from TOTEM software indicating tissue-specific enrichment for cluster 2 (A), 8 (B), 10 (C) and 21 (D) against rest of SCN clusters. AGL42: Quiescent center, ARL: Phloem + companion cells, COBL9: Root hair cells, CORTEX: Cortex, GL2: non-hair cells, J2261: Pericycle, JO121: Xylem pole pericycle, LRC: Laterac root cap, PET111: Columella, RM1000: Lateral root primordia, S17: Phloem pole pericycle, S18: Maturing xylem, S32: Protophloem, S4: Developing xylem, SCR5: Endodermis, SUC2: phloem companion cells.

Figure 12. Tissue-specific enrichment of cluster marker genes.
Results from TOTEM software indicating tissue-specific enrichment for cluster 2 (A), 8 (B), 10 (C) and 21 (D) against rest of SCN clusters. AGL42: Quiescent center, ARL: Phloem + companion cells, COBL9: Root hair cells, CORTEX: Cortex, GL2: non-hair cells, J2261: Pericycle, JO121: Xylem pole pericycle, LRC: Laterac root cap, PET111: Columella, RM1000: Lateral root primordia, S17: Phloem pole pericycle, S18: Maturing xylem, S32: Protophloem, S4: Developing xylem, SCR5: Endodermis, SUC2: phloem companion cells.

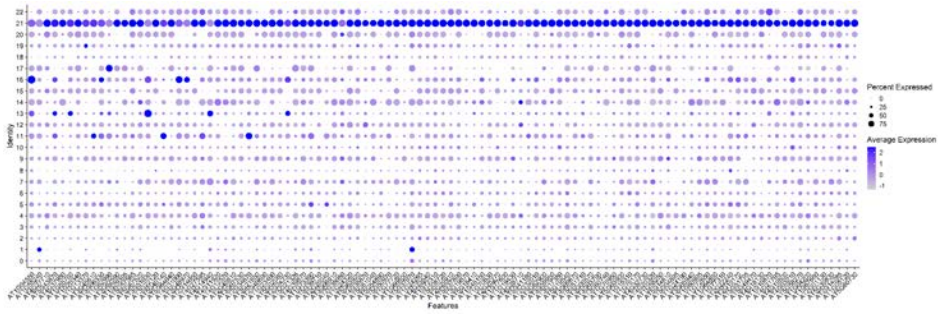

Figure 5.13: Expression of cluster 21 marker genes.
Expression of the 107 marker genes that show more unique expression in cluster 21 compared to the rest of clusters. Dot diameter indicates the proportion of cluster cells expressing a given gene, and color indicates the mean expression across cells in that cluster.

Figure 13. Expression of cluster 21 marker genes.
Expression of the 107 marker genes that showmore unique expression in cluster 21 compared to the rest of clusters. Dot diameter indicates the proportion of cluster cells expressing a given gene, and color indicates the mean expression across cells in that cluster.

Due to the unique features of cluster 21 cells, we decided to investigate the marker genes that differentiate this population from the others. To achieve this, genes that were more expressed in cluster 21 cells than in other clusters were manually selected. A total number of 107 genes were found to be clearly enriched in this cluster (Figure 5.13), some of which have already been characterized, for example BODENLOS (BDL), DNA-DAMAGE-REPAIR/TOLERATION PROTEIN 112 (DRT112), SIN3-LIKE 3 (SNL3), SABRE (SAB), KNOTTED-LIKE HOMEOBOX OF ARABIDOPSIS THALIANA 7 (KNAT7), UB-LIKE PROTEASE 1A (ULP1A), DOF TRANSCRIPTION FACTOR 6 (DOF6), TITAN 1 (TTN1), CELL CYCLE SWITCH PROTEIN 52 A2 (CCS52A2), AMINE OXIDASE1 (AO1) and PIN2 PROMOTER BINDING PROTEIN 1 (PPP1).

BDL is involved in cell specification and organogenesis (Hamann1999, Weijers et al., 2006, De Smet et al., 2010). DRT112 (PETE2) encodes a plastocyanin that functions in copper homeostasis (Abdel-Ghany, 2009).

SNL3 is involved in the regulation of transcription and genome stability (Bowen et al., 2010). SAB is involved for cortical microtubule orientation during cell elongation and polarity (Pietra et al., 2013) and in root epidermal hair cell patterning (Pietra et al., 2015). KNAT7 is a regulator of secondary wall biosynthesis (Li et al., 2012). ULP1A encodes a SUMO protease (Srivastava et al., 2020). DOF6 is involved in radial growth (Miyashima et al., 2019). TTN1 is related to cytoskeleton organization (Liu and Meinke, 1998). CCS52A2 (FZR1) is required for meristem organization and stem cell maintenance (Vanstraelen et al., 2009). AO1 encodes an amine oxidase involved in protoxylem differentiation (Ghuge et al., 2015). PPP1 is a regulator of PIN expression (Benjamins et al., 2016). The rest of the genes have not been characterized yet but have research potential as they show preferential expression in a very specific vascular stem cell population.

Analysis of the function of the 107 cluster 21 marker genes through GO enrichment analysis did not reveal any enrichment. However, the described function of the characterized genes suggests functions such as stem cell development, cell polarity, radial growth and vascular development. These processes are related to the nature of the provascular cells, as they divide anticlinaly and periclinaly and differentiate to form the vascular tissues (Scheres et al., 1995; Mähönen et al., 2000; Bishopp et al., 2011).

In conclusion, we propose that cluster 21 cells are a novel cell type corresponding to the vascular stem cells located just above the QC and in the middle section of the root, based on the following criteria:

(i) Cluster 21 was enriched in pBRAVO:GFP cells (Table 5.1). We used FACS for the isolation of specific cells, so the stem cells showing GFP

expression were selected in the cytometer. As shown in figure 5.5, the GFP expression in the SCN was higher in the cell located in the center of the VI just above the QC. When performing FACS, it is more probable to select these cells due to its higher GFP intensity, which explains the high number of these cells we found. In Denyer et al. (2019) and Jean-Baptiste et al. (2019), the population of this cell type was too small, so it was not recognized as one individual cluster.

(ii) Cluster 21 corresponded to stele cells because it expressed genes previously described as stele specific (Figure 5.9) and some of their marker genes were vascular specific such as BDL, KNAT7 and DOF6 (Figure 5.13).

(iii) Cluster 21 showed expression of genes involved in cell cycle in all stages, indicating that this population had molecular signatures different than cell cycle status that make them unique.

5.6 Deciphering the role of BRAVO in the stem cell niche with single-cell resolution

Our approach allowed the identification of different stem cell populations within the BRAVO expression domain. In addition, our experimental set up also included cells in WT and bravo mutant background with the objective of identifying the role of BRAVO in those different populations. To characterize the role of BRAVO, differential expression analysis between WT and *bravo* RNAseqs were performed in the distinct clusters of the integrated dataset containing SCN cells (2, 8, 10 and 21).

Our differential expression analysis yielded a low number of significant deregulated genes, probably due to the low cell number we obtained in each cluster, as sample size has been described as a key factor in this analysis (Soneson and Robinson, 2018). The gene expression analysis to compare bravo to WT cells, from either our data or published datasets, did not show differential expression in any of the analyzed cluster, except for 6 genes from cluster 21 (Table 5.2). In this case, cluster 21 showed the highest number of WT and *bravo* cells from our experiment: 42 and 24 cells respectively, and 13 WT cells from Denyer et al. (2019) and Jean-Baptiste et al. (2019) datasets.

Table 5.2: *BRAVO* regulated genes in cluster 21.

ATG	Name	LogFC *bravo* against WT	Adjusted p-value
AT2G02910	-	-0.30	0.0071
AT1G68310	AE7	0.26	0.0099
AT4G23540	-	0.64	0.0149
AT5G52810	SARD4	0.29	0.0213
AT1G76510	ARID4	0.25	0.0214
AT5G11380	DXS3	-0.88	0.0223

The 6 genes that were differentially expressed between *bravo* and WT cells are AT2G02910, AT1G68310 (AE7), AT4G23540, AT5G52810 (SARD4), AT1G76510 (ARID4) and AT5G11380 (DXS3) (Table 5.2). The genes more expressed in *bravo* were AE7, AT4G23540, SARD4 and ARID4, while the less expressed were AT2G02910 and DXPS3. The function of these six genes has been previously described: AE7 has been involved in nuclear genome integrity (Luo et al., 2012); SARD4 in Pipecolic acid biosynthesis for defense responses (Ding et al., 2016); DXPS3 was described as a putative 1-deoxy-D-xylulose 5-phosphate synthase (Carretero-Paulet et al., 2013); and AT4G23540, ARID4, and AT2G02910 remain

uncharacterized.

Altogether, we have found BRAVO regulated genes in the stem cell population of cluster 21 with single-cell resolution. Interestingly, among these genes is AE7 that have been involved in genome integrity, a key function of vascular initial cells for the arrest of cell cycle after damage stress (Luo et al., 2012). This might indicate a role of BRAVO in damage responses processes in the VI cells (Vilarrasa-Blasi et al., 2014). Unfortunately, we were unable to identify BRAVO regulated genes in other cell populations due to the low number of sequenced cells.

5.7 Future perspectives

In this chapter we generated a single-cell RNAseq atlas of the stem cell niche. Further analysis would help to elucidate the molecular signatures of the stem cells and the role of BRAVO in the different populations. To continue with this analysis, the following approaches are proposed:

- To increase the number of WT and *bravo* cells to identify differentially expressed genes in the different SCN subpopulations identified in this chapter.
- To perform Pseudotime analysis to identify possible developmental branches within the stem cells.
- To complete the integrated dataset with the use of published datasets containing more root cells data. Recently, in Wendrich et al. (2020) a complete atlas with data from more than 15000 cells was published, including a high number of initial cells. This study indicates

the separation of the initials based on the tissue that are going to develop, hence combining this data with ours might allow us to separate initial cell populations based on their cell type.

- To increase the number of pSUC2:BRL3:GFP and pSUC2:BRL3:GFP;*brl3-2* cells for the analysis to investigate the role of BRL3 in the phloem with single cell resolution.

- To validate experimentally our computational analysis in order to identify key molecular components of the stem cell niche involved in stem cell division and differentiation.

Chapter 6

General Discussion

General Discussion

The root stem cell niche is essential for plant growth and development. In the last years, several studies in the plant model Arabidopsis have started to shed light on the molecular mechanisms for stem cell division, differentiation and the maintenance of stem cell pools both in roots and shoots. Those advances are mostly linked to the development of new technologies that allow precise analysis of small cell populations. The present PhD dissertation advances in the molecular understanding of stem cell development in plants by focusing on the study of BRAVO, a root stem-cell specific transcription factor.

In chapter 2, we presented MyROOT software for the semiautomatic quantification of plant root length. In chapter 3, we used multidisciplinary approaches to unveil the role for BRAVO and WOX5 together in root growth and development. In chapter 4, we evaluated the transcriptomic impact of BRs and BRAVO in the QC and VI cells with cell-type resolutions. In chapter 5, we described the use of single-cell technology for the characterization of the root stem cell niche populations.

6.1 MyROOT software facilitates Arabidopsis primary root length measurements

Despite the existence of several softwares (Table 2.1), MyROOT covers a gap for the analysis of Arabidopsis seedling that was not addressed before. The determination of root length in such accuracy is key in the study of plant growth and developmental processes, where small root difference can lead to the identification of important genes (Benfey et al., 1993; Li et al., 2001; Mouchel et al., 2004; Rodrigues et al., 2009). We found that the implementation of primary root phenotyping algorithms in a platform independent, semi-automatic and user-friendly software to accurately measure root length achieved by using MyROOT will replace the so far used manual and time-consuming tools such as ImageJ.

MyROOT operates fast without losing accuracy in the final results

We confirmed that MyROOT gives the most precise root length measurements when compared with the more similar softwares BRAT and EZ-Rhizo (Table 2.2 and Figure 2.10). Remarkably, the accuracy is maintained both in the manual and in the batch processing mode of MyROOT (Figure 2.5 and 2.7), being therefore suitable for low-scale and high throughput experiments. The time required for this task is considerably reduced when using MyROOT compared to most of the softwares evaluated (Figure 2.6 and Table 2.2). In our experimental conditions, only BRAT operates in a faster manner, whereas the final results are less accurate (Table 2.2 and Figure 2.10). This can be explained because of

the limited control that BRAT offers for the adjustment of its internal parameters by the users to adapt to different imaging conditions, which may result in low root detection rates (Table 2.2). On the other hand, MyROOT easily allows the modification of different thresholds (scale and root mask threshold and hypocotyl detection method) to define the optimal parameters for the analysis.

MyROOT workflow allows adaptability to different experimental conditions

One of the main limitation of existing softwares is the adaptability to different experimental conditions, which limits the use of current tools. This fact explains the use of ImageJ, which is simple and easy to implement in any type of plant images. With this in mind, MyROOT was developed to adapt to several conditions in terms of scale, seedlings and hypocotyls detection.

A novel feature of MyROOT compared to existing softwares is the ability to automatically identify the scale by detecting a ruler over the imaged plate (Figure 2.3); thus being able to automatically adapt to different imaging conditions and settings; and therefore being able to work independently from specific hardware set ups (Table 2.1).

MyROOT2, the updated version of MyROOT, allows the manual and automatic identification of the seedlings over the plate (Figure 2.11). This feature enables the analysis of images with seedling located all over the plate, which might be relevant in different experimental set ups.

MyROOT software uses machine learning based algorithms to identify

Arabidopsis hypocotyls, which allows its identification in different mutants and experimental conditions even when they are overlapped or present different morphologies (Figure 2.9). In exceptional cases in which the hypocotyls are not automatically identified, or in the case that the software is used for the analysis of other plant species, they can be manually indicated by simply pointing over them. Machine learning has been recently started to be implemented in plant image analysis softwares as it allows precise identification of the plant over the image. This methodology has been already included in tools for the analyssis of complex root architecture systems and hypocotyls (Yasrab et al., 2019; Dobos et al., 2019).

In addition to the automatic processing of several images, MyROOT allows the user supervision during all the process. It displays intermediate results during the analysis and allows the modification of different parameters to get the optimal results. Despite that MyROOT only indicates the primary root length, the output is also saved in RSML format which allows its compatibility with other softwares that can determine other aspects of root architecture such as curvature or branching (Lobet et al., 2015).

Overall, we advanced the utility of MyROOT for the determination of Arabidopsis root length in a precise, fast and simple manner. It incorporates powerful algorithms for the identification of the scale and the seedlings over standard images of agar plates. They are incorporated in a user-friendly graphical interface that allows its supervision and manipulation during the different steps of the analysis.

Finally, MyROOT is a modularly designed software consisting of a group of specialized algorithms able to detect and analyze the measuring tape,

detect the roots, track the roots in a bottom-up fashion, and detect the hypocotyls. Therefore, any improvement to any of these components, or new algorithms for the determination of other features, can be easily included in subsequent versions of MyROOT. Examples of future improvements that could be included are the development of daily growth-monitoring algorithms that permit the detection of abnormal root growth patterns, the analysis of root system architecture beyond the primary root, and the identification of hypocotyls from other plant species. In the future, upgraded versions of our software could consist of a completely automatic operation connected to high-throughput facilities for massive characterization of root traits.

6.2 BRAVO and WOX5 interplay in the stem cell niche controls quiescence

In the Arabidopsis primary root apex, BRAVO and WOX5 are two transcription factors whose expressions co-localize mostly at the QC cells where they repress their divisions (Vilarrasa-Blasi et al., 2014; Forzani et al., 2014). In chapter 3, we used a multidisciplinary approach combining experimental data with mathematical modeling to show that BRAVO and WOX5 interplay at different levels to repress QC divisions. In addition, we show that the joint action of these cell-specific transcription factors promotes overall root growth and development.

BRAVO and WOX5 expression are mutually regulated

Our results indicate that BRAVO and WOX5 mutually promote each other expression. In WOX5 mutant and overexpressor plants, *BRAVO* expression is decreased and enhanced, respectively, compared to WT plants (Figures 3.5 and 3.6); supporting that WOX5 activates *BRAVO* expression. In BRAVO overexpression and loss-of-function mutant plants, *WOX5* expression is decreased and unaltered, respectively (Figures 3.8 and 3.9). These observations denote that neither of both TFs is downstream the other, as their mutual regulations are very distinct. We also found that BRAVO and WOX5 have a self-regulation as their expression levels are higher in their own mutant background (Figures 3.5 and 3.8). Altogether, we can infer that while WOX5 is able to induce *BRAVO*, BRAVO does not directly induce *WOX5* expression, but it drives partial inhibition of WOX5 self-regulation. These different regulatory mechanisms and the quantitative changes in gene expression they drive, suggest that the effect of WOX5 on *BRAVO* and thereby on BRAVO-mediated regulation can be more relevant than the effect BRAVO has upon *WOX5* and WOX5-mediated action.

BRAVO and WOX5 interact

Another important molecular link between BRAVO and WOX5 as revealed by our data is their physical protein-protein interaction (3.13). Major co-localization of BRAVO and WOX5 transcription factors in the QC suggest that they act as co-partners of a single complex particularly in the QC, where they converge. These confirmed protein interactions, together with the expression data, can be used to propose the mechanism

driving BRAVO and WOX5 circuit.

The mutual regulation between BRAVO and WOX5 involves WOX5 self-inhibition while it induces the expression of *BRAVO*, which in turn reverses WOX5 self-repression. Based on our data, it can be suggested that *WOX5* self-inhibition is through WOX5 bound to TPL and that BRAVO attenuates it by competing with TPL for binding WOX5. Moreover, BRAVO is found to ultimately down-regulate its own expression, although this probably occurs through other intermediate molecules, as BRAVO has been shown to activate itself by directly binding its own promoter (Vilarrasa-Blasi et al., 2014). By evaluating expression changes between the WT and the mutants we gained information on the overall BRAVO-WOX5 regulatory system. Its regulation results from the direct binding of these proteins to their promoters and from the transcriptional control driven by them, as far as these proteins bind each other and to additional regulators. Hence, interactions here described are effective since that they are the result of multiple, direct and indirect, regulatory mechanisms. For instance, *WOX5* self-repression can also involve a negative feedback where WOX5 activates a repressor or represses an activator, among other possibilities. In this context, control of auxin-ARF and auxin-IAA (Tian et al., 2014) as well as the PLETHORA genes (Burkart et al., 2019) were all shown to involve negative feedbacks with *WOX5*. WOX5 induction of *BRAVO* expression could be as well through a downstream target of WOX5.

Relevance of BRAVO and WOX5 molecular circuit in root growth and development

Both BRAVO and WOX5 transcription factors are repressors of QC divisions (Vilarrasa-Blasi et al., 2014; Forzani et al., 2014). We found similar phenotypes of higher percentage of divided QC cells in all *bravo*, *wox5* and *bravo wox5* double mutants, thus pointing to an interdependently function in this process (Figure 3.1). The finding that the effect of WOX5 on *BRAVO* is more relevant than the effect of BRAVO upon *WOX5* is consistent with the known SCN phenotypes of *bravo* and *wox5* mutants (Bennett et al., 2014; Forzani et al., 2014; Pi et al., 2015; Sarkar et al., 2007; Vilarrasa-Blasi et al., 2014), where *wox5* exhibits, besides a similar increased QC division phenotype as *bravo*, an overall distorted and disorganized SCN morphology and CSC premature differentiation that is absent in the *bravo* mutant (Figure 3.1).

Our analysis supports that QC division is controlled via BRAVO-WOX5 joint regulation, besides an additional regulation individually mediated by BRAVO. This joint regulation is expected to be mediated by BRAVO-WOX5 physical interaction. This scenario explains the phenotype of increased divisions at the QC upon BL treatment (González-García et al., 2011), by the response of BRAVO and WOX5 to this treatment and their respective roles as repressors of QC divisions. Actually, although the intensity and domain of expression of WOX5 increases in roots grown in BL medium, at the same time the BL treatment strongly represses BRAVO (Vilarrasa-Blasi et al., 2014). Hence, in the absence of its partner BRAVO, WOX5 no longer represses QC divisions in roots grown on BL. At a mechanistic level, the BRAVO-WOX5 protein complex may bind CYCLIN-D3:3,

as shown to occur for WOX5 (Forzani et al., 2014).

Interestingly, we also described that BRAVO and WOX5 promote root growth and lateral root development (Figures 3.2 and 3.3). We found that double mutant *bravo wox5* have a more exaggerated reduction in LR(s) density than the single mutants, which also have lower values of this parameter compared to the WT (Figure 3.3). In LR development, the formation of the organizing center and the stem cell niche occurs after LR initiation (Banda et al., 2019). A high number of genes are commonly expressed at the SCN of primary and LRs, such as *WOX5*, *PLT*, *SHR*, *SCR* or *TCP* (Goh et al., 2016; Shimotohno et al., 2018). Loss-of function of these genes leads to an increased number of aberrant lateral roots and reduced levels of *WOX5* (Shimotohno et al., 2018), and thus it is possible that BRAVO/WOX5 complex not only controls stem cell niche maintenance in the primary root, but also in the LRs. The consistent and overlapping role of BRAVO and WOX5 at promoting lateral root development also points to a relevant role of the BRAVO-WOX5 complex for this function.

Our study also sets a framework for future studies on the interplay between WOX5 and BR signaling in the control of CSC differentiation. WOX5 is known to repress CSC differentiation (Pi et al., 2015; Sarkar et al., 2007). However, upon BL treatment, and in *bes1-D* gain of function mutants, CSC differentiate prematurely (González-García et al., 2011) in apparent contradiction with the inhibitory role associated with WOX5, and its induced expression in these roots. One option comes from assuming that BL-induced CSC differentiation is independent from WOX5 and overrides WOX5-mediated repression. In this case, a tug-of-war between WOX5-mediated repression and BL-dependent activation of CSC differentiation

would tip the balance in favor of BR-action. Another possibility is that BR downstream effectors such as BES1-D inactivate WOX5 and/or impede its function. An increase of BES1-D by BL may boost WOX5 sequestration into WOX5-BES1-D complexes, since we showed that WOX5 and BES1-D physically interact. Assuming these complexes inactivate WOX5 function, CSC differentiation would no longer be repressed by WOX5 in the presence of BL. Moreover, the fact that BES1-D directly interacts with TOPLESS, and this co-repressor is also recruited by WOX5 to the inhibition of CSC differentiation (Pi et al., 2015), suggest that in plants treated with BL WOX5 function may further be impaired by most of TPL being bound to BES1-D.

To conclude, understanding of signaling networks operating in stem cell development is becoming essential to decipher plant growth and adaptation to the environment. Systems biology approaches provide a closer picture to reality unveiling how complex and dynamics network of cell-specific transcription factors act to preserve stem cell function in plants. Here, untapping the action of two main regulators of quiescent cell division, BRAVO and WOX5, not only discloses that these factors operate as a transcriptional complex in preserving stem cell function, but also unravels their joint roles in primary and lateral root development.

6.3 BRAVO mediates different transcriptomic responses in the quiescent center and vascular initial cells

In the QC BRAVO regulates genes involved in root hair development

Our transcriptomic analysis described in Chapter 4 revealed different role of BRAVO in both cell types, indicating BRAVO functioning in regulating different aspects of plant development depending on the tissue in which it is expressed. In agreement with this observation, BRAVO is expressed in seeds where it affects seed development by controlling cell wall metabolism such as cell division and expansion (Zhang et al., 2013b). BRAVO is expressed in the Arabidopsis flowers and it acts as a negative regulator of flowering (Chen et al., 2014).

We unveiled novel roles in which BRAVO might be involved, being root hair development the most remarkable one, as higher enrichment was found in the BRAVO regulated genes in the QC (Figure 4.6). Interestingly, other R2R3-MYB proteins were found to be involved in this process too. One is WEREWOLF (WER) which is responsible for generating the pattern of root-hair and non-hair cell types during root development (Wang et al., 2019b). Other one is MEMBRANE-ANCHORED MYB (maMYB) which participates in root hair elongation in Arabidopsis (Slabaugh et al., 2011). Both genes are expressed in several tissues along the root. In the case of BRAVO, we found that it might be acting non-cell autonomously as the genes were found to be regulated from the QC.

Root hair development has two phases: determination of root hair identity and root hair elongation. If BRAVO impacts in one or the other phase would be interesting to address, as BRAVO might be acting as a regulator of cell fate or as a regulator of cell elongation. Our transcriptomic results revealing genes involved in ROS, cytoskeleton and cell wall related processes (Figure 4.4), together with the role of other MYBs transcription factor in cell wall processes, might point out BRAVO involved mostly root hair elongation, as the mentioned processes are key for proper elongation (Jones et al., 2006). Nevertheless, experimental validation is essential to confirm our findings.

In the VI BRAVO mediates flavonoid and ROS responses

A cell-type approach was used to decipher the role of BRAVO in the QC and VI separately. Our results indicate BRAVO is mediating different transcriptomic responses in both cell types. In the VI, BRAVO regulates a high number of genes cells and acts mostly as a repressor of transcription (Figure 4.3). On the other hand, any phenotype was found in the vascular initial cells in *bravo* mutant (Figure 4.1, Vilarrasa-Blasi et al. (2014). These findings can be explained with the presence of BRAVO homologs regulating similar responses in those tissues. For example, MYB52 and MYB54 are BRAVO closest homologs and they are expressed in the root vascular tissues (Zhong et al., 2008; Dubos et al., 2010).

In the vascular initial cells, one of the processes in which BRAVO seems to be involved is related to flavonoid biosynthesis. We found some genes that are also BL regulated (Figure 4.11), and TFs downstream BRAVO and BL implicated in these processes (Figure 4.13). In agreement with previous

studies, BRAVO regulates the accumulation of anthocyanins and flavonols in the root, as bravo mutants show reduced levels of both compounds (Jeong et al., 2018). Moreover, other R2R3-MYB transcription factors, MYB11, MYB12 and MUB111 are also regulating flavonol biosynthesis (Tan et al., 2019). Flavonols are a class of phenylpropanoids that act as scavengers of ROS (Agati et al., 2007; Agati and Tattini, 2010; Peer et al., 2013). They are synthesized in the endopasmic reticulum and transported to different organelles (Agati et al., 2012). In addition to their role in ROS homeostasis, they also contribute to the regulation of signaling cascades involved in cell growth and differentiation. For example, flavonols regulate auxin transport through impacting in the localization of PIN proteins (Peer and Murphy, 2007; Michniewicz et al., 2007; Adamowski and Friml, 2015). However, the significance of flavonols in auxin signaling and its interplay with ROS responses has not been elucidated yet (Jansen et al., 2001; Peer et al., 2011, 2013; Pollastri and Tattini, 2011; Zhang and Peer, 2017). The biosynthesis of flavonols is also promoted by ABA (Berli et al., 2010, 2011). Altogether, we suggest BRAVO to be regulating flavonoid metabolism. In agreement with that, we found BRAVO regulating an enriched group of genes related to ROS responses (Figure 4.12 A and B). If there is a direct link between BRAVO, ROS and flavonols is not known, neither what is the relevance of this in the vascular initial cells or whether it has an impact in root developmental responses.

Further studies regarding if this relation is mediating stress responses or developmental signaling cascades can be performed. Flavonoid biosynthesis is promoted by several abiotic stresses (Pollastri and Tattini, 2011), and some MYBs transcription factors have already been linked to these responses (Tan et al., 2019). BRs are perceived in the plasma membrane

by different receptors. BRI1 which shows ubiquitous expression and BRL1 and BRL3 which are enriched in the SCN and vascular tissues. It is proposed that BRI1 mediates responses that drive root growth and development, whereas BRL1/BRL3 are more involved in stress responses and adaptation (Planas-Riverola et al., 2019). If BRAVO role is acting downstream BRI1 or BRL1/BRL3 remains unknown, so further investigation in this aspect would indicate if it is mediating stress responses.

Identification of BRs and BRAVO downstream components

The overlap between BL and BRAVO datasets reveals that more than 55% and 75% of the BRAVO regulated genes are not downstream BL pathway in the QC and VI respectively. This accounts for other signaling pathways different to BRs controlling BRAVO expression in the stem cell niche. In agreement to that, BRAVO expression is induced in seedlings after sucrose treatment and after ethylene (Jeong et al., 2018). Moreover, to ensure stem cell niche homeostasis, it is controlled by several signaling pathways (Aida et al., 2004; Helariutta et al., 2000; Sabatini et al., 2003; Sarkar et al., 2007).

Our transcriptomic analysis combining BL and BRAVO regulated datasets allowed the identification of the TFs mediating BRAVO response downstream BR signaling pathway. It helped to redefine the function of several TFs in stem cell activity, as most of them have not been associated to the root apex before. These TFs can be used for the identification of the transcriptional network in the QC and VI. Those TFs might be forming part of the same transcription factor complex together with BRAVO. Our experimental conditions consisted in growing the plants for 2 hours in a

BL supplemented media. The BR-mediated response changes along time (Vilarrasa-Blasi et al., 2014), so further experimental data including time series of BL treatments would permit to create spatiotemporal networks orchestrated by BRs and BRAVO in the stem cell niche.

BRAVO is directly regulated by BES1, so some of the identified TFs might be direct targets too. We found a low number of those TFs being BES1 or BZR1 direct targets, as described in Yu et al. (2011) and He et al. (2005). However, the absence of a confirmed interaction can be due to the experimental procedures. Experiments to confirm possible direct interactions between BES1, BZR1 and the identified TFs might help to understand if they are forming part of the same transcriptional complex.

6.4 Analysis of the stem cells transcriptome with single-cell resolution

The use of single cell technologies in plants has been applied mostly to whole-root studies in which complete root transcriptomic atlas were generated (Ryu et al., 2019; Shulse et al., 2019; Denyer et al., 2019; Zhang et al., 2019; Jean-Baptiste et al., 2019; Shahan et al., 2020; Wendrich et al., 2020). These resources are incredible valuable for plant development studies as they include the molecular signatures of each major root cell type. Nevertheless, there is usually little information regarding stem cells, which are mostly treated as a whole population. The lack of information about stem cell can be due to the low number of cells compared to the rest of tissues, which makes them more difficult approachable.

To fill this gap, we decided to enrich the transcriptomic maps with high-

resolution information about the stem cells. For that, we used FACS in pBRAVO:GFP expressing roots to isolate only those cells corresponding to the stem cell niche. Our original transcriptomes from stem cells were then integrated with available whole-root datasets (Denyer et al., 2019; Jean-Baptiste et al., 2019). Altogether, we generated a high-resolution dataset to study molecular signatures of the stem cells. Single-cell methodology was used because it allows to identify rare cell populations and to perform Pseudotime analysis to analyze developmental trajectories.

Identification of four cell populations in the stem cell niche

Root stem cells are located in a very specific microenvironment in the root apical meristem. They have unique characteristics that make them remain in a low differentiated state able to divide and develop the mature tissues. The SCN is formed by the QC located in the center and surrounded by the initials (Figure 1.2). The QC has the lower division rate which is maintained due to the action of internal and external factors (Aida et al., 2004; Helariutta et al., 2000; Sabatini et al., 2003; Sarkar et al., 2007). However, some questions remain open regarding the transcriptomic signatures of the different stem cell populations. Here, we generated a single cell transcriptomic map of the stem cell niche to evaluate the different stem cell populations.

Our analysis indicated the stem cell niche to be divided in four distinct populations. Two populations of cells were found to be mostly QC cells. The first one is cluster 8 which correspond to the undivided QC. It remains in a more quiescent state and it is characterized by the presence of genes involved in response to different stimulus. Supporting our findings,

when analyzing WOX5 regulated genes in the QC (Figure 4.14), we found enrichment in similar categories than the ones in cluster 8 marker genes (Figure 5.11). WOX5 acts in maintaining the QC in a quiescent state (Sarkar et al., 2007).

The second QC populations is cluster 10 which corresponds to actively dividing QC cells, as they show enrichment in G2/M phase cell cycle genes (Figure 5.10 A). QC cells remain in a quiescent state to be able to divide when a stimulus occur, for example, after genotoxic damage (Lozano-Elena et al., 2018). This agrees with our findings of enriched set of genes involved in response to stresses. Overall, we were able to separate QC cells based on their cell division status. This can help to understand the molecular signatures that maintain the QC in an undifferentiated state and allows the study of the influence of certain genes or conditions in those cells in both developmental stages.

Other two populations were found to be mostly VI cells. The first one is cluster 2 showing enrichment in protein-related processes (Figure 5.11 C). The other one is cluster 21 showing enrichment in several processes such as “meristem development” or “cell cycle”. This can be explained because of the nature of the stem cells being actively dividing and starting to differentiate in the vascular tissues (van den Berg et al., 1997).

Importantly, when giving identity to the different clusters, all of them seem to have expression of both QC and stele markers, suggesting that separation between both cell types was not complete. Clusters 2 and 10 were the ones showing less differences respect to the other clusters in the SCN (Figure 5.11 B), so increasing the number of cells for the analysis would help to identify the signatures of those populations with

more accuracy. We cannot discard the option of cluster 10 containing also the newly formed VI cell which also shows high mitotic activity. In agreement to that, TOTEM results showed preferential tissue enrichment of cluster 10 marker genes in the vascular initial cells (Figure 5.12 C).

Altogether, we identified four populations of stem cells with the BRAVO expression domain and highlighted the molecular processes that distinguish them compared to the rest of stem cells. Further characterization of the genes enriched in each population would help to understand their function in root growth and development.

New molecular insights of the vascular initial cells

Vascular initial cells are little studied, so their specific characteristics and role for root growth and development remains unknown. In this thesis we provide new insights in the transcriptomic signatures of this cell population using FACS and cell-type and single-cell transcriptomic analysis.

In chapter 5, the identification of a novel VI population was described. It is cluster 21 which correspond mostly to cells obtained in our original single-cell experiment of isolating pBRAVO:GFP expressing cells (Table 5.1). This observation, together with the higher intensity of pBRAVO:GFP in the VI cells just above the QC (Figure 3.5), pointed us to assign this cluster 21 features to those cells.

Deeper analysis of cluster 21 marker genes was done to analyze the function of those genes. Remarkably, a very low number of them were already characterized. We found some genes involved mainly in cell division and vascular development processes, which agrees with the nature of those

cells. One of the genes is DOF6 that has been involved in radial growth (Miyashima et al., 2019). Therefore, a complete analysis of these genes, and specifically the ones involved in cell division, would reveal genes involved both in periclinal and anticlinal divisions, being both types required for vascular development (De Rybel et al., 2013; Hardtke and Berleth, 1998). Most of the marker genes remain uncharacterized and their analysis would help to decipher this cell type characteristics.

In agreement with the lack of knowledge in the vascular initial cells, lowest enrichments were found when using TOTEM software and analyzing cluster 21 population that correspond mostly to VI cells (Figure 5.12 C). This can be due to the low number of genes identified as VI specific in Brady et al. (2007) experiments, but it can also indicate that those cells have unique molecular signatures that does not coincide with the ones from other cell types, further supporting the identity of a novel cell population.

One of the processes that is overrepresented in the VI cells is related to protein metabolism (Figure 5.11 C). Interestingly, we found BRAVO to be regulating genes in these processes too (Figure 4.10), suggesting a relevant role for BRAVO in these cells. Unfortunately, due to the low number of cells, we were not able to find the BRAVO-regulated genes specifically in cluster 2 cells. Experiments in this line would allow to decipher the role of BRAVO and its impact for plant development. Protein metabolism can be related to cell cycle and to other processes such as cell elongation or cell wall differentiation which are essential for vascular development (Ohashi-Ito et al., 2010; Yamaguchi et al., 2011).

Overall, our FACS coupled to scRNAseq approach allowed to identify four stem cell populations in the root apex. In addition, our single-cell

transcriptomic root atlas enriched in stem cells can also serve as resource for future studies regarding root stem cells. We have demonstrated the stem cell identity of our cells, and the utility of integrating several available scRNAseq datasets to strengthen other analysis.

After our analysis, some questions remain unknown and there were not addressed in this thesis. More insights in the differentiation process of the QC to the VI cells and the mature vascular tissues could be analyzed. Single-cell methodology allows Pseudotime analysis in which transcriptomic along a developmental trajectory changes can be evaluated. A more precise Pseudotime analysis can be performed regarding the stem cell niche, trying to decipher if different VI population give rise to different mature tissues, or if there is a certain point in which xylem and phloem formation diverges from the previous stem cell. These questions were not approached as the number of cells for the analysis were not high enough for this analysis.

In addition to stem cells, phloem cells were also isolated and sequenced, but they were not used to further analysis. The number of individual cells obtained was very low, only 9 in WT conditions. This was probably due to the low expression of the marker used in the meristematic zone and the fact that phloem cells are in the inner region of the root, which difficulties its isolation as protoplast with the cell wall enzymatic digestion. The information available about the phloem tissue with single-cell resolution is still scarce, as comprehensive studies regarding this tissue and the transcriptomic changes along its differentiation process are yet lacking.

6.5 Future perspectives

Mechanisms regulating stem cell maintenance and differentiation remain unknown. This thesis reveals new insights in the role of brassinosteroids and BRAVO transcription factor in the stem cell niche. For example, it is described how BRAVO interacts with WOX5 to regulate root growth. In addition, its role in other developmental processes such as hair cell development and cell wall biosynthesis was proposed. However, most of the results of chapters 4 and 5 were found computationally, and further experimental validation is required.

In chapters 3 and 4, the role of BRAVO in the stem cell niche was evaluated. Phenotypic characterization of *bravo* mutant revealed only defects in QC division in normal conditions. If BRAVO is involved in stress responses remain unknown. In this line, studies linking BRAVO with BRI1 or BRL1/BRL3 pathways are required, as BRL1/BRL3 have been linked to stress response and adaptation (Planas-Riverola et al., 2019). Experiments to address the redundancy of MYB transcription factors in the stem cells would also be relevant to characterize the role of BRAVO in those cells.

In chapter 5, single-cell transcriptomics were used to generate an atlas of the root stem cell niche. This resource can be used to unveil fundamental questions such as the presence of branches in the differentiation of the vascular cells. However, the low number of cells in our experiments did not allow to answer them. Further analysis comparing WT with *bravo* cells would be key to decipher the role of BRAVO in each cell population.

Finally, experimental validation regarding the characterization of the four

populations found in the stem cell niche would be essential to validate our findings. The expression in seedlings of the cluster 21 marker genes could be evaluated, and analysis of mutant and overexpressor lines of those genes would help to understand the function of that population for root development.

Conclusions

Conclusions

1. **MyROOT software permits accurate high-throughput Arabidopsis root length measurements while saving labor and time.**

2. **The use of machine learning technology enables the development of convenient tools for high-throughput analysis of plant root traits.**

3. **At the root stem cell niche BRAVO and WOX5 operate as a transcriptional complex in preserving stem cell function and overall root growth and development.**

    i. BRAVO and WOX5 have an epistatic effect in QC division.

    ii. BRAVO and WOX5 directly interact and the complex is relevant to control QC divisions.

    iii. There is a mutual regulation between BRAVO and WOX5 expression in the stem cell niche.

    iv. BRAVO and WOX5 interplay impacts in primary root length and lateral root development.

4. **Multidisciplinary approaches combining genetics, biochemistry and mathematical modeling are a powerful approach to unravel complex mechanisms involved in root development.**

5. **BRAVO drives cell-type specific transcriptional responses in the quiescent center and vascular stem cells.**

   i. BRAVO exerts a wider transcriptional response in the VI than in the QC cells.

   ii. BRAVO acts mostly as a transcriptional activator in the QC and a repressor in the VI cells.

   iii. BRAVO in the QC regulates transcription mostly in a non-cell autonomous manner, as there is enrichment in BRAVO-regulated genes that are reported to play a role in root outer cell layers.

   iv. Brassinosteroids regulate the transcription of cell-wall differentiation already at the vascular initial cells of the Arabidopsis primary root.

6. **Single-cell RNAseq allows the identification of different stem cell populations within the stem cell niche of Arabidopsis.**

   i. The vascular initial cells can be separated in two populations with different transcriptomic profiles.

   ii. Quiescent stem cells have unique molecular signatures that correspond to an enrichment in response to stress genes.

Material and methods

Material and methods

Plant material and growth conditions

Arabidopsis seeds were surface sterilized with 35% sodium hypochlorite followed by 5 washes with distilled sterile water. To synchronize germination, seeds were vernalized for 2 to 3 days at 4°C in darkness. Seeds were grown in vertically oriented 120x120 mm plates containing half-strength Murashige and Skoog (MS) medium without sucrose, supplemented with vitamins (0.5MS-) and 0.8% plant agar. Plates were sealed with Micropore tape (https://www.3m.com). Seeds were grown under long day conditions (16 hours light and 8 hours dark) at 22°C and 60% relative humidity for all the experiments.

After 5 to 7 days of growth in sterile conditions, seedlings were transferred to pots containing soil (composed by a mixture of soil:perlite:vermiculite at a proportion of 7:1:1). Plants were grown in long day conditions at 22°C and 60% relative humidity until desired. The Arabidopsis lines used in this thesis are summarized in Table 6.1.

Table 6.1: Arabidopsis plant lines used in this thesis.

Name	Genes	Description	Reference	Chapter
Col-0 (WT)	-	Wild type, ecotype Columbia-0	-	3, 4, 5
bravo-2	BRAVO	T-DNA insertion mutant	Vilarrasa-Blasi et al. (2014)	3
wox5-1	WOX5	T-DNA insertion mutant	Sarkar et al. (2007)	3
bravo-2 wox5-1	BRAVO, WOX5	Double knockout mutant	Betegón-Putze et al. (2020)	3
pBRAVO:GFP	BRAVO	Transcriptional fusion	Vilarrasa-Blasi et al. (2014)	3, 5
pBRAVO:GFP; *bravo-2*	BRAVO	Transcriptional fusion in BRAVO knockout mutant	Vilarrasa-Blasi et al. (2014)	3, 5
pBRAVO:GFP; *wox5-1*	BRAVO, WOX5	Transcriptional fusion in WOX5 knockout mutant	Betegón-Putze et al. (2020)	3
pBRAVO:GFP; *bravo-2 wox5-1*	BRAVO, WOX5	Transcriptional fusion in BRAVO and WOX5 knockout mutant	Betegón-Putze et al. (2020)	3
pWOX5:GFP	WOX5	Transcriptional fusion	Vilarrasa-Blasi et al. (2014)	3, 4
pWOX5:GFP; *bravo-2*	WOX5, BRAVO	Transcriptional fusion in BRAVO knockout mutant	Vilarrasa-Blasi et al. (2014)	3, 4
pWOX5:GFP; *wox5-1*	WOX5	Transcriptional fusion in WOX5 knockout mutant	Betegón-Putze et al. (2020)	3
pWOX5:GFP; *bravo-2 wox5-1*	BRAVO, WOX5	Transcriptional fusion in BRAVO and WOX5 knockout mutant	Betegón-Putze et al. (2020)	3

Name	Genes	Description	Reference	Chapter
35S:BRAVO:Ei	BRAVO	BRAVO overexpressor mutant	Vilarrasa-Blasi et al. (2014)	3
35S:BRAVO:Ei; pWOX5:GFP	BRAVO, WOX5	Transcriptional fusion in BRAVO overexpressor mutant	Betegón-Putze et al. (2020)	3
35S:WOX5:GR	WOX5	WOX5 overexpressor mutant	Sarkar et al. (2007)	3
pARF7:GFP	ARF7	Transcriptional fusion	Rademacher et al. (2011)	4
pARF7:GFP; *bravo-2*	ARF7, BRAVO	Transcriptional fusion in BRAVO knockout mutant	Vilarrasa-Blasi et al. (2014)	4
pSUC2:BRL3-GFP	SUC2, BRL3	BRL3 overexpression in the phloem	Ana Caño lab	5
pSUC2:BRL3-GFP;*brl3-2*	SUC2, BRL3	BRL3 overexpression in the phloem in BRL3 knockout mutant	Ana Caño lab	5

For the validation experiments of MyROOT software described in chapter 2, a set of BR-signaling mutant and overexpressor lines grown in control and osmotic stress conditions (240 nM sorbitol treatment for 4 days) were used (previously described in Fàbregas et al. (2018)). For the hypocotyl detection method, MyROOT was trained to identify hypocotyls by using 1259 positive examples (hypocotyls) and 7915 background and negative examples (parts of the image that did not contain hypocotyls). The positive samples corresponded to Col-0 wild-type, *bri1-116*, and a transgenic line overexpressing BRI1-GFP (35S:BRI1-GFP), which have morphologically different hypocotyls as shown in González-García et al. (2011).

Methods in plant physiology

Root length measurements

Root length from plate images was measured with ImageJ (http://imagej.nih.gov/ij/) and MyROOT (Betegon-Putze et al., 2019) softwares. In ImageJ, manual measurements were made using the Segmented line option. Each root was tracked by clicking several times from the starting point of the root to the root tip. Then, the length of the segmented line was measured and ImageJ obtained the root length in millimeters using the scale previously set.

The comparison between the root length measurements using MyROOT and ImageJ was evaluated by performing a regression curve and calculating the Pearson correlation coefficient. The comparison between the root length measurements using and not using the hypocotyl detection method was evaluated using Student's t-test. This test was selected due to the unequal number of seedlings detected under each condition.

MyROOT and ImageJ were run in an Intel CoreTM i7-6700 CPU computer.

Hormone and drug treatments

For brassinolide (BL) treatments, BL (Wako, Osaka, Japan) diluted in DMSO was added to 0.5MS- plates at a final concentration of 4nM. 4-day-old seedlings were transferred to 4nM BL plates for 48 hours before analysis.

For β-estradiol treatments, β-estradiol (Sigma) diluted in DMSO was added to 0.5MS- plates at a final concentration of 30 μM. To induce BRAVO expression, seedlings were grown in that media for 6 days. For dexamethasone treatments, dexamethasone (Sigma) diluted in EtOH was added to 0.5MS- plates at a final concentration of 1 μM. To induce WOX5 expression, seedlings were grown in that media for 6 days. For RT-qPCR experiments β-estradiol and dexamethasone treatments were applied for 24 hours.

Propidium Iodide staining

Propidium Iodide for in vivo visualization was performed by staining the 6-day-old seedlings with 10 μg/ml PI for 1-2 minutes.

To visualize propidium iodide staining in fixed roots, a modified version of the protocol modified Pseudo Schiff - Propidum Iodide (mPS-PI) staining was used (Truernit et al., 2008). 6 day old seedlings were incubated in 50% methanol and 10% acetic acid solution at 4^{o}C overnight (or longer if needed), rinsed twice with milli-Q water (5 minutes each), incubated in 1% periodic acid for 30 minutes, rinsed twice with milli-Q water (5 minutes each) and incubated in Schiff reagent with propidium iodide (100 mM sodium metabisulphite and 0.15 N HCl; propidium iodide to a final concentration of 100 μg/ml is freshly added) for 2 hours. The slides for microscopy were prepared by adding several drops of Hoyer's solution (30g gum Arabic, 200g chloral hydrate, 20g glycerol and 50 ml water) over the slides, laying the seedlings with tweezers and placing a coverslide on the top. They were let to dry in the dark for at least three days before microscopic analysis. For phloem morphology analysis, seedlings were

incubated in chloral hydrate solution (4g chloral hydrate, 1 mL glycerol and 2 mL water) overnight and the excess chloral hydrate was removed before preparing the slides with the Hoyer's solution.

Confocal images were taken with the 60X water-submerged objective. mPS-PI stained roots were used to evaluate QC division, CSC differentiation and stele width.

For QC division, roots were clasified as QC divided (D) if at least one of the QC cells showed a division plane and non-divided (ND) if none of the QC cells showed a division plane.

For columella stem cell differentiation, the number of columella stem cells (revealed by the absence of starch granules that are present and PI-stained in the columella cells) was scored.

Stele width was measured 50 μm away from the QC.

Lateral root analysis

Lateral root density was calculated by dividing the total number of emerged lateral roots (Malamy and Benfey, 1997) of individual seedlings by the mean of the root length of those seedling.

Lateral root analysis of 10 day-old plants was carried out by Ainoa Planas-Riverola in Dr. Caño-Delgado laboratory.

Imaging

Plant imaging

For the development of MyROOT software described in chapter 2, the pre-defined image acquisition conditions consist of placing the camera 50 cm above the plate with an illuminated support and the following settings:aperture 13, shutter speed 10, ISO 100 and Zoom 935 magnification. The plates were placed face down on a black surface and with a ruler (at least 1 cm long) horizontally positioned on top. The images were saved in JPEG format (size between 2.5 and 2.7 MB per image). Images were taken with a D7000 Nikon camera.

Confocal microscopy

Confocal imaging was performed on a FV 1000 confocal microscope (Olympus, Tokyo, Japan). Excitation and emission spectra were 484 nm and 489–505 nm for GFP, 561 nm and 600–650 nm for propidium iodide. Samples were visualized with the confocal microscope with 20X and 60X water-submerged objectives. Images were processed with the Olympus FV (Olympus, Tokio, Japan) and ImageJ software.

Confocal imaging shown in chapter 4 was performed on a LSM 710 confocal microscope (Zeiss, Jena, Germany).

For GFP quantification in chapter 3, images were taken in the middle plane of 6-day-old roots. The fluorescence intensity was quantified with ImageJ using the Integrated Density value obtained from individual plants. The quantified area was selected with a ROI that contained the SCN

(Figure 3.4). The laser settings for pBRAVO:GFP and pWOX5:GFP are different, as *WOX5* has a stronger expression than *BRAVO*. The analysis of pBRAVO:GFP in *bravo wox5* double mutant background was done with different confocal settings.

Methods in molecular biology

DNA extraction

For genotyping plants, DNA was extracted from Arabidopsis leaves according to the following rapid extraction protocol: a piece of leave was collected in a tube with 2 glass beads. Tissue was grinded in the Tissuelyser (Quiagen) for 1 min at 300 rev. Then, 400 μl of extraction buffer (0.4 M NaCl, 10 mM Tris-HCl pH8.0, 2 mM EDTA pH8.0 and 2% (v/v) SDS) were added to each sample and agitated with a vortex for 5 seconds. Samples were centrifuged for 5 min at 13000 rpm. 300 μl of the supernatant were transferred to a new tube and 300 μl of isopropanol were added to precipitate the DNA. Tubes were inverted 5 times to allow solutions to mix. Samples were incubated 5 min at room temperature and centrifuged 10 min at 13000 rpm. The supernatant was discarded and 500 μl of 70% ethanol were added to clean the pellet. Samples were centrifuged 10 min at 13000 rpm and the supernatant was discarded. Tubes were kept overnigth to dry at root temperature. DNA was resuspended in 50 μl of sterile-distilled water. DNA concentration and purity was then assessed with a Nanodrop 1000 spectrophotometer (Thermo Fisher Scientific). The different mutants described in this thesis were genotyped to select the homocygous plants. The sequences of the primers used for genotyping are

described in Table 6.2.

Table 6.2: Primers used for genotyping.

Primer	Sequence 5'-3'	Use
bravo-2 F	TCCCTTAATCCCTAAACCCAGC	Genotype *bravo-2* mutant
bravo-2 R	CCTGATGCAAGGGTACTATCG	Genotype *bravo-2* mutant
wox5-1 F	ATCTCATAAACCATGCATCGG	Genotype *wox5-1* mutant
wox5-1 R	TCGCTGGTTCCGATATACAAC	Genotype *wox5-1* mutant
brl3-2 F	TTTATCGAACACTTTGTGGGC	Genotype *brl3-2* mutant
brl3-2 R	CCAGTGAACTCGTTTGAGCTC	Genotype *brl3-2* mutant
LBb1.3	ATTTTGCCGATTTCGGAAC	Genotype T-DNA insertion mutants

RNA extraction

RNA was extracted from root tip tissue with the Maxwell®RSC Plant RNA Kit (Promega) using the Maxwell®RSC instrument (Promega) according to the manufacturer's recommendations, and concentrations were checked using NanoDrop 1000 spectrophotometer (Thermo Fisher Scientific).

Real time quantitative PCRs

Real time quantitative PCRs were carried out by Ainoa Planas-Riverola in Dr. Caño-Delgado laboratory.

cDNA was obtained from RNA samples by using the NZY First-Strand cDNA Synthesis Kit (NZYtech) according to the manufacturer's recom-

mendations. RT-qPCR amplifications were performed from 10ng of cDNA using SYBR Green I master mix (Roche) in 96-well plates according to the manufacturer's recommendations. The RT-qPCR was performed on a LightCycler 480 System (Roche). ACTIN2 (AT3G18780) was used as housekeeping gene for relativizing expression. Primers used for real time qPCR are described in Table 6.3.

Table 6.3: Primers used for real time qPCR.

Primer	**Sequence 5'-3'**	**Use**
RT-BRAVO F	TGTTAGCAGCTCATCGAGCCT	BRAVO RT-qPCR forward primer
RT-BRAVO R	GATGACGTGCCAATGGTTCTT	BRAVO RT-qPCR reverse primer
RT-WOX5 F	TGATCTGTTTCGAGCCGGTC	WOX5 RT-qPCR forward primer
RT-WOX5 R	AAACATTCTTGCTCTCTATCTTGCC	WOX5 RT-qPCR reverse primer
RT-ACTIN2 F	CTGGATCGGTGGTTCCATTC	ACTIN2 RT-qPCR forward primer
RT-ACTIN2 R	CCTGGACCTGCCTCATCATAC	ACTIN2 RT-qPCR reverse primer

Methods in biochemistry

Yeast two-hybrid assay

Yeast two-hybrid experiments were carried out by Nadja Bosch in Dr. Caño-Delgado laboratory.

Yeast two-hybrid assays were performed by the Matchmarker GAL4-based two-hybrid System (Clontech). Constructs were co-transformed into the yeast strain AH109 by the lithium acetate method (Gietz and Woods, 2002). The presence of the transgenes was confirmed by growth on SD-LW plates, and protein interaction was assessed by selection on SD-LWH plates. Interactions were observed after 4 days of incubation at 30°C.

FRET-FLIM assays

FRET-FLIM experiments were carried out by Dr. Yvonne Stahl and Rebecca Corinna Burkart in the Institute for Developmental Genetics, Heinrich-Heine University, Düsseldorf, Germany.

FLIM data acquisition was carried out using a confocal laser scanning microscope (LSM780 inverted microscope, Zeiss) equipped additionally with a time-correlated single-photon counting device with picosecond time resolution (Hydra Harp 400, PicoQuant). mVenus was excited at 485 nm with a pulsed (32 MHz) diode laser at 1.2 μW at the objective (40 x water immersion, C-Apochromat, NA 1.2, Zeiss). The emitted light was collected through the same objective and detected by SPAD detectors (PicoQuant) using a narrow range bandpass filter (534/35, AHF). Images were taken at 12.5 μs pixel time and a resolution of 138 nm/pixel in a 256x256 pixel image. A series of 40 frames was merged into one image and analysed using the Symphotime software package (PicoQuant).

The fluorescent lifetime of the collected photons in each merged image was analysed using the Symphotime software (PicoQuant). For this, a ROI covering the whole nucleus was created to reduce background fluorescence. All photons in this ROI were used to build a histogram of

the fluorescence decay. A double-exponential fit model was used to approximate the intensity-weighted average fluorescence lifetime [ns] of all photons of the ROI. The instrument response function was measured with KI-quenched erythrosine and used for reconvolution in the fitting process (Weidtkamp-Peters and Stahl, 2017). The data from replicate measurements was summarized in box plots created in R software (R Development Core Team, 2008). Statistical significance was tested by one-way ANOVA with a Sidakholm post-hoc test. Different letters indicate statistically significant differences ($p < 0.01$). For the creation of FLIM images, photons from individual pixels of a merged image were analysed for fluorescent lifetime using the Symphotime software (PicoQuant). A mono-exponential fit model was used, as the photon number in each pixel was too low for a double-exponential model (Stahl et al., 2013). The individual pixels are colour-coded according to their fluorescence lifetime.

Genome-wide transcriptomic experiments

Quiescent center and vascular initial bulk RNAseqs

These experiments were performed in the laboratory of Dr. Rosangela Sozzani the in North Carolina State University, Raleigh, USA [1].

The protocol used for these RNAseq experiments shown in chapter 4 is described in Clark et al. (2018).

For growing the plants, 400 mg of seeds were sterilized in a 50 ml conical tube. 50 ml of 50% bleach and 15 μl of 10% Tween were added, the tubes

[1] https://harvest.cals.ncsu.edu/sozzani-lab/

were shaken to disperse the seeds, shaked for 10 min at 110 rpm on orbital shaker and centrifuged to settle down the seeds. In a sterile hood, bleach was poured out and 45 ml of 100% ethanol were added, the tubes were shaken and centrifuged. The ethanol was poured out and 45 ml of sterile water was added, the tubes were shaken and centrifuged. The water wash step was repeated 8 times. The tubes were stored in dark at 4°C for two days for vernalization. Seeds were plated in MS0.5- square plates over mesh and grown for 5 days in the growth chamber. For BL treated plats, seedlings were transfered to MS0.5- plates supplemented with 10 nM BL for 2 hours. Three biological replicates were performed for each line and condition.

For protoplasting, root tips were cut and put in a petri dish over a 70 μm cell strainer in solution B and shaked at 85 rpm for 60 minutes stiring the roots after 20, 30 and 10 minutes. The liquid was transfered to a 15 ml conical tube and spin for 6 min at 200g. The supernatant was removed and the pellet resuspended in 350 μl of solution A. The resuspended solution was transferred to a 50 ml conical tube through a 70 μm strainer, the 15ml conical tube was rinsed again with another 350 μl of solution A and transferred to the 50 ml tube through the 70 μm strainer. All the liquid was then transferred to another 50 ml conical tube through a 40 μm strainer, and then to a polystyrene tube. Solution A was prepared by adding 50 mL of deionized water, 5.465 g of mannitol, 0.05 g of 0.01% BSA, 500 μl of 0.2 M Magnesium chloride, 500 μl of 0.2 M calcium chloride, 500 μl of 1 M MES and 500 μl of 1 M potassium chloride. Soluton B was prepared by adding 0.45 g cellulase and 0.03 g pectolyase to 30 ml aliquot of solution A.

For FACS, protoplasts were run through a high speed cell sorter using

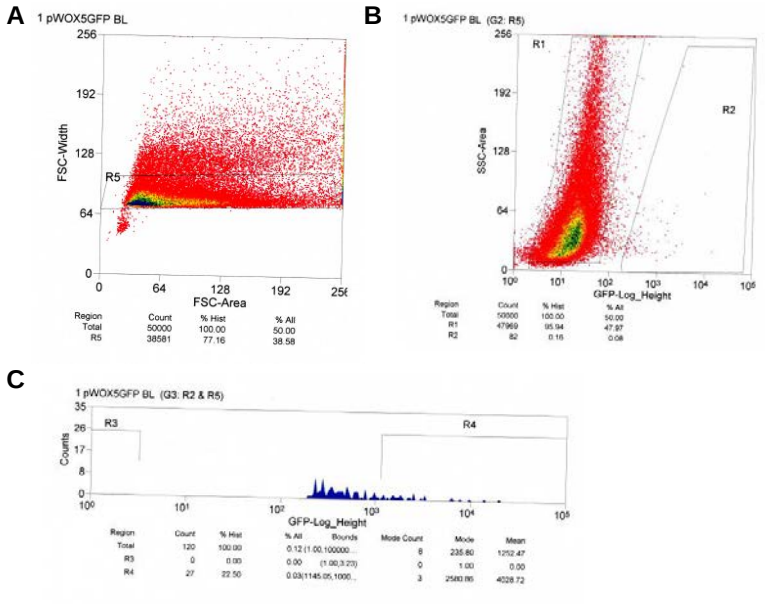

Figure 6.1: Fluorescence gates used for collecting GFP positive cells.

A) Forward scatter (FSC) width vs FSC area. R5 gate is set to exclude doublets. B) Side scatter (SSC) vs fluorescence (GFP) of R5 cells. Cell with higher GFP fluorescence value are selected in R2. C) Count histogram of the R2 gate. Only the brightest cells within R2 are selected in R4. The final population of sorted cells are in R4.

a 100 μm flow tip at a pressure of 20 PSI. Wild type protoplasts were used to set a gate of GFP-negative cells. GFP positive samples were run and a gate to obtain positive cells was set (Figure 6.1). Sorted cells were collected in 300 μl RLT Buffer with 3uL β-mercaptoethanol in 5ml polystyrene round bottom tubes and stored at -80 °C.

For RNA extraction, columns and buffers provided in the QIAGEN RNeasy Micro Kit were used. Sorted cells were thawed in hands, 300 μl 70% cold ethanol was added and vortexed for 2 seconds. 600 μl of the mixture was applied to the pink MiniElute column, spin at 1000 g for 1 min, then at

10000 g for 30 seconds, the flow-thorugh was reapplied to the column and spin at 10000 g for 30 seconds. 700 μl RW1 buffer were added to the column and spun at 10000 g for 30 seconds. 500 μl RPE buffer were added to the column and spun at 10000 g for 30 seconds. 500 μl of 80% ethanol were added and spun at 10000 g for 2 minutes. Columns were spun with open cap 5 minutes at max speed. The column was eluted with 12 μl nuclease free water, spun at 1000 g for 1 minute and 16000 g for 1 minute. The flow-thorugh was reapplied to the column and spun at 16000 g for 1 minute at 4^{o}C. RNA was analyzed in the Bioanalyzer and optimal RNA quality was defined as RIN $>$ 7.

cDNA libraries were prepared from the extracted RNA using the SMART-Seq v4 Ultra Low Input RNA Kit for Sequencing (Takara) and Low Input Library Preparation Kit (Clontech laboratories). Libraries size and quality was checked on a DNA High Sensitivity Bioanalyzer chip (Agilent).

RNAseq was performed using the HiSeq system (Illumina), 100 bp, single end reads.

Stem cell niche and phloem single-cell RNAseqs

These experiments were performed in the laboratory of Dr. Idan Efroni in the Hebrew University of Jerusalem, Rehovot, Israel [2].

For single-cell experiments described in Chapter 5, the protocol followed was adapted from Bagnoli et al. (2018).

For protoplasting, roots from pSUC2:BRL3:GFP expressing plants were cut and shaken in protoplasting solution for 20 minutes to separate the

[2] https://idanef.wixsite.com/efronilab

meristems. The meristems were transfered to another well containing 50μl of protoplasting solution and shaken for 1 hour. For pBRAVO:GFP roots, root tips were collected directly by cutting the seedlings growing in the agar plates and were shaken for 1 hour and 20 minutes in the protoplasting solution. The plant material was then filtered using a 40 μm strainer. The protoplasting solution was prepared by adding 1.5% Cellulase, 0.5% Macerozyme, 0.4M Mannitol, 20.48 mM Mes and 0.02M KCl; adjusting pH to 5.7; heating to 55 °C and cooling to room temperature; and adding 0.2% BSA and 0.02M $CaCl_2$.

For FACS, protoplasts were run through a high speed cell sorter. Wild type protoplasts were used to set a gate of GFP-negative cells. GFP positive samples were run and a gate to obtain positive cells was set. Single cells ('3 drops' purity mode) were sorted into 96-well DNA LoBind plates (Eppendorf) containing 5 μl of lysis buffer. The lysis buffer consisted of a 1:500 dilution of Phusion HF buffer (New England Biolabs), 1.25 μg/μl Proteinase K (Clontech) and 0.4 μM barcoded oligo-dT primer (E3V6NEXT, IDT). After sorting, plates were immediately spun down and frozen at -80°C.

For cDNA synthesis, the 96-well plates were incubated at 50°C for 10 minutes for digesting the proteins. Proteinase K was then heat-inactivated for 10 minutes at 80°C. 5 μl reverse transcription master mix consisting of 20 units Maxima H- enzyme (Thermo Fisher), 2x Maxima H- Buffer (Thermo Fisher), 2 mM each dNTPs (Thermo Fisher), 4 μM template-switching oligo (IDT) and 15% PEG 8000 (Sigma-Aldrich) was dispensed per well. cDNA synthesis and template-switching was performed for 90 minutes at 42°C. Barcoded cDNA was then pooled in 2 ml DNA LoBind tubes (Eppendorf) and cleaned-up using SPRI beads (following the manufacturer

instructions at a ratio of 1:1.8 ((μLsample:μLbeads)). Purified cDNA was eluted in 17 μl and residual primers digested with 0.5 μl Exonuclease I (Thermo Fisher) for 15 min at 37°C. After heat-inactivation for 15 min at 80°C, 30 μl PCR master mix consisting of 1.25 U Terra direct polymerase (Clontech), 1.66x Terra direct buffer and 0.33 μM SINGV6 primer (IDT) was added for amplification by PCR. The PCR progamm used was 3 min at 98°C for initial denaturation followed by 15 cycles of 15 sec at 98°C, 30 sec at 65°C and 4 min at 68°C. Final elongation was performed for 10 min at 72°C. All samples were purified using SPRI beads (following the manufacturer's instructions at a ratio of 1:1) with a final elution in 10 μL of nuclease free water (Invitrogen). Quality control was performed by PCR using SINGV6 primer. PCRBIO HS Taq Mix Red mix (PCR Biosystems) was used for the PCR following manufacturer's instructions. PCR programm was run with 56°C as Tm for 30 cycles. The cDNA was then quantified using the Quant-iT PicoGreen dsDNA Assay Kit (Thermo Fisher).

Library preparation was then done using Nextera XT DNA Library Prep kit (Illumina) following the manufacturer instructions with few modifications: starting from 1 ng of preamplified cDNA, reducing all the reagent volumen by half and increasing the number of PCR cycles to 15. The library was prepared using 5μM P5 primer (P5NEXTPT5, IDT) and 1 μM i7 primers. The i7 primer used was Nextera (XT) N7xx and the different adapters for each sample are described in table 6.4. library size and quality was checked on a DNA High Sensitivity Bioanalyzer chip (Agilent) and libraries were quantified using Quant-iT PicoGreen dsDNA Assay Kit (Thermo Fisher). Libraries were pooled for equimolarity, taking into account only the main peak. Selection of the main peak was done by running

the pooled library in a 1% agarose gel, and cutting out the band leaving out the primer concatamers (with size around 150bp). DNA from the band was extracted using the MinElute Kit (Qiagen) following manufacturer's recommendations. Final library size and quality was checked on a DNA High Sensitivity Bioanalyzer chip (Agilent) and quantified using Quant-iT PicoGreen dsDNA Assay Kit (Thermo Fisher).

Table 6.4: Samples and i7 adapters used for library preparation. pB: pBRAVO:GFP; pBb: pBRAVO:GFP;*bravo*; pS: pSUC2:BRL3:GFP; pSb: pSUC2:BRL3:GFP;*brl3*. Each sample corresponds to a 96-well plate.

Sample	Description	Adapter code and sequence
1	pS, pSb	A701 ATCACGAC
2	pS	A703 CAGATCCA
3	pB	A704 ACAAACGG
4	pBb	A706 AACCCCTC
5	pBb	A707 CCCAACCT
6	pB	A708 CACCACAC
7	pBb	A710 TGTGACCA
8	pB	A711 AGGGTCAA
9	pBb	A712 AGGAGTGG
10	pS, pSb	N704 GCTCAGGA
11	pSb	N707 GTAGAGAG
12	pSb, pBb	N708 CAGAGAGG

Libraries were paired-end sequenced on high output flow cells of an Illumina HiSeq 1500 instrument.

Bioinformatics

Bulk RNAseqs analysis

RNAseqs raw data analysis was performed in the laboratory of Dr. Ana Conesa in the University of Florida, Gainesville, USA [3].

QC and VI bulk RNAseqs described in chapter 4 were analyzed by programing in bash and R studio (R Development Core Team, 2008). Quality control was done with FastQC (available at https://www.bioinformatics.babraham.ac.uk/projects/fastqc/). The adaptor sequences were removed using cutadapt command. The mapping of the reads to the genome was done with STAR (Dobin et al., 2013) and the quantification of the reads with RSEM (Li and Dewey, 2011). Araport11 were used as transcripts of reference and TAIR10 as reference genome. In R studio, genes with 0 counts in all samples were removed. NOIseq was used for the bias detection, correction and normalization (Tarazona et al., 2015). ARSyNseq was used for batch effect correction as the sorting was detected as a confounded factor (Nueda et al., 2012). Genes with low number of counts (cpm < 4) were filtered. NOISeqBIO was used for analysis of differential expression between the different conditions (Tarazona et al., 2015). Regulated genes were selected with q value < 0.05 and Fold change > 1.

Gene Ontology enrichment analysis was done in Araport thalemine (Krishnakumar et al., 2014) selecting only significant categories (p-value $<$ 0.05 in Holm-Bonferroni test). REVIGO small 0.5 was used to reduce redundancy after GO enrichment analysis (Supek et al., 2011). GO representations were done in R studio using heatmap.2 function from gplots

[3] http://conesalab.org/

package.

Venn diagrams were performed with BioVenn (Hulsen et al. (2008), https://www.biovenn.nl/) and InteractiVenn tools (Heberle et al. (2015), http://www.interactivenn.net/).

Root tissue enrichments were performed with TOTEM software available at https://bioinformatics.cragenomica.es/totem/select.

Transcription factors were obtained from the Arabidpsis Transciption Factor Database (AtTFDB) available at AGRIS website (Davuluri et al., 2003). BES1 and BZR1 direct targets were obtained from Yu et al. (2011) and He et al. (2005)

Single-cell RNAseqs analysis

For SCN and phloem single-cell RNAseqs analysis described in chapter 5, raw data processing was performed by Dr. Idan Efroni. Following sequencing, FASTQ files were filtered for poly-A reads using a custom script and aligned to the TAIR10 genome using STAR 2.7.1. Read calling was performed using the zUMI pipeline (Parekh et al., 2018).

Subsequent bioinformatic analysis were performed in R studio (version 3.6.3) using Seurat package (version 3.1.5; Butler et al. (2018); Stuart et al. (2019)). SCN and phloem cells to use for further analysis were filtered based in different arguments: only cells with unique features higher than 400 and less than 7500, and only cells that have number of total molecules lower than 100000. The data was then normalized using the "LogNormalize" method. The 800 features that have high cell-to-cell vari-

ation in the datasets were extracted to be used in downstream analysis. The data was then scaled so all the genes have the same importance in the analysis. PCA analysis was performed using the variable genes as input. 15 PCs were selected for clustering the cells and as input for UMAP reduction for visualization. A resolution value of 0.8 was used in all clustering analyses.

Our dataset was integrated with available whole-root datasets from Denyer et al. (2019) and Jean-Baptiste et al. (2019). Integration of the three datasets were performed with IntegrateData function. 20 PCs were selected for clustering and UMAP reduction.

Cluster marker genes were identified with the FindMarker function selecting only positives markers at a minimum percentage of 25 %. For the identification of marker genes compared to specific clusters, selected clusters were specified in ident.2 parameter. Only genes with adjusted p value < 0.05 were selected. For cluster annotation, cell-type specific genes described in Denyer et al. (2019) and Jean-Baptiste et al. (2019) were used.

For pseudotime analysis, Monocle 3 (version 0.2.1; Trapnell et al. (2014)) was used. Transference of Seurat object to Monocle object was done with SeuratWrappers package (version 0.2.0).

Gene Ontology enrichment analysis was done in Araport thalemine (Krishnakumar et al., 2014) selecting only significant categories (p-value $<$ 0.05 in Holm-Bonferroni test). REVIGO small 0.5 was used to reduce redundancy after GO enrichment analysis (Supek et al., 2011). GO representations were done in R studio using heatmap.2 function from gplots package.

For the analysis of stage-specific cell cycle genes, genes described in Torii et al. (2020) were used.

Root tissue enrichments were performed with TOTEM software available at https://bioinformatics.cragenomica.es/totem/select.

Visualization of gene expression plots was generated with VlnPlot and DotPlot functions included in Seurat package.

Mathematical modeling

Mathematical modeling was carried out by Dr. Marta Ibañes and Josep Mercadal in the University of Barcelona, Spain.

A complete description of the methods related to mathematical modeling can be found in Betegón-Putze et al. (2020).

Parameter values for the BRAVO and WOX5 model used to generate data in Figure 3.12 are shown in Table 6.5.

MyROOT algorithms development

Algorithms included in MyROOT software were developped and implemented by Dr. Xavier Sevillano and Dr. Alejandro González from La Salle, Ramón LLull University, Barcelona, Spain.

MyROOT has been developed in MATLAB (version 8.3.0.532. Natick, Massachusetts: The MathWorks Inc., 2014). A complete description of the algorithms can be found in Betegon-Putze et al. (2019) and González

Table 6.5: Parameter values for the model of BRAVO and WOX5. Parameters used to generate the data in Figure 3.12. Parameter values used to perform the numerical simulations. All are in arbitrary units. The right-most column indicates the concentration and time scales in which these values could be meaningful in a biological context.

Parameter	Value	Units
α	0.3	nM/min
γ	25	nM/min
K_M	0.02	nM^{-1}
K_W	0.01	nM^{-1}
ε_M	0.2	-
ε_W	4	-
W_0	1.6	-
M_0	30	nM/min
W_1	0.001	nM^{-1}
d_M	0.01	min^{-1}
D_W	0.01	min^{-1}

et al. (2020).

MyROOT software installation and user guide

Installation guide for MyROOT software

1. Execute MyAppInstaller_mcr.exe.

2. In the Root Analysis Installer window press the *Next* button.

3. In the Installation Options window select the folder where you wish to install the software. By default, the selected folder is C:\Program Files\La Salle – Universidad Ramon Llull\Root_Analysis.

4. Mark the option *Add a shortcut to the desktop.*

5. Press the *Next* button.

6. In the Required Software window select the installation folder for the MATLAB Runtime (by default C:\Program Files\MATLAB\MATLAB Runtime).

7. Press the *Next* button.

8. In the License Agreement window mark the option *Yes*.

9. Press the *Next* button

10. In the Confirmation window press the *Install* button

11. Copy the HypocotylDetection folder to the Desktop (this folder is in the same folder as the .exe file used for the installation).

12. Open the software by pressing in the MyROOT Desktop icon.

Brief user guide for individual plates analysis using MyROOT software

1. Open the software in a PC.

2. Select and load the image to process by pressing the *LOAD IMG* button. Enter an image resize factor between 0 and 1 in the Scale edit box to reduce the size of the image and speed up the processing of high-resolution images.

3. Obtain the pixels-to-millimeters scale factor by pressing the *Ruler ID* button. If needed, edit the Ruler Threshold value to modify the sensitivity of the ruler detector and repeat step 3. If there is no ruler in the image, insert the correspondence between pixels and millimeters manually in the 10 mm equivalence box.

4. Start the root segmentation process by pressing the *Root Mask* button. Select the area where the roots are present by clicking in the image. Double click in one of the vertex to start generating the mask. In case the result is not satisfactory (e.g., over-segmented roots), modify the sensitivity factor in the Root Threshold edit box and repeat step 4.

5. Enter a value in the Root Length Threshold box to indicate the minimum percentage with respect to the longest root to be measured.

6. Start the root tracking and measurement process by pressing the *Root Detection* button.

7. Enter the path of the files containing the pre-trained hypocotyl detection models in the Hypocotyl Model Path edit box.

8. Optionally, to perform hypocotyl detection based on color descriptors only, check the *Only Color* checkbox, and to conduct a channel-wise color normalization process check the *Norm Color* checkbox.

9. Optionally, modify the threshold of the linSVM classifier by modifying the value in the edit box located next to the *Hypocotyl Detection* button.

10. Start the hypocotyl detection process by pressing the *Hypocotyl Detection* button.

11. If some of the hypocotyls were undetected, insert them manually by using the *Add* button. Press the *Enter* key and press the *Root Refinement* button to update root length measurements.

12. Remove the undesired roots from the measurement by typing the root identifier in the ID edit box and pressing the *Remove* button.

Press the *Visualize* button to refresh the image presented on MyROOT's visualization canvas.

13. Enter the path where you would like the results to be stored in the Results Path edit box.

14. Choose the type of data you want to save by checking the corresponding checkboxes.

15. Optionally, type an identification suffix that will be appended to the stored file names via the Root Label edit box.

16. Save the results by pressing the *SAVE* button

Brief user guide for batch processing using MyROOT software

1. Load one of the image of the folder to process and select the optimal parameters for the analysis (steps 2 to 9 in the previous user guide).

2. Enter the path where you would like the results to be stored in the Results Path edit box.

3. Choose the type of data you want to save by checking the corresponding checkboxes.

4. Optionally, type an identification suffix that will be appended to the stored file names via the Root Label edit box.

5. Indicate the name of the folder with the images to process (Name\) in the Folder Path box.

6. Press the *Process* button to start the analysis.

7. Select if using the hypocotyl detection method by clicking in the *Yes* or *No* button in the box that appears.

Availability of data and materials

MyROOT software versions, extended user manuals, a demo video and example images are available to the plant science community through the CRAG website (https://www.cragenomica.es/research-groups/brassinosteroid-signaling-in-plant-development/software and the Plant Image Analysis website (https://www.plant-image-analysis.org/; (Lobet et al., 2013). The executable application together with the datasets generated during the current study (from Figures 2.5, 2.7 and 2.9) are available in the [Zenodo] repository, [https://doi.org/10.5281/zenodo.2552250].

Bibliography

Abdel-Ghany, S. E. (2009). Contribution of plastocyanin isoforms to photosynthesis and copper homeostasis in arabidopsis thaliana grown at different copper regimes. *Planta*, 229:767–779.

Adamowski, M. and Friml, J. (2015). Pin-dependent auxin transport: action, regulation, and evolution. *The Plant cell*, 27:20–32.

Agati, G., Azzarello, E., Pollastri, S., and Tattini, M. (2012). Flavonoids as antioxidants in plants: location and functional significance. *Plant science*, 196:67–76.

Agati, G., Matteini, P., Goti, A., and Tattini, M. (2007). Chloroplast-located flavonoids can scavenge singlet oxygen. *The New phytologist*, 174:77–89.

Agati, G. and Tattini, M. (2010). Multiple functional roles of flavonoids in photoprotection. *The New phytologist*, 186:786–793.

Aida, M., Beis, D., Heidstra, R., Willemsen, V., Blilou, I., Galinha, C., Nussaume, L., Noh, Y.-S., Amasino, R., and Scheres, B. (2004). The plethora genes mediate patterning of the arabidopsis root stem cell niche. *Cell*, 119:109–120.

Armengaud, P., Zambaux, K., Hills, A., Sulpice, R., Pattison, R. J., Blatt, M. R., and Amtmann, A. (2009). Ez-rhizo: integrated software for the fast and accurate measurement of root system architecture. *The Plant*

journal, 57:945–956.

Arsenault, J., Poulcur, S., Messier, C., and Guay, R. (1995). Winthizo: a root measuring system with a unique overlap correction method. *HortScience*, 30(906).

Bagnoli, J. W., Ziegenhain, C., Janjic, A., Wange, L. E., Vieth, B., Parekh, S., Geuder, J., Hellmann, I., and Enard, W. (2018). Sensitive and powerful single-cell rna sequencing using mcscrb-seq. *Nature communications*, 9:2937.

Bai, L., Zhou, Y., Ma, X., Gao, L., and Song, C.-P. (2014). Arabidopsis cap1-mediated ammonium sensing required reactive oxygen species in plant cell growth. *Plant signaling & behavior*, 9:e29582.

Balcerowicz, D., Schoenaers, S., and Vissenberg, K. (2015). Cell fate determination and the switch from diffuse growth to planar polarity in arabidopsis root epidermal cells. *Frontiers in plant science*, 6:1163.

Balzergue, C., Dartevelle, T., Godon, C., Laugier, E., Meisrimler, C., Teulon, J.-M., Creff, A., Bissler, M., Brouchoud, C., Hagège, A., Müller, J., Chiarenza, S., Javot, H., Becuwe-Linka, N., David, P., Péret, B., Delannoy, E., Thibaud, M.-C., Armengaud, J., Abel, S., Pellequer, J.-L., Nussaume, L., and Desnos, T. (2017). Low phosphate activates stop1-almt1 to rapidly inhibit root cell elongation. *Nature communications*, 8:15300.

Banda, J., Bellande, K., von Wangenheim, D., Goh, T., Guyomarc'h, S., Laplaze, L., and Bennett, M. J. (2019). Lateral root formation in arabidopsis: A well-ordered lrexit. *Trends in plant science*, 24:826–839.

Bargmann, B. O. R., Vanneste, S., Krouk, G., Nawy, T., Efroni, I., Shani, E., Choe, G., Friml, J., Bergmann, D. C., Estelle, M., and Birnbaum, K. D. (2013). A map of cell type-specific auxin responses. *Molecular systems biology*, 9:688.

Baumberger, N., Steiner, M., Ryser, U., Keller, B., and Ringli, C. (2003). Synergistic interaction of the two paralogous arabidopsis genes lrx1 and lrx2 in cell wall formation during root hair development. *The Plant journal*, 35:71–81.

Beemster, G. T. and Baskin, T. I. (1998). Analysis of cell division and elongation underlying the developmental acceleration of root growth in arabidopsis thaliana. *Plant physiology*, 116:1515–1526.

Beemster, G. T. S., Fiorani, F., and Inzé, D. (2003). Cell cycle: the key to plant growth control? *Trends in plant science*, 8:154–158.

Benfey, P. N., Linstead, P. J., Roberts, K., Schiefelbein, J. W., Hauser, M. T., and Aeschbacher, R. A. (1993). Root development in arabidopsis: four mutants with dramatically altered root morphogenesis. *Development*, 119:57–70.

Benjamins, R., Barbez, E., Ortbauer, M., Terpstra, I., Lucyshyn, D., Moulinier-Anzola, J., Khan, M. A., Leitner, J., Malenica, N., Butt, H., Korbei, B., Scheres, B., Kleine-Vehn, J., and Luschnig, C. (2016). Ppp1, a plant-specific regulator of transcription controls arabidopsis development and pin expression. *Scientific reports*, 6:32196.

Bennett, T., van den Toorn, A., Willemsen, V., and Scheres, B. (2014). Precise control of plant stem cell activity through parallel regulatory inputs. *Development*, 141:4055–4064.

Berli, F. J., Fanzone, M., Piccoli, P., and Bottini, R. (2011). Solar uv-b and aba are involved in phenol metabolism of vitis vinifera l. increasing biosynthesis of berry skin polyphenols. *Journal of agricultural and food chemistry*, 59:4874–4884.

Berli, F. J., Moreno, D., Piccoli, P., Hespanhol-Viana, L., Silva, M. F., Bressan-Smith, R., Cavagnaro, J. B., and Bottini, R. (2010). Abscisic acid is involved in the response of grape (vitis vinifera l.) cv. malbec

leaf tissues to ultraviolet-b radiation by enhancing ultraviolet-absorbing compounds, antioxidant enzymes and membrane sterols. *Plant, cell & environment*, 33:1–10.

Betegon-Putze, I., Gonzalez, A., Sevillano, X., Blasco-Escamez, D., and Cano-Delgado, A. I. (2019). Myroot: a method and software for the semiautomatic measurement of primary root length in arabidopsis seedlings. *Plant J*, 98(6):1145–1156.

Betegón-Putze, I., Mercadal, J., Bosch, N., Planas-Riverola, A., Marquès-Bueno, M., Vilarrasa-Blasi, J., Frigola, D., Burkart, R. C., Martínez, C., Stahl, Y., Prat, S., Ibañes, M., and Caño-Delgado, A. I. (2020). Precise transcriptional control of cellular quiescence by bravo/wox5 complex in arabidopsis roots. *bioRxiv*.

Bhave, N. S., Veley, K. M., Nadeau, J. A., Lucas, J. R., Bhave, S. L., and Sack, F. D. (2009). Too many mouths promotes cell fate progression in stomatal development of arabidopsis stems. *Planta*, 229:357–367.

Birnbaum, K., Jung, J. W., Wang, J. Y., Lambert, G. M., Hirst, J. A., Galbraith, D. W., and Benfey, P. N. (2005). Cell type-specific expression profiling in plants via cell sorting of protoplasts from fluorescent reporter lines. *Nature methods*, 2:615–619.

Birnbaum, K., Shasha, D. E., Wang, J. Y., Jung, J. W., Lambert, G. M., Galbraith, D. W., and Benfey, P. N. (2003). A gene expression map of the arabidopsis root. *Science*, 302:1956–1960.

Birnbaum, K. D. (2018). Power in numbers: Single-cell rna-seq strategies to dissect complex tissues. *Annual review of genetics*, 52:203–221.

Bishopp, A., Help, H., El-Showk, S., Weijers, D., Scheres, B., Friml, J., Benková, E., Mähönen, A. P., and Helariutta, Y. (2011). A mutually inhibitory interaction between auxin and cytokinin specifies vascular pattern in roots. *Current biology*, 21:917–926.

Blilou, I., Xu, J., Wildwater, M., Willemsen, V., Paponov, I., Friml, J., Heidstra, R., Aida, M., Palme, K., and Scheres, B. (2005). The pin auxin efflux facilitator network controls growth and patterning in arabidopsis roots. *Nature*, 433:39–44.

Bowen, A. J., Gonzalez, D., Mullins, J. G. L., Bhatt, A. M., Martinez, A., and Conlan, R. S. (2010). Pah-domain-specific interactions of the arabidopsis transcription coregulator sin3-like1 (snl1) with telomere-binding protein 1 and always early2 myb-dna binding factors. *Journal of molecular biology*, 395:937–949.

Brady, S. M., Orlando, D. A., Lee, J.-Y., Wang, J. Y., Koch, J., Dinneny, J. R., Mace, D., Ohler, U., and Benfey, P. N. (2007). A high-resolution root spatiotemporal map reveals dominant expression patterns. *Science*, 318:801–806.

Burkart, R. C., Strotmann, V. I., Kirschner, G. K., Akinci, A., Czempik, L., Maizel, A., Weidtkamp-Peters, S., and Stahl, Y. (2019). Plethora and wox5 interaction and subnuclear localisation regulates arabidopsis root stem cell maintenance. *bioRxiv*.

Butler, A., Hoffman, P., Smibert, P., Papalexi, E., and Satija, R. (2018). Integrating single-cell transcriptomic data across different conditions, technologies, and species. *Nature biotechnology*, 36:411–420.

Cai, J., Zeng, Z., Connor, J. N., Huang, C. Y., Melino, V., Kumar, P., and Miklavcic, S. J. (2015). Rootgraph: a graphic optimization tool for automated image analysis of plant roots. *Journal of experimental botany*, 66:6551–6562.

Cannoodt, R., Saelens, W., and Saeys, Y. (2016). Computational methods for trajectory inference from single-cell transcriptomics. *European journal of immunology*, 46:2496–2506.

Cao, J., Packer, J. S., Ramani, V., Cusanovich, D. A., Huynh, C., Daza,

R., Qiu, X., Lee, C., Furlan, S. N., Steemers, F. J., Adey, A., Waterston, R. H., Trapnell, C., and Shendure, J. (2017). Comprehensive single-cell transcriptional profiling of a multicellular organism. *Science*, 357:661–667.

Caño-Delgado, A., Lee, J.-Y., and Demura, T. (2010). Regulatory mechanisms for specification and patterning of plant vascular tissues. *Annual review of cell and developmental biology*, 26:605–637.

Caño-Delgado, A., Yin, Y., Yu, C., Vafeados, D., Mora-García, S., Cheng, J.-C., Nam, K. H., Li, J., and Chory, J. (2004). Brl1 and brl3 are novel brassinosteroid receptors that function in vascular differentiation in arabidopsis. *Development*, 131:5341–5351.

Caño-Delgado, A. I., Metzlaff, K., and Bevan, M. W. (2000). The eli1 mutation reveals a link between cell expansion and secondary cell wall formation in arabidopsis thaliana. *Development*, 127:3395–3405.

Carlsbecker, A., Lee, J.-Y., Roberts, C. J., Dettmer, J., Lehesranta, S., Zhou, J., Lindgren, O., Moreno-Risueno, M. A., Vatén, A., Thitamadee, S., Campilho, A., Sebastian, J., Bowman, J. L., Helariutta, Y., and Benfey, P. N. (2010). Cell signalling by microrna165/6 directs gene dose-dependent root cell fate. *Nature*, 465:316–321.

Carretero-Paulet, L., Cairó, A., Talavera, D., Saura, A., Imperial, S., Rodríguez-Concepción, M., Campos, N., and Boronat, A. (2013). Functional and evolutionary analysis of dxl1, a non-essential gene encoding a 1-deoxy-d-xylulose 5-phosphate synthase like protein in arabidopsis thaliana. *Gene*, 524:40–53.

Chaiwanon, J. and Wang, Z.-Y. (2015). Spatiotemporal brassinosteroid signaling and antagonism with auxin pattern stem cell dynamics in arabidopsis roots. *Current biology*, 25:1031–1042.

Chen, J., Yang, L., Yan, X., Liu, Y., Wang, R., Fan, T., Ren, Y., Tang, X.,

Xiao, F., Liu, Y., and Cao, S. (2016). Zinc-finger transcription factor zat6 positively regulates cadmium tolerance through the glutathione-dependent pathway in arabidopsis. *Plant physiology*, 171:707–719.

Chen, L., Bernhardt, A., Lee, J., and Hellmann, H. (2014). Identification of arabidopsis myb56 as a novel substrate for crl3bpm e3 ligases. *Molecular plant*.

Chen, L., Zhang, L., and Yu, D. (2010). Wounding-induced wrky8 is involved in basal defense in arabidopsis. *Molecular plant-microbe interactions*, 23:558–565.

Chen, M., Liu, H., Kong, J., Yang, Y., Zhang, N., Li, R., Yue, J., Huang, J., Li, C., Cheung, A. Y., and Tao, L.-Z. (2011). Ropgef7 regulates plethora-dependent maintenance of the root stem cell niche in arabidopsis. *The Plant cell*, 23:2880–2894.

Cheng, Y., Zhu, W., Chen, Y., Ito, S., Asami, T., and Wang, X. (2014). Brassinosteroids control root epidermal cell fate via direct regulation of a myb-bhlh-wd40 complex by gsk3-like kinases. *eLife*.

Cheung, T. H. and Rando, T. A. (2013). Molecular regulation of stem cell quiescence. *Nature reviews. Molecular cell biology*, 14:329–340.

Choe, S., Dilkes, B. P., Fujioka, S., Takatsuto, S., Sakurai, A., and Feldmann, K. A. (1998). The dwf4 gene of arabidopsis encodes a cytochrome p450 that mediates multiple 22alpha-hydroxylation steps in brassinosteroid biosynthesis. *The Plant cell*, 10:231–243.

Chrispeels, M. J., Crawford, N. M., and Schroeder, J. I. (1999). Proteins for transport of water and mineral nutrients across the membranes of plant cells. *The Plant cell*, 11:661–676.

Clark, N. M., Buckner, E., Fisher, A. P., Nelson, E. C., Nguyen, T. T., Simmons, A. R., de Luis Balaguer, M. A., Butler-Smith, T., Sheldon, P. J., Bergmann, D. C., Williams, C. M., and Sozzani, R. (2019). Stem-

cell-ubiquitous genes spatiotemporally coordinate division through regulation of stem-cell-specific gene networks. *Nature communications*, 10:5574.

Clark, N. M., Fisher, A. P., Berckmans, B., Van den Broeck, L., Nelson, E. C., Nguyen, T. T., Bustillo-Avendaño, E., Zebell, S. G., Moreno-Risueno, M. A., Simon, R., Gallagher, K. L., and Sozzani, R. (2020). Protein complex stoichiometry and expression dynamics of transcription factors modulate stem cell division. *Proceedings of the National Academy of Sciences of the United States of America*, 117:15332–15342.

Clark, N. M., Fisher, A. P., and Sozzani, R. (2018). Identifying differentially expressed genes using fluorescence-activated cell sorting (facs) and rna sequencing from low input samples. *Methods in molecular biology*, 1819:139–151.

Clark, R. T., Famoso, A. N., Zhao, K., Shaff, J. E., Craft, E. J., Bustamante, C. D., McCouch, S. R., Aneshansley, D. J., and Kochian, L. V. (2013). High-throughput two-dimensional root system phenotyping platform facilitates genetic analysis of root growth and development. *Plant, cell & environment*, 36:454–466.

Consortium, T. M. (2020). A single-cell transcriptomic atlas characterizes ageing tissues in the mouse. *Nature*, 583:590–595.

Cruz-Ramírez, A., Díaz-Triviño, S., Blilou, I., Grieneisen, V. A., Sozzani, R., Zamioudis, C., Miskolczi, P., Nieuwland, J., Benjamins, R., Dhonukshe, P., Caballero-Pérez, J., Horvath, B., Long, Y., Mähönen, A. P., Zhang, H., Xu, J., Murray, J. A. H., Benfey, P. N., Bako, L., Marée, A. F. M., and Scheres, B. (2012). A bistable circuit involving scarecrow-retinoblastoma integrates cues to inform asymmetric stem cell division. *Cell*, 150:1002–1015.

Cruz-Valderrama, J. E., Gómez-Maqueo, X., Salazar-Iribe, A., Zúñiga-

Sánchez, E., Hernández-Barrera, A., Quezada-Rodríguez, E., and Gamboa-deBuen, A. (2019). Overview of the role of cell wall duf642 proteins in plant development. *International journal of molecular sciences*, 20.

Cui, H., Levesque, M. P., Vernoux, T., Jung, J. W., Paquette, A. J., Gallagher, K. L., Wang, J. Y., Blilou, I., Scheres, B., and Benfey, P. N. (2007). An evolutionarily conserved mechanism delimiting shr movement defines a single layer of endodermis in plants. *Science (New York, N.Y.)*, 316:421–425.

Dalal, N. and Triggs, B. (2005). Histograms of oriented gradients for human detection. In *2005 IEEE Computer Society Conference on Computer Vision and Pattern Recognition (CVPR'05)*, volume 1, pages 886–893 vol. 1.

D'Alessandro, S., Ksas, B., and Havaux, M. (2018). Decoding b-cyclocitral-mediated retrograde signaling reveals the role of a detoxification response in plant tolerance to photooxidative stress. *The Plant cell*, 30:2495–2511.

Davuluri, R. V., Sun, H., Palaniswamy, S. K., Matthews, N., Molina, C., Kurtz, M., and Grotewold, E. (2003). Agris: Arabidopsis gene regulatory information server, an information resource of arabidopsis cis-regulatory elements and transcription factors. *BMC bioinformatics*, 4:25.

de Luis Balaguer, M. A., Fisher, A. P., Clark, N. M., Fernandez-Espinosa, M. G., Möller, B. K., Weijers, D., Lohmann, J. U., Williams, C., Lorenzo, O., and Sozzani, R. (2017). Predicting gene regulatory networks by combining spatial and temporal gene expression data in , javax.xml.bind.jaxbelement@774712e3, root stem cells. *Proceedings of the National Academy of Sciences of the United States of America*,

114:E7632–E7640.

De Rybel, B., Adibi, M., Breda, A. S., Wendrich, J. R., Smit, M. E., Novák, O., Yamaguchi, N., Yoshida, S., Van Isterdael, G., Palovaara, J., Nijsse, B., Boekschoten, M. V., Hooiveld, G., Beeckman, T., Wagner, D., Ljung, K., Fleck, C., and Weijers, D. (2014). Plant development. integration of growth and patterning during vascular tissue formation in arabidopsis. *Science*, 345:1255215.

De Rybel, B., Mähönen, A. P., Helariutta, Y., and Weijers, D. (2016). Plant vascular development: from early specification to differentiation. *Nature reviews. Molecular cell biology*, 17:30–40.

De Rybel, B., Möller, B., Yoshida, S., Grabowicz, I., Barbier de Reuille, P., Boeren, S., Smith, R. S., Borst, J. W., and Weijers, D. (2013). A bhlh complex controls embryonic vascular tissue establishment and indeterminate growth in arabidopsis. *Developmental cell*, 24:426–437.

Deal, R. B. and Henikoff, S. (2011). The intact method for cell type-specific gene expression and chromatin profiling in arabidopsis thaliana. *Nature protocols*, 6:56–68.

Decaestecker, W., Buono, R. A., Pfeiffer, M. L., Vangheluwe, N., Jourquin, J., Karimi, M., Van Isterdael, G., Beeckman, T., Nowack, M. K., and Jacobs, T. B. (2019). Crispr-tsko: A technique for efficient mutagenesis in specific cell types, tissues, or organs in arabidopsis. *The Plant cell*, 31:2868–2887.

Deng, Y. and Lu, S. (2017). Biosynthesis and regulation of phenylpropanoids in plants. *Critical Reviews in Plant Sciences*, 36(4):257–290.

Denyer, T., Ma, X., Klesen, S., Scacchi, E., Nieselt, K., and Timmermans, M. C. P. (2019). Spatiotemporal developmental trajectories in the arabidopsis root revealed using high-throughput single-cell rna sequencing. *Developmental cell*, 48:840–852.e5.

Devaiah, B. N., Nagarajan, V. K., and Raghothama, K. G. (2007). Phosphate homeostasis and root development in arabidopsis are synchronized by the zinc finger transcription factor zat6. *Plant physiology*, 145:147–159.

Ding, P., Rekhter, D., Ding, Y., Feussner, K., Busta, L., Haroth, S., Xu, S., Li, X., Jetter, R., Feussner, I., and Zhang, Y. (2016). Characterization of a pipecolic acid biosynthesis pathway required for systemic acquired resistance. *The Plant cell*, 28:2603–2615.

Ding, Z. and Friml, J. (2010). Auxin regulates distal stem cell differentiation in arabidopsis roots. *Proceedings of the National Academy of Sciences of the United States of America*, 107:12046–12051.

Dinneny, J. R., Long, T. A., Wang, J. Y., Jung, J. W., Mace, D., Pointer, S., Barron, C., Brady, S. M., Schiefelbein, J., and Benfey, P. N. (2008). Cell identity mediates the response of arabidopsis roots to abiotic stress. *Science*, 320:942–945.

Dobin, A., Davis, C. A., Schlesinger, F., Drenkow, J., Zaleski, C., Jha, S., Batut, P., Chaisson, M., and Gingeras, T. R. (2013). Star: ultrafast universal rna-seq aligner. *Bioinformatics*, 29:15–21.

Dobos, O., Horvath, P., Nagy, F., Danka, T., and Viczián, A. (2019). A deep learning-based approach for high-throughput hypocotyl phenotyping. *Plant physiology*.

Dolan, L., Janmaat, K., Willemsen, V., Linstead, P., Poethig, S., Roberts, K., and Scheres, B. (1993). Cellular organisation of the arabidopsis thaliana root. *Development*, 119:71–84.

Doyle, S. M., Haeger, A., Vain, T., Rigal, A., Viotti, C., Łangowska, M., Ma, Q., Friml, J., Raikhel, N. V., Hicks, G. R., and Robert, S. (2015). An early secretory pathway mediated by gnom-like 1 and gnom is essential for basal polarity establishment in arabidopsis thaliana. *Proceedings*

of the National Academy of Sciences of the United States of America, 112:E806–E815.

Du, Y. and Scheres, B. (2017). Plethora transcription factors orchestrate de novo organ patterning during arabidopsis lateral root outgrowth. *Proceedings of the National Academy of Sciences of the United States of America*, 114:11709–11714.

Dubos, C., Stracke, R., Grotewold, E., Weisshaar, B., Martin, C., and Lepiniec, L. (2010). Myb transcription factors in arabidopsis. *Trends in plant science*, 15:573–581.

Dvořák Tomaštíková, E., Rutten, T., Dvořák, P., Tugai, A., Ptošková, K., Petrovská, B., van Damme, D., Houben, A., Doležel, J., and Demidov, D. (2020). Functional divergence of microtubule-associated tpx2 family members in , javax.xml.bind.jaxbelement@1e6c818d, . *International journal of molecular sciences*, 21.

Efroni, I. and Birnbaum, K. D. (2016). The potential of single-cell profiling in plants. *Genome biology*, 17:65.

Efroni, I., Ip, P.-L., Nawy, T., Mello, A., and Birnbaum, K. D. (2015). Quantification of cell identity from single-cell gene expression profiles. *Genome biology*, 16:9.

Efroni, I., Mello, A., Nawy, T., Ip, P.-L., Rahni, R., DelRose, N., Powers, A., Satija, R., and Birnbaum, K. D. (2016). Root regeneration triggers an embryo-like sequence guided by hormonal interactions. *Cell*, 165:1721–1733.

Epple, P., Mack, A. A., Morris, V. R. F., and Dangl, J. L. (2003). Antagonistic control of oxidative stress-induced cell death in arabidopsis by two related, plant-specific zinc finger proteins. *Proceedings of the National Academy of Sciences of the United States of America*, 100:6831–6836.

Espinosa-Ruiz, A., Martínez, C., de Lucas, M., Fàbregas, N., Bosch, N.,

Caño-Delgado, A. I., and Prat, S. (2017). Topless mediates brassinosteroid control of shoot boundaries and root meristem development in , javax.xml.bind.jaxbelement@29683561, . *Development*, 144:1619–1628.

Fàbregas, N., Li, N., Boeren, S., Nash, T. E., Goshe, M. B., Clouse, S. D., de Vries, S., and Caño-Delgado, A. I. (2013). The brassinosteroid insensitive1-like3 signalosome complex regulates arabidopsis root development. *The Plant cell*, 25:3377–3388.

Fàbregas, N., Lozano-Elena, F., Blasco-Escámez, D., Tohge, T., Martínez-Andújar, C., Albacete, A., Osorio, S., Bustamante, M., Riechmann, J. L., Nomura, T., Yokota, T., Conesa, A., Alfocea, F. P., Fernie, A. R., and Caño-Delgado, A. I. (2018). Overexpression of the vascular brassinosteroid receptor brl3 confers drought resistance without penalizing plant growth. *Nature communications*, 9:4680.

Fernández-Pérez, F., Vivar, T., Pomar, F., Pedreño, M. A., and Novo-Uzal, E. (2015). Peroxidase 4 is involved in syringyl lignin formation in arabidopsis thaliana. *Journal of plant physiology*, 175:86–94.

Forzani, C., Aichinger, E., Sornay, E., Willemsen, V., Laux, T., Dewitte, W., and Murray, J. A. H. (2014). Wox5 suppresses cyclin d activity to establish quiescence at the center of the root stem cell niche. *Current biology : CB*, 24:1939–1944.

French, A., Ubeda-Tomás, S., Holman, T. J., Bennett, M. J., and Pridmore, T. (2009). High-throughput quantification of root growth using a novel image-analysis tool. *Plant physiology*, 150:1784–1795.

Friml, J., Vieten, A., Sauer, M., Weijers, D., Schwarz, H., Hamann, T., Offringa, R., and Jürgens, G. (2003). Efflux-dependent auxin gradients establish the apical-basal axis of arabidopsis. *Nature*, 426:147–153.

Fuentes, S., Pires, N., and Østergaard, L. (2010). A clade in the quasimodo2 family evolved with vascular plants and supports a role for cell

wall composition in adaptation to environmental changes. *Plant molecular biology*, 73:605–615.

Fukuda, H. (1997). Tracheary element differentiation. *The Plant Cell*, 9(7):1147–1156.

Fulcher, N. and Sablowski, R. (2009). Hypersensitivity to dna damage in plant stem cell niches. *Proceedings of the National Academy of Sciences of the United States of America*, 106:20984–20988.

Galinha, C., Hofhuis, H., Luijten, M., Willemsen, V., Blilou, I., Heidstra, R., and Scheres, B. (2007). Plethora proteins as dose-dependent master regulators of arabidopsis root development. *Nature*, 449:1053–1057.

García-Gómez, M. L., Ornelas-Ayala, D., Garay-Arroyo, A., García-Ponce, B., Sánchez, M. d. l. P., and Álvarez Buylla, E. R. (2020). A system-level mechanistic explanation for asymmetric stem cell fates: Arabidopsis thaliana root niche as a study system. *Scientific reports*, 10:3525.

Ghuge, S. A., Carucci, A., Rodrigues-Pousada, R. A., Tisi, A., Franchi, S., Tavladoraki, P., Angelini, R., and Cona, A. (2015). The apoplastic copper amine oxidase1 mediates jasmonic acid-induced protoxylem differentiation in arabidopsis roots. *Plant physiology*, 168:690–707.

Gietz, R. D. and Woods, R. A. (2002). Transformation of yeast by lithium acetate/single-stranded carrier dna/polyethylene glycol method. *Methods in enzymology*, 350:87–96.

Glumov, N. I., Kolomiez, E. I., and Sergeev, V. V. (1995). Detection of the objects on the image using a sliding window mode. *Optics and Laser Technology*, 27(4):241–250.

Goh, T., Toyokura, K., Wells, D. M., Swarup, K., Yamamoto, M., Mimura, T., Weijers, D., Fukaki, H., Laplaze, L., Bennett, M. J., and Guyomarc'h, S. (2016). Quiescent center initiation in the arabidopsis lat-

eral root primordia is dependent on the scarecrow transcription factor. *Development*, 143:3363–3371.

Gonzali, S., Novi, G., Loreti, E., Paolicchi, F., Poggi, A., Alpi, A., and Perata, P. (2005). A turanose-insensitive mutant suggests a role for wox5 in auxin homeostasis in arabidopsis thaliana. *The Plant journal*, 44:633–645.

González, A., Sevillano, X., Betegón-Putze, I., Blasco-Escámez, D., Ferrer, M., and Caño-Delgado, A. I. (2020). Myroot 2.0: An automatic tool for high throughput and accurate primary root length measurement. *Computers and Electronics in Agriculture*, 168:105125.

González-García, M.-P., Pavelescu, I., Canela, A., Sevillano, X., Leehy, K. A., Nelson, A. D. L., Ibañes, M., Shippen, D. E., Blasco, M. A., and Caño-Delgado, A. I. (2015). Single-cell telomere-length quantification couples telomere length to meristem activity and stem cell development in arabidopsis. *Cell reports*, 11:977–989.

González-García, M.-P., Vilarrasa-Blasi, J., Zhiponova, M., Divol, F., Mora-García, S., Russinova, E., and Caño-Delgado, A. I. (2011). Brassinosteroids control meristem size by promoting cell cycle progression in arabidopsis roots. *Development (Cambridge, England)*, 138:849–859.

Grabov, A., Ashley, M. K., Rigas, S., Hatzopoulos, P., Dolan, L., and Vicente-Agullo, F. (2005). Morphometric analysis of root shape. *The New phytologist*, 165:641–651.

Grebe, M. (2012). The patterning of epidermal hairs in arabidopsis–updated. *Current opinion in plant biology*, 15:31–37.

Griffith, M. E., Mayer, U., Capron, A., Ngo, Q. A., Surendrarao, A., McClinton, R., Jürgens, G., and Sundaresan, V. (2007). The tormoz gene encodes a nucleolar protein required for regulated division planes and embryo development in arabidopsis. *The Plant cell*, 19:2246–2263.

Groszmann, M., Paicu, T., Alvarez, J. P., Swain, S. M., and Smyth, D. R. (2011). Spatula and alcatraz, are partially redundant, functionally diverging bhlh genes required for arabidopsis gynoecium and fruit development. *The Plant journal*, 68:816–829.

Grunewald, W., De Smet, I., De Rybel, B., Robert, H. S., van de Cotte, B., Willemsen, V., Gheysen, G., Weijers, D., Friml, J., and Beeckman, T. (2013). Tightly controlled wrky23 expression mediates arabidopsis embryo development. *EMBO reports*, 14:1136–1142.

Grunewald, W., De Smet, I., Lewis, D. R., Löfke, C., Jansen, L., Goeminne, G., Vanden Bossche, R., Karimi, M., De Rybel, B., Vanholme, B., Teichmann, T., Boerjan, W., Van Montagu, M. C. E., Gheysen, G., Muday, G. K., Friml, J., and Beeckman, T. (2012). Transcription factor wrky23 assists auxin distribution patterns during arabidopsis root development through local control on flavonol biosynthesis. *Proceedings of the National Academy of Sciences of the United States of America*, 109:1554–1559.

Gu, F., Bringmann, M., Combs, J. R., Yang, J., Bergmann, D. C., and Nielsen, E. (2016). Arabidopsis csld5 functions in cell plate formation in a cell cycle-dependent manner. *The Plant Cell*, 28(7):1722–1737.

Gupta, A., Rico-Medina, A., and Caño-Delgado, A. I. (2020). The physiology of plant responses to drought. *Science*, 368:266–269.

Gutierrez, C. (2009). The arabidopsis cell division cycle. *The arabidopsis book*, 7:e0120.

Hacham, Y., Holland, N., Butterfield, C., Ubeda-Tomas, S., Bennett, M. J., Chory, J., and Savaldi-Goldstein, S. (2011). Brassinosteroid perception in the epidermis controls root meristem size. *Development*, 138:839–848.

Haghverdi, L., Büttner, M., Wolf, F. A., Buettner, F., and Theis, F. J.

(2016). Diffusion pseudotime robustly reconstructs lineage branching. *Nature methods*, 13:845–848.

Hardtke, C. S. and Berleth, T. (1998). The arabidopsis gene monopteros encodes a transcription factor mediating embryo axis formation and vascular development. *The EMBO journal*, 17:1405–1411.

Hasan, S. A., Hayat, S., and Ahmad, A. (2011). Brassinosteroids protect photosynthetic machinery against the cadmium induced oxidative stress in two tomato cultivars. *Chemosphere*, 84:1446–1451.

Hauser, M. T., Morikami, A., and Benfey, P. N. (1995). Conditional root expansion mutants of arabidopsis. *Development*, 121:1237–1252.

He, J.-X., Gendron, J. M., Sun, Y., Gampala, S. S. L., Gendron, N., Sun, C. Q., and Wang, Z.-Y. (2005). Bzr1 is a transcriptional repressor with dual roles in brassinosteroid homeostasis and growth responses. *Science*, 307:1634–1638.

Heberle, H., Meirelles, G. V., da Silva, F. R., Telles, G. P., and Minghim, R. (2015). Interactivenn: a web-based tool for the analysis of sets through venn diagrams. *BMC bioinformatics*, 16:169.

Heidstra, R. and Sabatini, S. (2014). Plant and animal stem cells: similar yet different. *Nature reviews. Molecular cell biology*, 15:301–312.

Helariutta, Y., Fukaki, H., Wysocka-Diller, J., Nakajima, K., Jung, J., Sena, G., Hauser, M. T., and Benfey, P. N. (2000). The short-root gene controls radial patterning of the arabidopsis root through radial signaling. *Cell*, 101:555–567.

Helm, M., Schmid, M., Hierl, G., Terneus, K., Tan, L., Lottspeich, F., Kieliszewski, M. J., and Gietl, C. (2008). Kdel-tailed cysteine endopeptidases involved in programmed cell death, intercalation of new cells, and dismantling of extensin scaffolds. *American journal of botany*, 95:1049–1062.

Heyman, J., Cools, T., Canher, B., Shavialenka, S., Traas, J., Vercauteren, I., Van den Daele, H., Persiau, G., De Jaeger, G., Sugimoto, K., and De Veylder, L. (2016). The heterodimeric transcription factor complex erf115-pat1 grants regeneration competence. *Nature plants*, 2:16165.

Heyman, J., Cools, T., Vandenbussche, F., Heyndrickx, K. S., Van Leene, J., Vercauteren, I., Vanderauwera, S., Vandepoele, K., De Jaeger, G., Van Der Straeten, D., and De Veylder, L. (2013). Erf115 controls root quiescent center cell division and stem cell replenishment. *Science*, 342:860–863.

Heyman, J., Kumpf, R. P., and De Veylder, L. (2014). A quiescent path to plant longevity. *Trends in cell biology*, 24:443–448.

Hossain, M. S., Kawakatsu, T., Kim, K. D., Zhang, N., Nguyen, C. T., Khan, S. M., Batek, J. M., Joshi, T., Schmutz, J., Grimwood, J., Schmitz, R. J., Xu, D., Jackson, S. A., Ecker, J. R., and Stacey, G. (2017). Divergent cytosine dna methylation patterns in single-cell, soybean root hairs. *The New phytologist*, 214:808–819.

Hossain, Z., McGarvey, B., Amyot, L., Gruber, M., Jung, J., and Hannoufa, A. (2012). Diminuto 1 affects the lignin profile and secondary cell wall formation in arabidopsis. *Planta*, 235:485–498.

Hu, Z., Cools, T., and De Veylder, L. (2016). Mechanisms used by plants to cope with dna damage. *Annual review of plant biology*, 67:439–462.

Huang, H., Ullah, F., Zhou, D.-X., Yi, M., and Zhao, Y. (2019). Mechanisms of ros regulation of plant development and stress responses. *Frontiers in plant science*, 10:800.

Hulsen, T., de Vlieg, J., and Alkema, W. (2008). Biovenn - a web application for the comparison and visualization of biological lists using area-proportional venn diagrams. *BMC genomics*, 9:488.

Hyun, Y. and Lee, I. (2006). Kidari, encoding a non-dna binding bhlh

protein, represses light signal transduction in arabidopsis thaliana. *Plant molecular biology*, 61:283–296.

Ibañes, M., Fàbregas, N., Chory, J., and Caño-Delgado, A. I. (2009). Brassinosteroid signaling and auxin transport are required to establish the periodic pattern of arabidopsis shoot vascular bundles. *Proceedings of the National Academy of Sciences of the United States of America*, 106:13630–13635.

Imlau, A., Truernit, E., and Sauer, N. (1999). Cell-to-cell and long-distance trafficking of the green fluorescent protein in the phloem and symplastic unloading of the protein into sink tissues. *The Plant cell*, 11:309–322.

Ingkasuwan, P., Netrphan, S., Prasitwattanaseree, S., Tanticharoen, M., Bhumiratana, S., Meechai, A., Chaijaruwanich, J., Takahashi, H., and Cheevadhanarak, S. (2012). Inferring transcriptional gene regulation network of starch metabolism in arabidopsis thaliana leaves using graphical gaussian model. *BMC systems biology*, 6:100.

Iqbal, M. M., Hurgobin, B., Holme, A. L., Appels, R., and Kaur, P. (2020). Status and potential of single-cell transcriptomics for understanding plant development and functional biology. *Cytometry. Part A : the journal of the International Society for Analytical Cytology.*

Ishida, T., Kurata, T., Okada, K., and Wada, T. (2008). A genetic regulatory network in the development of trichomes and root hairs. *Annual review of plant biology*, 59:365–386.

Ishikawa, H. and Evans, M. L. (1995). Specialized zones of development in roots. *Plant physiology*, 109:725–727.

Islam, M. M., Ye, W., Matsushima, D., Munemasa, S., Okuma, E., Nakamura, Y., Biswas, S., Mano, J., and Murata, Y. (2016). Reactive carbonyl species mediate aba signaling in guard cells. *Plant & cell physi-*

ology, 57:2552–2563.

Iyer-Pascuzzi, A., Simpson, J., Herrera-Estrella, L., and Benfey, P. N. (2009). Functional genomics of root growth and development in arabidopsis. *Current opinion in plant biology*, 12:165–171.

Jain, A. K., Murty, M. N., and Flynn, P. J. (1999). Data clustering: A review. *ACM Comput. Surv.*, 31(3):264–323.

Jansen, M. A., van den Noort, R. E., Tan, M. Y., Prinsen, E., Lagrimini, L. M., and Thorneley, R. N. (2001). Phenol-oxidizing peroxidases contribute to the protection of plants from ultraviolet radiation stress. *Plant physiology*, 126:1012–1023.

Jean-Baptiste, K., McFaline-Figueroa, J. L., Alexandre, C. M., Dorrity, M. W., Saunders, L., Bubb, K. L., Trapnell, C., Fields, S., Queitsch, C., and Cuperus, J. T. (2019). Dynamics of gene expression in single root cells of arabidopsis thaliana. *The Plant cell*, 31:993–1011.

Jeong, C. Y., Kim, J. H., Lee, W. J., Jin, J. Y., Kim, J., Hong, S.-W., and Lee, H. (2018). Atmyb56 regulates anthocyanin levels via the modulation of atgpt2 expression in response to sucrose in arabidopsis . *Molecules and cells*, 41:351–361.

Jones, M. A., Raymond, M. J., and Smirnoff, N. (2006). Analysis of the root-hair morphogenesis transcriptome reveals the molecular identity of six genes with roles in root-hair development in arabidopsis. *The Plant journal*, 45:83–100.

Jürgens, G., Mayer, U., Busch, M., Lukowitz, W., and Laux, T. (1995). Pattern formation in the arabidopsis embryo: a genetic perspective. *Philosophical transactions of the Royal Society of London. Series B, Biological sciences*, 350:19–25.

Kajala, K., Shaar-Moshe, L., Mason, G. A., Gouran, M., Rodriguez-Medina, J., Kawa, D., Pauluzzi, G., Reynoso, M., Canto-Pastor, A.,

Lau, V., Artur, M. A. S., West, D. A., Manzano, C., Gray, S. B., Yao, A. I., Bajic, M., Formentin, E., Nirmal, N., Rodriguez, A., Pasha, A., Borowsky, A. T., Deal, R. B., Kliebenstein, D., Hvidsten, T. R., Provart, N. J., Sinha, N., Runcie, D. E., Bailey-Serres, J., and Brady, S. M. (2020). Innovation, conservation and repurposing of gene function in plant root cell type development. *bioRxiv*.

Kamata, N., Okada, H., Komeda, Y., and Takahashi, T. (2013). Mutations in epidermis-specific hd-zip iv genes affect floral organ identity in arabidopsis thaliana. *The Plant journal*, 75:430–440.

Kamiya, T., Borghi, M., Wang, P., Danku, J. M. C., Kalmbach, L., Hosmani, P. S., Naseer, S., Fujiwara, T., Geldner, N., and Salt, D. E. (2015). The myb36 transcription factor orchestrates casparian strip formation. *Proceedings of the National Academy of Sciences of the United States of America*, 112:10533–10538.

Kang, Y. H., Breda, A., and Hardtke, C. S. (2017). Brassinosteroid signaling directs formative cell divisions and protophloem differentiation in arabidopsis root meristems. *Development*, 144:272–280.

Karaiskos, N., Wahle, P., Alles, J., Boltengagen, A., Ayoub, S., Kipar, C., Kocks, C., Rajewsky, N., and Zinzen, R. P. (2017). The drosophila embryo at single-cell transcriptome resolution. *Science (New York, N.Y.)*, 358:194–199.

Kerk, N. M., Ceserani, T., Tausta, S. L., Sussex, I. M., and Nelson, T. M. (2003). Laser capture microdissection of cells from plant tissues. *Plant physiology*, 132:27–35.

Kiba, T., Inaba, J., Kudo, T., Ueda, N., Konishi, M., Mitsuda, N., Takiguchi, Y., Kondou, Y., Yoshizumi, T., Ohme-Takagi, M., Matsui, M., Yano, K., Yanagisawa, S., and Sakakibara, H. (2018). Repression of nitrogen starvation responses by members of the arabidopsis garp-type

transcription factor nigt1/hrs1 subfamily. *The Plant cell*, 30:925–945.

Kim, J.-Y., Symeonidi, E., Pang, T. Y., Denyer, T., Weidauer, D., Bezrutczyk, M., Miras, M., Zöllner, N., Wudick, M. M., Lercher, M., Chen, L.-Q., Timmermans, M. C., and Frommer, W. B. (2020). Unique and distinct identities and functions of leaf phloem cells revealed by single cell transcriptomics. *bioRxiv*.

Kim, K.-C., Lai, Z., Fan, B., and Chen, Z. (2008). Arabidopsis wrky38 and wrky62 transcription factors interact with histone deacetylase 19 in basal defense. *The Plant cell*, 20:2357–2371.

Kim, M. J., Ruzicka, D., Shin, R., and Schachtman, D. P. (2012). The arabidopsis ap2/erf transcription factor rap2.11 modulates plant response to low-potassium conditions. *Molecular plant*, 5:1042–1057.

Kinoshita, T., Caño-Delgado, A., Seto, H., Hiranuma, S., Fujioka, S., Yoshida, S., and Chory, J. (2005). Binding of brassinosteroids to the extracellular domain of plant receptor kinase bri1. *Nature*, 433:167–171.

Kodaira, K.-S., Qin, F., Tran, L.-S. P., Maruyama, K., Kidokoro, S., Fujita, Y., Shinozaki, K., and Yamaguchi-Shinozaki, K. (2011). Arabidopsis cys2/his2 zinc-finger proteins azf1 and azf2 negatively regulate abscisic acid-repressive and auxin-inducible genes under abiotic stress conditions. *Plant physiology*, 157:742–756.

Kärblane, K., Gerassimenko, J., Nigul, L., Piirsoo, A., Smialowska, A., Vinkel, K., Kylsten, P., Ekwall, K., Swoboda, P., Truve, E., and Sarmiento, C. (2015). Abce1 is a highly conserved rna silencing suppressor. *PloS one*, 10:e0116702.

Krishnakumar, V., Hanlon, M. R., Contrino, S., Ferlanti, E. S., Karamycheva, S., Kim, M., Rosen, B. D., Cheng, C.-Y., Moreira, W., Mock, S. A., Stubbs, J., Sullivan, J. M., Krampis, K., Miller, J. R., Micklem, G., Vaughn, M., and Town, C. D. (2014). Araport: the Arabidopsis

Information Portal. *Nucleic Acids Research*, 43(D1):D1003–D1009.

Krumova, S., Zhiponova, M., Dankov, K., Velikova, V., Balashev, K., Andreeva, T., Russinova, E., and Taneva, S. (2013). Brassinosteroids regulate the thylakoid membrane architecture and the photosystem ii function. *Journal of photochemistry and photobiology.*, 126:97–104.

Kubo, M., Udagawa, M., Nishikubo, N., Horiguchi, G., Yamaguchi, M., Ito, J., Mimura, T., Fukuda, H., and Demura, T. (2005). Transcription switches for protoxylem and metaxylem vessel formation. *Genes & development*, 19:1855–1860.

Kuijken, R. C. P., van Eeuwijk, F. A., Marcelis, L. F. M., and Bouwmeester, H. J. (2015). Root phenotyping: from component trait in the lab to breeding. *Journal of experimental botany*, 66:5389–5401.

Lakehal, A., Chaabouni, S., Cavel, E., Le Hir, R., Ranjan, A., Raneshan, Z., Novák, O., Păcurar, D. I., Perrone, I., Jobert, F., Gutierrez, L., Bakò, L., and Bellini, C. (2019). A molecular framework for the control of adventitious rooting by tir1/afb2-aux/iaa-dependent auxin signaling in arabidopsis. *Molecular plant*, 12:1499–1514.

Lara, A., Ródenas, R., Andrés, Z., Martínez, V., Quintero, F. J., Nieves-Cordones, M., Botella, M. A., and Rubio, F. (2020). Arabidopsis k+ transporter hak5-mediated high-affinity root k+ uptake is regulated by protein kinases cipk1 and cipk9. *Journal of experimental botany*, 71:5053–5060.

Laskowski, M. J., Williams, M. E., Nusbaum, H. C., and Sussex, I. M. (1995). Formation of lateral root meristems is a two-stage process. *Development*, 121:3303–3310.

Le Bot, J., Serra, V., Fabre, J., Draye, X., Adamowicz, S., and Pages, L. (2010). Dart: a software to analyse root system architecture and development from captured images. *Plant Soil*, 326(13).

Lee, H.-S., Kim, Y., Pham, G., Kim, J. W., Song, J.-H., Lee, Y., Hwang, Y.-S., Roux, S. J., and Kim, S.-H. (2015). Brassinazole resistant 1 (bzr1)-dependent brassinosteroid signalling pathway leads to ectopic activation of quiescent cell division and suppresses columella stem cell differentiation. *Journal of experimental botany*, 66:4835–4849.

Lee, J.-Y., Colinas, J., Wang, J. Y., Mace, D., Ohler, U., and Benfey, P. N. (2006). Transcriptional and posttranscriptional regulation of transcription factor expression in arabidopsis roots. *Proceedings of the National Academy of Sciences of the United States of America*, 103:6055–6060.

Levesque, M. P., Vernoux, T., Busch, W., Cui, H., Wang, J. Y., Blilou, I., Hassan, H., Nakajima, K., Matsumoto, N., Lohmann, J. U., Scheres, B., and Benfey, P. N. (2006). Whole-genome analysis of the short-root developmental pathway in arabidopsis. *PLoS biology*, 4:e143.

Li, B. and Dewey, C. N. (2011). Rsem: accurate transcript quantification from rna-seq data with or without a reference genome. *BMC bioinformatics*, 12:323.

Li, C. X., Yan, J. Y., Ren, J. Y., Sun, L., Xu, C., Li, G. X., Ding, Z. J., and Zheng, S. J. (2019). A wrky transcription factor confers aluminum tolerance via regulation of cell wall modifying genes. *Journal of integrative plant biology*.

Li, E., Bhargava, A., Qiang, W., Friedmann, M. C., Forneris, N., Savidge, R. A., Johnson, L. A., Mansfield, S. D., Ellis, B. E., and Douglas, C. J. (2012). The class ii knox gene knat7 negatively regulates secondary wall formation in arabidopsis and is functionally conserved in populus. *The New phytologist*, 194:102–115.

Li, J., Brader, G., and Palva, E. T. (2008). Kunitz trypsin inhibitor: an antagonist of cell death triggered by phytopathogens and fumonisin b1 in arabidopsis. *Molecular plant*, 1:482–495.

Li, J. and Chory, J. (1997). A putative leucine-rich repeat receptor kinase involved in brassinosteroid signal transduction. *Cell*, 90:929–938.

Li, J., Nam, K. H., Vafeados, D., and Chory, J. (2001). Bin2, a new brassinosteroid-insensitive locus in arabidopsis. *Plant physiology*, 127:14–22.

Li, J., Wen, J., Lease, K. A., Doke, J. T., Tax, F. E., and Walker, J. C. (2002). Bak1, an arabidopsis lrr receptor-like protein kinase, interacts with bri1 and modulates brassinosteroid signaling. *Cell*, 110:213–222.

Li, L., Shimada, T., Takahashi, H., Koumoto, Y., Shirakawa, M., Takagi, J., Zhao, X., Tu, B., Jin, H., Shen, Z., Han, B., Jia, M., Kondo, M., Nishimura, M., and Hara-Nishimura, I. (2013). Mag2 and three mag2-interacting proteins form an er-localized complex to facilitate storage protein transport in arabidopsis thaliana. *The Plant journal*, 76:781–791.

Li, L. and Xie, T. (2005). Stem cell niche: structure and function. *Annual review of cell and developmental biology*, 21:605–631.

Li, S. and Zachgo, S. (2013). Tcp3 interacts with r2r3-myb proteins, promotes flavonoid biosynthesis and negatively regulates the auxin response in arabidopsis thaliana. *The Plant journal*, 76:901–913.

Liang, T., Shi, C., Peng, Y., Tan, H., Xin, P., Yang, Y., Wang, F., Li, X., Chu, J., Huang, J., Yin, Y., and Liu, H. (2020). Brassinosteroid-activated bri1-ems-suppressor 1 inhibits flavonoid biosynthesis and coordinates growth and uv-b stress responses in plants. *The Plant Cell*.

Liebsch, D., Sunaryo, W., Holmlund, M., Norberg, M., Zhang, J., Hall, H. C., Helizon, H., Jin, X., Helariutta, Y., Nilsson, O., Polle, A., and Fischer, U. (2014). Class i knox transcription factors promote differentiation of cambial derivatives into xylem fibers in the arabidopsis hypocotyl. *Development*, 141:4311–4319.

Lima, J. V. and Lobato, A. K. S. (2017). Brassinosteroids improve photosystem ii efficiency, gas exchange, antioxidant enzymes and growth of cowpea plants exposed to water deficit. *Physiology and molecular biology of plants : an international journal of functional plant biology*, 23:59–72.

Liu, C. M. and Meinke, D. W. (1998). The titan mutants of arabidopsis are disrupted in mitosis and cell cycle control during seed development. *The Plant journal*, 16:21–31.

Liu, J., Magalhaes, J. V., Shaff, J., and Kochian, L. V. (2009). Aluminum-activated citrate and malate transporters from the mate and almt families function independently to confer arabidopsis aluminum tolerance. *The Plant journal*, 57:389–399.

Liu, X.-M., Nguyen, X. C., Kim, K. E., Han, H. J., Yoo, J., Lee, K., Kim, M. C., Yun, D.-J., and Chung, W. S. (2013). Phosphorylation of the zinc finger transcriptional regulator zat6 by mpk6 regulates arabidopsis seed germination under salt and osmotic stress. *Biochemical and biophysical research communications*, 430:1054–1059.

Lobet, G. (2017). Image analysis in plant sciences: Publish then perish. *Trends in plant science*, 22:559–566.

Lobet, G., Draye, X., and Périlleux, C. (2013). An online database for plant image analysis software tools. *Plant methods*, 9:38.

Lobet, G., Pagès, L., and Draye, X. (2011). A novel image-analysis toolbox enabling quantitative analysis of root system architecture. *Plant physiology*, 157:29–39.

Lobet, G., Pound, M. P., Diener, J., Pradal, C., Draye, X., Godin, C., Javaux, M., Leitner, D., Meunier, F., Nacry, P., Pridmore, T. P., and Schnepf, A. (2015). Root system markup language: toward a unified root architecture description language. *Plant physiology*, 167:617–627.

Long, Y., Stahl, Y., Weidtkamp-Peters, S., Postma, M., Zhou, W., Goedhart, J., Sánchez-Pérez, M.-I., Gadella, T. W. J., Simon, R., Scheres, B., and Blilou, I. (2017). In vivo fret-flim reveals cell-type-specific protein interactions in arabidopsis roots. *Nature*, 548:97–102.

Lopez-Anido, C. B., Vatén, A., Smoot, N. K., Sharma, N., Guo, V., Gong, Y., Anleu Gil, M. X., Weimer, A. K., and Bergmann, D. C. (2020). Single-cell resolution of lineage trajectories in the arabidopsis stomatal lineage and developing leaf. *bioRxiv*.

Lozano-Elena, F., Planas-Riverola, A., Vilarrasa-Blasi, J., Schwab, R., and Caño-Delgado, A. I. (2018). Paracrine brassinosteroid signaling at the stem cell niche controls cellular regeneration. *Journal of cell science*, 131.

Luecken, M. D. and Theis, F. J. (2019). Current best practices in single-cell rna-seq analysis: a tutorial. *Molecular systems biology*, 15:e8746.

Luo, D., Bernard, D. G., Balk, J., Hai, H., and Cui, X. (2012). The duf59 family gene ae7 acts in the cytosolic iron-sulfur cluster assembly pathway to maintain nuclear genome integrity in arabidopsis. *The Plant cell*, 24:4135–4148.

Ma, X., Denyer, T., and Timmermans, M. C. P. (2020). Pscb: A browser to explore plant single cell rna-sequencing data sets. *Plant physiology*, 183:464–467.

Ma, X., Zhang, Q., Zhu, Q., Liu, W., Chen, Y., Qiu, R., Wang, B., Yang, Z., Li, H., Lin, Y., Xie, Y., Shen, R., Chen, S., Wang, Z., Chen, Y., Guo, J., Chen, L., Zhao, X., Dong, Z., and Liu, Y.-G. (2015). A robust crispr/cas9 system for convenient, high-efficiency multiplex genome editing in monocot and dicot plants. *Molecular plant*, 8:1274–1284.

Malamy, J. E. and Benfey, P. N. (1997). Organization and cell differentiation in lateral roots of arabidopsis thaliana. *Development*, 124:33–44.

Marquès-Bueno, M. D. M., Morao, A. K., Cayrel, A., Platre, M. P., Barberon, M., Caillieux, E., Colot, V., Jaillais, Y., Roudier, F., and Vert, G. (2016). A versatile multisite gateway-compatible promoter and transgenic line collection for cell type-specific functional genomics in arabidopsis. *The Plant journal*, 85:320–333.

Martignago, D., Rico-Medina, A., Blasco-Escámez, D., Fontanet-Manzaneque, J. B., and Caño-Delgado, A. I. (2019). Drought resistance by engineering plant tissue-specific responses. *Frontiers in plant science*, 10:1676.

Mathieu, J., Yant, L. J., Mürdter, F., Küttner, F., and Schmid, M. (2009). Repression of flowering by the mir172 target smz. *PLoS biology*, 7:e1000148.

McInnes, L., Healy, J., and Melville, J. (2020). Umap: Uniform manifold approximation and projection for dimension reduction.

Mendoza, L. and Alvarez-Buylla, E. R. (2000). Genetic regulation of root hair development in arabidopsis thaliana: a network model. *Journal of theoretical biology*, 204:311–326.

Mähönen, A. P., Bishopp, A., Higuchi, M., Nieminen, K. M., Kinoshita, K., Törmäkangas, K., Ikeda, Y., Oka, A., Kakimoto, T., and Helariutta, Y. (2006a). Cytokinin signaling and its inhibitor ahp6 regulate cell fate during vascular development. *Science*, 311:94–98.

Mähönen, A. P., Bonke, M., Kauppinen, L., Riikonen, M., Benfey, P. N., and Helariutta, Y. (2000). A novel two-component hybrid molecule regulates vascular morphogenesis of the arabidopsis root. *Genes & development*, 14:2938–2943.

Mähönen, A. P., Higuchi, M., Törmäkangas, K., Miyawaki, K., Pischke, M. S., Sussman, M. R., Helariutta, Y., and Kakimoto, T. (2006b). Cytokinins regulate a bidirectional phosphorelay network in arabidopsis.

Current biology, 16:1116–1122.

Mähönen, A. P., Ten Tusscher, K., Siligato, R., Smetana, O., Díaz-Triviño, S., Salojärvi, J., Wachsman, G., Prasad, K., Heidstra, R., and Scheres, B. (2014). Plethora gradient formation mechanism separates auxin responses. *Nature*, 515:125–129.

Michniewicz, M., Zago, M. K., Abas, L., Weijers, D., Schweighofer, A., Meskiene, I., Heisler, M. G., Ohno, C., Zhang, J., Huang, F., Schwab, R., Weigel, D., Meyerowitz, E. M., Luschnig, C., Offringa, R., and Friml, J. (2007). Antagonistic regulation of pin phosphorylation by pp2a and pinoid directs auxin flux. *Cell*, 130:1044–1056.

Mitsuda, N., Iwase, A., Yamamoto, H., Yoshida, M., Seki, M., Shinozaki, K., and Ohme-Takagi, M. (2007). Nac transcription factors, nst1 and nst3, are key regulators of the formation of secondary walls in woody tissues of arabidopsis. *The Plant cell*, 19:270–280.

Miyashima, S., Roszak, P., Sevilem, I., Toyokura, K., Blob, B., Heo, J.-O., Mellor, N., Help-Rinta-Rahko, H., Otero, S., Smet, W., Boekschoten, M., Hooiveld, G., Hashimoto, K., Smetana, O., Siligato, R., Wallner, E.-S., Mähönen, A. P., Kondo, Y., Melnyk, C. W., Greb, T., Nakajima, K., Sozzani, R., Bishopp, A., De Rybel, B., and Helariutta, Y. (2019). Mobile pear transcription factors integrate positional cues to prime cambial growth. *Nature*, 565:490–494.

Moignard, V., Woodhouse, S., Haghverdi, L., Lilly, A. J., Tanaka, Y., Wilkinson, A. C., Buettner, F., Macaulay, I. C., Jawaid, W., Diamanti, E., Nishikawa, S.-I., Piterman, N., Kouskoff, V., Theis, F. J., Fisher, J., and Göttgens, B. (2015). Decoding the regulatory network of early blood development from single-cell gene expression measurements. *Nature biotechnology*, 33:269–276.

Moon, K. R., Stanley, J. S., Burkhardt, D., van Dijk, D., Wolf, G., and Kr-

ishnaswamy, S. (2018). Manifold learning-based methods for analyzing single-cell rna-sequencing data. *Current Opinion in Systems Biology*, 7:36 – 46. • Future of systems biology• Genomics and epigenomics.

Motte, H., Vanneste, S., and Beeckman, T. (2019). Molecular and environmental regulation of root development. *Annual review of plant biology*, 70:465–488.

Moubayidin, L., Di Mambro, R., Sozzani, R., Pacifici, E., Salvi, E., Terpstra, I., Bao, D., van Dijken, A., Dello Ioio, R., Perilli, S., Ljung, K., Benfey, P. N., Heidstra, R., Costantino, P., and Sabatini, S. (2013). Spatial coordination between stem cell activity and cell differentiation in the root meristem. *Developmental cell*, 26:405–415.

Mouchel, C. F., Briggs, G. C., and Hardtke, C. S. (2004). Natural genetic variation in arabidopsis identifies brevis radix, a novel regulator of cell proliferation and elongation in the root. *Genes & development*, 18:700–714.

Moussaieff, A., Rogachev, I., Brodsky, L., Malitsky, S., Toal, T. W., Belcher, H., Yativ, M., Brady, S. M., Benfey, P. N., and Aharoni, A. (2013). High-resolution metabolic mapping of cell types in plant roots. *Proceedings of the National Academy of Sciences of the United States of America*, 110:E1232–E1241.

Muraro, D., Mellor, N., Pound, M. P., Help, H., Lucas, M., Chopard, J., Byrne, H. M., Godin, C., Hodgman, T. C., King, J. R., Pridmore, T. P., Helariutta, Y., Bennett, M. J., and Bishopp, A. (2014). Integration of hormonal signaling networks and mobile micrornas is required for vascular patterning in arabidopsis roots. *Proceedings of the National Academy of Sciences of the United States of America*, 111:857–862.

Nagel, K. A., Putz, A., Gilmer, F., Heinz, K., Fischbach, A., Pfeifer, J., Faget, M., Blossfeld, S., Ernst, M., Dimaki, C., Kastenholz, B.,

Kleinert, A.-K., Galinski, A., Scharr, H., Fiorani, F., and Schurr, U. (2012). GROWSCREEN-rhizo is a novel phenotyping robot enabling simultaneous measurements of root and shoot growth for plants grown in soil-filled rhizotrons. *Functional Plant Biology*, 39(11):891.

Nakajima, K., Sena, G., Nawy, T., and Benfey, P. N. (2001). Intercellular movement of the putative transcription factor shr in root patterning. *Nature*, 413:307–311.

Nam, K. H. and Li, J. (2002). Bri1/bak1, a receptor kinase pair mediating brassinosteroid signaling. *Cell*, 110:203–212.

Nawy, T., Lee, J.-Y., Colinas, J., Wang, J. Y., Thongrod, S. C., Malamy, J. E., Birnbaum, K., and Benfey, P. N. (2005). Transcriptional profile of the arabidopsis root quiescent center. *The Plant cell*, 17:1908–1925.

Nelms, B. and Walbot, V. (2019). Defining the developmental program leading to meiosis in maize. *Science*, 364:52–56.

Neumann, U., Brandizzi, F., and Hawes, C. (2003). Protein transport in plant cells: in and out of the golgi. *Annals of botany*, 92:167–180.

Nolan, T. M., Vukašinović, N., Liu, D., Russinova, E., and Yin, Y. (2020). Brassinosteroids: Multidimensional regulators of plant growth, development, and stress responses. *The Plant cell*, 32:295–318.

Nueda, M. J., Ferrer, A., and Conesa, A. (2012). Arsyn: a method for the identification and removal of systematic noise in multifactorial time course microarray experiments. *Biostatistics*, 13:553–66.

Ogata, K., Kanei-Ishii, C., Sasaki, M., Hatanaka, H., Nagadoi, A., Enari, M., Nakamura, H., Nishimura, Y., Ishii, S., and Sarai, A. (1996). The cavity in the hydrophobic core of myb dna-binding domain is reserved for dna recognition and trans-activation. *Nature structural biology*, 3:178–187.

Ohashi-Ito, K. and Bergmann, D. C. (2007). Regulation of the arabidopsis

root vascular initial population by lonesome highway. *Development*, 134:2959–2968.

Ohashi-Ito, K., Oda, Y., and Fukuda, H. (2010). Arabidopsis vascular-related nac-domain6 directly regulates the genes that govern programmed cell death and secondary wall formation during xylem differentiation. *The Plant cell*, 22:3461–3473.

Ohashi-Ito, K., Saegusa, M., Iwamoto, K., Oda, Y., Katayama, H., Kojima, M., Sakakibara, H., and Fukuda, H. (2014). A bhlh complex activates vascular cell division via cytokinin action in root apical meristem. *Current biology*, 24:2053–2058.

Olsen, K. M., Lea, U. S., Slimestad, R., Verheul, M., and Lillo, C. (2008). Differential expression of four arabidopsis pal genes; pal1 and pal2 have functional specialization in abiotic environmental-triggered flavonoid synthesis. *Journal of plant physiology*, 165:1491–1499.

Ortega-Martínez, O., Pernas, M., Carol, R. J., and Dolan, L. (2007). Ethylene modulates stem cell division in the arabidopsis thaliana root. *Science*, 317:507–510.

Otsu, N. (1979). A threshold selection method from gray-level histograms. *IEEE Transactions on Systems, Man, and Cybernetics*, 9(1):62–66.

Pace, J., Lee, N., Naik, H. S., Ganapathysubramanian, B., and Lübberstedt, T. (2014). Analysis of maize (zea mays l.) seedling roots with the high-throughput image analysis tool ARIA (automatic root image analysis). *PLoS ONE*, 9(9):e108255.

Palm, D., Simm, S., Darm, K., Weis, B. L., Ruprecht, M., Schleiff, E., and Scharf, C. (2016). Proteome distribution between nucleoplasm and nucleolus and its relation to ribosome biogenesis in arabidopsis thaliana. *RNA biology*, 13:441–454.

Parekh, S., Ziegenhain, C., Vieth, B., Enard, W., and Hellmann, I. (2018).

zumis - a fast and flexible pipeline to process rna sequencing data with umis. *GigaScience*, 7.

Parker, J. S., Cavell, A. C., Dolan, L., Roberts, K., and Grierson, C. S. (2000). Genetic interactions during root hair morphogenesis in arabidopsis. *The Plant cell*, 12:1961–1974.

Peer, W. A., Blakeslee, J. J., Yang, H., and Murphy, A. S. (2011). Seven things we think we know about auxin transport. *Molecular plant*, 4:487–504.

Peer, W. A., Cheng, Y., and Murphy, A. S. (2013). Evidence of oxidative attenuation of auxin signalling. *Journal of experimental botany*, 64:2629–2639.

Peer, W. A. and Murphy, A. S. (2007). Flavonoids and auxin transport: modulators or regulators? *Trends in plant science*, 12:556–563.

Peng, T., Zhu, Q., Yin, P., and Tan, K. (2019). Scrabble: single-cell rna-seq imputation constrained by bulk rna-seq data. *Genome biology*, 20:88.

Petersson, S. V., Johansson, A. I., Kowalczyk, M., Makoveychuk, A., Wang, J. Y., Moritz, T., Grebe, M., Benfey, P. N., Sandberg, G., and Ljung, K. (2009). An auxin gradient and maximum in the arabidopsis root apex shown by high-resolution cell-specific analysis of iaa distribution and synthesis. *The Plant cell*, 21:1659–1668.

Pfister, A., Barberon, M., Alassimone, J., Kalmbach, L., Lee, Y., Vermeer, J. E. M., Yamazaki, M., Li, G., Maurel, C., Takano, J., Kamiya, T., Salt, D. E., Roppolo, D., and Geldner, N. (2014). A receptor-like kinase mutant with absent endodermal diffusion barrier displays selective nutrient homeostasis defects. *eLife*, 3:e03115.

Pi, L., Aichinger, E., van der Graaff, E., Llavata-Peris, C. I., Weijers, D., Hennig, L., Groot, E., and Laux, T. (2015). Organizer-derived wox5

signal maintains root columella stem cells through chromatin-mediated repression of cdf4 expression. *Developmental cell*, 33:576–588.

Pietra, S., Gustavsson, A., Kiefer, C., Kalmbach, L., Hörstedt, P., Ikeda, Y., Stepanova, A. N., Alonso, J. M., and Grebe, M. (2013). Arabidopsis sabre and clasp interact to stabilize cell division plane orientation and planar polarity. *Nature communications*, 4:2779.

Pietra, S., Lang, P., and Grebe, M. (2015). Sabre is required for stabilization of root hair patterning in arabidopsis thaliana. *Physiologia plantarum*, 153:440–453.

Piotrowski, M., Janowitz, T., and Kneifel, H. (2003). Plant c-n hydrolases and the identification of a plant n-carbamoylputrescine amidohydrolase involved in polyamine biosynthesis. *The Journal of biological chemistry*, 278:1708–1712.

Planas-Riverola, A., Gupta, A., Betegon-Putze, I., Bosch, N., Ibanes, M., and Cano-Delgado, A. I. (2019). Brassinosteroid signaling in plant development and adaptation to stress. *Development*, 146(5).

Pollastri, S. and Tattini, M. (2011). Flavonols: old compounds for old roles. *Annals of botany*, 108:1225–1233.

Potuschak, T., Lechner, E., Parmentier, Y., Yanagisawa, S., Grava, S., Koncz, C., and Genschik, P. (2003). Ein3-dependent regulation of plant ethylene hormone signaling by two arabidopsis f box proteins: Ebf1 and ebf2. *Cell*, 115:679–689.

Pound, M. P., French, A. P., Atkinson, J. A., Wells, D. M., Bennett, M. J., and Pridmore, T. (2013). Rootnav: navigating images of complex root architectures. *Plant physiology*, 162:1802–1814.

Qiu, P. (2020). Embracing the dropouts in single-cell rna-seq analysis. *Nature communications*, 11:1169.

Quigley, F., Rosenberg, J. M., Shachar-Hill, Y., and Bohnert, H. J. (2002).

From genome to function: the arabidopsis aquaporins. *Genome biology*, 3:RESEARCH0001.

R Development Core Team (2008). R: A language and environment for statistical computing. ISBN 3-900051-07-0.

Rademacher, E. H., Möller, B., Lokerse, A. S., Llavata-Peris, C. I., van den Berg, W., and Weijers, D. (2011). A cellular expression map of the arabidopsis auxin response factor gene family. *The Plant journal*, 68:597–606.

Reinhardt, D., Pesce, E.-R., Stieger, P., Mandel, T., Baltensperger, K., Bennett, M., Traas, J., Friml, J., and Kuhlemeier, C. (2003). Regulation of phyllotaxis by polar auxin transport. *Nature*, 426:255–260.

Rich-Griffin, C., Stechemesser, A., Finch, J., Lucas, E., Ott, S., and Schäfer, P. (2020). Single-cell transcriptomics: A high-resolution avenue for plant functional genomics. *Trends in plant science*, 25:186–197.

Ristova, D., Rosas, U., Krouk, G., Ruffel, S., Birnbaum, K. D., and Coruzzi, G. M. (2013). Rootscape: a landmark-based system for rapid screening of root architecture in arabidopsis. *Plant physiology*, 161:1086–1096.

Rodrigues, A., Santiago, J., Rubio, S., Saez, A., Osmont, K. S., Gadea, J., Hardtke, C. S., and Rodriguez, P. L. (2009). The short-rooted phenotype of the brevis radix mutant partly reflects root abscisic acid hypersensitivity. *Plant physiology*, 149:1917–1928.

Rodriguez, M. Z., Comin, C. H., Casanova, D., Bruno, O. M., Amancio, D. R., Costa, L. d. F., and Rodrigues, F. A. (2019). Clustering algorithms: A comparative approach. *PloS one*, 14:e0210236.

Rodriguez-Villalon, A. and Brady, S. M. (2019). Single cell rna sequencing and its promise in reconstructing plant vascular cell lineages. *Current opinion in plant biology*, 48:47–56.

Roppolo, D., De Rybel, B., Dénervaud Tendon, V., Pfister, A., Alassimone, J., Vermeer, J. E. M., Yamazaki, M., Stierhof, Y.-D., Beeckman, T., and Geldner, N. (2011). A novel protein family mediates casparian strip formation in the endodermis. *Nature*, 473:380–383.

Russinova, E., Borst, J.-W., Kwaaitaal, M., Caño-Delgado, A., Yin, Y., Chory, J., and de Vries, S. C. (2004). Heterodimerization and endocytosis of arabidopsis brassinosteroid receptors bri1 and atserk3 (bak1). *The Plant cell*, 16:3216–3229.

Ryu, K. H., Huang, L., Kang, H. M., and Schiefelbein, J. (2019). Single-cell rna sequencing resolves molecular relationships among individual plant cells. *Plant physiology*, 179:1444–1456.

Sabatini, S., Heidstra, R., Wildwater, M., and Scheres, B. (2003). Scarecrow is involved in positioning the stem cell niche in the arabidopsis root meristem. *Genes & development*, 17:354–358.

Saelens, W., Cannoodt, R., Todorov, H., and Saeys, Y. (2019). A comparison of single-cell trajectory inference methods. *Nature biotechnology*, 37:547–554.

Salazar-Henao, J. E., Lehner, R., Betegón-Putze, I., Vilarrasa-Blasi, J., and Caño-Delgado, A. I. (2016). Bes1 regulates the localization of the brassinosteroid receptor brl3 within the provascular tissue of the arabidopsis primary root. *Journal of experimental botany*, 67:4951–4961.

Sanagi, M., Lu, Y., Aoyama, S., Morita, Y., Mitsuda, N., Ikeda, M., Ohme-Takagi, M., Sato, T., and Yamaguchi, J. (2018). Sugar-responsive transcription factor bzip3 affects leaf shape in arabidopsis plants. *Plant biotechnology*, 35:167–170.

Sanz, L., Fernández-Marcos, M., Modrego, A., Lewis, D. R., Muday, G. K., Pollmann, S., Dueñas, M., Santos-Buelga, C., and Lorenzo, O. (2014). Nitric oxide plays a role in stem cell niche homeostasis through its in-

teraction with auxin. *Plant Physiology*, 166(4):1972–1984.

Sarkar, A. K., Luijten, M., Miyashima, S., Lenhard, M., Hashimoto, T., Nakajima, K., Scheres, B., Heidstra, R., and Laux, T. (2007). Conserved factors regulate signalling in arabidopsis thaliana shoot and root stem cell organizers. *Nature*, 446:811–814.

Satterlee, J. W., Strable, J., and Scanlon, M. J. (2020). Plant stem cell organization and differentiation at single-cell resolution. *bioRxiv*.

Schenk, P. M., Kazan, K., Rusu, A. G., Manners, J. M., and Maclean, D. J. (2005). The sen1 gene of arabidopsis is regulated by signals that link plant defence responses and senescence. *Plant physiology and biochemistry*, 43:997–1005.

Scheres, B. (2007). Stem-cell niches: nursery rhymes across kingdoms. *Nature reviews. Molecular cell biology*, 8:345–354.

Scheres, B., Di Laurenzio, L., Willemsen, V., Hauser, M. T., Janmaat, K., Weisbeek, P., and Benfey, P. N. (1995). Mutations affecting the radial organisation of the arabidopsis root display specific defects throughout the embryonic axis. *Development*, 121(1):53–62.

Schlereth, A., Möller, B., Liu, W., Kientz, M., Flipse, J., Rademacher, E. H., Schmid, M., Jürgens, G., and Weijers, D. (2010). Monopteros controls embryonic root initiation by regulating a mobile transcription factor. *Nature*, 464:913–916.

Shahan, R., Hsu, C.-W., Nolan, T. M., Cole, B. J., Taylor, I. W., Vlot, A. H. C., Benfey, P. N., and Ohler, U. (2020). A single cell arabidopsis root atlas reveals developmental trajectories in wild type and cell identity mutants. *bioRxiv*.

Shi, D.-Q., Liu, J., Xiang, Y.-H., Ye, D., Sundaresan, V., and Yang, W.-C. (2005). Slow walker1, essential for gametogenesis in arabidopsis, encodes a wd40 protein involved in 18s ribosomal rna biogenesis. *The*

Plant cell, 17:2340–2354.

Shimotohno, A., Heidstra, R., Blilou, I., and Scheres, B. (2018). Root stem cell niche organizer specification by molecular convergence of plethora and scarecrow transcription factor modules. *Genes & development*, 32:1085–1100.

Shou, W., Bergstrom, C. T., Chakraborty, A. K., and Skinner, F. K. (2015). Theory, models and biology. *eLife*, 4:e07158.

Shulse, C. N., Cole, B. J., Ciobanu, D., Lin, J., Yoshinaga, Y., Gouran, M., Turco, G. M., Zhu, Y., O'Malley, R. C., Brady, S. M., and Dickel, D. E. (2019). High-throughput single-cell transcriptome profiling of plant cell types. *Cell reports*, 27:2241–2247.e4.

Siligato, R., Wang, X., Yadav, S. R., Lehesranta, S., Ma, G., Ursache, R., Sevilem, I., Zhang, J., Gorte, M., Prasad, K., Wrzaczek, M., Heidstra, R., Murphy, A., Scheres, B., and Mähönen, A. P. (2016). Multisite gateway-compatible cell type-specific gene-inducible system for plants. *Plant physiology*, 170:627–641.

Skirycz, A., Radziejwoski, A., Busch, W., Hannah, M. A., Czeszejko, J., Kwaśniewski, M., Zanor, M.-I., Lohmann, J. U., De Veylder, L., Witt, I., and Mueller-Roeber, B. (2008). The dof transcription factor obp1 is involved in cell cycle regulation in arabidopsis thaliana. *The Plant journal*, 56:779–792.

Slabaugh, E., Held, M., and Brandizzi, F. (2011). Control of root hair development in arabidopsis thaliana by an endoplasmic reticulum anchored member of the r2r3-myb transcription factor family. *The Plant journal*, 67:395–405.

Slovak, R., Göschl, C., Su, X., Shimotani, K., Shiina, T., and Busch, W. (2014). A scalable open-source pipeline for large-scale root phenotyping of arabidopsis. *The Plant cell*, 26:2390–2403.

Smith, S. and De Smet, I. (2012). Root system architecture: insights from arabidopsis and cereal crops. *Philosophical transactions of the Royal Society of London. Series B, Biological sciences*, 367:1441–1452.

Sánchez-Rodríguez, C., Ketelaar, K., Schneider, R., Villalobos, J. A., Somerville, C. R., Persson, S., and Wallace, I. S. (2017). Brassinosteroid insensitive2 negatively regulates cellulose synthesis in , javax.xml.bind.jaxbelement@7c04b8c6, by phosphorylating cellulose synthase 1. *Proceedings of the National Academy of Sciences of the United States of America*, 114:3533–3538.

Soneson, C. and Robinson, M. D. (2018). Bias, robustness and scalability in single-cell differential expression analysis. *Nature methods*, 15:255–261.

Sozzani, R., Cui, H., Moreno-Risueno, M. A., Busch, W., Van Norman, J. M., Vernoux, T., Brady, S. M., Dewitte, W., Murray, J. A. H., and Benfey, P. N. (2010). Spatiotemporal regulation of cell-cycle genes by shortroot links patterning and growth. *Nature*, 466:128–132.

Srivastava, M., Srivastava, A. K., Orosa-Puente, B., Campanaro, A., Zhang, C., and Sadanandom, A. (2020). Sumo conjugation to bzr1 enables brassinosteroid signaling to integrate environmental cues to shape plant growth. *Current biology*, 30:1410–1423.e3.

Stahl, Y., Grabowski, S., Bleckmann, A., Kühnemuth, R., Weidtkamp-Peters, S., Pinto, K. G., Kirschner, G. K., Schmid, J. B., Wink, R. H., Hülsewede, A., Felekyan, S., Seidel, C. A. M., and Simon, R. (2013). Moderation of arabidopsis root stemness by clavata1 and arabidopsis crinkly4 receptor kinase complexes. *Current biology*, 23:362–371.

Stahl, Y., Wink, R. H., Ingram, G. C., and Simon, R. (2009). A signaling module controlling the stem cell niche in arabidopsis root meristems. *Current biology*, 19:909–914.

Stein, D. F., Chen, H., Vinyard, M. E., and Pinello, L. (2020). singlecellvr: interactive visualization of single-cell data in virtual reality. *bioRxiv*.

Stoppel, R., Manavski, N., Schein, A., Schuster, G., Teubner, M., Schmitz-Linneweber, C., and Meurer, J. (2012). Rhon1 is a novel ribonucleic acid-binding protein that supports rnase e function in the arabidopsis chloroplast. *Nucleic acids research*, 40:8593–8606.

Stracke, R., Werber, M., and Weisshaar, B. (2001). The r2r3-myb gene family in arabidopsis thaliana. *Current opinion in plant biology*, 4:447–456.

Stuart, T., Butler, A., Hoffman, P., Hafemeister, C., Papalexi, E., Mauck, W. M., Hao, Y., Stoeckius, M., Smibert, P., and Satija, R. (2019). Comprehensive integration of single-cell data. *Cell*, 177:1888–1902.e21.

Sun, B., Zhou, Y., Cai, J., Shang, E., Yamaguchi, N., Xiao, J., Looi, L.-S., Wee, W.-Y., Gao, X., Wagner, D., and Ito, T. (2019). Integration of transcriptional repression and polycomb-mediated silencing of , javax.xml.bind.jaxbelement@15302b9, in floral meristems. *The Plant cell*, 31:1488–1505.

Sun, Y., Fan, X.-Y., Cao, D.-M., Tang, W., He, K., Zhu, J.-Y., He, J.-X., Bai, M.-Y., Zhu, S., Oh, E., Patil, S., Kim, T.-W., Ji, H., Wong, W. H., Rhee, S. Y., and Wang, Z.-Y. (2010). Integration of brassinosteroid signal transduction with the transcription network for plant growth regulation in arabidopsis. *Developmental cell*, 19:765–777.

Supek, F., Bošnjak, M., Škunca, N., and Šmuc, T. (2011). Revigo summarizes and visualizes long lists of gene ontology terms. *PloS one*, 6:e21800.

Takahashi, T., Gasch, A., Nishizawa, N., and Chua, N. H. (1995). The diminuto gene of arabidopsis is involved in regulating cell elongation. *Genes & development*, 9:97–107.

Takatsuka, H. and Umeda, M. (2014). Hormonal control of cell division

and elongation along differentiation trajectories in roots. *Journal of experimental botany*, 65:2633–2643.

Tan, H., Man, C., Xie, Y., Yan, J., Chu, J., and Huang, J. (2019). A crucial role of ga-regulated flavonol biosynthesis in root growth of arabidopsis. *Molecular plant*, 12:521–537.

Tarazona, S., Furió-Tarí, P., Turrà, D., Pietro, A. D., Nueda, M. J., Ferrer, A., and Conesa, A. (2015). Data quality aware analysis of differential expression in rna-seq with noiseq r/bioc package. *Nucleic acids research*, 43:e140.

Tian, C., Du, Q., Xu, M., Du, F., and Jiao, Y. (2020). Single-nucleus rna-seq resolves spatiotemporal developmental trajectories in the tomato shoot apex. *bioRxiv*.

Tian, H., Wabnik, K., Niu, T., Li, H., Yu, Q., Pollmann, S., Vanneste, S., Govaerts, W., Rolcík, J., Geisler, M., Friml, J., and Ding, Z. (2014). Wox5-iaa17 feedback circuit-mediated cellular auxin response is crucial for the patterning of root stem cell niches in arabidopsis. *Molecular plant*, 7:277–289.

Torii, K., Kubota, A., Araki, T., and Endo, M. (2020). Time-series single-cell rna-seq data reveal auxin fluctuation during endocycle. *Plant & cell physiology*, 61:243–254.

Trapnell, C. (2015). Defining cell types and states with single-cell genomics. *Genome research*, 25:1491–1498.

Trapnell, C., Cacchiarelli, D., Grimsby, J., Pokharel, P., Li, S., Morse, M., Lennon, N. J., Livak, K. J., Mikkelsen, T. S., and Rinn, J. L. (2014). The dynamics and regulators of cell fate decisions are revealed by pseudotemporal ordering of single cells. *Nature biotechnology*, 32:381–386.

Truernit, E., Bauby, H., Dubreucq, B., Grandjean, O., Runions, J.,

Barthélémy, J., and Palauqui, J.-C. (2008). High-resolution whole-mount imaging of three-dimensional tissue organization and gene expression enables the study of phloem development and structure in arabidopsis. *The Plant cell*, 20:1494–1503.

Tunc-Ozdemir, M. and Jones, A. M. (2017). Brl3 and atrgs1 cooperate to fine tune growth inhibition and ros activation. *PloS one*, 12:e0177400.

Turco, G. M., Rodriguez-Medina, J., Siebert, S., Han, D., Valderrama-Gómez, M. ., Vahldick, H., Shulse, C. N., Cole, B. J., Juliano, C. E., Dickel, D. E., Savageau, M. A., and Brady, S. M. (2019). Molecular mechanisms driving switch behavior in xylem cell differentiation. *Cell reports*, 28:342–351.e4.

Ubeda-Tomás, S., Swarup, R., Coates, J., Swarup, K., Laplaze, L., Beemster, G. T. S., Hedden, P., Bhalerao, R., and Bennett, M. J. (2008). Root growth in arabidopsis requires gibberellin/della signalling in the endodermis. *Nature cell biology*, 10:625–628.

van den Berg, C., Willemsen, V., Hage, W., Weisbeek, P., and Scheres, B. (1995). Cell fate in the arabidopsis root meristem determined by directional signalling. *Nature*, 378:62–65.

van den Berg, C., Willemsen, V., Hendriks, G., Weisbeek, P., and Scheres, B. (1997). Short-range control of cell differentiation in the arabidopsis root meristem. *Nature*, 390:287–289.

van der Maaten, L. and Hinton, G. (2008). Visualizing data using t-sne. *Journal of Machine Learning Research*, 9(86):2579–2605.

Vanstraelen, M., Baloban, M., Da Ines, O., Cultrone, A., Lammens, T., Boudolf, V., Brown, S. C., De Veylder, L., Mergaert, P., and Kondorosi, E. (2009). Apc/c-ccs52a complexes control meristem maintenance in the arabidopsis root. *Proceedings of the National Academy of Sciences of the United States of America*, 106:11806–11811.

Vatén, A., Dettmer, J., Wu, S., Stierhof, Y.-D., Miyashima, S., Yadav, S. R., Roberts, C. J., Campilho, A., Bulone, V., Lichtenberger, R., Lehesranta, S., Mähönen, A. P., Kim, J.-Y., Jokitalo, E., Sauer, N., Scheres, B., Nakajima, K., Carlsbecker, A., Gallagher, K. L., and Helariutta, Y. (2011). Callose biosynthesis regulates symplastic trafficking during root development. *Developmental cell*, 21:1144–1155.

Venglat, S. P., Dumonceaux, T., Rozwadowski, K., Parnell, L., Babic, V., Keller, W., Martienssen, R., Selvaraj, G., and Datla, R. (2002). The homeobox gene brevipedicellus is a key regulator of inflorescence architecture in arabidopsis. *Proceedings of the National Academy of Sciences of the United States of America*, 99:4730–4735.

Verbelen, J.-P., De Cnodder, T., Le, J., Vissenberg, K., and Baluska, F. (2006). The root apex of arabidopsis thaliana consists of four distinct zones of growth activities: Meristematic zone, transition zone, fast elongation zone and growth terminating zone. *Plant signaling & behavior*, 1:296–304.

Vilarrasa-Blasi, J., González-García, M.-P., Frigola, D., Fàbregas, N., Alexiou, K. G., López-Bigas, N., Rivas, S., Jauneau, A., Lohmann, J. U., Benfey, P. N., Ibañes, M., and Caño-Delgado, A. I. (2014). Regulation of plant stem cell quiescence by a brassinosteroid signaling module. *Developmental cell*, 30:36–47.

Vissenberg, K., Claeijs, N., Balcerowicz, D., and Schoenaers, S. (2020). Hormonal regulation of root hair growth and responses to the environment in arabidopsis. *Journal of experimental botany*, 71:2412–2427.

Vragović, K., Sela, A., Friedlander-Shani, L., Fridman, Y., Hacham, Y., Holland, N., Bartom, E., Mockler, T. C., and Savaldi-Goldstein, S. (2015). Translatome analyses capture of opposing tissue-specific brassinosteroid signals orchestrating root meristem differentiation. *Proceed-*

ings of the National Academy of Sciences of the United States of America, 112:923–928.

Wang, F., Gao, Y., Liu, Y., Zhang, X., Gu, X., Ma, D., Zhao, Z., Yuan, Z., Xue, H., and Liu, H. (2019a). Bes1-regulated bee1 controls photoperiodic flowering downstream of blue light signaling pathway in arabidopsis. *The New phytologist*, 223:1407–1419.

Wang, J.-W., Wang, L.-J., Mao, Y.-B., Cai, W.-J., Xue, H.-W., and Chen, X.-Y. (2005). Control of root cap formation by microrna-targeted auxin response factors in arabidopsis. *The Plant cell*, 17:2204–2216.

Wang, M., Yang, K., and Le, J. (2015). Organ-specific effects of brassinosteroids on stomatal production coordinate with the action of too many mouths. *Journal of integrative plant biology*, 57:247–255.

Wang, P., Nolan, T. M., Yin, Y., and Bassham, D. C. (2020). Identification of transcription factors that regulate expression and autophagy in arabidopsis. *Autophagy*, 16:123–139.

Wang, W., Ryu, K. H., Barron, C., and Schiefelbein, J. (2019b). Root epidermal cell patterning is modulated by a critical residue in the werewolf transcription factor. *Plant physiology*, 181:1239–1256.

Wang, Z. Y., Seto, H., Fujioka, S., Yoshida, S., and Chory, J. (2001). Bri1 is a critical component of a plasma-membrane receptor for plant steroids. *Nature*, 410:380–383.

Wei, Z. and Li, J. (2016). Brassinosteroids regulate root growth, development, and symbiosis. *Molecular plant*, 9:86–100.

Weidtkamp-Peters, S. and Stahl, Y. (2017). The use of fret/flim to study proteins interacting with plant receptor kinases. *Methods in molecular biology*, 1621:163–175.

Welch, D., Hassan, H., Blilou, I., Immink, R., Heidstra, R., and Scheres, B. (2007). Arabidopsis jackdaw and magpie zinc finger proteins delimit

asymmetric cell division and stabilize tissue boundaries by restricting short-root action. *Genes & development*, 21:2196–2204.

Wendrich, J. R., Yang, B., Vandamme, N., Verstaen, K., Smet, W., Van de Velde, C., Minne, M., Wybouw, B., Mor, E., Arents, H. E., Nolf, J., Van Duyse, J., Van Isterdael, G., Maere, S., Saeys, Y., and De Rybel, B. (2020). Vascular transcription factors guide plant epidermal responses to limiting phosphate conditions. *Science*.

Wildwater, M., Campilho, A., Perez-Perez, J. M., Heidstra, R., Blilou, I., Korthout, H., Chatterjee, J., Mariconti, L., Gruissem, W., and Scheres, B. (2005). The retinoblastoma-related gene regulates stem cell maintenance in arabidopsis roots. *Cell*, 123:1337–1349.

Woerlen, N., Allam, G., Popescu, A., Corrigan, L., Pautot, V., and Hepworth, S. R. (2017). Repression of blade-on-petiole genes by knox homeodomain protein brevipedicellus is essential for differentiation of secondary xylem in arabidopsis root. *Planta*, 245:1079–1090.

Wolf, S., Mravec, J., Greiner, S., Mouille, G., and Höfte, H. (2012). Plant cell wall homeostasis is mediated by brassinosteroid feedback signaling. *Current biology*, 22:1732–1737.

Wolf, S., van der Does, D., Ladwig, F., Sticht, C., Kolbeck, A., Schürholz, A.-K., Augustin, S., Keinath, N., Rausch, T., Greiner, S., Schumacher, K., Harter, K., Zipfel, C., and Höfte, H. (2014). A receptor-like protein mediates the response to pectin modification by activating brassinosteroid signaling. *Proceedings of the National Academy of Sciences of the United States of America*, 111:15261–15266.

Wu, J., Wu, Q., Pagès, L., Yuan, Y., Zhang, X., Du, M., Tian, X., and Li, Z. (2018). Rhizochamber-monitor: a robotic platform and software enabling characterization of root growth. *Plant methods*, 14:44.

Xia, X.-J., Huang, L.-F., Zhou, Y.-H., Mao, W.-H., Shi, K., Wu, J.-X.,

Asami, T., Chen, Z., and Yu, J.-Q. (2009). Brassinosteroids promote photosynthesis and growth by enhancing activation of rubisco and expression of photosynthetic genes in cucumis sativus. *Planta*, 230:1185–1196.

Xiang, L., Nolan, T. M., Bao, Y., Elmore, M., Tuel, T., Gai, J., Shah, D., Huser, N. M., Hurd, A. M., McLaughlin, S. A., Howell, S. H., Walley, J. W., Yin, Y., and Tang, L. (2020). Robotic assay for drought (road): An automated phenotyping system for brassinosteroid and drought response. *bioRxiv*.

Xie, L., Yang, C., and Wang, X. (2011). Brassinosteroids can regulate cellulose biosynthesis by controlling the expression of cesa genes in arabidopsis. *Journal of experimental botany*, 62:4495–4506.

Xu, F., Meng, T., Li, P., Yu, Y., Cui, Y., Wang, Y., Gong, Q., and Wang, N. N. (2011). A soybean dual-specificity kinase, gmsark, and its arabidopsis homolog, atsark, regulate leaf senescence through synergistic actions of auxin and ethylene. *Plant physiology*, 157:2131–2153.

Xu, J., Hofhuis, H., Heidstra, R., Sauer, M., Friml, J., and Scheres, B. (2006). A molecular framework for plant regeneration. *Science*, 311:385–388.

Xu, Y., Yu, Z., Zhang, D., Huang, J., Wu, C., Yang, G., Yan, K., Zhang, S., and Zheng, C. (2018). Cystm, a novel non-secreted cysteine-rich peptide family, involved in environmental stresses in arabidopsis thaliana. *Plant & cell physiology*, 59:423–438.

Xu, Y.-H., Liu, R., Yan, L., Liu, Z.-Q., Jiang, S.-C., Shen, Y.-Y., Wang, X.-F., and Zhang, D.-P. (2012). Light-harvesting chlorophyll a/b-binding proteins are required for stomatal response to abscisic acid in arabidopsis. *Journal of experimental botany*, 63:1095–1106.

Yadav, R. K., Girke, T., Pasala, S., Xie, M., and Reddy, G. V. (2009).

Gene expression map of the arabidopsis shoot apical meristem stem cell niche. *Proceedings of the National Academy of Sciences of the United States of America*, 106:4941–4946.

Yamaguchi, M., Goué, N., Igarashi, H., Ohtani, M., Nakano, Y., Mortimer, J. C., Nishikubo, N., Kubo, M., Katayama, Y., Kakegawa, K., Dupree, P., and Demura, T. (2010). Vascular-related nac-domain6 and vascular-related nac-domain7 effectively induce transdifferentiation into xylem vessel elements under control of an induction system. *Plant physiology*, 153:906–914.

Yamaguchi, M., Mitsuda, N., Ohtani, M., Ohme-Takagi, M., Kato, K., and Demura, T. (2011). Vascular-related nac-domain7 directly regulates the expression of a broad range of genes for xylem vessel formation. *The Plant journal*, 66:579–590.

Yamamoto, R., Demura, T., and Fukuda, H. (1997). Brassinosteroids Induce Entry into the Final Stage of Tracheary Element Differentiation in Cultured Zinnia Cells. *Plant and Cell Physiology*, 38(8):980–983.

Yasrab, R., Atkinson, J. A., Wells, D. M., French, A. P., Pridmore, T. P., and Pound, M. P. (2019). RootNav 2.0: Deep learning for automatic navigation of complex plant root architectures. *GigaScience*, 8(11). giz123.

Yazdanbakhsh, N. and Fisahn, J. (2012). High-throughput phenotyping of root growth dynamics. *Methods in molecular biology*, 918:21–40.

Ye, H., Liu, S., Tang, B., Chen, J., Xie, Z., Nolan, T. M., Jiang, H., Guo, H., Lin, H.-Y., Li, L., Wang, Y., Tong, H., Zhang, M., Chu, C., Li, Z., Aluru, M., Aluru, S., Schnable, P. S., and Yin, Y. (2017). Rd26 mediates crosstalk between drought and brassinosteroid signalling pathways. *Nature communications*, 8:14573.

Yin, Y., Wang, Z. Y., Mora-Garcia, S., Li, J., Yoshida, S., Asami, T., and

Chory, J. (2002). Bes1 accumulates in the nucleus in response to brassinosteroids to regulate gene expression and promote stem elongation. *Cell*, 109:181–191.

Yoshiyama, K. O., Kimura, S., Maki, H., Britt, A. B., and Umeda, M. (2014). The role of sog1, a plant-specific transcriptional regulator, in the dna damage response. *Plant signaling & behavior*, 9:e28889.

Yu, X., Li, L., Li, L., Guo, M., Chory, J., and Yin, Y. (2008). Modulation of brassinosteroid-regulated gene expression by jumonji domain-containing proteins elf6 and ref6 in arabidopsis. *Proceedings of the National Academy of Sciences of the United States of America*, 105:7618–7623.

Yu, X., Li, L., Zola, J., Aluru, M., Ye, H., Foudree, A., Guo, H., Anderson, S., Aluru, S., Liu, P., Rodermel, S., and Yin, Y. (2011). A brassinosteroid transcriptional network revealed by genome-wide identification of besi target genes in arabidopsis thaliana. *The Plant journal*, 65:634–646.

Zappia, L., Phipson, B., and Oshlack, A. (2018). Exploring the single-cell rna-seq analysis landscape with the scrna-tools database. *PLoS computational biology*, 14:e1006245.

Zhang, H., Han, W., De Smet, I., Talboys, P., Loya, R., Hassan, A., Rong, H., Jürgens, G., Paul Knox, J., and Wang, M.-H. (2010). Aba promotes quiescence of the quiescent centre and suppresses stem cell differentiation in the arabidopsis primary root meristem. *The Plant journal*, 64:764–774.

Zhang, J., Mazur, E., Balla, J., Gallei, M., Kalousek, P., Medveďová, Z., Li, Y., Wang, Y., Prát, T., Vasileva, M., Reinöhl, V., Procházka, S., Halouzka, R., Tarkowski, P., Luschnig, C., Brewer, P. B., and Friml, J. (2020a). Strigolactones inhibit auxin feedback on pin-dependent auxin transport canalization. *Nature communications*, 11:3508.

Zhang, J. and Peer, W. A. (2017). Auxin homeostasis: the dao of catabolism. *Journal of experimental botany*, 68:3145–3154.

Zhang, P., Wang, R., Yang, X., Ju, Q., Li, W., Lü, S., Tran, L.-S. P., and Xu, J. (2020b). The r2r3-myb transcription factor atmyb49 modulates salt tolerance in arabidopsis by modulating the cuticle formation and antioxidant defence. *Plant, cell & environment*.

Zhang, T.-Q., Xu, Z.-G., Shang, G.-D., and Wang, J.-W. (2019). A single-cell rna sequencing profiles the developmental landscape of arabidopsis root. *Molecular plant*, 12:648–660.

Zhang, W., Swarup, R., Bennett, M., Schaller, G. E., and Kieber, J. J. (2013a). Cytokinin induces cell division in the quiescent center of the arabidopsis root apical meristem. *Current biology*, 23:1979–1989.

Zhang, Y., Jiao, Y., Liu, Z., and Zhu, Y.-X. (2015). Row1 maintains quiescent centre identity by confining wox5 expression to specific cells. *Nature communications*, 6:6003.

Zhang, Y., Liang, W., Shi, J., Xu, J., and Zhang, D. (2013b). Myb56 encoding a r2r3 myb transcription factor regulates seed size in arabidopsis thaliana. *Journal of integrative plant biology*, 55:1166–1178.

Zhao, X., Guo, X., Tang, X., Zhang, H., Wang, M., Kong, Y., Zhang, X., Zhao, Z., Lv, M., and Li, L. (2018). Misregulation of er-golgi vesicle transport induces er stress and affects seed vigor and stress response. *Frontiers in plant science*, 9:658.

Zhong, R., Lee, C., Zhou, J., McCarthy, R. L., and Ye, Z.-H. (2008). A battery of transcription factors involved in the regulation of secondary cell wall biosynthesis in arabidopsis. *The Plant cell*, 20:2763–2782.

Zhou, J., Wang, X., Lee, J.-Y., and Lee, J.-Y. (2013). Cell-to-cell movement of two interacting at-hook factors in arabidopsis root vascular tissue patterning. *The Plant Cell*, 25(1):187–201.

Zou, L.-J., Deng, X.-G., Zhang, L.-E., Zhu, T., Tan, W.-R., Muhammad, A., Zhu, L.-J., Zhang, C., Zhang, D.-W., and Lin, H.-H. (2018). Nitric oxide as a signaling molecule in brassinosteroid-mediated virus resistance to cucumber mosaic virus in arabidopsis thaliana. *Physiologia plantarum*, 163:196–210.

List of Figures

List of Tables

CV and publications

Isabel Betegón Putze
isabel@betegon.net
(+34)687924728

Address
Calle Clos, 9
Cerdanyola del Valles,
08290
Barcelona, Spain

Isabel Betegón Putze

Biotechnologist

Education

2020 - present, EAE Business School (Barcelona)
International MBA

2015 - 2020, Center for Research in Agricultural Genomics (CRAG, Barcelona)
PhD in Plant Biotechnology

In the group led by Dr. Caño-Delgado. PhD thesis entitled "Spatiotemporal analysis of brassinosteroid signaling in vascular stem cells". FPU fellowship from the Ministry of Science, Innovation and Universities.

Research stays in other institutions:

- In Dr. Idan Efroni laboratory (Hebrew University of Jerusalem, Rehovot, Israel). Single-cell transcriptomics of root stem cells.
- In Dr. Ana Conesa laboratory (University of Florida, Gainesville, USA). Bioinformatic analysis of stem cells transcriptomic profiles.
- In Dr. Rosangela Sozzani (North Carolina State University, Raleigh, USA). Identification of brassinosteroid-regulated genes in the stem cells.

2017 - 2020. Teaching in the Plant Physiology Department in the Autonomous University of Barcelona.

2014 - 2015, Autonomous University of Barcelona
Master in Advanced Genetics

2010 - 2014, University of Oviedo
Degree in Biotechnology

- August 2013 - December 2013: ERASMUS fellowship in the University of Turku (Finland).

Isabel Betegón Putze
isabel@betegon.net
(+34)687924728

Address
Calle Clos, 9
Cerdanyola del Valles,
08290
Barcelona, Spain

Publications

- Betegón-Putze I*, Mercadal J*, Bosch N*, Planas-Riverola A, Marquès-Bueno M, Vilarrasa-Blasi J, Frigola D, Burkart RC, Martinez C, Stahl Y, Prat S, Ibañes M and Caño-Delgado AI. Precise transcriptional control of cellular quiescence by BRAVO/WOX5 complex in Arabidopsis roots. BioRxiv (2020).
- González A, Sevillano X, Betegón-Putze I, Blasco-Escámez D, Ferrer M and Caño-Delgado AI. MyROOT 2.0. An automatic tool for high throughput and accurate primary root length measurement. Computers and Electronics in Agriculture (2020).
- Betegón-Putze I*, González A*, Sevillano X, Blasco-Escámez D and Caño-Delgado AI. MyROOT: a method and software for the semiautomatic measurement of primary root length in Arabidopsis seedlings. The Plant Journal (2019).
- Planas-Riverola A*, Gupta A*, Betegón-Putze I, Bosch N, Ibañes M and Caño-Delgado AI. Brassinosteroid signaling in plant development and adaptation to stress. Development (2019).
- Salazar-Henao JE*, Lehner R*, Betegón-Putze I, Vilarrasa-Blasi J and Caño-Delgado AI. BES1 regulates the localization of the brassinosteroid receptor BRL3 within the provascular tissue of the Arabidopsis primary root. Journal of Experimental Botany (2016).

Seminars and congresses

- Presentation in At the Forefront of Plant Research 2019 congress (Barcelona, April 2019). "MyROOT software for the semi-automatic measurement of primary root length in Arabidopsis seedlings".
- Presentation in the 4th Vascular meeting (Corsendork, Belgium, November 2018). "Brassinosteroid signaling in stem cell development".
- Presentation in the Annual congress of young researchers 2018 (Barcelona, July 2018). "MyROOT: A novel method and software for the semi-automatic measurement of plant root length".
- Presentation in the XIV Reunión de Biología Molecular de Plantas (Salamanca, July 2018). "MyROOT: A novel method and software for the semi-automatic measurement of plant root length".
- Presentation in the 28th International Conference on Arabidopsis Research (St Louis, USA, June 2017). "Brassinosteroid regulation of vascular development: a cell-type specific transcriptomic approach".
- Presentation in the 2th Vascular meeting (Corsendork, Belgium, November 2016). "Dissecting brassinosteroid action in vascular development".
- Poster in the VIII European Plant Science Retreat (Barcelona, June 2016). "BES1 regulated the localisation of the brassinosteroid receptor BRL3 within the provascular tissue of the Arabidopsis primary root".

Isabel Betegón Putze
isabel@betegon.net
(+34)687924728

Address
Calle Clos, 9
Cerdanyola del Valles,
08290
Barcelona, Spain

Languages

Oral and written communication

- Spanish
- English

Programming

- R (Advanced level)
- Python (Basic level)

the plant journal

SEB Society for Experimental Biology

The Plant Journal (2019) **98,** 1145–1156 doi: 10.1111/tpj.14297

TECHNICAL ADVANCE

MyROOT: a method and software for the semiautomatic measurement of primary root length in Arabidopsis seedlings

Isabel Betegón-Putze[1,‡], Alejandro González[2,‡], Xavier Sevillano[2], David Blasco-Escámez[1] and Ana I. Caño-Delgado[1,*,†]

[1]*Department of Molecular Genetics, Center for Research in Agricultural Genomics (CRAG) CSIC-IRTA-UAB-UB, Campus UAB, Bellaterra (Cerdanyola del Vallès), 08193, Barcelona, Spain, and*

[2]*GTM- Grup de Recerca en Tecnologies Mèdia, La Salle, Universitat Ramon Llull, 08022, Barcelona, Spain*

Received 20 September 2018; revised 18 February 2019; accepted 19 February 2019; published online 27 February 2019.

*For correspondence (e-mail ana.cano@cragenomica.es).

‡These authors contributed equally to this work.

†Present address: Department of Molecular Genetics, Centre de Recerca en Agrigenòmica (CRAG) CSIC-IRTA-UAB-UB, Campus UAB, Bellaterra (Cerdanyola del Vallès), E-08193, Barcelona, Spain.

SUMMARY

Root analysis is essential for both academic and agricultural research. Despite the great advances in root phenotyping and imaging, calculating root length is still performed manually and involves considerable amounts of labor and time. To overcome these limitations, we developed MyROOT, a software for the semi-automatic quantification of root growth of seedlings growing directly on agar plates. Our method automatically determines the scale from the image of the plate, and subsequently measures the root length of the individual plants. To this aim, MyROOT combines a bottom-up root tracking approach with a hypocotyl detection algorithm. At the same time as providing accurate root measurements, MyROOT also significantly minimizes the user intervention required during the process. Using Arabidopsis, we tested MyROOT with seedlings from different growth stages and experimental conditions. When comparing the data obtained from this software with that of manual root measurements, we found a high correlation between both methods (R^2 = 0.997). When compared with previous developed software with similar features (BRAT and EZ-Rhizo), MyROOT offered an improved accuracy for root length measurements. Therefore, MyROOT will be of great use to the plant science community by permitting high-throughput root length measurements while saving both labor and time.

Keywords: root length, software, root phenotyping, high-throughput image analysis, *Arabidopsis thaliana*, technical advance.

INTRODUCTION

The root, responsible for anchoring the plant to the soil, is an essential organ for overall plant growth and development. Characterization of different root traits is therefore important not only for understanding organ growth, but also for evaluating the impact of roots in agriculture (Kuijken *et al.*, 2015). As such, generating tools for precise, high-throughput phenotyping and imaging of roots is essential for plant research and agriculture. Phenotyping facilities, such as the ones available in the European Plant Phenotypic Network (http://www.plant-phenotyping-network.eu/), have started to implement tools for mass screening of roots.

Roots provide necessary structural and functional support for incorporation of nutrients and water from soil. In *Arabidopsis thaliana* (Arabidopsis), the primary root has a simplified anatomy that makes it very amenable for genetic and microscopic analysis (Dolan *et al.*, 1993; Ishikawa and Evans, 1995; Iyer-Pascuzzi *et al.*, 2009). Different root cell lineages are derived from a group of stem cells located at the root apex. Here, the stem cell niche is formed by a few (three to seven) quiescent center cells that occasionally divide asymmetrically to renew themselves and to form daughter stem cells. From the root apex, these cells actively divide in the meristematic zone and, before exiting the cell cycle in the transition zone, continue to elongate and differentiate in spatially separated regions of the root. In this way, primary root growth is determined by the

balance between cell division and cell elongation within the different zones of the root (van den Berg *et al.*, 1997; Beemster and Baskin, 1998; Verbelen *et al.*, 2006; Takatsuka and Umeda, 2014).

The most straightforward symptom of abnormal root growth or development can be identified by examining the length of the primary root in seedlings. Abnormalities in length can usually be observed and measured just 5–6 days after germination (DAG), which still reflect their embryonic origin (Jürgens *et al.*, 1995). Growth defects in the primary root of seedlings are not only consistent with overall growth defects, but also persistent along the entire plant life cycle (Benfey *et al.*, 1993; Potuschak *et al.*, 2003; González-Garcia *et al.*, 2011). Indeed, Arabidopsis root analyses were the foundations for multiple genetic screens that ultimately led to the identification of several key regulators of plant growth and development (Benfey *et al.*, 1993; Hauser *et al.*, 1995; Caño-Delgado *et al.*, 2000; Mouchel *et al.*, 2004; Ubeda-Tomas *et al.*, 2008).

Root analysis of young seedlings offers direct information regarding overall plant growth and viability. Despite important advances in plant imaging techniques such as microscopic visualization (Pfister *et al.*, 2014; González-Garcia *et al.*, 2015; Lobet, 2017), the root length of seedlings growing in agar plates is generally measured by manually indicating the position of each seedling or manually tracking each root using the ImageJ software (https://imagej.nih.gov/ij/). For this reason, the development and use of methods that enable automatic and accurate analysis of a large number of roots represents a step forward for high-throughput root analysis. Automatic analysis of root system architecture is just beginning to be implemented, and novel methods based on acquiring, processing, and obtaining quantitative data from root images are now available.

The available root softwares are designed for different purposes. Some of these are applied to crop phenotyping and are mainly focused on traits related to root architecture such as branching or biomass (Le Bot *et al.*, 2010; Lobet *et al.*, 2011; Nagel *et al.*, 2012; Pound *et al.*, 2013; Pace *et al.*, 2014; Kuijken *et al.*, 2015; Wu *et al.*, 2018). Conversely, other root softwares are oriented for the analysis of plant model species as Arabidopsis (Armengaud *et al.*, 2009; French *et al.*, 2009; Yazdanbakhsh and Fisahn, 2012; Slovak *et al.*, 2014). Most of these can reliably measure different root traits (primary root length, lateral roots, etc.) (Arsenault *et al.*, 1995; Le Bot *et al.*, 2010; Clark *et al.*, 2013; Ristova *et al.*, 2013; Slovak *et al.*, 2014; Cai *et al.*, 2015). The analysis usually requires intensive user intervention to set the optimal parameters for root detection and to identify the individual roots (Armengaud *et al.*, 2009; French *et al.*, 2009; Clark *et al.*, 2013). Despite time-consuming manual tracking of each single root, ImageJ is often used as a tool for primary root length quantification. A summary of the existing softwares for root analysis and its main features is given in Table S1.

Despite the numerous tools for root analysis, these lack the capability to precisely measure the primary root length of seedlings. This approach is key for genetic, physiological and developmental studies in the plant model Arabidopsis and is often done manually. Here, we present MyROOT, a software capable of semiautomatically calculating primary root length in a fast and user-friendly manner, and that is able to adapt to different imaging and experimental conditions. By automatically identifying the scale and precisely detecting all individual roots and hypocotyls growing on an agar plate from a JPEG image, this software simplifies and minimizes user intervention during the calculation of root length. MyROOT merely requires the user to define the region in which the seedlings are placed on the plate, and then subsequently operates in a semiautomatic fashion. We show that MyROOT can be used both in low-scale and high-throughput experiments due to the incorporation of a batch-processing option for automatic processing of several images without losing its accuracy.

As a proof of concept, MyROOT software was used for root length measurement of Arabidopsis wild-type and brassinosteroid (BR)-signaling mutants grown under control conditions, exogenous BR hormones treatment and for plants grown under osmotic stress conditions (Fabregas *et al.*, 2018). MyROOT software is available at https://www.cragenomica.es/research-groups/brassinosteroid-signaling-in-plant-development.

RESULTS

MyROOT is a software for high-throughput analysis of root length

Most root studies begin with an overall determination of root growth as estimated by manual, laborious and time-consuming measurements. To address this limitation, we developed a semiautomatic and non-invasive software for the high-throughput measurement of root length. This method is implemented in MATLAB as an automatic tool named MyROOT (Figure 1a). It is based on pictures of whole agar plates on which young seedlings are growing vertically on the surface, and implements novel algorithms capable of separately detecting the root and the hypocotyl of each individual seedling and estimating a hypocotyl curve based on the detection of some hypocotyls (Figure 1b–g).

MyROOT detects and measures root length by following a series of steps (Figure 1b–g, Box 1–3 and Video S1). First, a digital image of the plate containing the growing seedlings is taken and used for the analysis (Figures 1b and S1). The image has to include a ruler (at least 1 cm long) placed on top of the plate. From the JPEG image, the software: (i) detects 1 cm of the ruler to automatically compute the scale and calculate the equivalence between pixels and

millimeters (mm; Figure 1c); (ii) generates a binary mask from the manually selected area that allows for root segmentation (this separates those pixels that belong to a root from those of the background) (Figure 1d); (iii) measures the length of the roots through a root-tracking process (Figure 1e); (iv) computes a regression curve based on the detection of the hypocotyls to identify the starting point of each root (Figure 1f); (v) measures the root length again from the root tip to the end of the hypocotyl (Figure 1g); and (vi) exports the measurements and the generated masks to a new folder. Finally, the results are saved in: (i) a Microsoft Excel spreadsheet or a .txt file in which each root is identified by an ID tag, length value and a descriptive text label introduced by the user; (ii) an image showing the detected and measured roots; (iii) MATLAB variables including the intermediate data such as hypocotyl position and the detection curve that was generated while quantifying root length and (iv) a RSML file so the images can be analyzed with other compatible softwares (Lobet *et al.*, 2015).

One of the advantages of MyROOT is that it allows the user to supervise the different steps of the process as the results of each step are displayed before executing the following one. This feature enables the user to modify the different parameters (e.g., segmentation thresholds for ruler and root detection, and model for hypocotyl detection, etc.) at any point in the process to take into account different image conditions. Nonetheless, default parameter values have been set for satisfactory operation on a wide range of images for pre-defined acquisition conditions (see Experimental procedures). Furthermore, the position of any hypocotyl that is not automatically detected can be manually indicated, and undesired roots can be manually removed from the results before saving. In addition, MyROOT incorporates a batch processing option for an automatic high-throughput analysis in which the different parameters are set for the first image from a specific folder and automatically applied in the rest of these.

In summary, by determining the pixel-millimeter equivalence and detecting seedling morphology (roots and hypocotyls) from an image of a seedling-containing agar plate, MyROOT offers a valuable analytical tool for precisely measuring root growth in a semi-automatic manner. As such, this software clearly provides a solution to the timely task of manually quantifying root length.

Root detection and measurement process

MyROOT has been developed for the high-throughput, accurate, and non-invasive measurement of root length from seedlings growing in agar plates. In this respect, the three most crucial steps are to precisely determine the scale, identify the roots, and measure their length. The scale information is obtained from a piece of measuring tape that is placed on the surface of the Petri dish. This allows the measurements to be completely independent from the specific characteristics of the image capture system. The first step for detecting the ruler is based on its color contrast with the background. By computing the vertical and horizontal profiles of the image, the algorithm is designed to explore the entire image in search of a white patch (Figure S2a). As the border of the plate has a similar color contrast with the background, a median filter is applied to reduce the border effect. The maximum values in the filtered profiles define the image area where the white patch is present. Next, the resulting area is further cropped (Figure S2b) and processed (Figure S2c–e). By applying a threshold based on Otsu's algorithm (Otsu, 1979), the black lines representing cm and mm marks are not filtered out (Figure S2b). Finally, a horizontal profile of this binary image is generated (Figure S2d) in which the pixel-mm equivalence is defined as the difference between consecutive local maxima (Figure S2e). In case that there is not ruler tape in the image to analyze, MyROOT includes the option of manually indicating the correspondence between pixels and millimeters.

The core of the whole method is the root extraction and measurement process. To extract roots, the user must first manually define the area in which roots are present (note: only one row of seedlings should be included when defining the area). Then, with just a few mouse clicks from the user, a binary mask is generated that allows root segmentation. This later leads to the identification of individual roots through a root tracking process, and finally allows the individually identified roots to be measured (Figure 2). The root segmentation process can be divided into four main steps: (i) color normalization (Figure 2a), (ii) ridge detection (Figure 2b), (iii) root tracking (Figure 2c), and (iv) root identification (Figure 2d). During the color normalization step, the image is processed and a global working framework is set (i.e., all images going through this process become color-balanced and have the same lower and higher white values; Figure 2a). This allows the user to manage different initial conditions (illumination, color, and saturation, etc.) while continuing with the same subsequent steps of the pipeline. In the next step, a ridge (i.e., white contrasted area) detector identifies roots based on their contrast with the background (for this, the level of whiteness is irrelevant; Figure 2b). After the detection step, a final mask is generated for tracking the roots. Due to the linear disposition of the roots in the plate, we employed a bottom-up tracking approach. As such, tracking starts at the end point of each root and continues upward, row by row, until the hypocotyl detection curve is found (Figure 2c). Finally, the tracking of each root makes it possible to identify which pixels correspond to which root (Figure 2d).

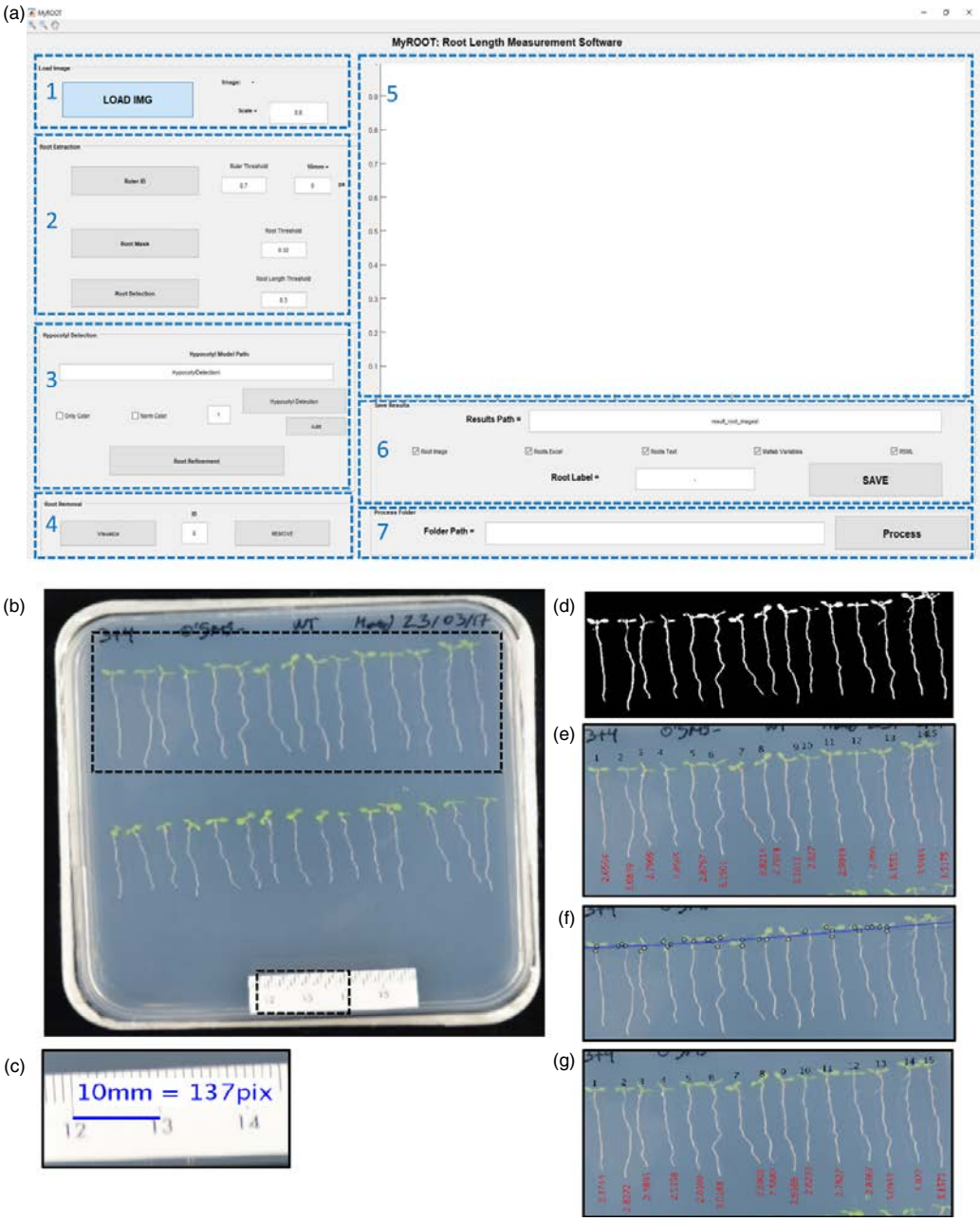

Figure 1. The graphical interface and steps of MyROOT.
(a) The graphical user interface of MyROOT is organized into seven sections: 1. Input image information, 2. Root extraction parameters, 3. Hypocotyl detection parameters, 4. Manual removal of roots, 5. Visualization of the image and the different detection steps, 6. Saving parameters, and 7. Batch processing (b) The input image required for analysis is a picture of the square plate in which the aligned seedlings are growing. By using information from this image, MyROOT performs the following steps: (c) Identification of the ruler to determine the scale (i.e., the equivalence between pixels and millimeters). (d) Root segmentation to identify the seedlings. (e) Root tracking to measure the roots. (f) Hypocotyl detection to identify the hypocotyls and separate them from the roots. (g) Root measurement to quantify the length of individual seedlings (i.e., the distance from the root tip to the end of the hypocotyl).

Once the root tracking process has been completed, each individual root is measured based on previous positions saved in the historical record. Specifically, root length is calculated in pixels by adding the distances between previous consecutive points and then applying the previously calculated pixel-mm equivalence. Next, a refinement process is applied in which the shortest roots, which are often associated with noise, are discarded. By default, MyROOT discards any root measurement shorter than 30% of the longest one. However, this percentage can be manually chosen by the user if need be. A second filter is then applied to keep those roots that terminate close to the previously calculated hypocotyl curve. If a root surpasses the hypocotyl curve, it is cut at this level. Finally, unique numeric identifiers (ID) are assigned to all roots that are not filtered out during processing.

As two roots can be located so close to one another that they cannot be detected as individual roots, MyROOT was trained with the following characteristics: (i) when a split occurs and a current root matches more than one detection (blue circle in Figure 2c), a new root sharing the same historical record is created, and (ii) when a fusion occurs and two roots match a single detection (yellow circle in Figure 2c), the shortest root is eliminated from the root set and added as a sub-root of the longest one; therefore indicating the root length of the primary root which is longer than the lateral roots.

To validate our software, we compared root length measurements obtained using MyROOT with manual measurements performed using ImageJ. We compared the root length values of different experiments. First, 6-days-old seedlings of wild type and BR-related mutants grown in control and in osmotic stress conditions (data published in Fabregas *et al.* (2018), $n > 600$, Figure 3), and second, the same seedlings over 6 consecutive days (from three to eight DAG; $n > 116$). We obtained a positive correlation between the measurements with both methods ($R^2 = 0.997$, Pearson's $r = 0.9985$). These results indicated that measurements made using our software coincided with manual measurements, thereby supporting the use of MyROOT for root length analysis in seedlings in different growth stages and experimental conditions.

We also evaluated the time required by MyROOT to determine root lengths, and compared it with the time needed for manual measurements using ImageJ, as it is widely used for the analysis of a low number of plates as a routine task in many plant biology laboratories. Importantly, we found that MyROOT reduces the time required to measure one plate by approximately half (Figure S3).

When using MyROOT for high-throughput experiments, the analysis of a batch of images can be done automatically after setting the optimal parameters for adapting to the imaging conditions of the experiment. The time required for the analysis of one row of seedlings of different plates was evaluated. MyROOT spends approximately 1 min per image when the hypocotyl detection is not performed and 1 min more if it is performed. Importantly, this process is completely automatic and does not require the user intervention. The accuracy of the batch processing was evaluated by comparing the results of the analysis of 10 different plates using MyROOT by single upload followed by individual setting of the optimal parameters and using MyROOT for a batch analysis of all of them automatically (Figure S4). The correlation obtained between both methods was positive ($R^2 = 0.996$, Pearson's $r = 0.9981$), therefore confirming that the batch processing option can be performed without losing accuracy in the final measurements.

Hypocotyl detection

One of the main advantages of MyROOT is its ability to identify hypocotyls of growing seedlings. This characteristic is important for accurately determining the start point of each root. The hypocotyl detection process is based on visual features extracted (appearance and color) from the image. These features were used to generate a hypocotyl model by introducing 1259 hypocotyls of seedlings of different ages and characteristics and 7915 samples with

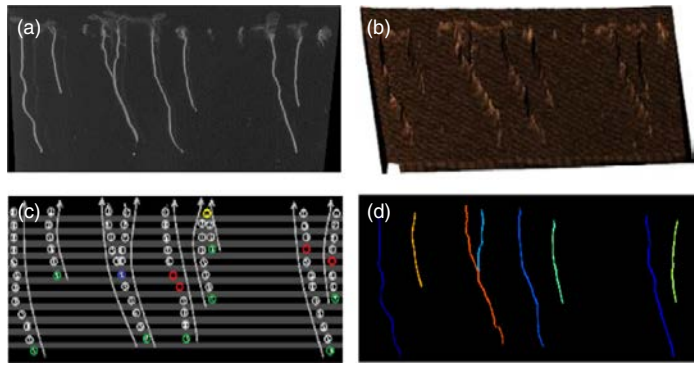

Figure 2. Root extraction method.
(a) Colors are normalized in the area where roots are present, and white roots are detected. (b) Segmentation is performed by applying a ridge detector. (c) Starting at the root tip, the roots are tracked using a bottom-up approach. (d) Each root is measured using its historical recorded tracking, and root length is calculated by taking into account the pixel-millimeter equivalence.

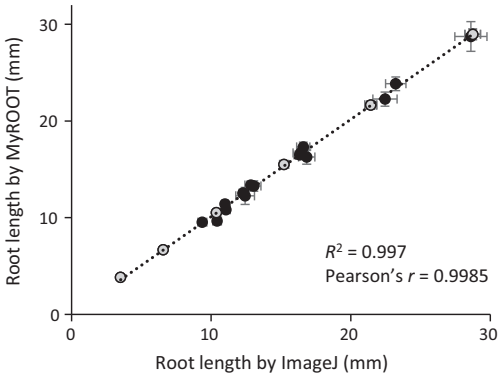

Figure 3. Validation of root length measurements.
Correlation of root length measurements using MyROOT (y axis) and ImageJ (x axis). Each point corresponds to a different experiment ($n > 20$ in each one): time course data from 3 DAG to 8 DAG seedlings (grey) and BR-related mutants in control and osmotic stress conditions (black, Fabregas *et al.*, 2018). Errors bars indicate the standard error. For the time course experiment, seedlings that were not measured by MyROOT in at least four time points were discarded.

background information (see Experimental procedures). The learned model is able to determine whether a given sample is a hypocotyl or not. To extract visual features, we implemented the histogram of oriented gradient (HOG) (Dalal and Triggs, 2005) method. The HOG method is based on the orientation of the contours in the image, and generates a histogram that represents the appearance/shape of the sample. For extracting color features, color distribution histograms representing the amount of color in a given sample area are used (Figure 4a). To train the model, we implemented a linear support vector machine classifier that uses appearance and color features from the hypocotyl images. This classifier generates the best hyperplane that classifies samples as positive (hypocotyls) and negative (no hypocotyls) examples. During the hypocotyl detection stage, the sliding window approach (Glumov *et al.*, 1995) is used to perform an exhaustive search for hypocotyls. Finally, by keeping the highest scored windows as true positives, polynomial regression is used to define a curve that passes through all the detected hypocotyls. Although the user can manually insert the location of the hypocotyls, this curve enables the position of undetected hypocotyls to be estimated, and therefore corrects the curve tracing. The intersection between the hypocotyl detection curve and each root is used to define the root start point.

We first evaluated our hypocotyl detection process in terms of different hypocotyl detection models. Both the precision-recall curve (Figure 4b) and the number of false positives per image (FPPI; Figure 4c) were calculated for three different models that differ in the type of feature they use for describing hypocotyls: only color information, only appearance information (via HOG features), or both types of information (HOG + color).

Upon analyzing the precision-recall curve of each model, we found the HOG + color model to be the most robust (Figure 4b). In the case of FPPI, the lowest miss rate was also found when using the HOG + color model (Figure 4c). These results indicated that when considering both color and appearance (i.e., the HOG + color model), a higher number of hypocotyls were identified than when using only one of the features. Therefore, this validates our MyROOT method because it incorporates both HOG and color information.

Next, we evaluated the influence of different regression curve models on the root measurement refinement used to set up the limits of individual roots (Figure 4d). To create these curves, a regression upon the detected hypocotyls was performed. To define which regression model gives the better fit, we tested different polynomial models that were evaluated in terms of the average distance (in pixels) between the real hypocotyl position and the point of intersection between the root and the regression curve (Figure 4d). The results indicated that when using a hypocotyl regression curve of order 4, a good balance between accuracy and flexibility that is able to account for small changes in hypocotyl position is reached. Therefore, we chose to employ this regression curve in our software.

The use of the hypocotyl detection method permits the fine identification of the starting point of the root (Figure 5a–d). Whereas, depending on the user judgement, this option can be skipped, therefore reducing the time of the measurement process but losing accuracy in the final root length results (Figure 5e). We compared the root length measurements of two plates, one containing seedlings with standard hypocotyls (Col-0 wild type plants) and other with shorter hypocotyls and roots (Col-0 wild type in osmotic stress conditions), using and skipping the hypocotyl detection step (Figure 5a–d). In both plates, when using the method, only the primary root is measured (Figure 5a, c), whereas when it is not used, some parts of the hypocotyl are measured too (Figure 5b,d). When not using the hypocotyl detection method, we only found statistically significant differences in the root length of the shorter seedlings, as the proportion of hypocotyl length measured significantly increased the overall root length measurement (Figure 5e, $n > 30$). These results highlighted the importance of the hypocotyl detection process for accurately measuring the root length, but also point to just using it when the experiment requires high precision.

Comparison of MyROOT with available root softwares

The choice of software is usually based in a balance between the appropriateness of the characteristics of the

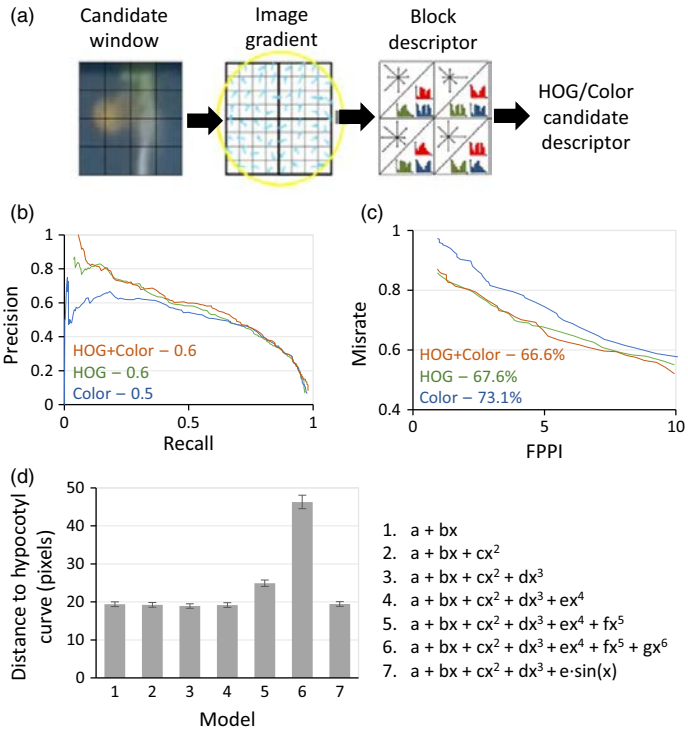

Figure 4. Hypocotyl detection method and validation.
(a) Scheme of the hypocotyl detection method. A candidate window is defined as a square area inside the image. To describe a candidate, appearance/shape (HOG) and color information are extracted. Appearance information is extracted to calculate the gradient of the image (i.e., the direction of the contours within the image at each pixel). Histograms of Oriented Gradient (HOG) and the histograms of color are calculated over regular spaced, non-overlapping cells inside the candidate window (forming the block descriptor). Finally, all color/HOG cell histograms are concatenated to obtain the candidate window description. (b) Precision-Recall curve for three different models of hypocotyl detection (HOG, Color and HOG + Color). The curve is obtained by changing the threshold that defines the frontier between positive and negative samples. For each threshold, the precision (well classified ratio) and the recall (poor classified ratio) were calculated. The area under the curve represents the robustness of the classifier, with a higher value indicating greater robustness (a higher well classified ratio to poor classified ratio over the entire range of the classifier). (c) False Positives Per Image (FPPI) curve for three different models of hypocotyl detection (HOG, Color and HOG+Color). The curve plots the miss rate against the FPPI. In this way, the average miss rate over a specific FPPI range (1–10) represents the sensitivity of the classifier to not miss good samples and keep the false positive ratio low. (d) The average distance in pixels between the real hypocotyl position and the point of intersection between the root and the polynomial regression curves, for polynomial regression curves of orders 1–6 and an extra model including a sine component. Error bars indicate the standard error.

software to the experimental design, the accuracy of the measurements obtained and the time required for the analysis (Table S1). We compared the accuracy and the time spent by MyROOT with BRAT and EZ-Rhizo, the two most similar software tools, in the quantification of primary root length of two independent plates containing Arabidopsis seedlings (Figure S4 and Table S2).

We first compared the root length obtained with the three softwares with the ImageJ results. The absolute difference of mean root length between the measurements obtained with the softwares and with ImageJ show that MyROOT differs 1.39 mm and 0.22 mm for plates 1 and 2 respectively. With regard to this parameter, our results indicated the better performance of MyROOT in comparison with BRAT (15.08 mm and 1.77 mm) and to EZ-Rhizo (2.67 mm and 2.42 mm) (Table S2).

Root detection on the plate was similar between MyROOT (> 90%) and EZ-Rhizo (> 96%), yet MyROOT provided more accurate measurements (Figure S5 and Table S2). In addition, due to the incorporation of the hypocotyl detection method, MyROOT requires less user intervention to clearly indicate the roots, this is reflected in a reduction in the time spent for the analysis. We spent around 3 min to analyze each plate when using MyROOT, 0.5 min with BRAT and 15 min with EZ-Rhizo (Table S2). Some seedlings on the plates analyzed had overlapping hypocotyls. We found that MyROOT was able to identify these and correctly indicate the shoot–root junction in

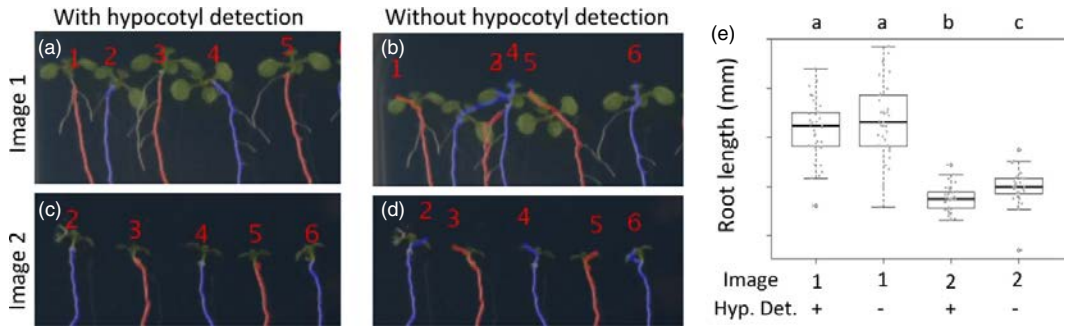

Figure 5. Evaluation of hypocotyl detection method for the root length measurements using MyROOT.
(a–d) Qualitative analysis of the hypocotyl detection method in two different images. (e) Root length measurement of seedling grown in two different plates (showed in (a–d)) using and not using the hypocotyl detection method. Different letters indicate statistically significant differences (*P*-value <0.05; Student's *t*-test, $n > 30$).

cases with higher precision than EZ-Rhizo and BRAT, which presented a more basic algorithm for the hypocotyl detection based only on color and shoot border curvature information, respectively. These observations highlight the utility and importance of the hypocotyl detection method incorporated in MyROOT and its capacity to identify the individual seedlings and the precise starting point of each root.

Overall, MyROOT fills a specific gap in root phenotyping by allowing a precise, fast and semi-automatic quantification of primary root length of seedlings on a plate and a batch of plates.

DISCUSSION

In this study, we presented MyROOT software for the quantification of plant root length. Despite the existence of other software (Table S1), MyROOT covers a gap in analysis of Arabidopsis seedling not previously addressed. The determination of root length in such accuracy is key in the study of plant growth and developmental processes, in which small root differences can lead to the identification of important genes (Benfey *et al.*, 1993; Li *et al.*, 2001; Mouchel *et al.*, 2004; Rodrigues *et al.*, 2009). We found that the implementation of primary root phenotyping algorithms in a platform using independent, semi-automatic and user-friendly software to accurately measure root length achieved by using MyROOT will replace the current manual and time-consuming tools such as ImageJ.

MyROOT gives the most precise root length measurements when compared with similar software BRAT and EZ-Rhizo (Figure S5 and Table S2). Importantly, the accuracy is maintained both in the manual and in the batch processing mode of MyROOT (Figures 3 and S4), being therefore suitable for high-throughput experiments. Under our experimental conditions, only BRAT operates in a faster manner, whereas the final results are less accurate (Figure S5 and Table S2). This can be explained because of the limited control that BRAT offers for the adjustment of its internal parameters by the users to adapt to different imaging conditions, which may result in low root detection rates (Table S2). Conversely, MyROOT easily allows the modification of different thresholds (scale and root mask threshold and hypocotyl detection method) to define the optimal parameters for the analysis.

Another novel feature of MyROOT compared with existing softwares is the ability to automatically identify the scale by detecting a ruler over the imaged plate; therefore being able to automatically adapt to different imaging conditions and settings; and therefore being able to work independently from specific hardware set ups (Table S1).

Importantly, MyROOT is the only software that uses machine learning-based algorithms to identify Arabidopsis hypocotyls, which allows its identification in different mutants and experimental conditions even when they are overlapped or present different morphologies. In exceptional cases in which the hypocotyls are not automatically identified, or when the software is used for the analysis of other plant species, they can be manually indicated by simply pointing over them.

In addition to the automatic processing of several images, MyROOT allows the user supervision during all the process. It displays intermediate results during the analysis and allows the modification of different parameters to get the optimal results. Despite that MyROOT only indicates the primary root length, the output is also saved in rsml software that allows its compatibility with other software that can determine other aspects of root architecture such as curvature or branching.

Overall, this article advances the utility of MyROOT for determination of Arabidopsis root length in a precise, fast and simple manner. It incorporates powerful algorithms to identify scale and seedlings over standard images of agar

plates. These are incorporated in a user-friendly graphical interface that allows supervision and manipulation during the different steps of the analysis.

Finally, MyROOT is a modularly designed software consisting of a group of specialized algorithms able to detect and analyze measuring tape, detect roots, track roots in a bottom-up fashion and detect hypocotyls. Therefore, any improvement to any of these components, or new algorithms to determine other features, can be easily included in subsequent versions of MyROOT. Examples of future improvements that could be included are the development of daily growth-monitoring algorithms that permit the detection of abnormal root growth patterns, analysis of root system architecture beyond the primary root, and identification of hypocotyls from other plant species. In the future, upgraded versions of our software could consist of a completely automatic operation connected to high-throughput facilities for large-scale characterization of root traits.

CONCLUSION

MyROOT is a software capable of semiautomatically measuring the length of the primary root of Arabidopsis seedlings. It automatically recognizes the scale of the image, and detects the hypocotyls and root tips from young seedlings growing vertically in agar plates. This information is then used to accurately calculate the root length of each individual plant. This software was designed in such a way that only a simple image of the plate is required for analysis. Importantly, MyROOT is even able to recognize hypocotyls of different ages and morphologies, and can therefore be applied in a large range of experiments.

Here, our validation experiments demonstrated the high precision of measurements made with MyROOT, thereby proving that this software can be used within the research community to perform high-throughput experiments in a less time-consuming manner.

EXPERIMENTAL PROCEDURES

Plant material and growth conditions

Arabidopsis thaliana Col-0 seeds were surface sterilized with a 5-min incubation in 1.5% sodium hypochlorite, followed by five washes in distilled sterile water. Seeds were stratified for 48 h at 4°C in the dark to synchronize germination. Seeds were sown in 12 × 12-cm plates containing half-strength Murashige and Skoog (½MS) medium without sucrose and supplemented with vitamins. Seeds were distributed individually in the plate in two rows with around 15 seeds per row. The plates were incubated for 3–8 days vertically oriented under long day conditions (16 h of light and 8 h of dark) at 22°C and 60% relative humidity.

Statistical analysis

The comparison between the root length measurements using MyROOT and ImageJ was evaluated by performing a regression curve and calculating the Pearson correlation coefficient. The comparison between the root length measurements using and not using the hypocotyl detection method was evaluated using Student's *t*-test. This test was selected due to the unequal number of seedlings detected under each condition.

Plant Imaging and computer settings

Images were taken with a D7000 Nikon camera. The pre-defined image acquisition conditions consist of placing the camera 50 cm above the plate with an illuminated support and the following settings: aperture 13, shutter speed 10, ISO 100 and Zoom ×35 magnification. The plates were placed face down on a black surface and with a ruler (at least 1 cm long) horizontally positioned on top (Figure S1). The images were saved in JPEG format (size between 2.5 and 2.7 MB per image). MyROOT and ImageJ were run in an Intel® Core™ i7-6700 CPU computer.

Box 1 Installation guide for MyROOT software

1. Execute MyAppInstaller_mcr.exe.
2. In the Root Analysis Installer window click the *Next* button.
3. In the Installation Options window select the folder where you wish to install the software. By default, the selected folder is C:\Program Files\La Salle – Universidad Ramon LIuII\Root_Analysis.
4. Mark the option *Add a shortcut to the desktop*.
5. Click the *Next* button.
6. In the Required Software window select the installation folder for the MATLAB Runtime (by default C:\Program Files \MATLAB\MATLAB Runtime).
7. Click the *Next* button.
8. In the License Agreement window mark the option *Yes*.
9. Click the *Next* button.
10. In the Confirmation window click the *Install* button.
11. Copy the HypocotylDetection folder to the desktop (this folder is in the same folder as the .exe file used for the installation).
12. Open the software by clicking in the MyROOT desktop icon.

Box 2 Brief user guide for individual plates analysis using MyROOT software

1. Open the software in a PC.
2. Select and load the image to process by pressing the *LOAD IMG* button. Enter an image resize factor between 0 and 1 in the Scale edit box to reduce the size of the image and speed up the processing of high-resolution images.
3. Obtain the pixels-to-millimeters scale factor by clicking the *Ruler ID* button. If needed, edit the Ruler Threshold value to modify the sensitivity of the ruler detector and repeat step 3. If there is no ruler in the image, insert the correspondence between pixels and millimeters manually in the 10 mm equivalence box.
4. Start the root segmentation process by clicking the *Root Mask* button. Select the area where the roots are present by clicking in the image. Double click in one of the vertex to start generating the mask. In case the result is not satisfactory (e.g. oversegmented roots), modify the sensitivity factor in the Root Threshold edit box and repeat step 4.
5. Enter a value in the Root Length Threshold box to indicate the minimum percentage with respect to the longest root to be measured.
6. Start the root tracking and measurement process by clicking the *Root Detection* button.
7. Enter the path of the files containing the pre-trained hypocotyl detection models in the Hypocotyl Model Path edit box.
8. Optionally, to perform hypocotyl detection based on color descriptors only, check the *Only Color* checkbox, and to conduct a channel-wise color normalization process check the *Norm Color* checkbox.
9. Optionally, modify the threshold of the linSVM classifier by modifying the value in the edit box located next to the Hypocotyl Detection button.
10. Start the hypocotyl detection process by clicking the *Hypocotyl Detection* button.
11. If some of the hypocotyls were undetected, insert them manually by using the *Add* button. Click the *Enter* key and click the *Root Refinement* button to update root length measurements.
12. Remove the undesired roots from the measurement by typing the root identifier in the ID edit box and clicking the *Remove* button. Click the *Visualize* button to refresh the image presented on MyROOT's visualization canvas.
13. Enter the path where you would like the results to be stored in the Results Path edit box.
14. Choose the type of data you want to save by checking the corresponding checkboxes.
15. Optionally, type an identification suffix that will be appended to the stored file names via the Root Label edit box.
16. Save the results by clicking the *SAVE* button.

Box 3 Brief user guide for batch processing using MyROOT software

1. Load one of the image of the folder to process and select the optimal parameters for the analysis (steps 2 to 9 in BOX 2).
2. Enter the path where you would like the results to be stored in the Results Path edit box.
3. Choose the type of data you want to save by checking the corresponding checkboxes.
4. Optionally, type an identification suffix that will be appended to the stored file names via the Root Label edit box.
5. Indicate the name of the folder with the images to process (Name\) in the *Folder Path* box.
6. Click the *Process* button to start the analysis.
7. Select if using the hypocotyl detection method by clicking in the *Yes* or *No* button in the box that appears.

Hypocotyl detection model

The software was trained to identify hypocotyls by using 1259 positive examples (hypocotyls) and 7915 background and negative examples (parts of the image that did not contain hypocotyls). The positive samples corresponded to Col-0 wild-type, *bri1-116,* and a transgenic line overexpressing BRI1-GFP, which have morphologically different hypocotyls as shown in González-Garcia *et al.* (2011).

Availability of data and materials

MyROOT has been developed in MATLAB (version 8.3.0.532. Natick, Massachusetts: The MathWorks Inc., 2014). It will be made available to the plant sciences community through the Plant Image Analysis website (plant-image-analysis.org; Lobet *et al.*, 2013) as a standalone executable application. The executable application together with the datasets generated during the current study (from Figures 3, 5 and S4) are available

in the [Zenodo] repository, [https://doi.org/10.5281/zenodo.2552250].

ACKNOWLEDGMENTS

We would like to thank Caño-Delgado Laboratory members for helping with manual root length measurements and comments on the manuscript. AIC-D is a recipient of a BIO2016-78150-P grant funded by the Spanish Ministry of Economy and Competitiveness and Agencia Estatal de Investigación (MINECO/AEI) and Fondo Europeo de Desarrollo Regional (FEDER), and a European Research Council, ERC Consolidator Grant (ERC-2015-CoG – 683163). IB-P is funded by the FPU15/02822 grant from the Spanish Ministry of Education, Culture and Sport. DB-E is funded by the ERC-2015-CoG – 683163 granted to the AIC-D laboratory. This project has received funding from the European Research Council (ERC) under the European Union's Horizon 2020 Research and Innovation Programme (Grant Agreement No. 683163). This work was supported by the CERCA Programme from the Generalitat de Catalunya. We acknowledge financial support from the Spanish Ministry of Economy and Competitiveness (MINECO), through the 'Severo Ochoa Programme for Centres of Excellence in R&D' 2016–2019 (SEV-2015-0533)'.

CONFLICT OF INTEREST

The authors declare no conflicts of interest.

AUTHOR CONTRIBUTIONS

AIC-D conceived the idea. AG and XS developed the algorithms for the method. AG, XS, IB-P and DB-E performed the validation experiments. IB-P and DB-E acquired the dataset. XS and AIC-D designed and supervised the study. IB-P, AG, XS and AIC-D wrote the manuscript.

SUPPORTING INFORMATION

Additional Supporting Information may be found in the online version of this article.

Figure S1. Laboratory setup for taking pictures of the plates.

Figure S2. The ruler identification process.

Figure S3. Evaluation of the time required to measure root length.

Figure S4. Validation of MyROOT batch analysis processing.

Figure S5. Comparison of MyROOT, BRAT and EZ-Rhizo softwares.

Table S1. Comparison of available semi-automatic softwares for quantification of root traits.

Table S2. Comparison of MyROOT, BRAT and EZ-Rhizo softwares.

Video S1. Demo video of MyROOT software.

REFERENCES

Armengaud, P., Zambaux, K., Hills, A., Sulpice, R., Pattison, R.J., Blatt, M.R. and Amtmann, A. (2009) EZ-Rhizo: integrated software for the fast and accurate measurement of root system architecture. *Plant J.* **57**, 945–956.

Arsenault, J., Poulcur, S., Messier, C. and Guay, R. (1995) Winrhizo: a root measuring system with a unique overlap correction method. *HortScience*, **30**, 906.

Beemster, G.T. and Baskin, T.I. (1998) Analysis of cell division and elongation underlying the developmental acceleration of root growth in Arabidopsis thaliana. *Plant Physiol.* **116**, 1515–1526.

Benfey, P.N., Linstead, P.J., Roberts, K., Schiefelbein, J.W., Hauser, M.T. and Aeschbacher, R.A. (1993) Root development in Arabidopsis: four mutants with dramatically altered root morphogenesis. *Development*, **119**, 57–70.

van den Berg, C., Willemsen, V., Hendriks, G., Weisbeek, P. and Scheres, B. (1997) Short-range control of cell differentiation in the Arabidopsis root meristem. *Nature*, **390**, 287–289.

Cai, J., Zeng, Z., Connor, J.N., Huang, C.Y., Melino, V., Kumar, P. and Miklavcic, S.J. (2015) RootGraph: a graphic optimization tool for automated image analysis of plant roots. *J. Exp. Bot.* **66**, 6551–6562.

Caño-Delgado, A.I., Metzlaff, K. and Bevan, M.W. (2000) The eli1 mutation reveals a link between cell expansion and secondary cell wall formation in Arabidopsis thaliana. *Development*, **127**, 3395–3405.

Clark, R.T., Famoso, A.N., Zhao, K., Shaff, J.E., Craft, E.J., Bustamante, C.D., McCouch, S.R., Aneshansley, D.J. and Kochian, L.V. (2013) High-throughput two-dimensional root system phenotyping platform facilitates genetic analysis of root growth and development. *Plant, Cell Environ.* **36**, 454–466.

Dalal, N. and Triggs, B. (2005) Histograms of oriented gradients for human detection. *IEEE Computer Society Conference on Computer Vision and Pattern Recognition*, **1**, 886–893.

Dolan, L., Janmaat, K., Willemsen, V., Linstead, P., Poethig, S., Roberts, K. and Scheres, B. (1993) Cellular organisation of the Arabidopsis thaliana root. *Development*, **119**, 71–84.

Fabregas, N., Lozano-Elena, F., Blasco- Escámez , D. *et al.* (2018) Overexpression of the vascular brassinosteroid receptor BRL3 confers drought resistance without penalizing plant growth. *Nat. Commun.* **9**, 4680.

French, A., Ubeda-Tomas, S., Holman, T.J., Bennett, M.J. and Pridmore, T. (2009) High-throughput quantification of root growth using a novel image-analysis tool. *Plant Physiol.* **150**, 1784–1795.

Glumov, N.I., Kolomiyetz, E.I. and Sergeyev, V.V. (1995) Detection of objects on the image using a sliding window mode. *Opt. Laser Technol.* **27**, 241–249.

González-Garcia, M.P., Vilarrasa-Blasi, J., Zhiponova, M., Divol, F., Mora-Garcia, S., Russinova, E. and Caño-Delgado, A.I. (2011) Brassinosteroids control meristem size by promoting cell cycle progression in Arabidopsis roots. *Development*, **138**, 849–859.

González-Garcia, M.P., Pavelescu, I., Canela, A., Sevillano, X., Leehy, K.A., Nelson, A.D., Ibanes, M., Shippen, D.E., Blasco, M.A. and Caño-Delgado, A.I. (2015) Single-cell telomere-length quantification couples telomere length to meristem activity and stem cell development in Arabidopsis. *Cell Rep.* **11**, 977–989.

Hauser, M.T., Morikami, A. and Benfey, P.N. (1995) Conditional root expansion mutants of Arabidopsis. *Development*, **121**, 1237–1252.

Ishikawa, H. and Evans, M.L. (1995) Specialized zones of development in roots. *Plant Physiol.* **109**, 725–727.

Iyer-Pascuzzi, A., Simpson, J., Herrera-Estrella, L. and Benfey, P.N. (2009) Functional genomics of root growth and development in Arabidopsis. *Curr. Opin. Plant Biol.* **12**, 165–171.

Jürgens, G., Mayer, U., Busch, M., Lukowitz, W. and Laux, T. (1995) Pattern formation in the Arabidopsis embryo: a genetic perspective. *Philos. Trans. R. Soc. Lond. B Biol. Sci.* **350**, 7.

Kuijken, R.C., van Eeuwijk, F.A., Marcelis, L.F. and Bouwmeester, H.J. (2015) Root phenotyping: from component trait in the lab to breeding. *J. Exp. Bot.* **66**, 5389–5401.

Le Bot, J., Serra, V., Fabre, J., Draye, X., Adamowicz, S. and Pages, L. (2010) DART: a software to analyse root system architecture and development from captured images. *Plant Soil*, **326**, 13.

Li, J., Nam, K.H., Vafeados, D. and Chory, J. (2001) BIN2, a new brassinosteroid-insensitive locus in Arabidopsis. *Plant Physiol.* **127**, 14–22.

Lobet, G. (2017) Image analysis in plant sciences: publish then perish. *Trends Plant Sci.* **22**, 559–566.

Lobet, G., Pages, L. and Draye, X. (2011) A novel image-analysis toolbox enabling quantitative analysis of root system architecture. *Plant Physiol.* **157**, 29–39.

Lobet, G., Draye, X. and Perilleux, C. (2013) An online database for plant image analysis software tools. *Plant Methods*, **9**, 38.

Lobet, G., Pound, M.P., Diener, J. *et al.* (2015) Root system markup language: toward a unified root architecture description language. *Plant Physiol.* **167**, 617–627.

Mouchel, C.F., Briggs, G.C. and Hardtke, C.S. (2004) Natural genetic variation in Arabidopsis identifies BREVIS RADIX, a novel regulator of cell proliferation and elongation in the root. *Genes Dev.* **18**, 700–714.

Nagel, K.A., Putz, A., Gilmer, F. *et al.* (2012) GROWSCREEN-Rhizo is a novel phenotyping robot enabling simultaneous measurements of root and shoot growth for plants grown in soil-filled rhizotrons. *Funct. Plant Biol.* **39**, 891–904.

Otsu, N. (1979) A threshold selection method from gray-level histograms. *IEEE Trans. Syst. Man Cybern.* **9**, 5.

Pace, J., Lee, N., Naik, H.S., Ganapathysubramanian, B. and Lubberstedt, T. (2014) Analysis of maize (*Zea mays* L.) seedling roots with the high-throughput image analysis tool ARIA (Automatic Root Image Analysis). *PLoS ONE* **9**, e108255.

Pfister, A., Barberon, M., Alassimone, J. *et al.* (2014) A receptor-like kinase mutant with absent endodermal diffusion barrier displays selective nutrient homeostasis defects. *ELife* **3**, e03115.

Potuschak, T., Lechner, E., Parmentier, Y., Yanagisawa, S., Grava, S., Koncz, C. and Genschik, P. (2003) EIN3-dependent regulation of plant ethylene hormone signaling by two Arabidopsis F box proteins: EBF1 and EBF2. *Cell*, **115**, 679–689.

Pound, M.P., French, A.P., Atkinson, J.A., Wells, D.M., Bennett, M.J. and Pridmore, T. (2013) RootNav: navigating images of complex root architectures. *Plant Physiol.* **162**, 1802–1814.

Ristova, D., Rosas, U., Krouk, G., Ruffel, S., Birnbaum, K.D. and Coruzzi, G.M. (2013) RootScape: a landmark-based system for rapid screening of root architecture in Arabidopsis. *Plant Physiol.* **161**, 1086–1096.

Rodrigues, A., Santiago, J., Rubio, S., Saez, A., Osmont, K.S., Gadea, J., Hardtke, C.S. and Rodriguez, P.L. (2009) The short-rooted phenotype of the brevis radix mutant partly reflects root abscisic acid hypersensitivity. *Plant Physiol.* **149**, 1917–1928.

Slovak, R., Goschl, C., Su, X., Shimotani, K., Shiina, T. and Busch, W. (2014) A scalable open-source pipeline for large-scale root phenotyping of Arabidopsis. *Plant Cell*, **26**, 2390–2403.

Takatsuka, H. and Umeda, M. (2014) Hormonal control of cell division and elongation along differentiation trajectories in roots. *J. Exp. Bot.* **65**, 2633–2643.

Ubeda-Tomas, S., Swarup, R., Coates, J., Swarup, K., Laplaze, L., Beemster, G.T., Hedden, P., Bhalerao, R. and Bennett, M.J. (2008) Root growth in Arabidopsis requires gibberellin/DELLA signalling in the endodermis. *Nat. Cell Biol.* **10**, 625–628.

Verbelen, J.P., De Cnodder, T., Le, J., Vissenberg, K. and Baluska, F. (2006) The root apex of *Arabidopsis thaliana* consists of four distinct zones of growth activities: meristematic zone, transition zone, fast elongation zone and growth terminating zone. *Plant Signal. Behav.* **1**, 296–304.

Wu, J., Wu, Q., Pages, L., Yuan, Y., Zhang, X., Du, M., Tian, X. and Li, Z. (2018) RhizoChamber-Monitor: a robotic platform and software enabling characterization of root growth. *Plant Methods*, **14**, 44.

Yazdanbakhsh, N. and Fisahn, J. (2012) High-throughput phenotyping of root growth dynamics. *Methods Mol. Biol.* **918**, 21–40.